UNIVERSITY OF OKLAHOMA

GRADUATE COLLEGE

A FRAMEWORK-BASED FINITE ELEMENT APPROACH FOR SOLVING LARGE DEFORMATION PROBLEMS IN MULTI-PHASE POROUS MEDIA

A Dissertation

SUBMITTED TO THE GRADUATE FACULTY

in partial fulfillment of the requirements for the

degree of

Doctor of Philosophy

By

NADARAJAH RAVICHANDRAN
Norman, Oklahoma
2005

UMI Number: 3203319

ProQuest Information and Learning Company
300 North Zeeb Road
P.O. Box 1346
Ann Arbor, MI 48106-1346

A FRAMEWORK-BASED FINITE ELEMENT APPROACH FOR SOLVING LARGE DEFORMATION PROBLEMS IN MULTI-PHASE POROUS MEDIA

A Dissertation APPROVED FOR THE
SCHOOL OF CIVIL ENGINEERING AND ENVIRONMENTAL SCIENCE

BY

_____
K. K. Muraleetharan

_____
G. A. Miller

_____
M. Zaman

_____
K.D. Mish

_____
L. White

_____
L. M. Taylor

Dedicated to My Mother

ACKNOWLEDGEMENT

I would like to express my sincere gratitude to my major advisor Dr. K.K. Muraleetharan for his encouragement, invaluable guidance, friendship, and financial support throughout this research program. During these years, his enthusiasm and broad view on research has had a great impact on me. I have learned a lot from him, both in the disciplines of research and about the attitude for life. It was a distinct privilege for me to work with Dr Muraleetharan. I would also like to thank the Muraleetharan family for providing my wife and me a home away from home.

I extend my appreciation to Drs. G.A Miller, M. Zaman, K.D. Mish, L. White, and L.M.Taylor for serving on my dissertation committee. I would like to especially thank Dr. L.M. Taylor for the helpful discussions and encouragement during this research program. Special thanks are attributed to Mr. Colin Potter of TeraScale, LLC for his technical support. Thanks are also given to my fellow graduate students Chunyang Liu, Danny Krier and other members of the Geotechnical Engineering group for their friendships.

I am grateful to the University of Oklahoma for the opportunity to pursue my graduate studies in the field of Geotechnical Engineering. This research was supported by two National Science Foundation (NSF) grants (Grant No. CMS-0112950 and CMS-0301457), and this support is acknowledged.

I would like to thank all my primary and secondary school teachers for showing me the importance of education in life and my family for their unconditional love and support. Most importantly, I thank my wife Thulasi for her help, sacrifices, and patience during my studies.

Table of Contents

List of Figures

List of Tables

ABSTRACT

Many researchers have recognized the importance of unsaturated soil mechanics and studies on unsaturated soils are at a new pace within the current research community. Unsaturated soils are three-phase porous media consisting of a solid skeleton, pore liquid and pore gas. The overall behavior of unsaturated soils is influenced not only by these three bulk phases, but also by the interfaces between them. Therefore, a rigorous solution for the behavior of unsaturated soils requires the consideration of the interactions between the bulk phases and the interfaces at the governing equation level. In a typical finite element solution of these governing equations, the relative accelerations of the fluids are neglected and the equations are solved by considering the solid skeleton displacement, pore water pressure and pore air pressure as the nodal unknowns. The influence of the accelerations of the pore liquid and pore gas pressures has not been carefully studied. However, for certain high frequency problems, such as blast loading of unsaturated soils, the effect of relative accelerations of the fluids may be significant. The consideration of the relative accelerations leads to the full finite element formulation for unsaturated soils, where solid displacement, liquid displacement, gas displacement, pore water pressure and pore gas pressure, all have to be considered as the nodal unknowns.

Solving the full formulation using finite element techniques requires tremendous computational capacity because of increased number of nodal unknowns and the nonlinear behavior of the soil skeleton. A single processor machine will not be adequate to solve real world problems. In such cases, the problem domain can be divided and distributed among a number of processors and solved. Writing finite element computer codes to run on multiple processors, however, requires a significant amount of computer

science knowledge that will not be readily available to a geotechnical engineer. A framework-based finite element technique can be used to simplify this effort. The framework provides the programming foundation upon which the core finite element algorithms can run in parallel using much of the existing code of the framework. The framework frees the finite element code developers from dealing with the computer science aspects of parallel computing as well as providing many common services necessary to such computations. A new high performance computational tool has been developed to analyze the static and dynamic behavior of saturated and unsaturated soils. The new tool is developed using a parallel finite element framework from TeraScale, LLC and is named TeraDysac. The TeraDysac is capable of running on multiple processors. The current version has been successfully tested on a two-processor machine.

The performance of the uniform gradient element formulation is studied by simulating settlement of a footing and dynamic behavior of a saturated clay embankment and a level ground. Significant hourglassing is seen for the footing problem when the uniform gradient elements were used without any hourglass control. The hourglass modes triggered by the stress gradients underneath the footing were found to propagate in all directions. The proposed hourglass control scheme is shown to be effective in controlling the excitation of hourglass modes. It is also found that for the dynamic problems that involves only body forces very little hourglassing was seen even when uniform gradient elements were used without any hourglass controls. The solid stiffness and solid damping hourglass control parameters show minor impact on displacement and pore pressure time histories. On the other hand, the fluid stiffness parameter shows significant influence on the displacement and pore pressure time histories. From the parametric study on the fluid

stiffness hourglass control parameter, it is recommended that this parameter should be less than 0.1%.

In the finite element simulation of dynamics of porous media, governing equations are derived and solved assuming that the material undergoes small deformation. However, liquefaction induced ground deformation and wetting induced slope failures are a few examples of large deformation problems. Therefore, large deformation analysis is required to correctly predict the behavior of porous media. A large deformation theory is developed for the saturated and unsaturated porous media and implemented within the TeraScale framework. The dynamic behavior of saturated and unsaturated porous media is studied using both small and large deformation analyses. The analyses show that the settlements are over predicted by small deformation analysis compared to the large deformation analysis.

The full formulation and a reduced formulation for unsaturated soils are implemented within the TeraScale framework. A centrifuge shaking experiment on unsaturated low permeable Minco Silt is simulated using both full and reduced formulations. It has been found that the reduced formulation predicts the dynamic response of the unsaturated Minco Silt embankment reasonably well. The reduced formulation is computationally very efficient. Therefore, it can be concluded that the reduced formulation is sufficient to predict the dynamic behavior of unsaturated Minco Silt.

1 INTRODUCTION

1.1 General

Most engineering structures are ultimately supported on the earth's surface that may consist of fully saturated soil, unsaturated soil and fully dry soil. One category of soil can become another due to seasonal variations. The mechanical behavior of each category of soil is different. The behavior of saturated and dry soils has been well studied in the past several decades. The study of unsaturated soil behavior is, however, a relatively new field. Geotechnical engineering structures designed with the knowledge of saturated and/or dry soils is inadequate to predict the performance of structures under unsaturated soil conditions. Therefore, construction of safe and economical structures requires extensive study of unsaturated soil behavior.

Describing any real world problem in terms of mathematical equations for numerical modeling requires a clear understanding of the physical phenomena. Our material of interest in this study is porous media, which consists of solid particles, and voids in between solid particles. The voids can be filled completely or partially with a liquid or a gas. In the case of a fully saturated soil, the voids are completely filled with a liquid. Hence, there will be two bulk phases: solid and liquid and one interface: solid-liquid interface. If the voids are completely filled with air, it is called a dry soil that has again two bulk phases: solid and air and one interface: solid-air interface. If the voids are

partly filled with a liquid and the rest with a gas, it is called an unsaturated soil which has three bulk phases: solid, liquid and gas and three interfaces: solid-liquid, liquid-gas and gas-solid. The unsaturated soil is the most difficult soil to study because of the additional bulk phase and the interfaces. It has also been found that the liquid pressure in the unsaturated soil system is always negative. The mechanical behavior of the unsaturated soil is governed not only by the behavior of the bulk phases and interfaces but also by the interaction between bulk phases and interfaces (Fredlund and Rahardjo, 1993). The behavior of bulk phases and interfaces can vary when the amount of liquid (degree of saturation) present within the voids vary.

1.2 Mathematical Description and Solution Procedure

The mathematical equations governing the behavior of the unsaturated soil system are derived based on physical laws. The balance of mass, balance of linear momentum, balance of angular momentum and the first and second laws of thermodynamics are used to derive the mathematical equations (for example, Wei, 2001). The mathematical equations will become more and more complicated when the true behavior has to be modeled. Difficulties arise when it comes to finding the solution of these complicated equations for a real word problem. In such cases, it is common to simplify the equations by neglecting less important terms and also terms that cause difficulties in finding the solution. In the case of unsaturated soils, the acceleration terms of the liquid and gas phases have been neglected in the solution procedure. Neglecting these terms from the governing equations will alter the actual physical problem to be solved. These acceleration terms not only contribute to inertial forces in dynamic problems, such as earthquake loading and blast loading of unsaturated soils but also cause the fluid phases

to move. Flow of liquid and gas phases changes the degree of saturation of the soil. When the degree of saturation changes, the behavior of unsaturated soil will change. Therefore, investigation of the effects of these terms on the overall behavior of the unsaturated soils is essential for safe and economical design of geotecnical engineering structures.

1.3 Efficient Computational Techniques for the Finite Element Method

Closed form solution to the nonlinear equations governing the dynamic behavior of porous media is impossible to find for a real problem. Therefore, numerical techniques such as the finite element method are widely used to solve the governing equations. In the finite element method, the problem domain is divided into finite number of small elements and the solutions are approximated within these elements. The number of finite elements increases with the size of the problem and the required accuracy. The computational cost will increase with the number of elements. Therefore, it is important to find a way to increase the efficiency of the computations in the finite element method so that large problems can be analyzed with reasonable accuracy.

The Gauss quadrature integration procedure is commonly used to evaluate the element matrices and vectors associated with the finite element method. In practice, evaluating the elemental integrands (e.g., computing constitutive parameters at all the Gauss quadrature points) can be a substantial component of the computational effort in performing a finite element approximation. The constitutive calculations become more costly when nonlinear elastoplastic constitutive models are used. Therefore, a lower order numerical integration scheme is desirable. For example, a one-point integration can be used to increase the efficiency of the computation. This approach has been successfully

used in solid and structural mechanics together with the hourglass control algorithm (Flanagan and Belytschko, 1981). However, this approach has not been applied in the fully coupled dynamic analysis of saturated or unsaturated porous media. Therefore, the applicability and the efficiency of single-point integration scheme in the numerical modeling of geotechnical engineering structures will be investigated in order to increase the computational effeciency.

1.4 Large Deformation Analysis in Numerical Modeling

The amount of strain and deformation experienced by geotechnical engineering structures vary depending on the type of load, soil, environmental conditions, etc. Liquefaction induced slope failures due to earthquake loadings, and soil deformation during pile driving and cone penetration tests are a few examples of large deformation problems in geotechnical engineering. Numerical modeling of these problems has been an important research area. Small strain and small deformation theories have been commonly used in such numerical modeling. However, predicting the soil behavior accurately requires special considerations associated with large deformations. Large deformation theories have been developed for saturated soils (Kiousis et al., 1988; Manzari, 2004) and implemented using the finite element method. A large deformation theory for unsaturated soils will be derived and implemented.

1.5 High-Performance Computational Framework

Investigating the dynamic behavior of saturated and unsaturated soils through finite element modeling requires a significant computational capacity due to the complicated and nonlinear nature of the soil behavior. The behavior of unsaturated soils is more complicated compared to the saturated soils because of the additional bulk phase

and the interfaces. Compared to the saturated soils, the computational effort required to solve an unsaturated soil problem is very high, e.g., 16 degrees of freedom per element for saturated soils and 24 degrees of freedom per element for unsaturated soils for 4-node quadrilateral elements. It has been observed that solving a reasonable size problem with a single processor in a personal computer takes weeks and sometimes months. This difficulty can be overcome by parallel computational techniques where the problem domain is divided and distributed over a number of processors and solved. Then, the computational time can be reduced drastically. Even though the parallel computing technology is widely used to solve such problems, the knowledge of developing parallel computing codes is not easy for civil engineering researchers because of the required in-depth knowledge of computer science techniques. Developing finite element computer codes with parallel capabilities is a very difficult task for civil engineers.

A framework-based finite element technique can be used to simplify this effort. The framework provides the programming foundation upon which the core finite element algorithms can run in parallel using much of its existing code. The framework frees the finite element code developers from dealing with the computer science aspects of parallel computing as well as providing many common services necessary to such computations. A new high performance computational tool has been developed based upon the TeraScale framework (TeraScale, 2001) to analyze the static and dynamic behavior of saturated and unsaturated soils.

In this research, the governing equations for the dynamics of unsaturated soils incorporating large deformation theories are derived. The governing equations for saturated and unsaturated soils incorporating small and large deformation theories are

implemented within the TeraScale finite element framework. The resulting computer code is named TeraDysac. The applicability and efficiency of the uniform gradient (single point integration) element together with an hourglass control scheme for the fully coupled analysis of porous media is investigated. The effects of accelerations of the fluid phases in the overall dynamic behavior of unsaturated soil are also investigated. The resulting computer code is named TeraDysac.

1.6 Objectives

Given below is a list of objectives of this dissertation.

1. To implement the fully coupled governing equations for the dynamics of saturated porous media within the TeraScale framework and develop a high performance computational tool for analyzing large problems.
2. To investigate the performance of the uniform gradient method of integrating the element matrices and vectors in the dynamic analysis of porous media.
3. To develop a theoretical framework for large deformation analysis of saturated and unsaturated soil and implement it within the TeraScale framework and investigate the importance of large deformation analysis in the simulation of dynamics of porous media.
4. To investigate the influence of accelerations of the fluid phases in the overall dynamic behavior of unsaturated soils.
5. To implement the full formulation for unsaturated, which considers the pressure fields also as primary unknowns together with displacement fields, and investigate the

advantages of full formulation over the usual displacement based formulation that eliminates the pressure fields at the governing equation level.

1.7 Thesis Layout

This thesis is divided into 10 chapters. Following this introductory chapter, Chapter 2 presents the literature review on the topics related to the research program. Chapter 3 presents the governing equations and finite element formulations for saturated and unsaturated soils. The finite element framework that is used to implement the governing equations derived in Chapter 3, is briefly discussed in Chapter 4. The numerical model is validated against the experimental results in Chapter 5. The applicability of the uniform gradient method of evaluating the element matrices in the simulation of dynamic behavior of porous media is discussed in Chapter 6. A theoretical framework for large deformation analysis of porous media is given in Chapter 7. The importance of large deformation analysis over the small deformation analysis is also discussed in Chapter 7. The finite element model incorporating the large deformation theories is validated in Chapter 8. The importance of acceleration terms in the overall behavior of unsaturated soils is also discussed in Chapter 8. Conclusions drawn from this study and recommendations and suggestions for future work are presented in Chapter 9. Cited previous work related to this study is listed in Chapter 10.

2 LITERATURE REVIEW

2.1 Porous Media

Unsaturated porous media consists of three bulk phases: solid, liquid and gas as shown in Fig. 2.1. In addition to these three bulk phases there exists three interfaces: solid-liquid interface, liquid-gas interface and gas-solid interface as shown in Fig. 2.2. On the other hand, saturated porous media, a special case of unsaturated porous media, consists of two bulk phases: solid and liquid, and one interface: solid-liquid interface. Because of the large number of bulk phases and interfaces, the study of unsaturated porous media becomes complicated. Among the three interfaces, the liquid-gas interface, which is also known as contractile skin and characterized by surface tension, plays an important roll in the behavior of an unsaturated soil system (Fredlund and Rahardjo, 1993). Wei (2001) and Wei and Muraleetharan (2002a, 2002b) have shown that the solid-gas and solid-liquid interfaces can also affect the whole behavior of the unsaturated soil system to a certain level. The overall mechanical behavior of unsaturated porous media is influenced not only by the behavior of bulk phases and interfaces but also by the interaction among various bulk phases and interfaces. Therefore, coupling the interaction of the bulk phases and interfaces at the governing equation level is important for correctly characterizing the unsaturated soil behavior.

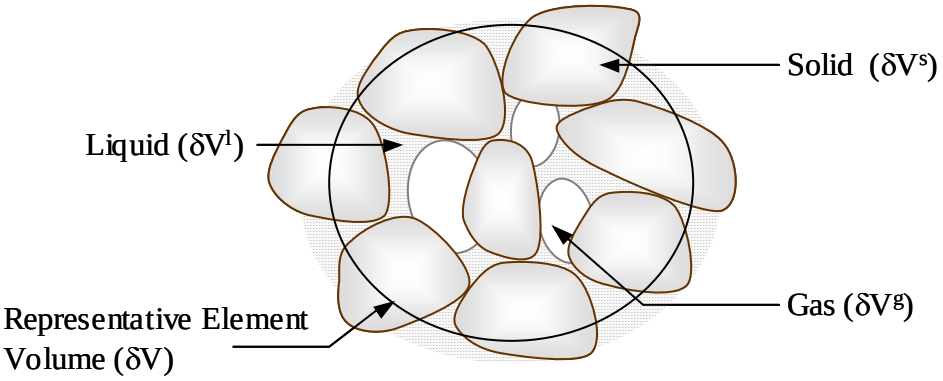

Figure 2.1: Unsaturated soil system

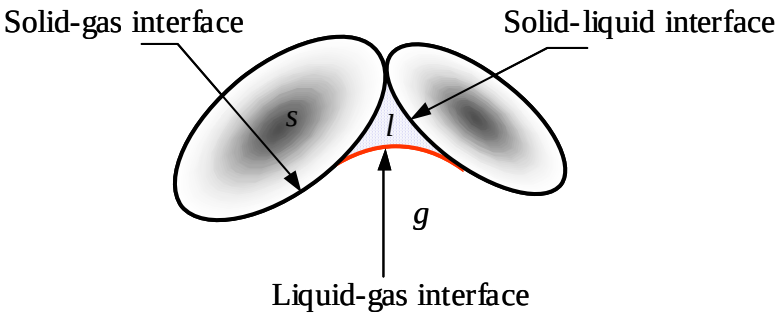

Figure 2.2: Interfaces and interface junctions

There are many approaches used in the past to describe the unsaturated soil system and apply the physical laws to derive the mathematical equations describing its behavior. Because of the complexities involved with unsaturated soils, initial attempts to describe the physical processes have relied on descriptive models that are more or less intuitive or empirical in nature (Gouse, 1966; Butterworh and Hewitt, 1979). The formulations of these models usually begins with a physical description of the system in which each phase is considered to be separate and occupying a portion of the space. However, the final set of field equations are written in terms of material properties for each phase that are continuous and defined over the whole space. The second approach used to develop governing equations for an unsaturated soil system is the continuum theory of mixtures

(Truesdell and Toupin, 1960). In this approach, it is assumed that all the existing phases are simultaneously present everywhere and occupy the whole domain. Continuous field variables are defined to account for the behavior of each phase and for the interaction among individual phases. The balance equations, which involve these variables, are postulated as an extension of the classical single-phase continuum equations. The third approach used to derive the multi-phase equations employs the technique of local volume averaging (Hassanizadeh and Gray, 1979). In this approach the system is assumed to consists, as in reality, of interpenetrating continua, each phase occupying only a part of the domain and separated by highly irregular interfaces. The usual field variables, associated with each phase and these variables, are continuous within each phase, but discontinuous over the entire domain. Muraleetharan and Wei (1999a), Wei (2001), and Wei and Muraleetharan (2002a, 2002b) developed a set of governing equations to describe the behavior of unsaturated soils using what they called the Theory of Mixtures with Interfaces (TMI). The TMI is based on the concept of local volume averaging and it gives explicit consideration to the interaction between various interfaces.

2.2 Effective Stress Concept and Stress State Variables in Unsaturated Porous Media

Terzaghi (1936) proposed the concept of 'effective stress' to describe the consolidation process of fully saturated porous media. The Terzaghi's effective stress equation is expressed by the following equation in terms of soil mechanics sign convention.

$$\boldsymbol{\sigma}' = \boldsymbol{\sigma} - \mathbf{I}\, p^{l} \tag{2.1}$$

where $\boldsymbol{\sigma}'$ is effective stress tensor, $\boldsymbol{\sigma}$ is total stress tensor, $\mathbf{I}$ is identity tensor and p^l is the liquid pressure.

The proposed effective stress equation is independent of the soil properties and the validity of the effective stress as a stress state variable for saturated soils has been well accepted and experimentally verified by many researchers (Bishop and Eldin, 1950; Skempton, 1961).

The effective stress concept, similar to saturated porous media, was extended to unsaturated porous media using a single stress variable, but considering the unsaturated medium as a three-phase system (Biot, 1941; Bishop, 1959; Aitchison, 1965; Aitchison et al., 1973). Among those various propositions, Bishop's equation (Eq. 2.2) gained widespread reference.

$$\boldsymbol{\sigma}' = \left(\boldsymbol{\sigma} - \mathbf{I}\, p^g\right) + \chi\left(p^g - p^l\right)\mathbf{I} \tag{2.2}$$

where p^g is the gas pressure and χ is a parameter related to the degree of saturation of the soil. The magnitude of the χ parameter is unity for a saturated soil and zero for a dry soil. Jennings and Burland (1962) showed that Bishop's equation did not provide an adequate relationship between volume change and effective stress for most soils, particularly those below a critical degree of saturation.

Matyas and Radhakrishna (1968) introduced the concept of state parameters in describing the volume change behavior of unsaturated soils. Volume change was presented as a three-dimensional surface with respect to the state parameters, $\left(\boldsymbol{\sigma} - \mathbf{I}\, p^g\right)$ and $\left(p^g - p^l\right)$. Barden et al., (1969) also suggested that the volume change of unsaturated soils be analyzed in terms of two stress-state variables, i.e. $\left(\boldsymbol{\sigma} - \mathbf{I}\, p^g\right)$ and

$\left(p^g - p^l\right)$. Fredlund and Morgenstern (1977) suggested that any of the three combinations: net normal stress $\left(\boldsymbol{\sigma} - \mathbf{I}\, p^g\right)$, matric suction $\left(p^g - p^l\right)$, and $\left(\boldsymbol{\sigma} - \mathbf{I}\, p^l\right)$ can be used to analyze unsaturated soils. Fredlund (1978) suggested that net stress $\left(\boldsymbol{\sigma} - \mathbf{I}\, p^g\right)$ and matric suction $\left(p^g - p^l\right)$ is the most advantageous combinations. These two stress state variables have gained widespread reference in the current state of the art in unsaturated soil mechanics and also will be used in this dissertation.

Any stress measure used in an analysis should have a corresponding conjugate strain measure. Using TMI and considering energy dissipation mechanisms within an unsaturated soil, Muraleetharan et al., (2005), Wei (2001) and Wei and Muraleetharan (2002a, 2002b) showed what they called a pseudo effective stress (Eq. 2.3) is conjugated with the plastic strains of the solid skeleton.

$$\boldsymbol{\sigma}' = \left(\boldsymbol{\sigma} - \mathbf{I}\, p^g\right) + n^l \left(p^g - p^l\right)\mathbf{I} \tag{2.3}$$

where n^l is the volume fraction of liquid (volume of liquid/total volume). They also showed that the matric suction $\left(p^g - p^l\right)$ is conjugated with the rate of change plastic n^l. They proposed that the pseudo effective stress and matric suction be used as the stress state variables. This approach seems promising as a general framework to develop elastoplastic constitutive models.

2.3 Relationship Between Matric Suction and Water Content

As matric suction is one of the two stress state variables used for characterizing the unsaturated soil behavior, it has to be understood very well. The matric suction is directly related to the amount of water present in the unsaturated soil. The Soil Water Characteristic Curve (SWCC), is the relationship between the amount of water in the

unsaturated soil system and the matric suction. SWCC contains important information concerning the amount of water contained in the pores for a given suction, the pore size distribution and stress state of the soil water. Numerical modeling of unsaturated soil behavior requires a mathematical description of SWCC. Many researchers (Gardner, 1958; Brooks and Corey, 1964; van Genuchten, 1980; Fredlund and Xing, 1994) have worked on establishing the SWCC for different soils and have approximated the experimental results with mathematical equations.

Brooks and Corey (1964) equation (Eq. 2.4) is one of the first models proposed for the SWCC, and still remains a popular model. The shape of the SWCC is assumed to be an exponentially decreasing function for soil suctions greater than the air entry value and constant for suctions less than the air entry value. The equation uses two fitting parameters: a and n. The parameter a is related to the air entry value of the soil and parameter n is related to the pore size distribution index in the unsaturated soil.

$$\begin{cases} \Theta = 1 & \psi < a \\ \Theta = \left(\frac{\psi}{a}\right)^{-n} & \psi > a \end{cases} \tag{2.4}$$

where ψ is matric suction and Θ is normalized water content given by $\Theta = \frac{\theta - \theta_r}{\theta_s - \theta_r}$,

where θ is water content, θ_s is saturated water content and θ_r is residual water content .

The advantage of this model is that both the parameters have physical meanings and the effect of each parameter can readily be seen. The downside of the Brooks-Corey's model is that it does not provide a continuous mathematical function for the entire range of suction. The degree of saturation can vary anywhere from zero to 100% during dynamic

analysis of unsaturated soils. The abrupt change in the curve at the value of a can give rise to numerical instability when modeling unsaturated soil behavior.

In 1980, van Genuchten proposed another model for SWCC. The model is a continuous function over the entire range of suction. The equation uses three fitting parameters; namely, a, n and m. The parameter a is related to the inverse of the air entry value; the parameter n is related to the pore size distribution of the soil and the parameter m is related to the asymmetry of the SWCC. The mathematical form of the van Genuchten model is given by:

$$\Theta = \frac{1}{\left[1 + (a\psi)^n\right]^m} \tag{2.5}$$

Fredlund and Xing (1994) also proposed a three-parameter model (Eq. 2.6) for SWCC. Their equation is somewhat similar to that of van Genuchten (1980) equation.

$$\Theta = \frac{1}{\left[\ln\left[e + \left(\frac{\psi}{a}\right)^n\right]\right]^m} \tag{2.6}$$

The advantages of the Fredlund and Xing (1994) model are as follows: more flexibility to fit a wide variety of data sets; the soil parameters are meaningful; the effect of one parameter can be distinguished from the effect of other two parameters. It has been also observed that the Fredlund and Xing (1994) model required fewer iterations to converge to the best fit parameters than the van Genuchten (1980) three parameter model (Fredlund and Xing, 1994).

2.4 Flow of Fluids in Unsaturated Soils

The coefficient of permeabilities of liquid and gas are two of the engineering soil properties that can vary over a wide range. For example, it is not uncommon for the coefficient of permeability of liquid in a given soil to vary as much as four orders of magnitude as the degree of saturation changes. This wide range of variation in coefficient of permeability has proven to be a major obstacle in analyzing the flow of fluids in unsaturated porous media. The coefficient of permeabilities for a given unsaturated soil are primarily determined by the amount of each fluid in the system and can be predicted from the soil water characteristic curve. van Genuchten (1980) and Fredlund and Xing (1994) have also proposed empirical equations for coefficient of permeabilities of unsaturated soils.

2.5 Constitutive Models for Unsaturated Soils

If we want to predict the behavior of structures made of soils accurately under complex loading conditions, it is important to model the stress-strain behavior of the soil skeleton realistically. An elastic material behavior assumption is used in many analyses. This is mainly because of the computational efficiency. However, elastic behavior assumption is a very poor assumption for soils under most loading conditions.

Alonso et al., (1990) proposed an elastoplastic constitutive model for describing the stress-strain behavior of unsaturated soils. This model is formulated within the framework of hardening plasticity using two independent stress state variables: net stress and matric suction. The model is able to represent, in a consistent and unified manner, many of the fundamental features of the behavior of unsaturated soil. However, this model does not represent the irreversible nature of expansion in swelling clays, the

decrease in collapse potential when confining stress becomes larger than a critical or threshold value, and the non-linear characteristics of the strength envelope.

Wheeler and Sivakumar (1995) modified Alonso et al.,'s model to include an isotropic normal compression hyperline, representing soil states when isotropically loaded to virgin condition, a critical state hyperline, representing soil state when sheared to ultimate or critical conditions, and a section of the state boundary hypersurface, joining the critical state and normal compression hyperlines. This modified model is capable of predicting the pattern of swelling and collapse observed during wetting, the elasto-plastic compression behavior during isotropic loading and the increase in shear strength with suction. One major uncertainty within this model is the nature of the relationship describing the elastoplastic variation of the specific water volume. Knowledge of the relationships describing the variation of specific volume is necessary in order to predict the water movement during drained loading. A description of variation of specific volume is also important for undrained loading, when the soil response is entirely dependent on the equations governing the specific volume.

Wheeler (1996) extended the previously proposed model to include the relationships describing the variation of specific volume that defines the volume of water within a given element of soil. The proposed form of the elastoplastic variation of specific water volume was based on the consideration of the soil fabric, i.e., there exists a saturated microstructure within individual clay packets and an unsaturated macrostructure of relatively large inter-packets of voids. The coupling of specific water volume within the elastoplastic model was achieved with two additional parameters.

Muraleetharan and Nedunuri (1998) developed an elastoplastic constitutive model for unsaturated soils incorporating the key concepts proposed by Alonso et al., (1990), Wheeler and Sivakumar (1995) and Wheeler (1996), but using a bounding surface model as the base model, i.e., at zero suction. This unsaturated model was also developed considering the net stress and matric suction as the stress state variables and is capable of predicting the monotonic and cyclic behavior of unsaturated soils.

The base bounding surface model used by Muraleetharan and Nedunuri (1998) was originally developed by Dafalias and Herrmann (1982) for predicting the behavior of saturated clays and modified by various other researchers (Dafalias, 1986; Dafalias and Herrmann, 1986; Ananadarajah and Dafalias, 1986). The prominent feature of the bounding surface concept is that plastic deformations can occur for stress states inside the yield surface. In classical plasticity theory, no plastic deformations are allowed inside the yield surface. The classical yield surface formulation is transformed into a bounding surface formulation based on the concept that for any stress point inside the surface, a unique “image” point can be defined on the surface by means of a radial mapping rule. The value of the plastic modulus depends on the distance between the actual stress point and its “image” on the bounding surface. The gradient of the bounding surface is used to define the direction of the plastic loading for the actual stress point.

Since the base model used by Muraleetharan and Nedunuri (1998) is specifically developed for clays, their unsaturated soil model can be expected to make better predictions for unsaturated clays compared to unsaturated sands and silts.

2.6 Finite Element Modeling of Porous Media

The governing equations for static and dynamic problems involve nonlinear differential equations. Finding closed form solutions for these equations is not possible for most of the geotechnical engineering problems. In such cases numerical methods such as the Finite Element Method (FEM) are widely used to find an approximate solution for the problem. Finite Element procedures are well developed for many engineering problems (for example, Zienkiewicz, 1977). The important steps involved in the finite element modeling of porous media are discussed in the subsequent sections.

2.6.1 Spatial Discretization of Field Equations

In the solution procedure of equations governing the dynamics of porous media using a finite element technique, a decision has to be made on what field variables are used as primary unknowns. In the case of a saturated porous media, the final set of fully coupled governing equations consists of solid displacement, $\mathbf{u}$, liquid displacement, $\mathbf{U}$, and pore water pressure, p (Zienkiewicz and Shiomi, 1984). One can use all three variables as the primary unknowns in the finite element solution. The full formulation ($\mathbf{u} - \mathbf{U} - p$) is the most general form and can be applied to saturated porous media filled with compressible or incompressible fluid. However, as far as the author knows, there is no published literature available on the solution of the full formulation. If the fluid is assumed to be compressible, the pore water pressure can be eliminated at the governing equation level or at element level and the final set of equations will have solid displacement and fluid displacement as nodal variables. This reduced formulation is called $\mathbf{u} - \mathbf{U}$ formulation and was used by Zienkiewicz and Shiomi (1984) and Muraleetharan et al., (1994). If the fluid is assumed to be incompressible, then the full

formulation or a penalty formulation has to be used and pore pressure should be eliminated at equation level (Zienkiewicz and Shiomi, 1984). In quasi-static or slow motion phenomena, which are typical of consolidation behavior of soils, all the acceleration terms in the equation of motion become negligible and can be confidently omitted. The simplified equations can be expressed in terms of solid displacement and pore water pressure. This formulation is called the $\mathbf{u}-p$ formulation and is used especially in the numerical simulation of consolidation phenomena (for example, Herrmann and Mish, 1983). If only fluid acceleration terms are neglected, a $\mathbf{u}-p$ formulation for dynamic problems can also be developed that will be applicable for medium speed such as such as earthquakes (Zienkiewicz and Shiomi, 1984).

A similar approach is extended to the finite element simulation of unsaturated porous media. There has been only one form of finite element equations solved for the dynamics of unsaturated porous media. In this form, the accelerations relative to the solid skeleton of the liquid and gas phases are neglected and the equations are solved considering solid displacement, liquid pressure and gas pressure as the primary nodal unknowns ($\mathbf{u}\,p^l\,p^g$ formulation). The $\mathbf{u}\,p^l\,p^g$ formulation is commonly used in computational geomechanics (Schrefler et al., 1990; Muraleetharan and Wei, 1999b; Wei 2001). Four-node quadrilateral elements with continuous bilinear displacement and a pressure interpolation function have been used in the $\mathbf{u}\,p^l\,p^g$. This violates the Babuska-Brezzi conditions that are described in Section 2.6.4, for solvability and convergence. The degree of saturation can also be introduced in the formulation and considered as a primary nodal unknown (Xikui and Zienkiewicz, 1992).

2.6.2 Element Technology for Finite Element Method

Lower-order elements when applied to incompressible material tend to lock volumetrically. In volumetric locking, the displacements are under-predicted by large factors. It is not uncommon for the displacement to be an order of magnitude too small for otherwise reasonable meshes. Although incompressible materials are quite rare in linear stress analysis, many materials behave in a nearly incompressible manner in the nonlinear region. For example, the plastic deformation of elastoplastic material shows incompressible behavior. The issue of incompressibility is an important problem in the simulation of saturated and unsaturated porous media because of the nearly incompressible nature of the liquid phase present in these soils. Therefore, the ability to treat incompressible materials effectively is important in the nonlinear finite element analysis of porous media. There are two methods commonly employed to eliminate the occurrence of volumetric locking in the modeling of incompressible materials and they are:

1. Selective-Reduced integration procedures in which certain terms of the weak form are underintegrated.
2. Multi-field elements in which the pressure or stress and strain fields are also considered as independent variables.

2.6.3 Selective-Reduced Integration

The concept of selective integration was first employed by Doherty et al., (1969) to obtain improved bending behavior in simple four-node elasticity elements. For incompressible or nearly incompressible materials, full quadrature of the nodal internal forces may cause an element to lock, i.e. the displacements are very small and do not

converge, or very slowly converge. The easiest way to circumvent this difficulty is to use selective-reduced integration. In selective reduced integration, the volumetric stress is under integrated, whereas the remainder of the stress matrix is fully integrated. For this purpose, the stress tensor is decomposed into hydrostatic and deviatoric components

$$\sigma_{ij} = \sigma^{vol} + \sigma_{ij}^{dev}$$

where

$$\sigma^{vol} = \frac{1}{3}\sigma_{kk},\ \sigma_{ij}^{dev} = \sigma_{ij} - \delta_{ij}\sigma^{vol}$$

The rate-of-deformation is similarly split into dilatational (volumetric) and deviatoric components that are defined by

$$D_{ij}^{dev} = D_{ij} - \frac{1}{2}\delta_{ij}D_{kk},\ D_{ij}^{vol} = \frac{1}{3}\delta_{ij}D_{kk}$$

where D_{ij} is the rate of deformation tensor.

Reduced integration was first devised by Zienkiewicz et al., (1971) to alleviate shear locking in plate bending. It saves a great deal of computational cost. For example, full integration (full Gauss quadrature) of the stiffness of a 4-node quadrilateral element requires four integration points, and for the 8-noded hexahedral element, eight integration points. Use of reduced integration only requires the evaluation of **all** the matrices at one point, the element centroid. One-point quadrature thus provides tremendous cost benefits in linear and nonlinear analyses. The reduced integration technique also provides the added benefit of eliminating spurious constraints in bending and incompressible applications, as demonstrated by Malkus and Hughes (1978).

Application of selective and reduced integration in the field of soil mechanics has lagged behind its common usage in the solid mechanics community. Solving the governing equations using finite element techniques involves several integrals, which should be evaluated over each element. In the case of the fully coupled analysis of porous media, the integrals consist of components of the solid skeleton and pore fluid fields. It should be noted here that the compressibility of the pore water in the saturated soils is small compared to the actual soil skeleton. Therefore, the problem of volumetric locking will arise not only in the calculation of consistent nodal point forces but also in the calculation of the fluid stiffness matrix. Typically, in 2-dimensions, a four-point Gauss quadrature integration rule is used to evaluate the matrices related to the solid skeleton and a single point integration rule is used to evaluate the fluid stiffness matrix. However, utilization of four-point quadrature rule to evaluate the solid stiffness matrix requires a large computational effort, as discussed before, due to the iterative process involved in nonlinear constitutive modeling.

The reduced (one-point) integration scheme is very useful in nonlinear analysis in which the finite element equation is solved by iterative methods, and involves large-scale computations. However, a single point integration scheme results in certain deformation modes, which are called hourglass modes or zero energy modes. If these modes are not controlled, hourglassing can grow without limit and obscure the actual solution.

Maenchen and Sack (1964) were the first to observe the hourglass modes in finite difference analysis. Little thought was given in the finite difference literature as to the origin of these hourglass modes. Further investigating along this line, Petschek and Hanson (1968) identified that the absence of bilinear terms in the velocity field accounts

for the hourglass modes. Belytschko (1974) established this idea in a finite element context. A number of techniques have been employed, with varying degrees of success, to control hourglassing. These can be divided into two types:

(1) Artificial viscosity: In this method, nodal forces proportional to and opposing a measure of the hourglassing deformation rate are introduced (Maenchen and Sack, 1964). There is no additional storage required for this method; only a relatively small increase in computational effort is required. On the other hand, control is often ineffective unless an extremely large viscous constant is used, which can result in reduction of the stable time step and distortion of the solution.

(2) Artificial stiffness: In this method, which is of relatively recent origin, forces proportional to and opposing the hourglass deformation itself are used (Flanagan and Belytschko, 1981; Belytschko et al., 1983). Some additional storage and about the same increase in computational effort as for artificial viscosity are required. Artificial stiffness is much more effective than artificial viscosity for hourglass control.

2.6.4 Mixed Formulation and Babuska-Brezzi Restriction

Standard displacement-based finite element methods are known to behave poorly for nearly incompressible or dilatant/contractant elastoplastic media, exhibiting volumetric locking effect and failing to correctly reproduce ultimate loads in limit state analyses. Well-known finite elements, which overcome these difficulties, include enhanced-assumed strain (EAS) elements (Simo and Rifai, 1990) or high-order mixed displacement–pressure formulations (Zienkiwicz and Taylor, 2000).

Mixed finite element formulations were first discussed by Fraeijs de Veubeke (1965) and Herrmann (1965). Herrmann (1965) developed a reduced form of Reissner’s

variational principle particularly suited to problems of incompressible and nearly incompressible elasticity and, based upon this principle, established the first effective finite elements for such cases. Prior to this development many displacement models were applied to these problems, and poor behavior was typically observed. The reasons for this were not understood at the time. Certain elements derived from Herrmann's formulation also failed. Hughes and Allik (1969) traced this failure to correspondence between mixed and displacement models, contained within Fraeijs de Veubeke's limitation principle (Fraeijs de Veubeke, 1965).

Galerkin Methods applied to nearly incompressible or incompressible material in the setting of a mixed finite element method have to fulfill the Ladyzenskaya-Babuska-Brezzi condition or the much simpler Zienkiewicz-Taylor patch test (Zienkiewicz and Taylor, 2000), to achieve unique solvability, convergence and robustness (Brezzi and Fortin, 1991). This imposes severe restrictions on the choice of the solution spaces for the unknowns. If these conditions are not satisfied the solution will show significant oscillations, rendering it useless. This prohibits the use of convenient elements that employ equal order shape functions for both, the displacements and the pressure, i.e., the four-node quadrilateral element with continuous bilinear displacements and pressure fields.

The commonly used mixed elements with discontinuous pressure and continuous pressure elements are shown in Figs. 2.3 and 2.4. The four-node quadrilateral element is commonly used in computational geomechnaics to achieve computational efficiency. If the pressure fields have to be used together with the displacement field, the pressure field has to be discontinuous as shown in Fig. 2.3(a) to satisfy the Babuska-Brezzi condition.

Use of continuous bilinear pressure approximation in the four-node quadrilateral element (Fig. 2.4(a)) will violate the Babuska-Brezzi condition. However, the bilinear approximation for pressure and displacement fields has been used in the simulation of unsaturated soils for the sake of simplicity (Schrefler and Simoni, 1990; Wei, 2001).

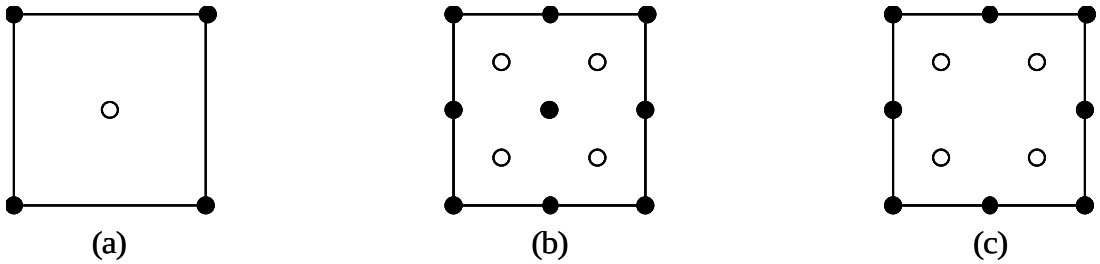

Figure 2.3: Discontinuous pressure elements

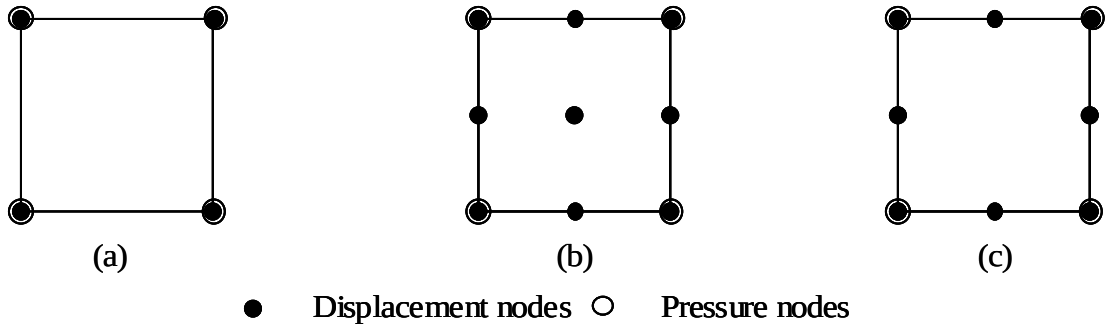

Figure 2.4: Continuous pressure field elements

2.6.5 Pressure Oscillation in Reduced and Mixed Formulations

The pressure field in the reduced and selective integration penalty function formulation is to be viewed as discontinuous from element to element. In fact, all displacement derivatives for C^0 isoparametric elements are, in general, discontinuous across element boundaries. Thus, for plotting purpose, it is desirable to employ a smoothing procedure, which redefines the field under consideration in terms of the displacement shape functions.

With specific reference to the pressure, there is at least one other reason for employing a smoothing procedure. It was mentioned earlier that, in certain situations,

discontinuous-pressure; mixed-method finite elements exhibit a rank-deficiency in the assembled pressure equations. By the equivalence theorem, problems are also to be expected with the pressure field in the penalty function formulation. These problems typically manifest themselves as pressure oscillations. For example, if four-node, quadrilateral elements are employed in a square mesh, with an even number of square elements in each direction, subjected to all velocity boundary conditions, then a checkboard pressure oscillation is produced. Despite the pressure oscillations, the velocity field remains acceptable.

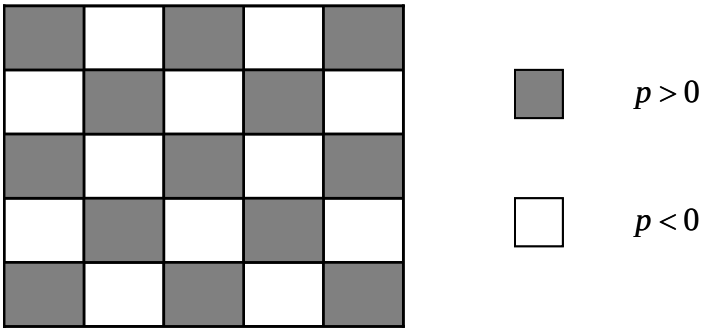

Figure 2.5: Checker-boarding mode, a consequence of pressure instability

2.7 Finite Deformation Analysis in Porous Media

Nonlinear response of geotechnical engineering structures typically results from plastic yielding and finite deformation of the solid skeleton. There are many classical geotechnical applications where nonlinear effects due to these two factors could critically influence the outcome of a numerical prediction. The large movement of slopes due to wetting and/or dynamic loading, collapse of embankments, lateral moments of level ground and tilting of structures due to earthquake loading, and movement of soil during cone and pile penetration are some of the examples where soils undergo finite deformations. The impact of finite deformation and elastoplastic response is most

evident in soft clays where movements develop with time due to consolidation, a phenomenon that involves transient interaction between the solid and fluid phases of the solid-fluid mixture.

In the development of theories for finite deformation analysis of elastoplastic materials, the decomposition of total strain is an important issue. The multiplicative decomposition and additive decomposition are equally used (Taylor and Becker, 1983; Simo and Hughes, 1986). In the multiplicative decomposition method, the deformation gradient, $\mathbf{F}$, is decomposed into an elastic part, $\mathbf{F}^e$, and a plastic part, $\mathbf{F}^p$ as shown in Eq.2.7 and Fig. 2.6 (Simo and Hughes, 1986). This method completely circumvents the rate issue in finite deformation analysis (Hughes, 1984; Nagtegaal and Jong, 1981), and allows for the development of large elastic strains.

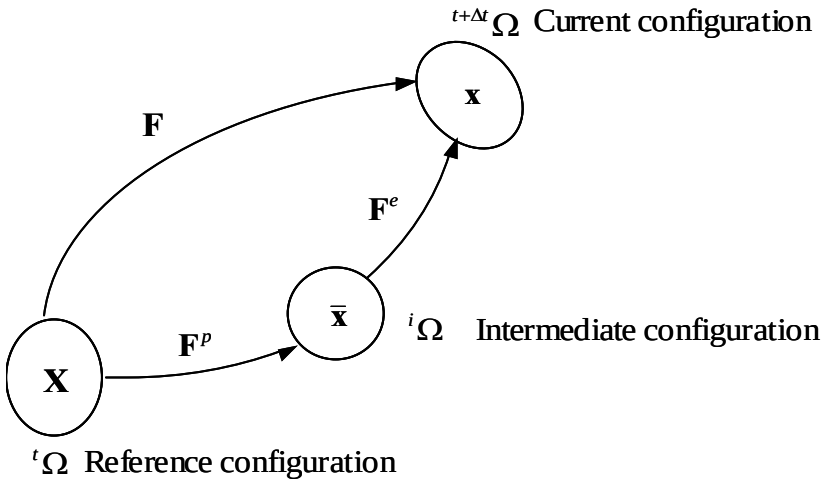

Figure 2.6: Multiplicative decomposition of deformation gradient

$$\mathbf{F} = \mathbf{F}^e \mathbf{F}^p \tag{2.7}$$

In particular, a more recent development (Simo and Taylor, 1991; Simo, 1992) indicates that the multiplicative decomposition technique can be exploited to such an extent that

the resulting algorithm may inherit all the features of the classical models of infinitesimal plasticity. The downside of this method is that a new constitutive equation has to be developed.

In the case of additive decomposition method, the deformation gradient is decomposed into elastic and plastic components as shown in Eq. 2.7. This method has been successfully used in the simulation of saturated porous media (Manzari, 1996, 2004; Kiousis et al., 1988).

$$\mathbf{F} = \mathbf{F}^e + \mathbf{F}^p \tag{2.8}$$

The additive decomposition is valid when the elastic components of the total strain are small. This assumption is a reasonable one for modeling saturated and unsaturated soils because these soils produce very small elastic strains. Advantage of this method is that the existing constitutive models cam be used.

2.7.1 Objective Stress Rates

The large deformation analysis with large rotations requires the use of constitutive relationships in a form that satisfy the principle of material frame indifference. A constitutive equation in rate form typically relates a spatial stress rate to the rate of deformation. Consequently, the requirement of material frame indifference for the constitutive relation mandates the use of a stress rate, which is objective (co-rotational) with respect to arbitrary rigid body translations and rotations. Numerous objective stress rates and formulations have been developed which satisfy this requirement. Szabo and Balla (1988) studied the advantages and disadvantages of some objective stress rates at very large deformations. They identified that most of the stress rates show similar behavior when the strain is below 40 percent. Beyond this limit, the Jaumann stress rate

and Truesdell stress rate show oscillations. The Green-Naghdi stress rate does not show oscillation and this stress rate can be used for very large strains.

2.8 Framework Based Finite Element Application Development

The governing equations for static and dynamic problems involve nonlinear differential equations. Finding closed form solutions for these equations is not possible for most of the geotechnical engineering problems. For these problems numerical methods such as the Finite Element Method (FEM) are widely used to find an approximate solution. FEM procedures are well developed for many engineering problems (Zienkiewicz et al., 1977). Historically, the finite element application developer has been an engineer trained in some specific field of mechanics. Typically they spend an inordinate portion of their software development time dealing with computer science aspects rather than focusing on algorithms and mechanics. A finite element framework insulates the engineer from the computer science aspects and lets the engineer concentrate on the computational mechanics aspects of the application.

A finite element framework represents a collection of software components for building finite element applications. By collecting these common calculations into a single toolkit, the framework enables the application developer to use these components in many different applications. Consequently, the amount of work and code required for developing and maintaining an application is greatly reduced. In addition to the computer science details, the framework may also provide the tools for parallel coding. The major coding required for running an analysis on multiple processors is hidden behind the framework. The major advantage of using a framework is, that the physics of a problem is completely separated from the computer science aspects of solving that problem. This

also helps in adding new physics (for example, changing a dynamic soil analysis code to predict contaminant transport as well) to an existing code developed within a framework.

Many researchers are realizing the advantage of using a finite element framework for developing applications for simulating geotechnical engineering problems. Two of the finite element frameworks currently available are OpenSees (Open System for Earthquake Engineering Simulation) and TeraScale (TeraScale, 2001). The TeraScale framework is used in this study to develop a high performance computational tool for static and dynamic analysis of saturated and unsaturated soils. A detailed description of the TeraScale framework is given in Chapter 4.

3 MATHEMATICAL MODELING OF POROUS MEDIA

3.1 Introduction

A model is an idealized and simplified representation of reality by using the language of mathematics. Most of the engineering problems can be represented by a set of mathematical equations and these equations are derived based on some well known physical principles such as conservation of mass, conservation of linear momentum, conservation of angular momentum, conservation of energy, and laws of thermodynamics. It is important to have a clear understanding of the physical phenomena (reality) before starting to develop mathematical equations that govern the physical behavior. The capability of the mathematical models to represent the true behavior depends on how clearly the physical problem is understood and whether or not all the factors influencing the physical behavior have been identified. It is worthwhile to note at this point that even if the actual behavior is very well understood, some of the complicated behavior in reality cannot be always represented with mathematical equations. In such situations, the true behavior is simplified with reasonable assumptions. These assumptions are made based on what features are important to predict a particular behavior.

In this chapter, general forms of the mathematical equations required for fully characterizing the dynamic behavior of saturated and unsaturated soils are derived. Wei (2001) also presented similar equations, but the governing equations are derived and presented here in forms that are more suitable for various finite element implementations of these equations. The general form does not apply any restrictions to the range of deformation, i.e., the finite deformation theories can be simply incorporated into these equations. The finite element formulations for various forms of these equations are also derived in this chapter.

3.2 Motion of Unsaturated Soils

The volume spanned by the solid phase is considered as the Representative Elementary Volume (R.E.V) and its motion is given by $\phi^s(\mathbf{X},t)$. The fluids that occupied the voids in the reference configuration may move out of the R.E.V. and occupy a volume spanned by a different current configuration. Similarly, the fluids that occupy the voids in a different reference configuration can move into the current configuration that is being considered (Fig. 3.1). Therefore, there will be net flow across the closed R.E.V. This net fluid flow has to be accounted for in deriving the mass balance equations for the unsaturated soils.

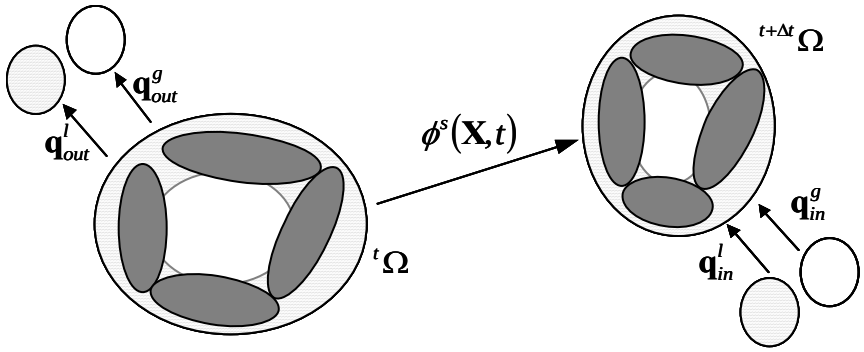

Figure 3.1: Motion of the unsaturated soil system

3.3 Governing Equations for Unsaturated Soils

3.3.1 Mass Balance for the Solid Phase:

The mass of the solid phase within an arbitrary R.E.V at time $t + \Delta t$

$$m^s(\Omega) = \int_{t+\Delta t}\int_{\Omega} \left(n^s \rho^s\right) d\Omega \tag{3.1}$$

where ρ^s is the density of the solid phase and n^s is the volume fraction of the solid phase and is given by $n^s = \frac{\Omega^s}{\Omega}$ where Ω^s is volume of solid phase and Ω is total volume of R.E.V. Applying the law of conservation of mass to Eq. 3.1 and then the Reynold's transport theorem, the following equation can be obtained.

$$\frac{D^s}{Dt}\left(n^s \rho^s\right) + \left(n^s \rho^s\right) \mathrm{div}\left(\mathbf{v}^s\right) = 0 \tag{3.2}$$

where $\mathbf{v}^s$ is the absolute velocity vector of the solid phase and $\frac{D^s}{Dt}$ is the material time derivative. The material time derivatives for the other phases will be taken with respect to the solid phase. Therefore, the superscript s in the material derivative will be omitted in the subsequent derivations. By taking the partial time derivatives and dividing by ρ^s, the equation reduces to:

$$\frac{n^s}{\rho^s}\frac{D\rho^s}{Dt} + \frac{Dn^s}{Dt} + n^s div\left(\mathbf{v}^s\right) = 0 \tag{3.3}$$

The density of the solid phase is a function of the inter particle pressure (compression positive) and it can be expressed as:

$$\rho^s = \rho^s\left(p^s\right)$$

$$\frac{D\rho^s}{Dt} = \frac{D\rho^s}{Dp^s}\frac{Dp^s}{Dt}$$

$$\frac{1}{\rho^s}\frac{D\rho^s}{Dt} = \frac{1}{\rho^s}\frac{D\rho^s}{Dp^s}\frac{Dp^s}{Dt}$$

Substituting for the derivative of the density into Eq. 3.3, Eq. 3.4 can be obtained.

$$\frac{n^s}{K^s}\dot{p}^s + \dot{n}^s + n^s \mathrm{div}\left(\mathbf{v}^s\right) = 0 \tag{3.4}$$

The physical meaning of each components of the above equation can be explained as follows: the first component represents the change in volume due to the compressibility of the solid grains, the second component represents the change in porosity of the solid grains and the third component represents the change in volume due to the volumetric strain of the solid skeleton. To be consistent with the subsequent derivations, the volume fraction of the solid phase is expressed in terms of the total porosity of the unsaturated soils as follows.

$$n^s + n = 1$$

$$n^s = \left(1 - n\right)$$

Substituting for n^s and $\dot{n}^s$ in Eq. 3.4 and neglecting the compressibility of the solid particles, Eq. 3.4 can be reduced to:

$$-\dot{n} + \left(1 - n\right)\mathrm{div}\left(\mathbf{v}^s\right) = 0 \tag{3.5}$$

3.3.2 Mass Balance for the Liquid phase:

Similar to the solid phase, the mass balance equation for the liquid phase can be written as follows.

$$\frac{D^l}{Dt}\left(n^l \rho^l\right) + n^l \rho^l \mathrm{div}\left(\mathbf{v}^l\right) = 0 \tag{3.6}$$

where $\mathbf{v}^l$ is the velocity vector of the liquid phase and n^l is volume fraction of the liquid phase and is given by

$n^l = \frac{\Omega^l}{\Omega}$ where Ω^l is volume of liquid phase in the R.E.V.

Since the flow of the liquid phase is described with respect to the solid phase. The material time derivatives associated with the liquid phase have to be taken with respect to the solid phase. The material time derivative reference can be converted to the solid phase by the following equation.

$$\frac{D^l}{Dt}(\ ) = \frac{D}{Dt}(\ ) + \text{grad}(\ )\cdot \mathbf{v}^{l,s} \tag{3.7}$$

where $\mathbf{v}^{l,s}$ is the absolute relative velocity vector of the liquid phase with respect to the solid phase.

Incorporating Eq. 3.7 into Eq. 3.6, the mass balance for the liquid phase in the R.E.V spanned by the solid phase is obtained as:

$$\frac{n^l}{\rho^l}\frac{D}{Dt}\left(\rho^l\right) + \frac{D}{Dt}\left(n^l\right) + \frac{1}{\rho^l}\text{grad}\left(n^l\rho^l\right)\cdot\left(\mathbf{v}^{l,s}\right) + n^l\text{div}\left(\mathbf{v}^l\right) = 0 \tag{3.8}$$

Expressing the density of the liquid in terms of its pressure (compression positive) under the isothermal condition, Eq. 3.8 can be reduced to:

$$\frac{n^l}{K^l}\dot{p}^l + \dot{n}^l + n^l\text{div}\left(\mathbf{v}^l\right) + \frac{1}{\rho^l}\text{grad}\left(n^l\rho^l\right)\cdot\left(\mathbf{v}^{l,s}\right) = 0 \tag{3.9}$$

where K^l is the bulk modulus of the liquid phase and is given by $\frac{1}{K^l}\frac{Dp^l}{Dt} = \frac{1}{\rho^l}\frac{D\rho^l}{Dt}$

3.3.3 Mass Balance for the Gas Phase

Following a similar procedure, the mass balance equation for the gas phase can be written as:

$$\frac{n^g}{K^g}\dot{p}^g + \dot{n}^g + n^g \operatorname{div}\left(\mathbf{v}^g\right) + \frac{1}{\rho^g}\operatorname{grad}\left(n^g \rho^g\right)\cdot\left(\mathbf{v}^{g,s}\right) = 0 \tag{3.10}$$

where $\mathbf{v}^{g,s}$ is the relative velocity of the gas phase with respect to the solid phase, and n^g is the volume fraction of the gas phase and is given by $n^g = \frac{\Omega^g}{\Omega}$

where Ω^g is the volume of the liquid phase in the R.E.V, K^g is the bulk modulus of the gas phase and is given by $\frac{1}{K^g}\frac{Dp^g}{Dt} = \frac{1}{\rho^g}\frac{D\rho^g}{Dt}$

The volume fraction of the gas phase can be removed from the mass balance equation by substituting in terms of total porosity and volume fraction of the liquid phase as follows.

$$n^g = n - n^l \tag{3.11}$$

Substituting Eq. 3.5 into Eq.3.11, the time derivative of the volume fraction of the gas phase can be written as:

$$\dot{n}^g = (1-n)\operatorname{div}\left(\mathbf{v}^s\right) - \dot{n}^l \tag{3.12}$$

Substituting Eq. 3.11 and 3.12 into Eq.3.10, the mass balance equation for the gas phase can be reduced to:

$$(1-n)\operatorname{div}\left(\mathbf{v}^s\right) + \left(n-n^l\right)\operatorname{div}\left(\mathbf{v}^g\right) + \frac{\left(n-n^l\right)}{K^g}\dot{p}^g - \dot{n}^l + \frac{1}{\rho^g}\operatorname{grad}\left(n^g\rho^g\right)\cdot\left(\mathbf{v}^{g,s}\right) = 0 \tag{3.13}$$

3.3.4 Constitutive Equation for the Volume Fraction of the Liquid Phase

The amount of water present in the unsaturated soil is directly related to the matric suction through the Soil Water Characteristic Curve (SWCC). The matric suction is one

of the two stress state variables controlling the overall behavior of the unsaturated soils. The volume fraction of the liquid phase is expressed as a function of the volumetric strain of the solid skeleton and the matric suction as follows (Wei, 2001).

$$n^l = n^l\left(\varepsilon_v, S\right) \tag{3.14}$$

where S is the matric suction and is given by $S = p^g - p^l$ and ε_v is volumetric strain of the solid skeleton.

Then, the time derivative of the volume fraction of the liquid phase is given by:

$$\dot{n}^l = \frac{\partial n^l}{\partial \varepsilon_v}\mathrm{div}\left(\mathbf{v}^s\right) + \frac{\partial n^l}{\partial S}\left(\dot{p}^g - \dot{p}^l\right) \tag{3.15}$$

It is required to calculate the derivative of the volume fraction of the liquid phase with respect to the volumetric strain of the solid skeleton and the matric suction to calculate the time derivative of the liquid phase.

Substituting Eq. 3.15 into Eq. 3.9 and Eq. 3.13, the following equations can be derived.

Liquid phase:

$$\begin{aligned}&\left(\frac{\partial n^l}{\partial \varepsilon_v}\right)\mathrm{div}\left(\mathbf{v}^s\right) + \left(n^l\right)\mathrm{div}\left(\mathbf{v}^l\right) + \left(\frac{n^l}{K^l} - \frac{\partial n^l}{\partial S}\right)\dot{p}^l + \left(\frac{\partial n^l}{\partial S}\right)\dot{p}^g \\ &+ \frac{1}{\rho^l}\mathrm{grad}\left(n^l \rho^l\right)\cdot\left(\mathbf{v}^{l,s}\right) = 0\end{aligned} \tag{3.16}$$

Gas phase:

$$\begin{aligned}&\left(1 - n - \frac{\partial n^l}{\partial \varepsilon_v}\right)\mathrm{div}\left(\mathbf{v}^s\right) + \left(n - n^l\right)\mathrm{div}\left(\mathbf{v}^g\right) + \left(\frac{\partial n^l}{\partial S}\right)\dot{p}^l + \left(\frac{\left(n - n^l\right)}{K^g} - \frac{\partial n^l}{\partial S}\right)\dot{p}^g \\ &+ \frac{1}{\rho^g}\mathrm{grad}\left(\left(n - n^l\right)\rho^g\right)\cdot\left(\mathbf{v}^g - \mathbf{v}^s\right) = 0\end{aligned} \tag{3.17}$$

3.3.5 Linear Momentum Balance for the Mixture

The linear momentum balance for a single phase (α - phase) is given by:

$$n^{\alpha}\rho^{\alpha}\frac{D^{\alpha}}{Dt}\left(\mathbf{v}^{\alpha}\right)=\operatorname{div}\left(\boldsymbol{\sigma}^{\alpha}\right)+n^{\alpha}\rho^{\alpha}\mathbf{g} \tag{3.18}$$

where $\boldsymbol{\sigma}^{\alpha}$ is the stress tensor acting on the α-phase and $\mathbf{g}$ is the gravitation acceleration vector. Expanding Eq. 3.18 and rearranging the components of the momentum balance for the unsaturated soil mixture can be written as:

$$\begin{aligned} &n^{s}\rho^{s}\frac{D\mathbf{v}^{s}}{Dt}+n^{l}\rho^{l}\left(\frac{D\mathbf{v}^{l}}{Dt}+\operatorname{grad}\left(\mathbf{v}^{l}\right)\cdot\mathbf{v}^{l,s}\right)+n^{g}\rho^{g}\left(\frac{D\mathbf{v}^{g}}{Dt}+\operatorname{grad}\left(\mathbf{v}^{g}\right)\cdot\mathbf{v}^{g,s}\right) \\ &=\operatorname{div}\left(\boldsymbol{\sigma}\right)+\rho\mathbf{g} \end{aligned} \tag{3.19}$$

where $\boldsymbol{\sigma}$ is the total stress tensor and is given by $\boldsymbol{\sigma}=\boldsymbol{\sigma}^{s}+\boldsymbol{\sigma}^{l}+\boldsymbol{\sigma}^{g}$ and ρ is the total density of the unsaturated soil and is given by $\rho=n^{s}\rho^{s}+n^{l}\rho^{l}+n^{g}\rho^{g}$

3.3.6 Linear Momentum Balance for the Liquid Phase

Describing the flow of the liquid and gas phase within the unsaturated soil system is important to correctly model the overall behavior. The momentum balance equations for these fluids are simply the Darcy's flow equation for the liquid phase (Eq.3.20). The major resistance to the flow of liquid in the unsaturated soil system is the drag force from the solid skeleton and the major driving force is the liquid pressure gradient (Fig. 3.2).

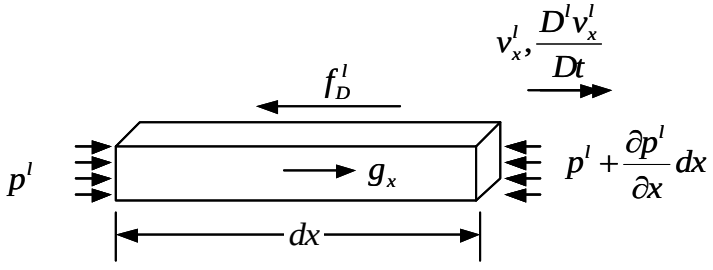

Figure 3.2: Motion of liquid phase

$$\rho^l \frac{D^l}{Dt}\left(\mathbf{v}^l\right) + \operatorname{div}\left(p^l\right) - \rho^l \mathbf{g} = -\boldsymbol{\mu}^l \cdot \mathbf{v}^{l,s} \tag{3.20}$$

where $\boldsymbol{\mu}^l$ is the viscosity tensor of the liquid phase.

The soil mechanics sign convention (positive in compression) is applied to the pressure term in the above equation. Taking material time derivatives with respect to the solid phase, the flow equation (Eq. 3.20) becomes:

$$\rho^l \left(\frac{D\mathbf{v}^l}{Dt} + \operatorname{grad}\left(\mathbf{v}^l\right) \cdot \mathbf{v}^{l,s} \right) + \operatorname{div}\left(p^l\right) - \rho^l \mathbf{g} = -\boldsymbol{\mu}^l \cdot \mathbf{v}^{l,s}$$

The viscosity of the liquid phase is related to the permeability of the liquid phase through the following equation.

$$\left(\frac{\boldsymbol{\mu}^l}{n^l} \right) = \frac{1}{\mathbf{k}^l}$$

Substituting for the viscosity tensor and rearranging the components, the following equation can be derived for the linear momentum balance for the liquid phase in the unsaturated soil system.

$$\rho^l \frac{D\mathbf{v}^l}{Dt} + \rho^l \operatorname{grad}\left(\mathbf{v}^l\right) \cdot \mathbf{v}^{l,s} + \frac{n^l}{\mathbf{k}^l} \cdot \mathbf{v}^{l,s} + \operatorname{div}\left(p^l\right) - \rho^l \mathbf{g} = 0 \tag{3.21}$$

3.3.7 Linear Momentum Balance for the Gas Phase

The major resistance to the flow of gas is the drag force from the solid skeleton presence on the path of the gas flow and the major driving force is the gas pressure gradient (Fig. 3.3). Following similar procedure as for the liquid phase, the momentum balance for the gas phase can be written as shown in Eq. 3.22.

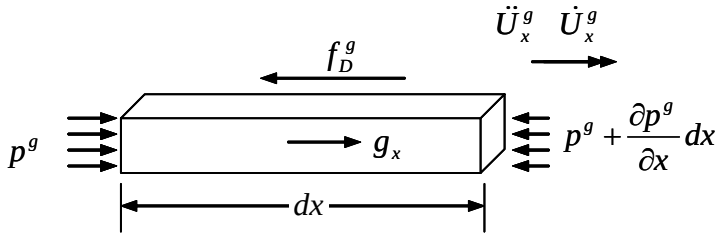

Figure 3.3: Motion of gas phase

$$\rho^g \frac{D\mathbf{v}^g}{Dt} + \rho^g \text{grad}\left(\mathbf{v}^g\right) \cdot \mathbf{v}^{g,s} + \frac{n^g}{\mathbf{k}^g} \cdot \mathbf{v}^{g,s} + \text{div}\left(p^g\right) - \rho^g \mathbf{g} = 0 \tag{3.22}$$

3.3.8 The Convective Terms

The convective acceleration terms $\rho^l \text{grad}\left(\mathbf{v}^l\right) \cdot \mathbf{v}^{l,s}$ and $\rho^g \text{grad}\left(\mathbf{v}^g\right) \cdot \mathbf{v}^{g,s}$ in the momentum balance equations of the liquid and gas phases and terms $\frac{1}{\rho^l} \text{grad}\left(n^l \rho^l\right) \cdot \left(\mathbf{v}^{l,s}\right)$ and $\frac{1}{\rho^g} \text{grad}\left(n^g \rho^g\right) \cdot \left(\mathbf{v}^{g,s}\right)$ in the mass balance equations are neglected in the subsequent derivations because of numerical complexities.

In most past research, the relative acceleration and velocity terms were also neglected to obtain simplified equations. It can be argued that these relative terms are not significant because of the very small permeabilities associated with the liquid and gas phases of the unsaturated soil system. However, these terms may important to correctly predict the dynamic behavior of the unsaturated soils. It also tightly couples the individual phases of the unsaturated soils at the governing equation level. The significant of the accelerations and velocities of the pore fluids particularly on the dynamic behavior of the unsaturated soils are investigated by solving complete and reduced formulations and comparing the results. Finite element forms for complete and reduced formulations are derived in the next section.

3.4 Complete Formulation

In this formulation, the relative accelerations and relative velocities of the liquid and gas phases are taken into account. Substituting for the relative velocities in terms of absolute velocities of the liquid and gas phases, the mathematical equations describing the motion of the unsaturated soil system are summarized below.

The index "*j*" is reserved for direction and the index "*i*" is used primarily as repeated index. Bar (¯) is used to indicate the nodal and element values of the variable and the hat (^) is used for specified boundary values in the derivation of finite element equations. The governing equations are rewritten in the indicial notation form as follows.

Linear momentum balance for the mixture:

$$n^s \rho^s \ddot{u}_j + n^l \rho^l \ddot{U}^l_j + n^g \rho^g \ddot{U}^g_j - \sigma_{ij,i} - \rho g_j = 0 \tag{3.23}$$

Linear momentum balance for the liquid:

$$\rho^l \ddot{U}^l_j - \left(k^{*l}_{ij} n^l\right)\dot{u}_i + \left(k^{*l}_{ij} n^l\right)\dot{U}^l_i + \left(\delta_{ij} p^l\right)_{,i} - \rho^l g_j = 0 \tag{3.24}$$

Linear momentum balance for the gas:

$$\rho^g \ddot{U}^g_j - \left(k^{*g}_{ij} n^g\right)\dot{u}_i + \left(k^{*g}_{ij} n^g\right)\dot{U}^g_i + \left(\delta_{ij} p^g\right)_{,i} - \rho^g g_j = 0 \tag{3.25}$$

Mass balance for the liquid:

$$\left(\frac{\partial n^l}{\partial \varepsilon_v}\right)\dot{u}_{i,i} + n^l \dot{U}^l_{i,i} + \left(\frac{n^l}{\Gamma^l} - \frac{\partial n^l}{\partial S}\right)\dot{p}^l + \left(\frac{\partial n^l}{\partial S}\right)\dot{p}^g = 0 \tag{3.26}$$

Mass balance for the gas:

$$\left(1 - n - \frac{\partial n^l}{\partial \varepsilon_v}\right)\dot{u}_{i,i} + n^g \dot{U}^g_{i,i} + \left(\frac{\partial n^l}{\partial S}\right)\dot{p}^l + \left(\frac{n^g}{\Gamma^g} - \frac{\partial n^l}{\partial S}\right)\dot{p}^g = 0 \tag{3.27}$$

Note: the mass balance of the solid phase has been used in deriving Eq. 3.26 and 3.27.

3.4.1 The Full ($\mathbf{u}\mathbf{U}^l\mathbf{U}^g - p^l p^g$) Form of the Complete Formulation

There are various finite element forms that can be derived from the above governing equations. If the liquid has to be considered as an incompressible material, the full formulation is the only possible form. In the full formulation, the solid displacement ($\mathbf{u}$), liquid displacement ($\mathbf{U}^l$), gas displacement ($\mathbf{U}^g$), liquid pressure (p^l) and gas pressure (p^g) all are considered as primary unknowns in the solution procedure. To satisfy the convergence condition explained by Babuska-Brezzi condition (Section 2.6.4), the interpolation function space for the pressure fields has to be one order less than that of displacement fields. This leads to a constant pressure field approximation for the pressure fields when bilinear interpolation fields are used for displacement fields. Fig. 3.4 shows the nodal and element unknowns for the full formulation. To date this formulation has not been implemented into a finite element code. It should be noted, however, that tremendous computational effort will be required to solve the full formulation because of the large number of element degrees of freedom.

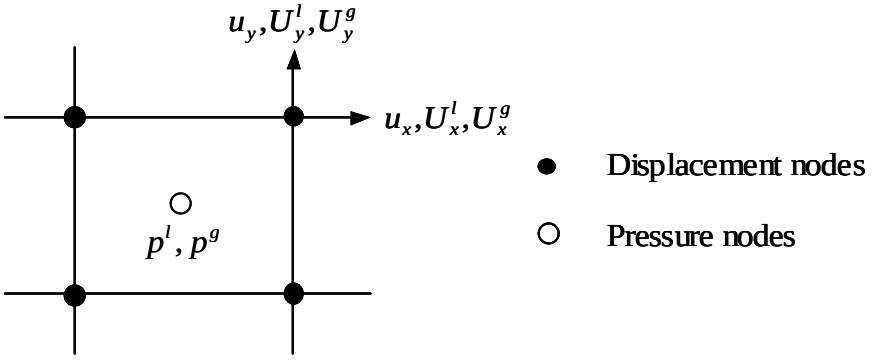

Figure 3.4: Continuous bilinear displacement and constant pressure approximation in two dimensions

3.4.1.1 Weak formulation of momentum balance equation for the mixture

The weak formulation is obtained by taking the product of the momentum balance equation with the test function as follows:

$$\int_{t+\Delta t\Omega}\left(n^s\,\rho^s\,\ddot{u}_j + n^l\rho^l\,\ddot{U}^l_j + n^g\rho^g\ddot{U}^g_j - \sigma_{ij,i} - \rho g_j\right)d\Omega = 0 \text{ in } {}^{t+\Delta t}\Omega$$

$$\int_{t+\Delta t\Omega}\phi^s_j\left(n^s\,\rho^s\,\ddot{u}_j + n^l\rho^l\,\ddot{U}^l_j + n^g\rho^g\ddot{U}^g_j - \sigma_{ij,i} - \rho g_j\right)d\Omega = 0$$

where ϕ^s_j is a test function for the momentum balance for the mixture.

Rearranging the components and Green's , the following equation can be derived

$$\int_{t+\Delta t\Omega}\phi^s_j\,n^s\rho^s\,\ddot{u}_j\,d\Omega + \int_{t+\Delta t\Omega}\phi^s_j\,n^l\rho^l\,\ddot{U}^l_j\,d\Omega + \int_{t+\Delta t\Omega}\phi^s_j\,n^g\rho^g\,\ddot{U}^g_j\,d\Omega - \int_{t+\Delta t\Omega}\left(\phi^s_j\sigma_{ij}\right)_{,i}d\Omega$$
$$+ \int_{t+\Delta t\Omega}\left(\phi^s_j\right)_{,i}\sigma_{ij}\,d\Omega - \int_{t+\Delta t\Omega}\phi^s_j\,\rho\,g_j\,d\Omega = 0$$

Traction Boundary Condition

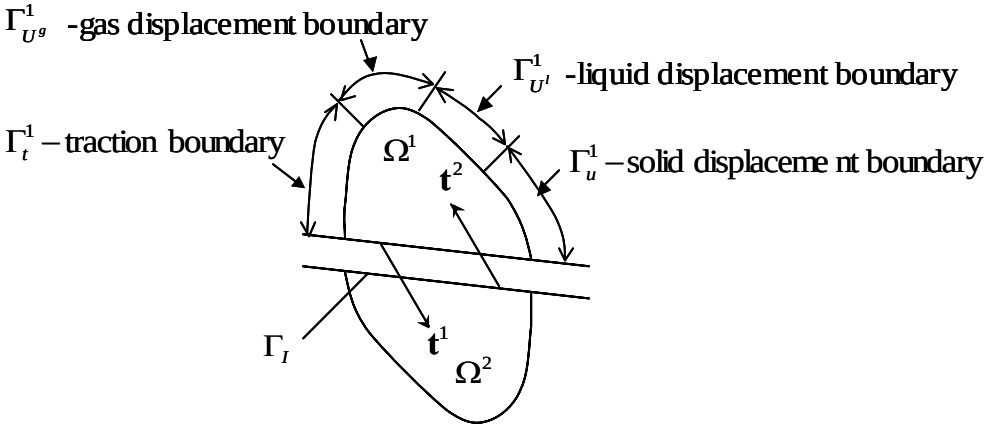

Figure 3.5: Schematic of the boundaries of multi phase porous media

Applying the Gauss theorem to the 4th integral and substituting the traction boundary conditions (Fig. 3.5), we get:

$$\int_{t+\Delta t\Omega} \phi_j^s \, n^s \rho^s \, \ddot{u}_j \, d\Omega + \int_{t+\Delta t\Omega} \phi_j^s \, n^l \, \rho^l \ddot{U}_j^l \, d\Omega + \int_{t+\Delta t\Omega} \phi_j^s \, n^g \rho^g \ddot{U}_j^g \, d\Omega + \int_{t+\Delta t\Omega} \left(\phi_j^s\right)_{,i} \sigma_{ij} \, d\Omega$$
$$= \int_{t+\Delta t\Omega} \phi_j^s \, \rho \, g_j \, d\Omega + \int_{t+\Delta t\Gamma_t} \phi_j^s \left(\hat{t}_j\right) d\Gamma \tag{3.28}$$

where $e_i \sigma_{ij} = \hat{t}_j$ on ${}^{t+\Delta t}\Gamma_t$ and e_i is the unit normal to the surface ${}^{t+\Delta t}\Gamma_t$.

3.4.1.2 Weak formulation of momentum balance equation for the liquid and gas phase

Following similar procedures, the weak form of the momentum balance equation for the liquid can be reduced to:

$$\int_{t+\Delta t\Omega} \phi_j^l \, \rho^l \ddot{U}_j^l \, d\Omega - \int_{t+\Delta t\Omega} \phi_j^l \left(k_{ij}^{*l} \, n^l\right) \dot{u}_i \, d\Omega + \int_{t+\Delta t\Omega} \phi_j^l \left(k_{ij}^{*l} \, n^l\right) \dot{U}_i^l \, d\Omega + \int_{t+\Delta t\Omega} \left(\phi_j^l \, \delta_{ij} \, p^l\right)_{,i} d\Omega$$
$$- \int_{t+\Delta t\Omega} \left(\phi_j^l\right)_{,i} \delta_{ij} \, p^l \, d\Omega - \int_{t+\Delta t\Omega} \phi_j^l \, \rho^l \, g_j \, d\Omega = 0$$

where ϕ_j^l is a test function for the momentum balance for liquid phase.

$\phi_j^l \delta_{ij} p^l$ is piecewise continuously differentiable even though a constant pressure approximation is expected to use for the pressure field. Then, applying the Gauss's theorem for the fourth integral and substituting the liquid pressure boundary conditions, we get:

$$\int_{t+\Delta t\Omega} \phi_j^l \, \rho^l \ddot{U}_j^l \, d\Omega - \int_{t+\Delta t\Omega} \phi_j^l \left(k_{ij}^{*l} \, n^l\right) \dot{u}_i \, d\Omega + \int_{t+\Delta t\Omega} \phi_j^l \left(k_{ij}^{*l} \, n^l\right) \dot{U}_i^l \, d\Omega - \int_{t+\Delta t\Omega} \left(\phi_j^l\right)_{,i} \left(\delta_{ij} \, p^l\right) d\Omega$$
$$= \int_{t+\Delta t\Omega} \phi_j^l \, \rho^l \, g_j \, d\Omega - \int_{t+\Delta t\Gamma_p} \phi_j^l \left(e_i \, \delta_{ij} \, \hat{p}^l\right) d\Gamma \tag{3.29}$$

where $\hat{p}^l$ is the specified liquid pressures on the liquid pressure boundary.

Similarly the weak form of the momentum balance for the gas phase can be derived as follows:

$$\int_{t+\Delta t\,\Omega} \phi_j^g \; \rho^g \; \ddot{U}_j^g \; d\Omega - \int_{t+\Delta t\,\Omega} \phi_j^g \left(k_{ij}^{*g} \; n^g\right) \dot{u}_i \; d\Omega + \int_{t+\Delta t\,\Omega} \phi_j^g \left(k_{ij}^{*g} \; n^g\right) \dot{U}_i^g \; d\Omega$$
$$- \int_{t+\Delta t\,\Omega} \left(\phi_j^g\right)_{,i} \left(\delta_{ij} \; p^g\right) d\Omega = \int_{t+\Delta t\,\Omega} \phi_j^g \; \rho^g \; g_j \; d\Omega - \int_{t+\Delta t\,\Gamma_p} \phi_j^g \left(e_i \; \delta_{ij} \; \hat{p}^g\right) d\Gamma \tag{3.30}$$

where ϕ_j^g is a test function and $\hat{p}^g$ is the specified gas pressures on the gas pressure boundary.

3.4.1.3 Weak formulation of mass balance equations

The weak form of the mass balance equation for the liquid and gas phases can be derived as follows:

Liquid phase:

$$\int_{t+\Delta t\,\Omega} \phi^{lp} \left(\frac{\partial n^l}{\partial \varepsilon_v}\right) \dot{u}_{i,i} \; d\Omega + \int_{t+\Delta t\,\Omega} \phi^{lp} \; n^l \; \dot{U}_{i,i}^l \; d\Omega + \int_{t+\Delta t\,\Omega} \phi^{lp} \left(\frac{n^l}{\Gamma^l} - \frac{\partial n^l}{\partial S}\right) \dot{p}^l \; d\Omega$$
$$+ \int_{t+\Delta t\,\Omega} \phi^{lp} \left(\frac{\partial n^l}{\partial S}\right) \dot{p}^g \; d\Omega = 0 \tag{3.31}$$

$$\int_{t+\Delta t\,\Omega} \phi^{gp} \left(1 - n - \frac{\partial n^l}{\partial \varepsilon_v}\right) \dot{u}_{i,i} \; d\Omega + \int_{t+\Delta t\,\Omega} \phi^{gp} \; n^g \; \dot{U}_{i,i}^g \; d\Omega + \int_{t+\Delta t\,\Omega} \phi^{gp} \left(\frac{\partial n^l}{\partial S}\right) \dot{p}^l \; d\Omega$$
$$+ \int_{t+\Delta t\,\Omega} \phi^{gp} \left(\frac{n^g}{\Gamma^g} - \frac{\partial n^l}{\partial S}\right) \dot{p}^g \; d\Omega = 0 \tag{3.32}$$

where ϕ^{lp} ϕ^{gp} are test functions

3.4.2 The Matrix Form

The test functions and other fields are expressed in terms of the nodal quantities and appropriate shape functions. In this study, an isoparametric quadrilateral element with bilinear continuous approximation is assumed for the solid, liquid and gas displacements fields and discontinuous constant approximation is used for the pressure fields.

$\phi_j^{\alpha} = N_I^{\alpha} \overline{\phi}_{I\,j}$ and $\overline{\phi}_{I\,j}$ are the nodal values of the test functions.

$u_j = N_I^s \overline{u}_{I\,j}$, $U_j^l = N_I^l \overline{U}_{I\,j}^l$ and $U_j^g = N_I^g \overline{U}_{I\,j}^g$

where the repeated index "I" means summation over all nodes and "j" indicates the coordinate direction.

$$p^l = N^{lp}\ \overline{p}^l$$

$$p^g = N^{gp}\ \overline{p}^g$$

3.4.2.1 Matrix form of momentum balance equation for the mixture

Most of the elastoplastic constitutive equations are developed considering the net stress and matric suction as the stress state variables. Therefore, the total stress in the momentum balance equation is replaced by net stress as follows.

$$\sigma_{ij} = \sigma''_{ij} - \delta_{ij}\ p^g$$

Substituting into Eq. 3.28, we get:

$$\phi_{I\,j} \int_{t+\Delta t\,\Omega} N_I^s\ n^s \rho^s\ \ddot{u}_j\, d\Omega + \phi_{I\,j} \int_{t+\Delta t\,\Omega} N_I^s\ n^l\ \rho^l\ \ddot{U}_j^l\, d\Omega + \phi_{I\,j} \int_{t+\Delta t\,\Omega} N_I^s\ n^g \rho^g\ \ddot{U}_j^g\, d\Omega$$
$$+ \phi_{I\,j} \int_{t+\Delta t\,\Omega} \left(N_I^s\right)_{,i} \left(\sigma''_{ij} - \delta_{ij}\ p^g\right) d\Omega = \phi_{I\,j} \int_{t+\Delta t\,\Omega} N_I^s\ \rho\, g_j\, d\Omega + \phi_{I\,j} \int_{t+\Delta t\,\Gamma} N_I^s\ \left(\hat{t}_j\right) d\Gamma$$

$$\phi_{I\,j} \int_{t+\Delta t\,\Omega} N_I^s\ n^s \rho^s\ \ddot{u}_j\, d\Omega + \phi_{I\,j} \int_{t+\Delta t\,\Omega} N_I^s\ n^l\ \rho^l\ \ddot{U}_j^l\, d\Omega + \phi_{I\,j} \int_{t+\Delta t\,\Omega} N_I^s\ n^g \rho^g\ \ddot{U}_j^g\, d\Omega$$
$$- \phi_{I\,j} \int_{t+\Delta t\,\Omega} \left(N_I^s\right)_{,i} \left(\delta_{ij}\ p^g\right) d\Omega + \phi_{I\,j} \int_{t+\Delta t\,\Omega} \left(N_I^s\right)_{,i} \left(\sigma''_{ij}\right) d\Omega = \phi_{I\,j} \int_{t+\Delta t\,\Omega} N_I^s\ \rho\, g_j\, d\Omega + \phi_{I\,j} \int_{t+\Delta t\,\Gamma} N_I^s\ \left(\hat{t}_j\right) d\Gamma$$

Substituting for the accelerations and pressures fields in terms of nodal and or element values, we get:

$$\int_{t+\Delta t\Omega} N_I^s \left(n^s \rho^s\right) N_J^s \, d\Omega \quad \ddot{\bar{u}}_j + \int_{t+\Delta t\Omega} N_I^s \left(n^l \rho^l\right) N_J^l \, d\Omega \quad \ddot{\bar{U}}_j^l + \int_{t+\Delta t\Omega} N_I^s \left(n^g \rho^g\right) N_J^g \, d\Omega \quad \ddot{\bar{U}}_j^g$$
$$- \int_{t+\Delta t\Omega} N_{I,i}^s \, \delta_{ij} \, N^{gp} d\Omega \quad \bar{p}^g + \int_{t+\Delta t\Omega} N_{I,i}^s \left(\sigma_{ij}''\right) d\Omega = \int_{t+\Delta t\Omega} N_I^s \, \rho \, g_j \, d\Omega + \int_{t+\Delta t\Gamma} N_I^s \left(\hat{t}_j\right) d\Gamma \tag{3.33}$$

3.4.2.2 Matrix form of momentum balance equation for the liquid and gas phases

Substituting for the test functions and other primary variables in terms of nodal variables, the following equations can be derived.

Liquid phase:

$$\int_{t+\Delta t\Omega} N_I^l \left(\rho^l\right) N_J^l \, d\Omega \quad \ddot{\bar{U}}_j^l - \int_{t+\Delta t\Omega} N_I^l \left(k_{ij}^{*l} n^l\right) N_J^s \, d\Omega \quad \dot{\bar{u}}_i + \int_{t+\Delta t\Omega} N_I^l \left(k_{ij}^{*l} n^l\right) N_J^l d\Omega \quad \dot{\bar{U}}_i^l$$
$$- \int_{t+\Delta t\Omega} N_{I,i}^l \, \delta_{ij} \, N^{lp} \, d\Omega \quad \bar{p}^l = \int_{t+\Delta t\Omega} N_I^l \left(\rho^l g_j\right) d\Omega - \int_{t+\Delta t\Gamma} N_I^l \left(e_i \, \delta_{ij} \, \hat{p}^l\right) d\Gamma \tag{3.34}$$

Gas Phase:

$$\int_{t+\Delta t\Omega} N_I^g \left(\rho^g\right) N_J^g \, d\Omega \quad \ddot{\bar{U}}_j^g - \int_{t+\Delta t\Omega} N_I^g \left(k_{ij}^{*g} n^g\right) N_J^s \, d\Omega \quad \dot{\bar{u}}_i + \int_{t+\Delta t\Omega} N_I^g \left(k_{ij}^{*g} n^g\right) N_J^g \, d\Omega \quad \dot{\bar{U}}_i^g$$
$$- \int_{t+\Delta t\Omega} N_{I,i}^g \, \delta_{ij} \, N^{gp} \, d\Omega \quad \bar{p}^g = \int_{t+\Delta t\Omega} N_I^g \left(\rho^g g_j\right) d\Omega - \int_{t+\Delta t\Gamma} N_I^g \left(e_i \, \delta_{ij} \, \hat{p}^g\right) d\Gamma \tag{3.35}$$

3.4.2.3 Matrix form of mass balance equation for the liquid and gas phases

Liquid phase:

$$\int_{t+\Delta t\Omega} N^{lp} \left(\frac{\partial n^l}{\partial \varepsilon_v}\right) N_{J,i}^s d\Omega \quad \dot{\bar{u}}_i + \int_{t+\Delta t\Omega} N^{lp} \left(n^l\right) N_{J,i}^l \, d\Omega \quad \dot{\bar{U}}_i^l$$
$$+ \int_{t+\Delta t\Omega} N^{lp} \left(\frac{n^l}{\Gamma^l} - \frac{\partial n^l}{\partial S}\right) N^{lp} \, d\Omega \quad \dot{\bar{p}}^l + \int_{t+\Delta t\Omega} N^{lp} \left(\frac{\partial n^l}{\partial S}\right) N^{gp} \, d\Omega \quad \dot{\bar{p}}^g = 0 \tag{3.36}$$

Gas Phase:

$$\int_{t+\Delta t}\int_{\Omega} N^{gp}\left(1-n-\frac{\partial n^{l}}{\partial \varepsilon_{v}}\right)N^{s}_{J,i}\,d\Omega\quad \bar{\dot{u}}_{i}+\int_{t+\Delta t}\int_{\Omega} N^{gp}\left(n^{g}\right)N^{g}_{J,i}\,d\Omega\;\bar{\dot{U}}^{g}_{i}$$
$$+\int_{t+\Delta t}\int_{\Omega} N^{gp}\left(\frac{\partial n^{l}}{\partial S}\right)N^{lp}\,d\Omega\;\bar{\dot{p}}^{l}+\int_{t+\Delta t}\int_{\Omega} N^{gp}\left(\frac{n^{g}}{\Gamma^{g}}-\frac{\partial n^{l}}{\partial S}\right)N^{gp}\,d\Omega\quad \bar{\dot{p}}^{g}=0 \tag{3.37}$$

The shape functions for solid displacement, N^{s}, liquid displacement, N^{l}, and gas displacement, N^{g}, are assumed to be the same and bilinear. The shape functions for gas pressure and liquid pressure are the same and constant and discontinuous. Therefore, it should be noted that there is no summation over nodal indices for the pressure approximation in the equation. These approximations will be used throughout this dissertation.

The system of equations (Eqs. 3.33, 3.34, 3.35, 3,36 and 3.37) can be written in the following general and compact form.

$$\mathbf{M}\,\ddot{\mathbf{x}}+\mathbf{C}\,\dot{\mathbf{x}}+\mathbf{K}\,\mathbf{x}+\mathbf{f}_{\text{int}}=\mathbf{f}_{ext}$$

where $\mathbf{M}$ is the mass matrix, $\mathbf{C}$ is the damping matrix, $\mathbf{K}$ is the fluid stiffness matrix, $\mathbf{f}_{\text{int}}$ is the internal force vector, $\mathbf{f}_{ext}$ is the external force vector and $\mathbf{x}$ is the generalized displacement vector given by

$$\mathbf{x}=\begin{Bmatrix} u \\ U^{l} \\ U^{g} \\ p^{l} \\ p^{g} \end{Bmatrix}$$

where u is the solid displacement, U^{l} is the liquid displacement, U^{g} is the gas displacement, p^{l} is the liquid pressure and p^{g} is the gas pressure.

This formulation is computationally intense. This formulation will have 26×26 element degrees of freedom for four-node quadrilateral element and 74×74 element degrees of freedom for eight-node brick element in 2D and 3D, respectively.

3.4.3 The Irreducible ($\mathbf{uU}^l\mathbf{U}^g$) Form of the Complete Formulation

If the liquid phase in the unsaturated soil system can be assumed to be a compressible material, then the pore liquid pressure and pore gas pressure terms in the momentum balance equations can be eliminated using the mass balance equations at the governing equation level. In this case, only the solid displacement, liquid displacement and gas displacements are considered as primary unknowns (Fig. 3.7) in the solution procedure. The liquid and the gas pressures are calculated outside the solver using the mass balance equations when the volumetric strain of the solid, liquid and gas are known. To author's knowledge this form also has not been used previously in any finite element implementation.

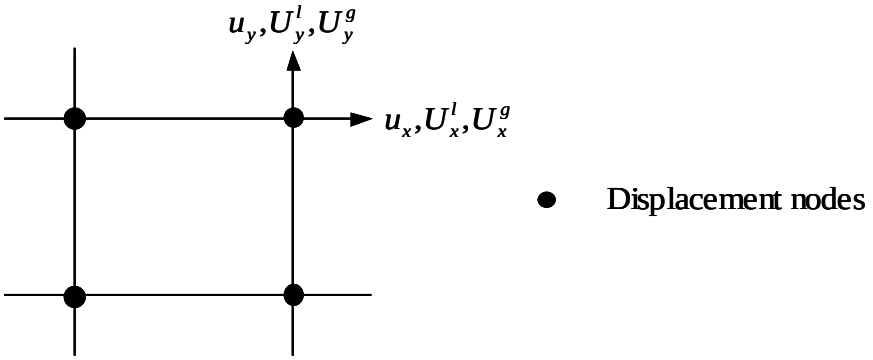

Figure 3.6: Nodal variables for the uUU formulation for the full form

The mass balance equations are rewritten in the following form for the shake of convenience.

$$a_{11}\ \dot{p}^l + a_{12}\ \dot{p}^g = -b_{11}\,\dot{u}_{k,k} - b_{12}\ \dot{U}^l_{k,k}$$

$$a_{21}\ \dot{p}^{l} + a_{22}\ \dot{p}^{g} = -b_{21}\,\dot{u}_{k,k} - b_{22}\,\dot{U}^{g}_{k,k}$$

The coefficients are defined as follows.

$$a_{11} = \left(\frac{n^{l}}{\Gamma^{l}} - \frac{\partial n^{l}}{\partial S}\right), a_{12} = \left(\frac{\partial n^{l}}{\partial S}\right), b_{11} = \left(\frac{\partial n^{l}}{\partial \varepsilon_{v}}\right),\ b_{12} = n^{l}$$

$$a_{21} = \left(\frac{\partial n^{l}}{\partial S}\right), a_{22} = \left(\frac{n^{g}}{\Gamma^{g}} - \frac{\partial n^{l}}{\partial S}\right), b_{21} = \left(1 - n - \frac{\partial n^{l}}{\partial \varepsilon_{v}}\right) \text{ and } b_{22} = \left(n^{g}\right)$$

where Γ^{l} and Γ^{g} are defined before. The above set of equations can be solved for p^{l} and p^{g}. The pore liquid pressure is given by:

$$p^{l} = \mu^{11}\ u_{k,k} + \mu^{12}\,U^{l}_{k,k} + + \mu^{13}\,U^{g}_{k,k}$$

where,

$$\mu^{11} = \left(\frac{a_{12}b_{21}}{\left(a_{22}a_{11} - a_{12}a_{21}\right)} - \frac{a_{22}b_{11}}{\left(a_{22}a_{11} - a_{12}a_{21}\right)}\right)$$

$$\mu^{12} = -\left(\frac{a_{22}b_{12}}{\left(a_{22}a_{11} - a_{12}a_{21}\right)}\right)$$

$$\mu^{13} = \left(\frac{a_{12}b_{22}}{\left(a_{22}a_{11} - a_{12}a_{21}\right)}\right)$$

The pore gas pressure is given by:

$$p^{g} = \mu^{21}\,u_{k,k} + \mu^{22}\,U^{l}_{k,k} + \mu^{23}\,U^{g}_{k,k}$$

where,

$$\mu^{21} = \left(\frac{a_{21}b_{11}}{\left(a_{22}a_{11} - a_{12}a_{21}\right)} - \frac{a_{11}b_{21}}{\left(a_{22}a_{11} - a_{12}a_{21}\right)}\right)$$

$$\mu^{22} = \left(\frac{a_{21}b_{12}}{\left(a_{22}a_{11} - a_{12}a_{21}\right)}\right)$$

$$\mu^{23} = -\left(\frac{a_{11} b_{22}}{\left(a_{22} a_{11} - a_{12} a_{21}\right)} \right)$$

Now, the liquid and gas pressure terms can be eliminated from the balance equations. The resulting equations will have only the displacement or the time derivatives of the displacement of the bulk phases. The momentum balance for the liquid phase is reduced as follows.

$$\rho^l \ddot{U}_j^l - \left(k_{ij}^{*l} n^l\right) \dot{u}_i + \left(k_{ij}^{*l} n^l\right) \dot{U}_i^l + \left(\delta_{ij} p^l\right)_{,i} - \rho^l g_j = 0$$

$$\rho^l \ddot{U}_j^l - \left(k_{ij}^{*l} n^l\right) \dot{u}_i + \left(k_{ij}^{*l} n^l\right) \dot{U}_i^l + \mu^{11} \delta_{ij} u_{k,ki} + \mu^{12} \delta_{ij} U_{k,ki}^l + \mu^{13} \delta_{ij} U_{k,ki}^g - \rho^l g_j = 0$$

Similarly, the momentum balance for the gas phase is reduced as follows.

$$\rho^g \ddot{U}_j^g - \left(k_{ij}^{*g} n^g\right) \dot{u}_i + \left(k_{ij}^{*g} n^g\right) \dot{U}_i^g + \left(\delta_{ij} p^g\right)_{,i} - \rho^g g_j = 0$$

$$\rho^g \ddot{U}_j^g - \left(k_{ij}^{*g} n^g\right) \dot{u}_i + \left(k_{ij}^{*g} n^g\right) \dot{U}_i^g + \mu^{21} \delta_{ij} u_{k,ki} + \mu^{22} \delta_{ij} U_{k,ki}^l + \mu^{23} \delta_{ij} U_{k,ki}^g - \rho^g g_j = 0$$

The final set of equations governing the motion of the unsaturated soil system is reduced to the following three equations.

$$n^s \rho^s \ddot{u}_j + n^l \rho^l \ddot{U}_j^l + n^g \rho^g \ddot{U}_j^g - \sigma_{ij,i} - \rho g_j = 0 \tag{3.38}$$

$$\rho^l \ddot{U}_j^l - \left(k_{ij}^{*l} n^l\right) \dot{u}_i + \left(k_{ij}^{*l} n^l\right) \dot{U}_i^l + \mu^{11} u_{i,ij} + \mu^{12} U_{i,ij}^l + \mu^{13} U_{i,ij}^g - \rho^l g_j = 0 \tag{3.39}$$

$$\rho^g \ddot{U}_j^g - \left(k_{ij}^{*g} n^g\right) \dot{u}_i + \left(k_{ij}^{*g} n^g\right) \dot{U}_i^g + \mu^{21} u_{i,ij} + \mu^{22} U_{i,ij}^l + \mu^{23} U_{i,ij}^g - \rho^g g_j = 0 \tag{3.40}$$

3.4.3.1 Weak form of the momentum balance equation for the mixture

From the $\mathbf{u}\mathbf{U}^l\mathbf{U}^g$ formulation, the weak form of the momentum balance equation for the mixture is given by:

$$\begin{aligned} &\int_{t+\Delta t_\Omega} \phi_j^s \, n^s \rho^s \, \ddot{u}_j \, d\Omega + \int_{t+\Delta t_\Omega} \phi_j^s \, n^l \, \rho^l \ddot{U}_j^l \, d\Omega + \int_{t+\Delta t_\Omega} \phi_j^s \, n^g \rho^g \, \ddot{U}_j^g \, d\Omega + \int_{t+\Delta t_\Omega} \left(\phi_j^s\right)_{,i} \sigma_{ij} \, d\Omega \\ &= \int_{t+\Delta t_\Omega} \phi_j^s \, \rho \, g_j \, d\Omega + \int_{t+\Delta t_{\Gamma_t}} \phi_j^s \left(\hat{t}_j\right) d\Gamma \end{aligned} \tag{3.41}$$

3.4.3.2 Weak form of the momentum balance equation for the liquid and gas phases

Liquid phase:

$$\int_{t+\Delta t\Omega}\left(\phi_j^l\ \rho^l\ \ddot{U}_j^l\right)d\Omega-\int_{t+\Delta t\Omega}\left(\phi_j^l\ k_{ij}^{*l}n^l\ \dot{u}_i\right)d\Omega+\int_{t+\Delta t\Omega}\left(\phi_j^l\ k_{ij}^{*l}n^l\ \dot{U}_i^l\right)d\Omega-\int_{t+\Delta t\Omega}\left(\phi_{j,j}^l\ \mu^{11}\ u_{i,i}\right)d\Omega$$
$$-\int_{t+\Delta t\Omega}\left(\phi_{j,j}^l\ \mu^{12}\ U_{i,i}^l\right)d\Omega-\int_{t+\Delta t\Omega}\left(\phi_{j,j}^l\ \mu^{13}\ U_{i,i}^g\right)d\Omega-\int_{t+\Delta t\Omega}\left(\phi_j^l\ \rho^l\ g_j\right)d\Omega=0 \tag{3.42}$$

Gas phase:

$$\int_{t+\Delta t\Omega}\left(\phi_j^g\ \rho^g\ \ddot{U}_j^g\right)d\Omega-\int_{t+\Delta t\Omega}\left(\phi_j^g\ k_{ij}^{*g}n^g\dot{u}_i\right)d\Omega+\int_{t+\Delta t\Omega}\left(\phi_j^g\ k_{ij}^{*g}n^g\ \dot{U}_i^g\right)d\Omega-\int_{t+\Delta t\Omega}\left(\phi_{j,j}^g\ \mu^{21}\ u_{i,i}\right)d\Omega$$
$$-\int_{t+\Delta t\Omega}\left(\phi_{j,j}^g\ \mu^{22}\ U_{i,i}^l\right)d\Omega-\int_{t+\Delta t\Omega}\left(\phi_{j,j}^g\ \mu^{23}U_{i,i}^g\right)d\Omega-\int_{t+\Delta t\Omega}\left(\phi_j^g\ \rho^g\ g_j\right)d\Omega=0 \tag{3.43}$$

3.4.3.3 Matrix form of the momentum balance equation for the mixture

Replacing the total stress in terms of net stress and substituting for the pore gas pressure, the following equation can be derived.

$$\int_{t+\Delta t\Omega}\phi_j^s\ n^s\rho^s\ \ddot{u}_j\ d\Omega+\int_{t+\Delta t\Omega}\phi_j^s\ n^l\rho^l\ddot{U}_j^l\ d\Omega+\int_{t+\Delta t\Omega}\phi_j^s\ n^g\rho^g\ddot{U}_j^g\ d\Omega-\int_{t+\Delta t\Omega}\left(\phi_j^s\right)_{,i}\delta_{ij}\ \mu^{21}u_{k,k}d\Omega$$
$$-\int_{t+\Delta t\Omega}\left(\phi_j^s\right)_{,i}\delta_{ij}\mu^{22}U_{k,k}^l d\Omega-\int_{t+\Delta t\Omega}\left(\phi_j^s\right)_{,i}\delta_{ij}\mu^{23}U_{k,k}^g d\Omega+\int_{t+\Delta t\Omega}\left(\phi_j^s\right)_{,i}\left(\sigma_{ij}''\right)d\Omega=\int_{t+\Delta t\Omega}\phi_j^s\ \rho\ g_j d\Omega$$
$$+\int_{t+\Delta t\Gamma_t}\phi_j^s\left(\hat{t}_j\right)d\Gamma$$

Substituting for test functions, accelerations and displacements, we get:

$$\int_{t+\Delta t\Omega}N_I^s\left(n^s\rho^s\right)N_J^s\ d\Omega\quad\ddot{\bar{u}}_j+\int_{t+\Delta t\Omega}N_I^s\left(n^l\rho^l\right)N_J^l\ d\Omega\quad\ddot{\bar{U}}_j^l+\int_{t+\Delta t\Omega}N_I^s\left(n^g\rho^g\right)N_J^g\ d\Omega\quad\ddot{\bar{U}}_j^g$$
$$-\int_{t+\Delta t\Omega}N_{I,i}^s\ \delta_{ij}\left(\mu^{21}\right)N_{J,k}^s\ d\Omega\quad\bar{u}_k-\int_{t+\Delta t\Omega}N_{I,i}^s\ \delta_{ij}\left(\mu^{22}\right)N_{J,k}^l d\Omega\quad\bar{U}_k^l \tag{3.44}$$
$$-\int_{t+\Delta t\Omega}N_{I,i}^s\ \delta_{ij}\left(\mu^{23}\right)N_{J,k}^g d\Omega\quad\bar{U}_k^g+\int_{t+\Delta t\Omega}N_{I,i}^s\left(\sigma_{ij}''\right)d\Omega=\int_{t+\Delta t\Omega}N_I^s\left(\rho g_j\right)d\Omega+\int_{t+\Delta t\Gamma_t}N_I^s\left(\hat{t}_j\right)d\Gamma$$

3.4.3.4 Matrix form of the momentum balance equation for the liquid and gas phases

Liquid phase:

$$\begin{aligned}
&\int_{t+\Delta t\Omega} N_I^l \left(\rho^l\right) N_J^l \, d\Omega \quad \ddot{\overline{U}}_j^l - \int_{t+\Delta t\Omega} N_I^l \left(k_{ij}^{*l} n^l\right) N_J^s \, d\Omega \quad \ddot{\overline{u}}_i + \int_{t+\Delta t\Omega} N_I^l \left(k_{ij}^{*l} n^l\right) N_J^l \, d\Omega \quad \dot{\overline{U}}_i^l \\
&- \int_{t+\Delta t\Omega} N_{I,j}^l \left(\mu^{11}\right) N_{J,i}^s \, d\Omega \quad \overline{u}_i - \int_{t+\Delta t\Omega} N_{I,j}^l \left(\mu^{12}\right) N_{J,i}^l \, d\Omega \quad \overline{U}_i^l \\
&- \int_{t+\Delta t\Omega} N_{I,j}^l \left(\mu^{13}\right) N_{J,i}^g d\Omega \quad \overline{U}_i^g = \int_{t+\Delta t\Omega} N_I^l \left(\rho^l \, g_j\right) d\Omega
\end{aligned} \tag{3.45}$$

Gas phase:

$$\begin{aligned}
&\int_{t+\Delta t\Omega} N_I^g \left(\rho^g\right) N_J^g \, d\Omega \quad \ddot{\overline{U}}_j^g - \int_{t+\Delta t\Omega} N_I^g \left(k_{ij}^{*g} n^g\right) N_J^s \, d\Omega \quad \ddot{\overline{u}}_i + \int_{t+\Delta t\Omega} N_I^g \left(k_{ij}^{*g} n^g\right) N_J^g \, d\Omega \quad \dot{\overline{U}}_i^g \\
&- \int_{t+\Delta t\Omega} N_{I,j}^g \left(\mu^{21}\right) N_{J,i}^s \, d\Omega \quad \overline{u}_i - \int_{t+\Delta t\Omega} N_{I,j}^g \left(\mu^{22}\right) N_{J,i}^l \, d\Omega \quad \overline{U}_i^l \\
&- \int_{t+\Delta t\Omega} N_{I,j}^g \left(\mu^{23}\right) N_{J,i}^g \, d\Omega \quad \overline{U}_i^g = \int_{t+\Delta t\Omega} N_I^g \left(\rho^g \, g_j\right) d\Omega
\end{aligned} \tag{3.46}$$

The above equations can be written in a compact form as follows.

$$\mathbf{M}\,\ddot{\mathbf{x}} + \mathbf{C}\,\dot{\mathbf{x}} + \mathbf{K}\,\mathbf{x} + \mathbf{f}_{\text{int}} = \mathbf{f}_{ext}$$

where $\mathbf{x}$ is given by

$$\mathbf{x} = \begin{Bmatrix} u \\ U^l \\ U^g \end{Bmatrix}$$

All the element matrices are 24×24 and 72×72 in size for 2D and 3D, respectively. All the vectors are 24×1 and 72×1 in size for 2D and 3D, respectively.

3.5 Reduced Formulation

In this formulation, the system of equations is simplified by neglecting the relative velocities and relative accelerations of the liquid and gas phases. Thus, the flow of liquid and gas phases is not taken into consideration. The change in pore liquid and gas

pressures is only affected by the deformation of the solid phase. This condition replicates the undrained condition for the unsaturated soils. Experimental studies on the flow through unsaturated soils reveals that the permeability of the fluids is small compared to the permeability of fluids in the saturated and dry soils. Therefore, the undrained condition assumption for analyzing the dynamic behavior of unsaturated soils may give reasonable results.

When the accelerations and velocities of the fluids are neglected, there will be only three equations left: momentum balance for the mixture, mass balance equation for the liquid phase and mass balance equation for the gas phase. The equations are summarized as follows.

Linear momentum balance for the mixture:

$$\rho \ddot{u}_j - \sigma_{ij,i} - \rho g_j = 0 \text{ in } {}^{t+\Delta t}\Omega \tag{3.47}$$

Mass balance for the liquid:

$$\left(n^l + \frac{\partial n^l}{\partial \varepsilon_v} \right) \dot{u}_{i,i} + \left(\frac{n^l}{\Gamma^l} - \frac{\partial n^l}{\partial p^c} \right) \dot{p}^l + \left(\frac{\partial n^l}{\partial p^c} \right) \dot{p}^g = 0 \text{ in } {}^{t+\Delta t}\Omega \tag{3.48}$$

Mass balance for the gas:

$$\left(1 - n^l - \frac{\partial n^l}{\partial \varepsilon_v} \right) \dot{u}_{i,i} + \left(\frac{\partial n^l}{\partial p^c} \right) \dot{p}^l + \left(\frac{n^g}{\Gamma^g} - \frac{\partial n^l}{\partial p^c} \right) \dot{p}^g = 0 \text{ in } {}^{t+\Delta t}\Omega \tag{3.49}$$

The above governing equations look uncoupled at the governing equation level, but there are actually coupled through constitutive equation in which matric suction is one of the stress state variables governing the mechanical behavior of unsaturated soils

3.5.1 The Full ($\mathbf{u} - p^l p^g$) Form of the Reduced Formulation

Again, to combat the incompressible behavior of the liquid phase, in addition to the solid displacement, the pressure fields should also be considered as primary unknowns. The element and nodal unknowns for this formulation is shown in Fig. 3.7.

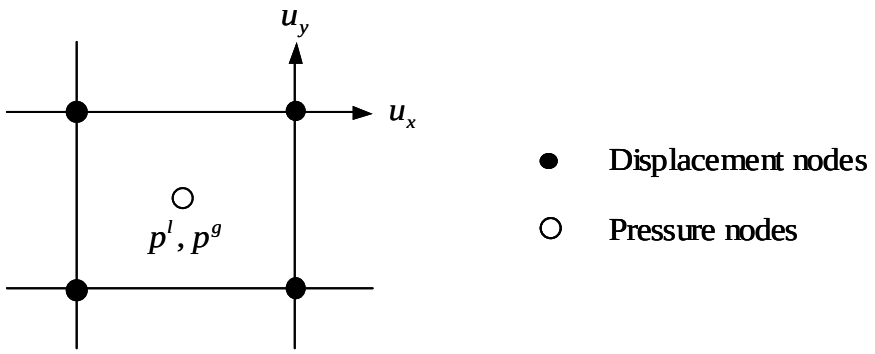

Figure 3.7: Continuous bilinear displacement and pressure interpolations in two dimensions

3.5.1.1 Weak and matrix formulation of momentum balance equation for the mixture

$$\int_{t+\Delta t\Omega} \left(\rho \ddot{u}_j - \sigma_{ij,i} - \rho g_j\right) d\Omega = 0 \text{ in } {}^{t+\Delta t}\Omega$$

$$\int_{t+\Delta t\Omega} \phi_j^s \left(\rho \ddot{u}_j\right) d\Omega - \int_{t+\Delta t\Omega} \phi_j^s \left(\sigma_{ij,i}\right) d\Omega - \int_{t+\Delta t\Omega} \phi_j^s \left(\rho g_j\right) d\Omega = 0$$

where ϕ_j^s is a test function for the momentum balance equation. Integrating the second integral by parts, we get:

$$\int_{t+\Delta t\Omega} \phi_j^s \left(\rho \ddot{u}_j\right) d\Omega - \int_{t+\Delta t\Omega} \left(\phi_j^s \sigma_{ij}\right)_{,i} d\Omega + \int_{t+\Delta t\Omega} \left(\phi_j^s\right)_{,i} \sigma_{ij}\, d\Omega - \int_{t+\Delta t\Omega} \phi_j^s \left(\rho g_j\right) d\Omega = 0$$

The Gauss theorem is used to convert a closed volume integral into a surface integral. The surface integral can be related to the external boundary conditions applied to the system. Utilizing the Gauss theorem for the second integral on the L.H.S, we get:

$$\int_{t+\Delta t\Omega} \phi_j^s \left(\rho \ddot{u}_j\right) d\Omega - \int_{t+\Delta t\Gamma} n_i \left(\phi_j^s \sigma_{ij}\right) d\Gamma + \int_{t+\Delta t\Omega} \left(\phi_j^s\right)_{,i} \sigma_{ij}\, d\Omega - \int_{t+\Delta t\Omega} \phi_j^s \left(\rho\, g_j\right) d\Omega = 0$$

Inserting the traction boundary conditions into the equations, we get

$$\int_{t+\Delta t\Omega} \phi_j^s \left(\rho \ddot{u}_j\right) d\Omega - \int_{t+\Delta t\Gamma_t} \phi_j^s \hat{t}_j\, d\Gamma + \int_{t+\Delta t\Omega} \left(\phi_j^s\right)_{,i} \sigma_{ij}\, d\Omega - \int_{t+\Delta t\Omega} \phi_j^s \left(\rho\, g_j\right) d\Omega = 0$$

Rearranging the components

$$\int_{t+\Delta t\Omega} \phi_j^s \left(\rho \ddot{u}_j\right) d\Omega + \int_{t+\Delta t\Omega} \left(\phi_j^s\right)_{,i} \sigma_{ij}\, d\Omega = \int_{t+\Delta t\Omega} \phi_j^s \left(\rho\, g_j\right) d\Omega + \int_{t+\Delta t\Gamma_t} \phi_j^s \hat{t}_j\, d\Gamma$$

Substituting the total stress in terms of net stress, we get:

$$\begin{aligned} &\int_{t+\Delta t\Omega} N_I^s (\rho) N_J^s d\Omega \quad \bar{\ddot{u}}_j - \int_{t+\Delta t\Omega} N_{I,i}^s \delta_{ij} N^{gp} d\Omega \quad \bar{p}^g + \int_{t+\Delta t\Omega} N_{I,i}^s \left(\sigma_{ij}''\right) d\Omega \\ &= \int_{t+\Delta t\Omega} N_I^s \left(\rho\, g_j\right) d\Omega + \int_{t+\Delta t\Gamma_t} N_I^s \hat{t}_j\, d\Gamma \end{aligned} \tag{3.50}$$

3.5.1.2 Matrix formulation of mass balance equation for the liquid and gas phase

Liquid phase:

$$\begin{aligned} &\int_{t+\Delta t\Omega} N^{lp} \left(n^l + \frac{\partial n^l}{\partial \varepsilon_v}\right) N_{J,i}^s\, d\Omega \quad \bar{\dot{u}}_i + \int_{t+\Delta t\Omega} N^{lp} \left(\frac{n^l}{\Gamma^l} - \frac{\partial n^l}{\partial p^c}\right) N^{lp}\, d\Omega \quad \bar{\dot{p}}^l \\ &+ \int_{t+\Delta t\Omega} N^{lp} \left(\frac{\partial n^l}{\partial p^c}\right) N^{gp}\, d\Omega \quad \bar{\dot{p}}^g = 0 \end{aligned} \tag{3.51}$$

Gas Phase:

$$\begin{aligned} &\int_{t+\Delta t\Omega} N^{gp} \left(1 - n^l - \frac{\partial n^l}{\partial \varepsilon_v}\right) N_{J,i}^s\, d\Omega \quad \bar{\dot{u}}_i + \int_{t+\Delta t\Omega} N^{gp} \left(\frac{\partial n^l}{\partial p^c}\right) N^{lp}\, d\Omega \quad \bar{\dot{p}}^l \\ &+ \int_{t+\Delta t\Omega} N^{gp} \left(\frac{n^g}{\Gamma^g} - \frac{\partial n^l}{\partial p^c}\right) N^{gp}\, d\Omega \quad \bar{\dot{p}}^g = 0 \end{aligned} \tag{3.52}$$

The general matrix form has a mass matrix and a damping matrix. This formulation does not have any pore fluid stiffness matrix in the formulation.

$$\mathbf{M}\,\ddot{\mathbf{x}} + \mathbf{C}\,\dot{\mathbf{x}} + \mathbf{K}\,\mathbf{x} + \mathbf{f}_{\text{int}} = \mathbf{f}_{ext}$$

where $\mathbf{x}$ is given by

$$\mathbf{x} = \begin{Bmatrix} u \\ p^l \\ p^g \end{Bmatrix}$$

3.5.1.3 The irreducible (u) form of the reduced formulation

If the liquid phase can be considered as a compressible material, then the solid displacement alone can be considered as the primary unknown as shown in Fig. 3.8.

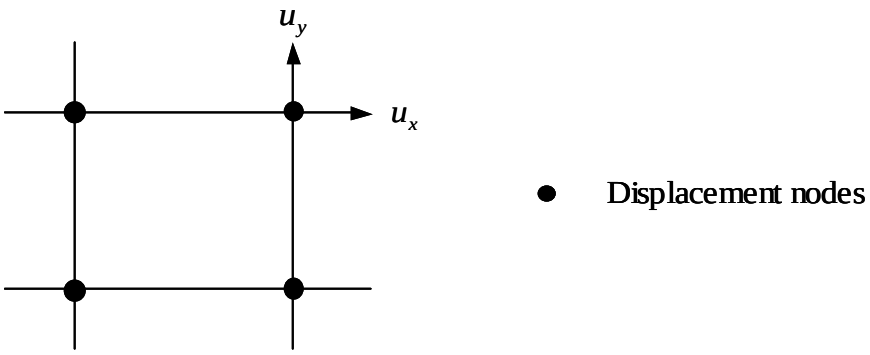

Figure 3.8: Continuous bilinear displacement interpolations in two dimensions

In this formulation only the solid displacement is considered as the nodal unknown. The liquid and gas pressures are calculated outside the solver using the mass balance equations.

3.5.1.4 Matrix formulation of momentum balance for the mixture

The liquid pressure and gas pressure are reduced from the mass balance equations to the following form:

$$p^l = \left(\frac{a_{12} b_{21}}{\left(a_{22} a_{11} - a_{12} a_{21}\right)} - \frac{a_{22} b_{11}}{\left(a_{22} a_{11} - a_{12} a_{21}\right)} \right) u_{k,k}$$

$$p^g = \left(\frac{a_{21} b_{11}}{(a_{22} a_{11} - a_{12} a_{21})} - \frac{a_{11} b_{21}}{(a_{22} a_{11} - a_{12} a_{21})} \right) u_{k,k}$$

where $a_{11} = \left(\frac{n^l}{\Gamma^l} - \frac{\partial n^l}{\partial S} \right)$, $a_{12} = \left(\frac{\partial n^l}{\partial S} \right)$ and $b_{11} = \left(\frac{\partial n^l}{\partial \varepsilon_v} \right)$,

$$a_{21} = \left(\frac{\partial n^l}{\partial S} \right), \; a_{22} = \left(\frac{n^g}{\Gamma^g} - \frac{\partial n^l}{\partial S} \right), \text{ and } b_{21} = \left(1 - n^l - \frac{\partial n^l}{\partial \varepsilon_v} \right)$$

$$\int_{t+\Delta t \Omega} \phi_j^s (\rho \ddot{u}_j) d\Omega - \int_{t+\Delta t \Omega} (\phi_j^s)_{,i} \delta_{ij} \mu^g u_{k,k} d\Omega + \int_{t+\Delta t \Omega} (\phi_j^s)_{,i} (\sigma''_{ij}) d\Omega = \int_{t+\Delta t \Omega} \phi_j^s (\rho g_j) d\Omega + \int_{t+\Delta t \Gamma_t} \phi_j^s \hat{t}_j d\Gamma$$

$$\begin{aligned} &\int_{t+\Delta t \Omega} N_I^s (\rho) N_J^s d\Omega \;\; \ddot{\bar{u}}_j - \int_{t+\Delta t \Omega} N_{I,i}^s \; \delta_{ij} \mu^g N_{J,k}^s \; d\Omega \;\; \bar{u}_k + \int_{t+\Delta t \Omega} N_{I,i}^s \; (\sigma''_{ij}) d\Omega \\ &= \int_{t+\Delta t \Omega} N_I^s (\rho g_j) d\Omega + \int_{t+\Delta t \Gamma_t} N_I^s \hat{t}_j d\Gamma \end{aligned} \tag{3.53}$$

where

$$\mu^l = \left(\frac{a_{12} b_{21}}{(a_{22} a_{11} - a_{12} a_{21})} - \frac{a_{22} b_{11}}{(a_{22} a_{11} - a_{12} a_{21})} \right)$$

$$\mu^g = \left(\frac{a_{21} b_{11}}{(a_{22} a_{11} - a_{12} a_{21})} - \frac{a_{11} b_{21}}{(a_{22} a_{11} - a_{12} a_{21})} \right)$$

$$\mathbf{M} \; \ddot{\mathbf{x}} + \mathbf{K} \; \mathbf{x} + \mathbf{f}_{\text{int}} = \mathbf{f}_{ext}$$

where $\mathbf{x} = \{u\}$

The liquid pressure and the gas pressures are calculated using the mass balance equations outside the solver using the volumetric strain of the solid phase.

Mass balance for the liquid:

$$\left(n^l + \frac{\partial n^l}{\partial \varepsilon_v} \right) \dot{u}_{i,i} + \left(\frac{n^l}{\Gamma^l} - \frac{\partial n^l}{\partial p^c} \right) \dot{p}^l + \left(\frac{\partial n^l}{\partial p^c} \right) \dot{p}^g = 0$$

Mass balance for the gas:

$$\left(1-n^{l}-\frac{\partial n^{l}}{\partial \varepsilon_{v}}\right)\dot{u}_{i,i}+\left(\frac{\partial n^{l}}{\partial p^{c}}\right)\dot{p}^{l}+\left(\frac{n^{g}}{\Gamma^{g}}-\frac{\partial n^{l}}{\partial p^{c}}\right)\dot{p}^{g}=0$$

3.6 Governing Equations for Saturated Porous Media

The key governing equations for the dynamics of saturated porous media are summarized below (Zienkiewicz and Shiomi, 1984; Muraleetharan et al., 1994).

Linear momentum balance for the mixture:

$$\sigma'_{ji,j}+\left(1-n^{l}\right)p_{,i}+\left(1-n^{l}\right)\rho^{s}b_{i}-\left(1-n^{l}\right)\rho^{s}\ddot{u}_{i}+\left(n^{l}\right)^{2}\mathbf{k}^{-1}\left(\dot{U}_{i}-\dot{u}_{i}\right)=0 \tag{3.54}$$

Linear momentum balance for the liquid phase:

$$-n^{l}p_{,i}+n^{l}\rho^{l}b_{i}-n^{l}\rho^{l}\ddot{U}_{i}-\left(n^{l}\right)^{2}\mathbf{k}^{-1}\left(\dot{U}_{i}-\dot{u}_{i}\right)=0 \tag{3.55}$$

Mass balance for the mixture:

$$\frac{\dot{p}}{\Gamma}=-n^{l}\dot{U}_{i,i}+\left(1-n^{l}\right)\dot{u}_{i,i} \tag{3.56}$$

3.6.1 Full Formulation for Saturated Soils

Similar to unsaturated soils, the full formulation can be derived considering the solid displacement, liquid displacement and liquid pressure as the primary unknowns. The advantage of using these variables as the primary unknown is the same as discussed for the saturated soils. The full formulation for the saturated soils has never been attempted, but it is the only form possible when the compressibility of the fluid is negligible and when no penalty procedure is used. Following the notations used by Zienkiewicz and Shiomi (1984), the matrix form of the system of equations can be written as follows.

$$\mathbf{M}_s\ddot{\bar{\mathbf{u}}} + \mathbf{C}_1\dot{\bar{\mathbf{u}}} - \mathbf{C}_2\dot{\bar{\mathbf{U}}} - G_1\bar{\mathbf{p}} + \mathbf{K} = \bar{\mathbf{f}}_s \tag{3.57}$$

$$-\mathbf{G}_1^T\bar{\mathbf{u}} + \mathbf{P}\bar{\mathbf{p}} - \mathbf{C}_2^T\bar{\mathbf{U}} = \bar{\mathbf{f}}_p \tag{3.58}$$

$$\mathbf{M}_f\ddot{\mathbf{U}} - \mathbf{C}_2^T\dot{\bar{\mathbf{u}}} + \mathbf{C}_3\dot{\bar{\mathbf{U}}} + \mathbf{G}_2\bar{\mathbf{p}} = \bar{\mathbf{f}}_f \tag{3.59}$$

$$\begin{bmatrix} \mathbf{M}_s & 0 & 0 \\ 0 & 0 & 0 \\ 0 & 0 & \mathbf{M}_f \end{bmatrix}\begin{Bmatrix} \ddot{\bar{\mathbf{u}}} \\ \ddot{\bar{\mathbf{p}}} \\ \ddot{\bar{\mathbf{U}}} \end{Bmatrix} + \begin{bmatrix} \mathbf{C}_1 & 0 & -\mathbf{C}_2 \\ 0 & 0 & 0 \\ -\mathbf{C}_2^T & 0 & \mathbf{C}_3 \end{bmatrix}\begin{Bmatrix} \dot{\bar{\mathbf{u}}} \\ \dot{\bar{\mathbf{p}}} \\ \dot{\bar{\mathbf{U}}} \end{Bmatrix} + \begin{bmatrix} \mathbf{K} & -\mathbf{G}_1 & 0 \\ -\mathbf{G}_1^T & \mathbf{P} & -\mathbf{G}_2^T \\ 0 & -\mathbf{G}_2 & 0 \end{bmatrix}\begin{Bmatrix} \bar{\mathbf{u}} \\ \bar{\mathbf{p}} \\ \bar{\mathbf{U}} \end{Bmatrix} = \begin{Bmatrix} \bar{\mathbf{f}}_s \\ \bar{\mathbf{f}}_p \\ \bar{\mathbf{f}}_f \end{Bmatrix}$$

where

$$\mathbf{K} = \int_{t+\Delta t\Omega} N_{k,i}\sigma'_{ij}\,d\Omega$$

$$\mathbf{G}_1 = \int_{t+\Delta t\Omega} N^u_{k,i}(1-n)N^p_L\,d\Omega$$

$$\mathbf{G}_2 = \int_{t+\Delta t\Omega} N^U_{k,i}(n)N^p_L\,d\Omega$$

$$\mathbf{P} = \int_{t+\Delta t\Omega} N^p_k\left(\tfrac{1}{Q}\right)N^p_L\,d\Omega$$

$$\mathbf{C}_1 = \int_{t+\Delta t\Omega} N^u_k\left(n^2\right)N^u_L\,d\Omega$$

$$\mathbf{C}_2 = \int_{\Omega} N^u_k\left(n^2\right)\delta_{ij}k^{-1}N^U_L\,d\Omega$$

$$\mathbf{C}_3 = \int_{t+\Delta t\Omega} N^U_k\left(n^2\right)\delta_{ij}k^{-1}N^U_L\,d\Omega$$

$$\mathbf{M}_s = \int_{t+\Delta t\Omega} N^u_k(1-n)\rho^s\delta_{ij}N^u_L\,d\Omega$$

$$\mathbf{M}_f = \int_{t+\Delta t\Omega} N^U_k(n)\rho^f\delta_{ij}N^U_L\,d\Omega$$

3.6.2 Irreducible ($\mathbf{uU}$) Formulation

If the fluid is assumed to be compressible, then the liquid pressure can be eliminated from the equations and the final set of equations can be expressed in terms of the solid and liquid displacement. This formulation is called as $\mathbf{uU}$ formulation. The matrix form of the $\mathbf{uU}$ formulation has the following form:

$$\begin{bmatrix} \mathbf{M}_s & 0 \\ 0 & \mathbf{M}_f \end{bmatrix} \begin{Bmatrix} \ddot{\overline{\mathbf{u}}} \\ \ddot{\overline{\mathbf{U}}} \end{Bmatrix} + \begin{bmatrix} \mathbf{C}_1 & -\mathbf{C}_2 \\ -\mathbf{C}_2^T & \mathbf{C}_3 \end{bmatrix} \begin{Bmatrix} \dot{\overline{\mathbf{u}}} \\ \dot{\overline{\mathbf{U}}} \end{Bmatrix} + \begin{bmatrix} \mathbf{K}+\mathbf{K}_1 & \mathbf{K}_2 \\ \mathbf{K}_2^T & \mathbf{K}_3 \end{bmatrix} \begin{Bmatrix} \overline{\mathbf{u}} \\ \overline{\mathbf{U}} \end{Bmatrix} = \begin{Bmatrix} \bar{\mathbf{f}}_u \\ \bar{\mathbf{f}}_U \end{Bmatrix}$$

The coefficients are given by

$$\mathbf{K}_1 = \int_\Omega N^u_{K,i} (1-n)^2 \Gamma N^u_{L,j} d\Omega$$

$$\mathbf{K}_2 = \int_\Omega N^U_{K,i} n^l (1-n^l) \Gamma N^u_{L,j} d\Omega$$

$$\mathbf{K}_3 = \int_\Omega N^U_{K,i} (n^l)^2 \Gamma N^U_{L,j} d\Omega$$

3.7 Updated Lagrangian Formulation for Large Deformation Analysis

For small deformation analysis, the current configuration at time $t+\Delta t$ coincides with the reference configuration at time 0. Therefore, the integrals associated with the element matrices can be evaluated. However, for large deformation analysis, the current configuration and the reference configurations are not the same because of the large deformation of the material, and the current configuration is not known at time $t+\Delta t$. Therefore, the equilibrium position at time $t+\Delta t$ cannot be found.

Therefore, the governing equations have to be transferred to a known configuration. In the case of an updated Lagrangian formulation, the configurations from time 0 to t are known. Therefore, the field equations can be written at time $t+\Delta t$ on the

configuration at time t. The detail formulation of these equations for saturated and unsaturated soils is shown in Chapters 7 and 8, respectively.

3.8 Time Integration Procedure

Time integration of the spatially discritized governing equations is one of the important steps in numerical analysis of dynamic problems for achieving accurate results and saving substantial computational effort. In many dynamic problems, only low-frequency modes are of interest, since the major contribution to the overall behavior comes from low frequency modes. Furthermore, in dynamic analysis using finite element methods some of the high frequency modes are due to the spatial discretization of the problem domain rather than due to the real behavior of the material. Hence, it is desirable to have a time integration algorithm, which poses some form of numerical dissipation, to damp out any spurious participation of high frequency modes. Desirable properties of a time integration algorithm are: unconditionally stable, posses numerical dissipation that can be controlled by a parameter other than the time increment and weak influences of numerical dissipation to the low frequency modes.

Conditionally stable algorithms require that the size of the time step employed be inversely proportional to the highest frequency of the discrete system. In practice, this is a severe limitation as accuracy in the lower modes can be attained with time steps, which are very large compared with the period of the highest mode. For unconditionally stable algorithms, a time step may be selected independent of stability considerations and thus can save substantial saving of computational effort.

The Newmark's family of time integration methods (1959) is widely used in the dynamic analysis of geotechnical engineering problems. The amount of dissipation can

be continuously controlled by a parameter other than time step. The Newmark's method is unconditionally stable for linear problems when the parameters, β and γ associated with the method, are selected such that $\gamma \geq 0.5$ and $\beta \geq 0.25(\gamma + 0.5)^2$. γ and β are free parameters, which govern the stability and numerical dissipation of the algorithm. The amount of dissipation, for a fixed time step, is increased by increasing γ. The disadvantage of Newmark's method is that it has second order accuracy in linear problems only when $\gamma = 0.5$ and $\beta = 0.25(\gamma + 0.5)^2$, which applies restriction in controlling the numerical dissipation of higher frequency modes. For other values of β and γ, it has only first order accuracy (Hughes, 1983). In addition, for the values at which the method gives second order accuracy, the Newmark's method does not posses any numerical dissipation.

Hilber, Hughes and Taylor (1977) improved Newmark's method by incorporating an additional parameter α. This improved method is called α-method and it shows second order accuracy and unconditional stability when the parameters α, β and γ are selected such that $-\frac{1}{3} \leq \alpha \leq 0$, $\gamma = 0.5(1 - 2\alpha)$ and $\beta \geq 0.25(1 - \alpha^2)$ in linear problems. This integration rule, increases the range of numerical dissipation. The numerical dissipation, for a given time step, is increased by increasing the absolute value of α.

For nonlinear problems, as in this research, when an algorithm is used in a consistent linear manner (Hughes and Pister, 1978) some of the conditions derived for linear problems are applicable to the nonlinear problems to a certain extent. For example, the necessary and sufficient stability conditions derived for the linear problems become only the necessary condition for stability in nonlinear problems (Hughes, 1983). In this

research, the α-method together with the predictor corrector algorithm proposed by Hughes (1983) is used to integrate the spatially discretized nonlinear governing equations in the time domain. Muraleetharan et al., (1994) used a similar algorithm to study dynamics of saturated soils.

3.8.1 α – Method with Predictor and Multi-Corrector Algorithm

The general form of the dynamic governing equation can be written as follows using the α-method.

$$\mathbf{M}\,\mathbf{a}_{n+1} + (1+\alpha)\mathbf{C}\,\mathbf{v}_{n+1} - \alpha\,\mathbf{C}\,\mathbf{v}_n + (1+\alpha)\mathbf{K}_p\,\mathbf{d}_{n+1} - \alpha\,\mathbf{K}_p\,\mathbf{d}_n + (1+\alpha)\mathbf{p}_{n+1} - \alpha\,\mathbf{p}_n = (1+\alpha)\mathbf{f}_{n+1} - \alpha\,\mathbf{f}_n$$

where

$$\mathbf{v}_{n+1} = \mathbf{v}_n + \Delta t\left[(1-\gamma)\mathbf{a}_n + \gamma\,\mathbf{a}_{n+1}\right],$$

$$\mathbf{d}_{n+1} = \mathbf{d}_n + \Delta t\,\mathbf{v}_n + \Delta t^2\left[(0.5-\beta)\mathbf{a}_n + \beta\,\mathbf{a}_{n+1}\right],$$

where n is the time step and $\Delta t = t_{n+1} - t_n$

The fully discretized, in space and time, governing equation gets the following form.

$$\mathbf{M}^{\mathrm{i}}_{\mathrm{eff}}\,\Delta\mathbf{a}^{i+1} = \mathbf{f}^{\mathrm{i}}_{\mathrm{eff}} \tag{3.60}$$

where $\mathbf{M}_{\mathrm{eff}}$ is the effective stiffness and given by:

$$\mathbf{M}_{\mathrm{eff}} = \mathbf{M} + \left((1+\alpha)\gamma\,\Delta t\right)\mathbf{C} + \left((1+\alpha)\beta\,\Delta t^2\right)\mathbf{K}_p + \left((1+\alpha)\beta\,\Delta t^2\right)\mathbf{K}_T^i$$

where $\mathbf{K}_T$ is the global tangent stiffness matrix given by $\mathbf{K}_T = \dfrac{\partial \mathbf{p}_{n+1}}{\partial \mathbf{d}_{n+1}}$

and $\mathbf{f}_{\mathrm{eff}}$ is the effective force vector and given by:

$$\mathbf{f}^{\mathrm{i}}_{\mathrm{eff}} = (1+\alpha)\mathbf{f}_{n+1} - \alpha\,\mathbf{f}_n - \mathbf{M}\,\mathbf{a}^{\mathrm{i}}_{n+1} - (1+\alpha)\mathbf{C}\,\mathbf{v}^{\mathrm{i}}_{n+1} + \alpha\,\mathbf{C}\,\mathbf{v}_n - (1+\alpha)\mathbf{K}_p\,\mathbf{d}^{\mathrm{i}}_{n+1} + \alpha\,\mathbf{K}_p\,\mathbf{d}_n - (1+\alpha)\mathbf{p}^{i}_{n+1} + \alpha\,\mathbf{p}_n$$

The incremental acceleration is calculated by solving the Eq. 3.60 and these acceleration increments are used to calculate the acceleration, velocity, and displacement for the next iteration as follows.

$$a_{n+1}^{i+1} = a_{n+1}^{i} + \Delta a^{i+1}$$

$$v_{n+1}^{i+1} = v_{n+1}^{i} + \gamma\, a_{n+1}^{i+1}\Delta t$$

$$d_{n+1}^{i+1} = d_{n+1}^{i} + \beta\, a_{n+1}^{i+1}\Delta t^{2}$$

The convergence of the solution is verified for both the effective force and the acceleration as follows.

$$\frac{\left\|\Delta \mathbf{a}^{i+1}\right\|}{\left\|\mathbf{a}_{n+1}^{i+1}\right\|} \leq \varepsilon$$

The equations derived in this chapter are implemented within a finite element framework. A detail description of the finite element framework used is given in the next chapter.

4 FINITE ELEMENT FRAMEWORK

4.1 Introduction

An important step in the design and evaluation of geotechnical and structural systems during earthquakes is the determination of stresses, deformations, and measures of damage induced by ground motion. This process includes four major ingredients: (1) development of a mathematical model representing the geometry, topology, materials, loads, and boundary conditions of the system, (2) spatial discretization to give the governing equations of motion, (3) numerical computation to solve the discretized equations, and (4) processing of the solutions to evaluate the performance of the components and the system. This entire process can broadly be described as simulation in the sense of simulating the behavior of a system in an earthquake loading.

> As long as there were no machines, programming was no problem at all; when we had a few weak computers, programming became a mild problem, and now we have gigantic computers, programming has become an equally gigantic problem (Dijkstra, 1972).

This research focuses on information technology techniques for improving simulation of geotechnical engineering structures. In each of the steps involved in a simulation, there have been important and wide-ranging research advances over the past

decades. Geotechnical engineers use a variety of specialized or general software ("codes") depending on the appropriateness of the mathematical models implemented in the codes, the available computational resources, or individual and organizational experience and policies. In the research area, there are tremendous needs for improvements in simulation methods, for example, new models, computational procedures and visualization of performance. Individual researchers often have customized versions of specialized codes or work within the limits imposed by commercial, general-purpose computer codes.

Typically, development of finite element codes is started by research organizations. Then the codes are transferred to private companies, where the codes are extended and enhanced for commercial use. The researchers have been left with a multitude of rather incomplete code fragments, each tailored to a specific topic of interest. Due to advances in programming and because of the conventional, inflexible design, scientists usually could not rely on existing code and had to start practically from scratch for each new research project.

An important question is, how well does this approach fit into simulation, particularly in regards to utilizing the dramatic improvements in information technology? The current software approaches make it difficult for researchers and developers to improve simulation methods that take advantage of the rapid changes in parallel and distributed processing, networking, databases, visualization, and entirely new approaches to computing such as application service providers, peer-to-peer computing and computational grids. The inability to exchange and communicate software implementations of models, computational methods, and performance evaluation

methods is a significant drag on research and on transfer of new methods to industry and engineering professionals.

From the perspective of an engineer conducting a simulation, there are a number of desirable requirements, such as capabilities for using, selecting, and sharing models for materials, elements, components, and entire substructures. The models should be independent of the simulation methods used to compute the state of the model so as to provide flexibility in how simulations are performed. There should be interfaces between models, databases, and visualization tools to provide capabilities for interrogating and investigating the model and results of the simulation. A scenario for such a framework is that engineers have access libraries of material models, component models, model building tools, computational resources, visualization tools, and performance evaluation over the network.

In this research program, an attempt has been made to develop a high performance computational tool incorporating the latest technologies in simulation methods. A finite element framework that provides the capabilities discussed above, is used to develop a software tool for analyzing dynamics of porous media.

4.2 Finite Element Framework

A framework represents a collection of software components for building finite element applications. By collecting these software components into a single toolkit, a framework enables the application developer to leverage these components into many different applications. Consequently, the amount of work and code required for developing and maintaining an application is greatly reduced.

Historically, the finite element applications developer has been an engineer trained in some specific field of mechanics. Typically, they spend an inordinate portion of their software development time dealing with computer science details rather than focusing on algorithms and mechanics. The finite element framework insulates the engineer from the computer science details and lets the engineer concentrate on the computational mechanics aspects of the application.

The realm of high performance, parallel, finite element application provides a rich set of common abstractions upon which to build a computational framework. Examples of common services or tasks found in finite element applications include:

1. Input/Output services
2. Memory management
3. Parallel gather/scatter operations and global reductions
4. Mathematical libraries and algorithmic controls
5. Linear algebra solution services

The common thread that runs through all these services is that they are essentially computer science or mathematical exercises that are not dependent upon physics equations or formulations in which a civil engineer is an expert. It is precisely these services that require the most attention when porting scientific applications between different hardware platforms. Generally, the scientific or physics parts of any application compile, link and run correctly on disparate hardware platforms with little porting effort. The vast majority of the porting effort goes into dealing with the highly system dependent intricacies of such tasks as Input/Output services, memory management and locating/linking the proper support libraries. By placing these services into a common

framework, all finite element applications built using the framework leverage the porting efforts required to move between new hardware platforms.

Finite element application developers, such as university researchers and finite element software developers, are the main users of the framework. The designers and analysts are the customers of the finite element application built using the framework.

4.3 TeraScale (TSC) Framework Services

In this research, a finite element framework called TeraScale (TSC; TeraScale, 2001) is used to develop applications for analyzing dynamics of porous media. The common services provided by the TSC framework for developing an application are described in the proceeding sections.

4.3.1 Generic Data Model

The Data Model is a generic container object (DataModel) for holding meta data. The data model has an XML (eXtensible Markup Language) representation, which allows the framework to read and write data across the Internet.

4.3.2 Finite Element Procedural Abstractions

Procedural abstractions are a set of algorithmic abstractions that is common to all finite element applications. For example, physics algorithm, element based algorithm, material algorithm, etc.

4.3.3 Parallel Mesh Object (PMO)

The PMO is a high-level mesh object for the finite element application. The PMO is fundamentally structured to support parallel computation in Single Program Multiple Data manner (SPMD).

The TSC framework makes use of the TSC parallel Mesh Object (PMO) to represent the mesh. The PMO is a stand-alone library that can be deployed independent of the TSC framework. The PMO provides a coherent array of services for computing on a finite element mesh distributed over some set of processors. The PMO can be thought as a virtual mesh object that is cognizant of where all its pieces reside across the parallel platform. The concept of general subsetting mechanisms for nodes, edges and faces is supported, with full capabilities to create, query, and access the mesh data.

The PMO contains the abstraction of mesh reader and mesh writer. These define a set of interfaces for reading and writing finite element data to permanent storage. The concept is quite simple; the application accesses data through the set of interfaces defined upon the mesh object. The mesh object performs read/write on demand (i.e., it does not read/write anything from file unless requested to do so). The particular flavor of mesh reader or mesh writer that is given to the mesh object can be changed at run time. Mesh readers and writers for alternate mesh formats can be derived with minimal effort. The advantage is that any finite element application can use a new mesh reader without changing any code in the finite element application. If the finite element application reads and writes its mesh through the PMO, then it can instantly leverage any new file formats available through the library of mesh readers and mesh writers.

4.3.4 Finite Element Infrastructure

Finite element infrastructure consists of the basic core libraries of finite element applications necessary to support general-purpose physic applications. This consists of an element library, which holds all the discrete calculus methods necessary for the application.

4.3.5 Scalable Linear Equation Solver

The equation solver is a common interface to linear solver services for the scalable solution of sparse systems of equations on distributed and shared memory parallel architectures. This abstraction allows the interchange or selection of different linear algebra solvers and/or preconditioners without modifying the physics implementation.

The TSC Framework provides a common interface to linear solver services for scalable solution of sparse systems of equations on distributed and shared memory parallel architectures. The interface to linear algebra packages is based upon a finite element view of the process that augments the native solver view. The underlying linear algebra representation of the assembled global element operators and right-hand-sides is hidden from the physics application developer. This abstraction layer allows the interchange or selection of different linear algebra solvers and/or preconditioners without modifying the physics implementation.

4.3.6 Multi-Physics Infrastructure

The framework also provides the facilities to rapidly couple single physics applications into a multi-physics package based on solution transfer operator. These operators are parallel in nature and highly scalable.

4.4 Developing Parallel Finite Element Computer Code using a Framework

One of the motivations for using a finite element framework to develop a computer code is to make use of the parallel and distributed processing facility provided by the framework. Solution of three-dimensional problems and complicated two-dimensional

problems such as a full formulation for unsaturated soils requires tremendous computational capacity.

The TSC framework architecture is designed to minimize the amount of specialized parallel coding that the finite element applications developer must understand and code. Ideally, the engineer simply writes code in a serial mode with no regard for parallel issues. However, the application developer cannot be completely isolated from all parallel issues. The computational framework provides the application developer a set of interfaces that isolate the parallel coding to a few simple interfaces.

The TSC framework is based upon a "SPMD Model" (Single Program Multiple Data). The SPMD model is based upon the concept that the finite element mesh is decomposed (i.e., partitioned) into a set of sub-meshes that are assigned to each processor and spread onto the individual processors. Once the mesh is distributed over a number of processors, each processor executes a copy of the same application on the piece of the mesh that it has been assigned. A fundamental aspect of the partitioning process is to embed into the partitioned/spread sub-meshes the information about mesh entities that are shared by multiple processors. These parallel data structures are discussed in Section 4.5.

The TSC framework hides these parallel aspects behind well-defined interfaces that are familiar to the finite element applications developer. One important guideline that is used in the design of the finite element framework is that there will be no performance penalty for running the parallel framework code on a single processor. In general, applications built upon the framework should run seamlessly on any of: a single processor CPU, Parallel hardware based upon shared memory architecture and distributed memory architectures and clusters of shared memory machines.

4.5 Partitioning the Model for Parallel Computation

Solving a large problem on a parallel computer with distributed memory usually requires that the data for the problem be partitioned somehow among the processors. The quality of the partition affects the speed of solution; a good partition divides the work up evenly and requires as little communication as possible.

There are numerous partitioning algorithms that can be used. The two most common are topological partitioning and geometrical partitioning. In topological partitioning, the partitioner application performs a graph analysis of the connection of the mesh to minimize the number of shared nodes across processor boundaries. A geometrical partitioner uses some algorithm to slice up the mesh in space and is typically much faster than a topological partitioner. In general, applications will run slightly faster with a good topological partitioning than with a simple geometric partitioning. However, there are numerous finite element algorithms that require a geometric partitioning (e.g., contact between two bodies) in order to achieve parallel performance. TSC provides a geometric partitioner application, which is based upon the recursive coordinate bisection algorithm. The TSC partitioner is designed to be able to accommodate new algorithms in the future should they be deemed necessary or desirable.

Fig. 4.1 shows an embankment mesh and its partitioning across 2 processors. The mesh contains nodes, edges, faces, and elements, referred to as mesh entities. The nodes, edges, and faces that reside on the inter-processor boundaries are shared between multiple processors. In some cases, elements can be shared as well. TSC's implementation of the SPMD model requires that one processor own the mesh entity while the other processors simply have a copy of the mesh entity. Also, the TSC SPMD

model requires every mesh entity to have a unique global ID (i.e., unique across all processors).

The partitioner application reads in the original mesh and spreads it into pieces for each processor. Fig. 4.1 shows the mesh partitioned into two pieces, each of which resides in its own mesh file after partitioning. While it is not formally a part of the computational framework, the partitioning services are a fundamental infrastructure requirement for deploying parallel finite element applications. Furthermore, the SPMD model usually takes advantage of independent parallel Input/Output. That is, each processor can write output to its own independent disk (hence there is no contention for the disk amongst processors). As a consequence, upon completion of the analysis there may be a set of files that must be recombined (i.e., results file, restart file, history file). This calls for a "departitioner" service that puts them back together again. The partitioner and departitioner services are provided along with the TSC framework.

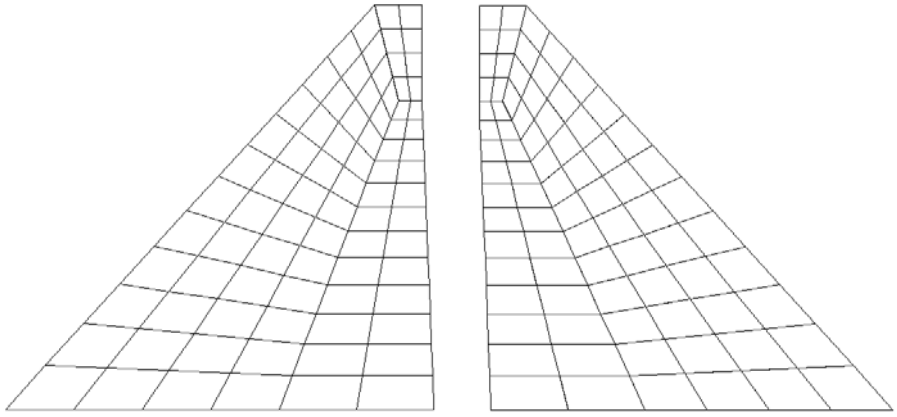

Figure 4.1: Two way partitioning of an embankment mesh

4.6 Organizational Structure of the TSC Framework

The TSC framework provides a predefined set of abstractions for the procedural flow of algorithms for the finite element application. These abstractions are in the form of a set of C^{++} base classes. An abstract base class cannot be used directly, but a specific class can be derived for the implementation of some required methods in the base class with specific interfaces. The common finite element calculations are grouped into six major classes: Application, Procedure, Physics, Element Block, Section and Material, and are discussed briefly in the proceeding sub sections.

4.6.1 Application

Application is the overall global construct for a finite element application and holds the finite element application together. It holds certain global data made available throughout the application (e.g., all the data model objects instantiations).

4.6.2 Procedure

The procedure class represents a container for different physics objects and the algorithms to perform multi-physics coupling. The multi-physics can be sequentially invoked transforming field data from one to another. The procedure class's main responsibility is to manage the time marching algorithm. This includes advancing the state of the fields and global reductions and reading/writing the "state" for the mesh object.

4.6.3 Physics

The Physics class is a container class that holds a collection of element block objects and the algorithms required to perform a single subset of physics. Generally, this

represents a single physics but it could hold tightly coupled multi-physics where the set of physics is coupled through the solver. The Physics' main job is to advance the solution one increment in "time" at the request of the Procedure class. The physics layer of the framework maps cleanly onto the traditional notion of a finite element code. The nodal fields are registered in this object. Different physics will have different nodal unknowns which will requires a different physics object to be derived. A very simple example is that two different physics objects are used for implementing the complete formulation and the reduced formulation presented in Chapter 3 because of different nodal unknowns.

4.6.4 Element Block

The Element Block class is a container class that holds either a section object or a material object. An element block object is derived to hold a particular element type and physics formulation. For example, the uniform gradient element formulation (element type) for unsaturated soils (physics type). It also holds the algorithms to compute the element response to the global nodal fields. The concept of work set is used to define element variables and perform element calculations.

4.6.5 Section

The section object holds the physical representation of the element at each integration station of the element. The section object also holds algorithms to integrate the section. For solid elements, the section only holds the material object (see below). For a complicated element, such as a layered shell, the section holds descriptions for the geometric lay-up of the shell layers, the integration rules for integrating through the layers, and the material objects for each of the layers.

4.6.6 Material

A material object integrates the material response through time at a set of material points in the model. The usual constitutive equation is incorporated into this class. Any material routine written in FORTRAN or any other language can be simply ported into the material base class and used in the finite element application. The TSC framework provides a straightforward mechanism to call FORTRAN from C^{++}.

4.7 The High Performance Computational Tool - TeraDysac

The application developed in this research for analyzing the dynamics of saturated and unsaturated soils are named TeraDysac. The current version of the TeraDysac has two separate applications: one for saturated soils and the other one for unsaturated soils. These codes will be combined together in the future to make a single application for soils.

4.7.1 Capabilities of the Current Version of the TeraDysac for Saturated Soils

The organization of the TeraDysac for saturated soils is shown in Fig. 4.2. There is one physics and five element blocks.

1. Type of Deformation

   Depending on the users requirement, the user can perform small deformation analysis or large deformation analysis.

2. Type of Element Formulation

   The user can select uniform gradient element with hourglass control or full Gauss quadrature element formulation.

3. Static analysis procedure

In the current version, the static analysis is performed dynamically by setting the mass matrix to zero. In addition to that, the time integration parameters can also be adjusted to obtain reasonable results.

4. Irreducible formulation and full formulation

The irreducible formulation uses solid displacement and liquid displacement as nodal unknowns and the full formulation uses solid displacement and liquid displacement as nodal unknowns and pore pressure as an element unknown.

5. 2D and 3D capabilities

Four nodded isoparameteric quadrilateral elements are used for 2D analysis and eight nodded brick elements are used for 3D analysis.

6. Elastic and elastoplastic constitutive models

Elastoplastic constitutive models for clay and sand based on the bounding surface concept are implemented. Linear elastic model can also be used to represent the soil skeleton.

4.7.2 Capabilities of the Current Version of the TeraDysac for Unsaturated Soils

The organization of the TeraDysac for unsaturated soils is shown in Fig. 4.3. The TeraDysac for unsaturated soils has three physics applications and six element blocks.

1. Complete formulation

In this formulation, the accelerations and velocities of the pore liquid and gas phases are taken into account. The effect of relative velocities and accelerations of the pore fluid can be investigated using this formulation.

a. Full form

In this form, solid displacement, fluid displacement, and gas displacement are considered as nodal unknowns and liquid pressure and gas pressure are considered as element unknowns.

b. Irreducible form

In this method, solid displacement, liquid displacement and gas displacements are used as nodal unknowns. The liquid and gas pressures are calculated outside the solver.

2. Reduced formulation

In this method, the accelerations and velocities of the fluids are neglected at the governing equation level. The undrained behavior of the unsaturated soils can be investigated using this formulation.

a. Full form

Solid displacement is used as nodal unknown and liquid pressure and gas pressure are used as element unknowns.

b. Irreducible form

Solid displacement is used as nodal unknown and the liquid and gas pressures are calculated outside the solver.

2D versions of TeraDysac for saturated and unsaturated soils are capable of running on parallel. These codes have been tested on two processors. The simulations shown in this dissertation for unsaturated soils were run on two processors. The verification runs of the TeraDysac for 3-D problems on multiple processors are currently under investigation. The main problem faced in the 3-D analysis on multiple processors is the lack of good preconditioner for the iterative solvers.

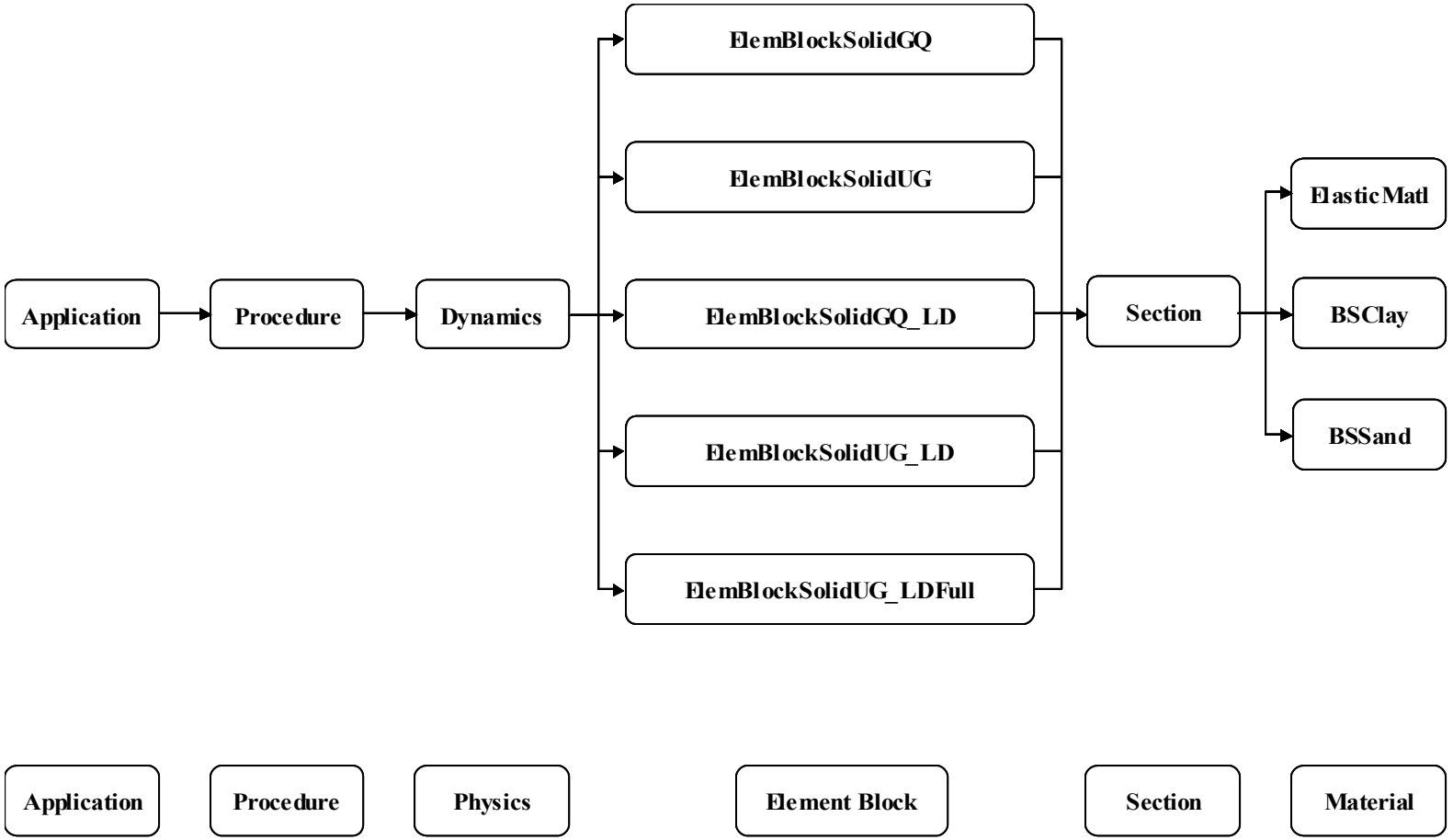

Figure 4.2: Current TeraDysac organization for saturated soils

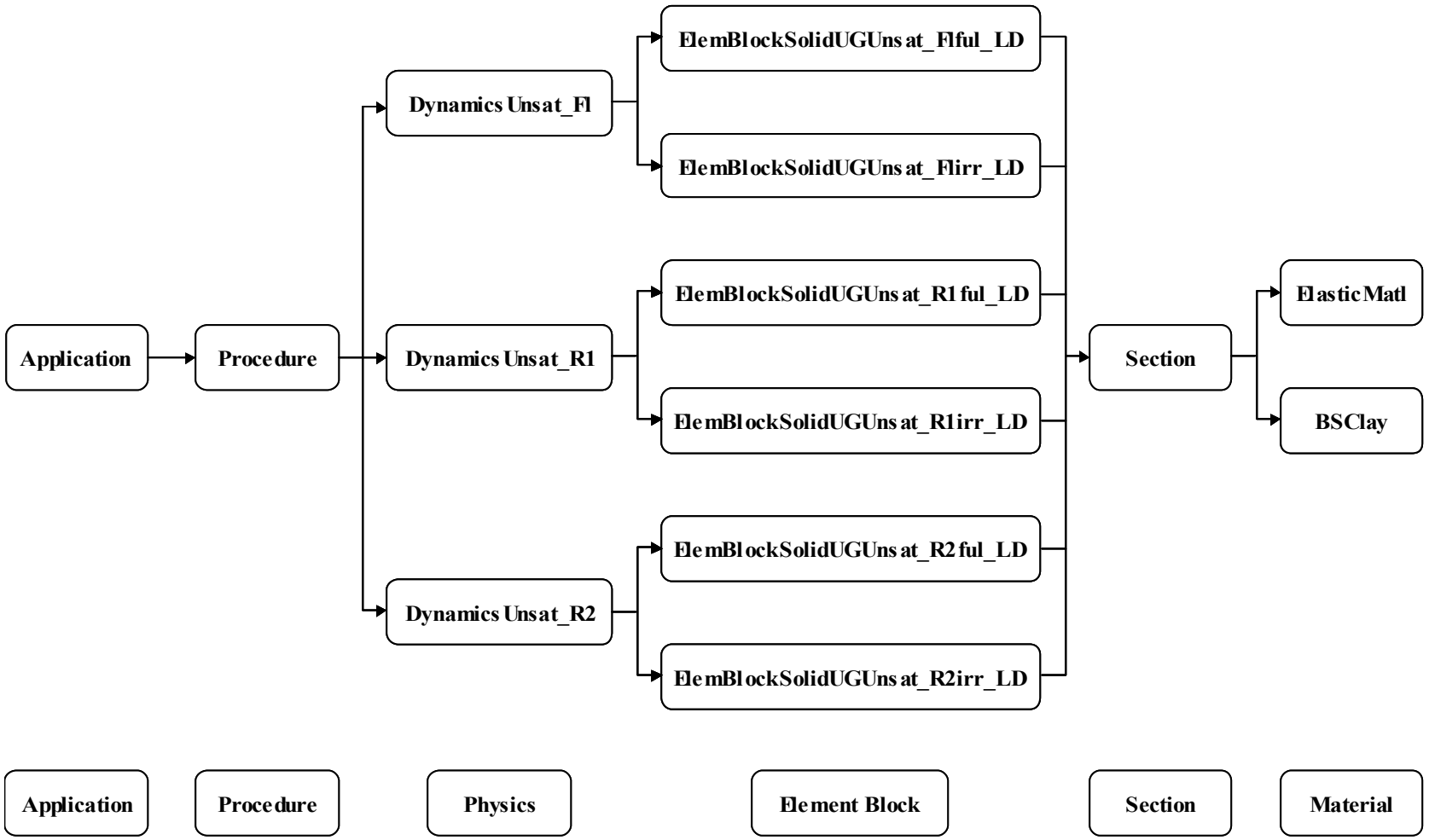

Figure 4.3: Current TeraDysac organization for unsaturated soils

4.8 Pre and Post Processing in TeraDysac

4.8.1 Target Code Template

Every finite element application has some prescribed feature base. That is, there are capabilities and algorithms within the finite element code that users can invoke if they provide the proper data for a particular feature. A target code template (TCT) is a file that holds the entire set of features for a particular finite element code (the “target code”). The TCT can be created or modified for a finite element application with the TSC Configurator application. Configurator is a software tool available within the TSC system. Configurator has a graphical user interface that allows the user to precisely define all the features for a particular code. Furthermore, default values can also be defined for certain features.

4.8.2 Data Model

A huge amount of data has to be given as input to a finite element software. The amount of data will vary depending on the complexity of the problem to be analyzed and how complicated the finite element software is. Traditionally, these data are given in sequence in a text file prepared by an engineer. This text file is created following a manual or handout given by the code developer. Giving a huge amount of data in a text file is very inconvenient and it is easy to make mistakes.

The TSC provides a Graphical User Interface (GUI) to create an input file for TeraDysac. The input file is called the data model in the TSC system. The data model is created within the GUI using rules of the TCT explained in the previous section. The TCT and the Data Model for the dynamic analysis of soils are shown in Fig.4.4. Note that the various items created by the configurator for the TCT (e.g. Analysis) shows as folder

tabs in the Data model. In addition, the same TCT and Data Model can be reused for different analyses with a different feature base. There is no penalty for leaving data in the data model, which is not needed for the particular analysis, i.e. leaving the data for bounding surface model for sand in the Data Model while doing an analysis using bounding surface clay model.

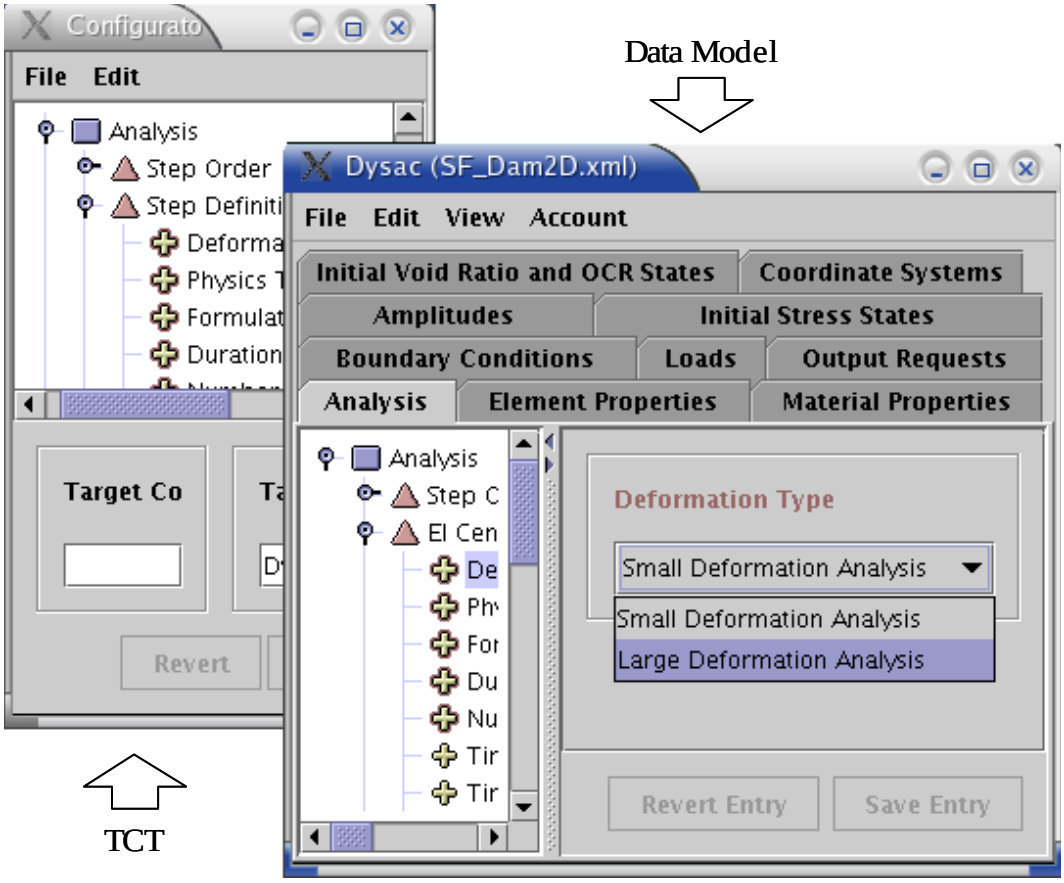

Figure 4.4: TCT and Data Model for TeraDysac

5 VALIDATION OF TERADYSAC FOR SATURATED SOILS

5.1 Introduction

The governing equations derived for the saturated porous media in Chapter 3 are implemented within the TeraScale framework. The resulting computer code is named TeraDysac. TeraDysac predictions with four-node Gauss Quadrature elements (single-point integration for fluid stiffness terms) are first verified against manual calculations for single and two element problems with an elastic material model. TeraDysac predictions are then validated against a centrifuge model test of an embankment subjected to base shaking (Kutter, 1982). Use of uniform gradient elements (single-point integration for all the terms) in TeraDysac is discussed in Chapter 6.

5.2 Verification with Manual Calculations

The finite element model developed in this study was verified against hand calculations for one and two element problems. The matrices were formed in Microsoft Excel and the complete problem was solved for simple loads with elastic constitutive model. These calculations were done for the first five time increments and the results were found to be consistent with the TeraDysac predictions.

5.3 Summary of Centrifuge Model Test

The centrifuge model test carried out at the Cambridge University (Kutter, 1982) is used for validation purposes. The model embankment (Fig. 5.1) was consolidated into blocks from slurry of Speswhite Kaolin in a large consolidometer to a vertical stress of 125 kPa. The blocks of clay were then extruded from the consolidometer and trimmed into a symmetrical triangular cross-section with 26.6 deg slopes to get the embankment model for the centrifuge test. During trimming, care was taken to cover the clay blocks with thin plastic wrap to prevent significant drying or wetting of the clay. With these precautions, the pore water suctions during model making were maintained in the range of 25-45 kPa, indicating that the models did not suffer significant swelling or drying that could drastically affect the soil properties.

During the centrifuge test, the centrifugal acceleration was gradually brought up to 80g. Then the water was introduced at equal heights on both sides of the embankment as shown in Fig.5.1. Water was not introduced before spin-up to prevent excessive swelling of the clay. The model was then allowed to consolidate until pore pressure came into hydrostatic equilibrium with the water levels at the sides of the embankment. Then, a base acceleration-time history shown in Fig. 5.6 was applied to the model.

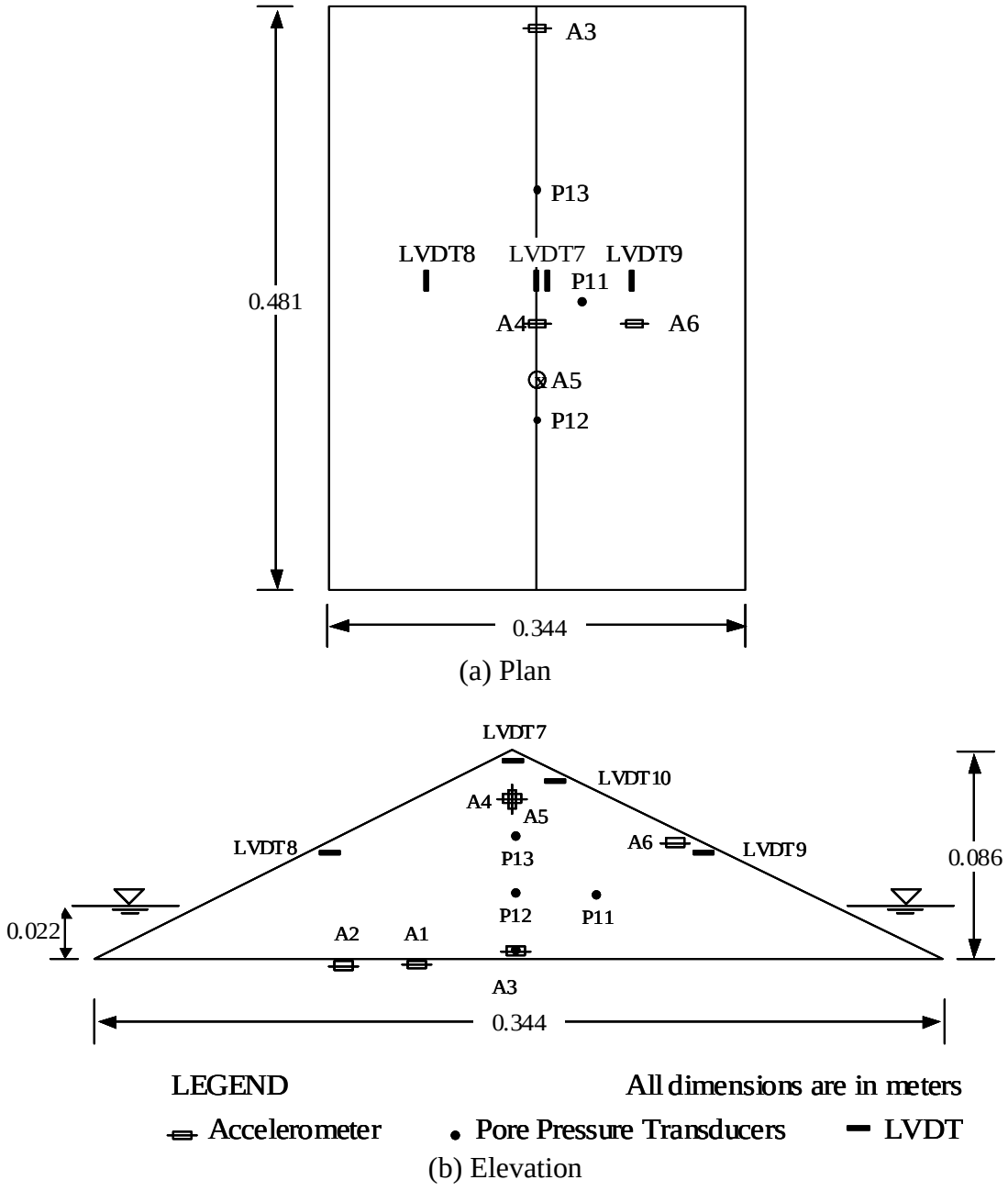

Figure 5.1: Centrifuge experimental setup (a) Plan view and (b) Elevation (after Kutter, 1982)

5.4 Numerical Modeling of Centrifuge Experiment

The actual three-dimensional centrifuge experiment (Section 5.3) is simulated using a two-dimensional plane strain numerical model. It is assumed that the boundary effects are negligible in this simulation. The finite element mesh for the centrifuge model

is shown in Fig.5.2. The analysis was done in two steps: static analysis and dynamic analysis. It has been shown that the initial stresses play an important role in dynamic response of embankments (Ravchandran, 2004). A static analysis was carried out prior to the dynamic analysis to obtain the correct initial stresses. A fixed base boundary condition is used for both static and dynamic analysis. An elastoplatic constitutive model was used to represent the stress-strain behavior of the solid skeleton and is described in the next sub section.

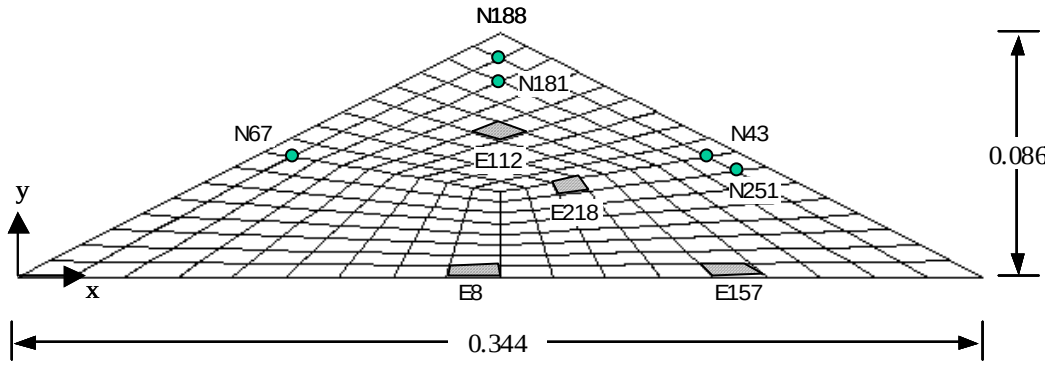

Figure 5.2: Finite element mesh of the model embankment (all dimensions are in meters and model scale)

5.4.1 Constitutive Model for Cohesive Soils

If the true behavior of structures made of soils must be accurately predicted under complex loading conditions, it is important to model the stress-strain behavior of the soil skeleton realistically. An elastic material behavior assumption is used in many analyses. This is mainly for computational efficiency. However, elastic behavior assumption is a very poor assumption for soils under most loading conditions. Here, we use an elastoplastic phenomenological constitutive model based on the bounding surface concept to represent the stress-strain behavior of the soil skeleton (Dafalias & Herrmann, 1986). A schematic diagram of the bounding surface is shown in Fig.5.3.

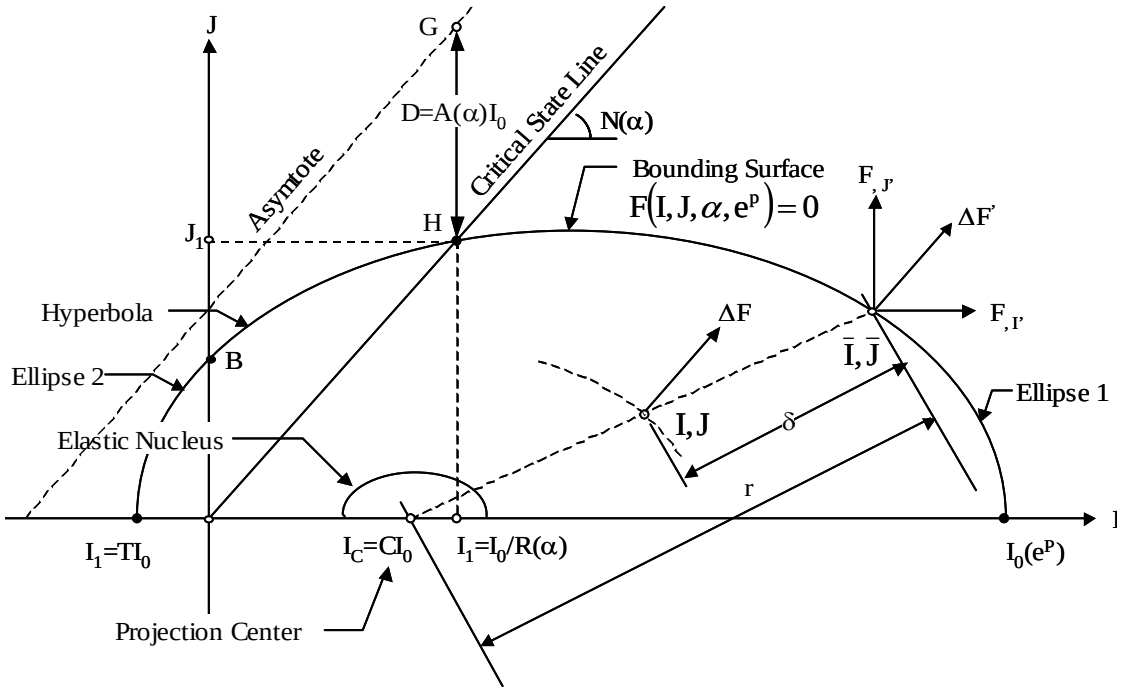

Figure 5.3: Schematic illustration of bounding surface in stress invariant space

The prominent feature of the bounding surface concept is that plastic deformations can occur for stress points inside the bounding surface. In classical plasticity theory, no plastic deformations are allowed inside the yield surface. The classical yield surface formulation is transformed into a bounding surface formulation based on the concept that for any stress point inside the surface, a unique "image" point can be defined on the surface by means of a radial mapping rule (Fig. 5.3). The value of the plastic modulus depends on the distance between the actual stress point and its "image" on the bounding surface. The gradient of the bounding surface is used to define the direction of the plastic loading for the actual stress point.

The material properties and the bounding surface model parameter of the Speswhite Kaolin are obtained from the experimental results (Muraleetharan et al., 1994). The bounding surface model parameters are listed in Table 5.1.

Table 5.1: Soil properties and model parameters for Speswhite Kaolin

Parameter	Value
Initial void ratio (e_0)	1.48
Liquid limit (LL) (%)	69
Specific gravity	2.62
Plasticity index (PI) (%)	31
Permeability (m/s)	1.733×10^{-10}
Traditional Model Parameters	
Slope of isotropic consolidation line on $e - \ell n\ p'$ plot (λ)	0.25
Slope of elastic rebound line on $e - \ell n\ p'$ plot (κ)	0.05
Slope of critical state line in $q - p'$ space (compression) (M_c)	0.88
Poisson's ratio (ν)	0.3
Ratio of extension to compression value of M (M_e / M_c)	1.0
Bounding Surface Configuration Parameters	
Value of parameter defining the ellipse1 in compression (R_C)	2.4
Value of parameter defining the hyperbola in compression (A_C)	0.01
Parameter defining the ellipse 2 (tension zone) (T)	0.01
Projection center parameter (C)	0.0
Elastic nucleus parameter (S)	1.0
Ratio of triaxial extension to compression value of R (R_e / R_c)	0.92
Ratio of triaxial extension to compression value of A (A_e / A_c)	1.2
Hardening Parameters	
Shape hardening parameter in triaxial compression (h_c)	3.0
Ratio of triaxial extension to compression value of h (h_e/h_c)	1.0
Hardening parameter on I-Axis (h_o)	2.0

5.4.1.1 Static Analysis

The static analysis was carefully performed to exactly simulate the model making and experimental procedures. The gravitational acceleration was first increased to 80 g in 2400 seconds and maintained at 80 g for another 5820 seconds (Fig. 5.4(a)). Pore pressures on the submerged nodes along the embankment sides were increased from zero to hydrostatic pressure in 1380 seconds to simulate the introduction of water on both sides (Fig. 5.4(b)). Ponding the reservoir could not be simulated using the current version of the TeraDysac because, pressure boundary conditions could not be specified in the displacement formulation. Because of the importance of the initial stresses for the dynamic analysis, a true static analysis computer program (SAC2) (Herrmann and Mish, 1983) was used to obtain the initial stresses.

Pore water pressure contours in the model embankment at the end of the static analysis (8220 sec) are shown in Fig. 5.5(a). Pore water pressures obtained from the analysis clearly show that pore pressures are in hydrostatic equilibrium with the water levels on both sides. The contours of index $(I + J/N)$ are shown in Fig. 5.5(b). I is the first invariant of the effective stress tensor (Eq. 5.1) and J is the square root of the second invariant of the deviatoric stress tensor (Eq. 5.2) (also see Fig. 5.3). N is the slope of the critical state line in I-J space.

$$I = \sigma'_{kk} \tag{5.1}$$

$$J = \sqrt{\frac{1}{2} s_{ij} s_{ij}} \tag{5.2}$$

where σ'_{ij} is the effective stress tensor, and s_{ij} is the deviatoric stress tensor.

The $(I + J/N)$ value is considered as an indicator of the proximity of the initial stresses to the critical state line. The initial stresses will be closer to the critical state line for smaller absolute values of $(I + J/N)$. When the initial stress state is close to the critical state line, then the soil will show dilative and contractive behavior and this will be replicated in the development of cyclic dynamic pore water pressures.

The shear stress contours and vertical stress contours at the end of the static analysis are shown in Figs. 5.5(c) and 5.5(d). Higher shear stresses are concentrated at the bottom left and right of the embankment. This will also produce more cyclic pore water pressures around these areas.

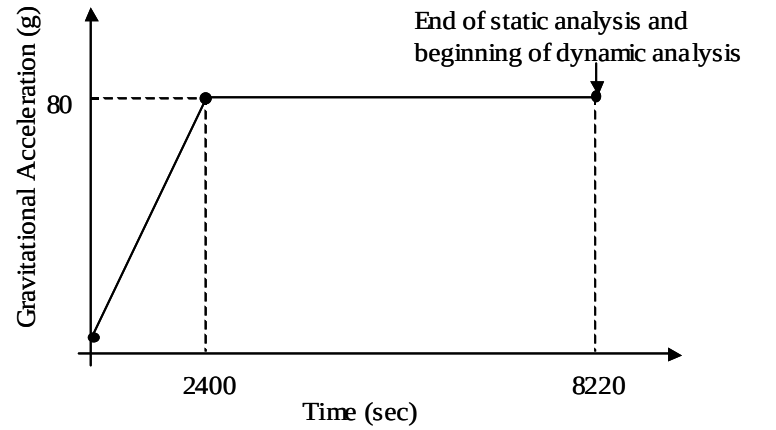

(a) Centrifuge spin-up history

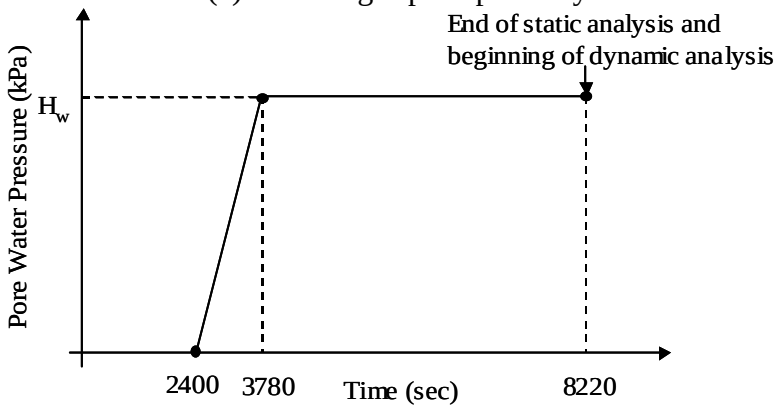

(b) Reservoir ponding history

Figure 5.4: Centrifuge spin-up and reservoir ponding history for the model embankment for static analysis

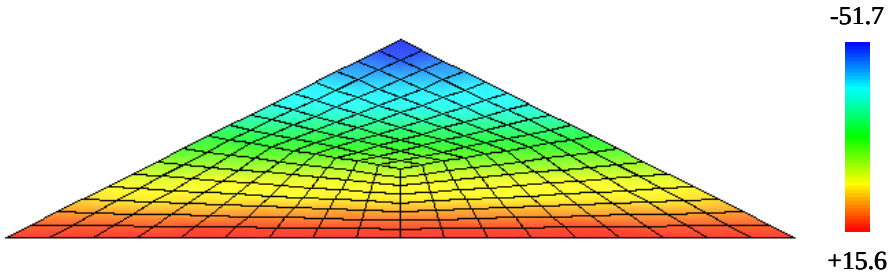

(a) Contours of pore water pressure in the model embankment at the end of the static analysis

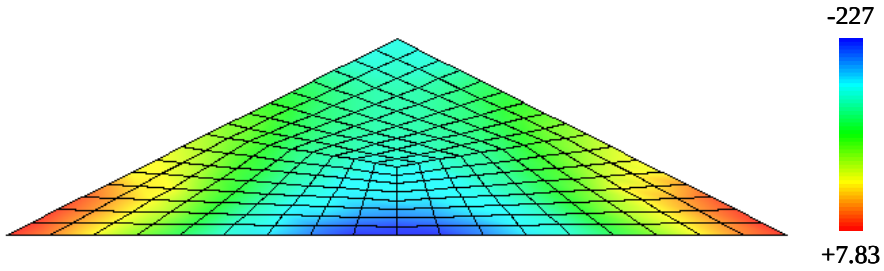

(b) Contours of the index $(I + J / N)$ in the model embankment at the end of the static analysis

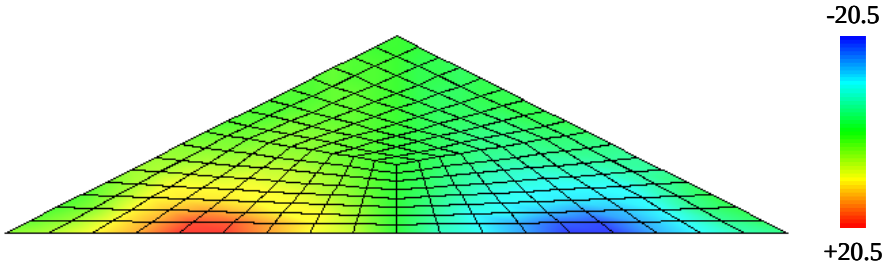

(c) Contours of shear stress in the model embankment at the end of the static analysis

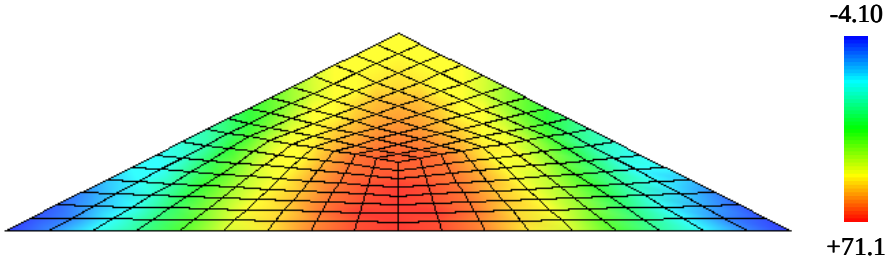

(d) Contours of vertical stress in the model embankment at the end of the static analysis

Figure 5.5: Stresses and pore water pressure contours at the end of static analysis

5.4.1.2 Dynamic Analysis

With the initial stresses calculated from the static analysis, a dynamic analysis was carried out using TeraDysac. The horizontal base motion shown in Fig. 5.6 was applied to the embankment.

The horizontal displacement at the crest (N188) of the embankment is shown in Fig. 5.7(a). All the results are plotted in model dimensions. There was no horizontal displacement measurement available for the node N188. The prediction shows that the crest continuously moved to the right with a slight cyclic component. The predicted and measured vertical settlements at node N188 are compared in Fig. 5.7(b). The numerical model slightly over predicts the settlement at Node N188. It is observed that the numerical prediction begins to show settlement earlier than measured response and is consistent with the applied base motion. Measured and predicted horizontal displacements at node N67 are shown in Fig. 5.8. The horizontal displacement at node N67 is predicted well by the numerical model. The negative horizontal displacement means that the model moved to the left at this point. Measured and predicted displacements at node N43 are shown in Fig. 5.9. It can be seen that at this point the model moved to the right.

The measured and predicted dynamic pore water pressure-time histories in elements E112 are shown in Fig. 5.10. Predicted pore water pressures in elements E8 and E157 are shown in Figs. 5.11(a) and (b), respectively. The pore water pressure in E112 is well predicted. Among predicted pore pressure-time histories in all the elements, the pore pressure-time history in E157 shows higher cyclic and dilative (negative pore pressure)

behavior. This can be explained by the smaller $(I + J/N)$ value and higher shear stresses around E157.

Comparison between measured and predicted horizontal and vertical acceleration time histories at node N181 are shown in Figs. 5.12 and 5.13, respectively. The vertical and horizontal acceleration-time histories at node N251 are shown in Figs. 5.14 and 5.15, respectively. Only the horizontal acceleration measurement is available at N251. The frequency of the predicted and measure accelerations matches well. However, the amplitudes of the predicted accelerations are higher than that of the measured values, especially at node N181. The maximum amplitude of the input base motion acceleration is around 200 ms^{-2}. The measured and predicted accelerations show higher amplitudes than that of applied. This observation clearly shows that the base motion is amplified at the crest of the embankment.

At this point we can conclude that the numerical model reasonably captures the dynamic response of a saturated clay embankment. Muraleetharan et al., (1994) also predicted the behavior of the centrifuge model used here. Overall the predictions shown here are better than those shown by Muraleetharan et al., (1994). This is likely due to the finer mesh used in this study.

The analyses were run on single and dual processors of similar specifications (Intel-Xeon processor with 3.0 GHz clock speed). The single processor took 16 min and 30 sec and two processors took 23 min and 30 sec. The speedup gained is 1.43. This is a reasonable speedup for the problem (225 elements and 252 nodes) used to validate the numerical model. For larger problems, the speedup is expected to be even higher because

the processors will spend more time doing calculations rather communicating with each other.

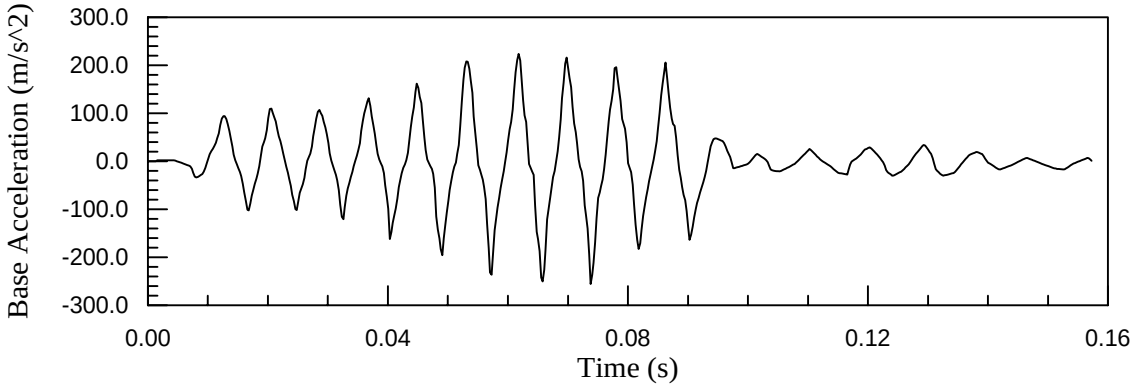

Figure 5.6: Horizontal base motion (model dimensions)

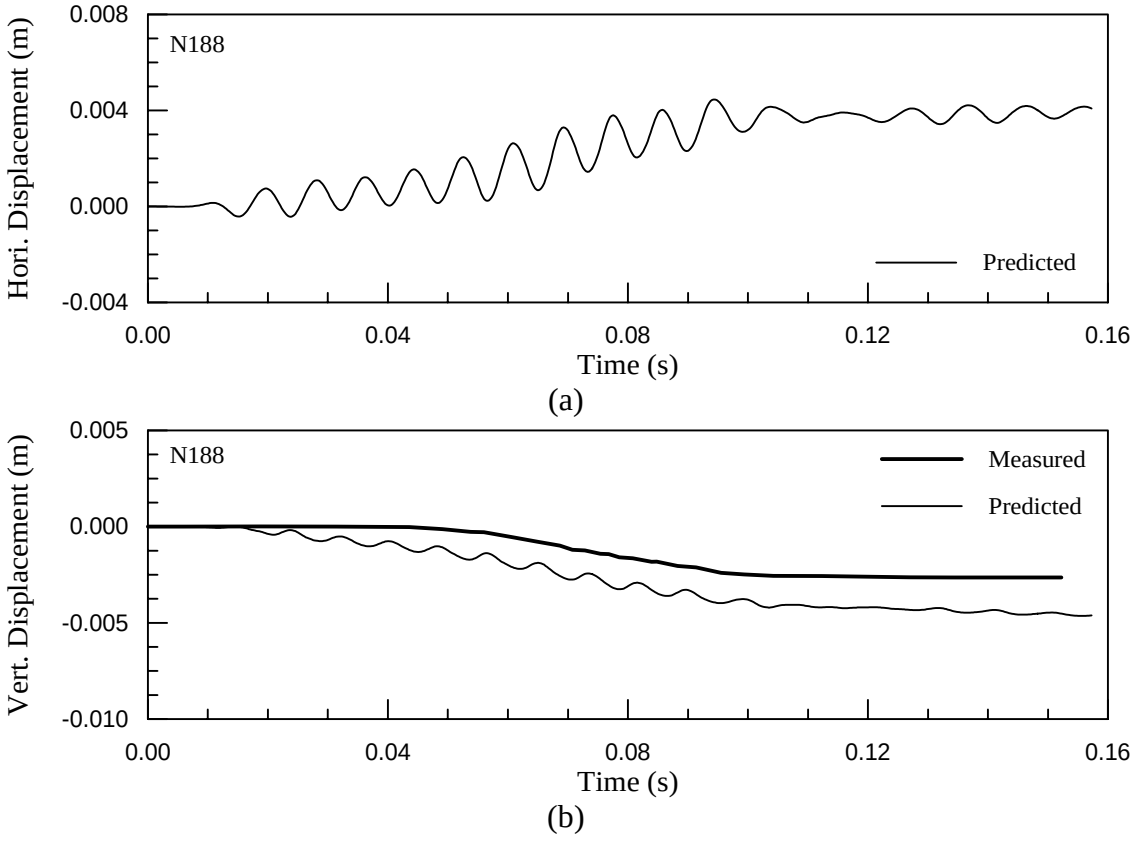

Figure 5.7: Comparison between the measured and predicted horizontal and vertical displacement-time histories at node N188

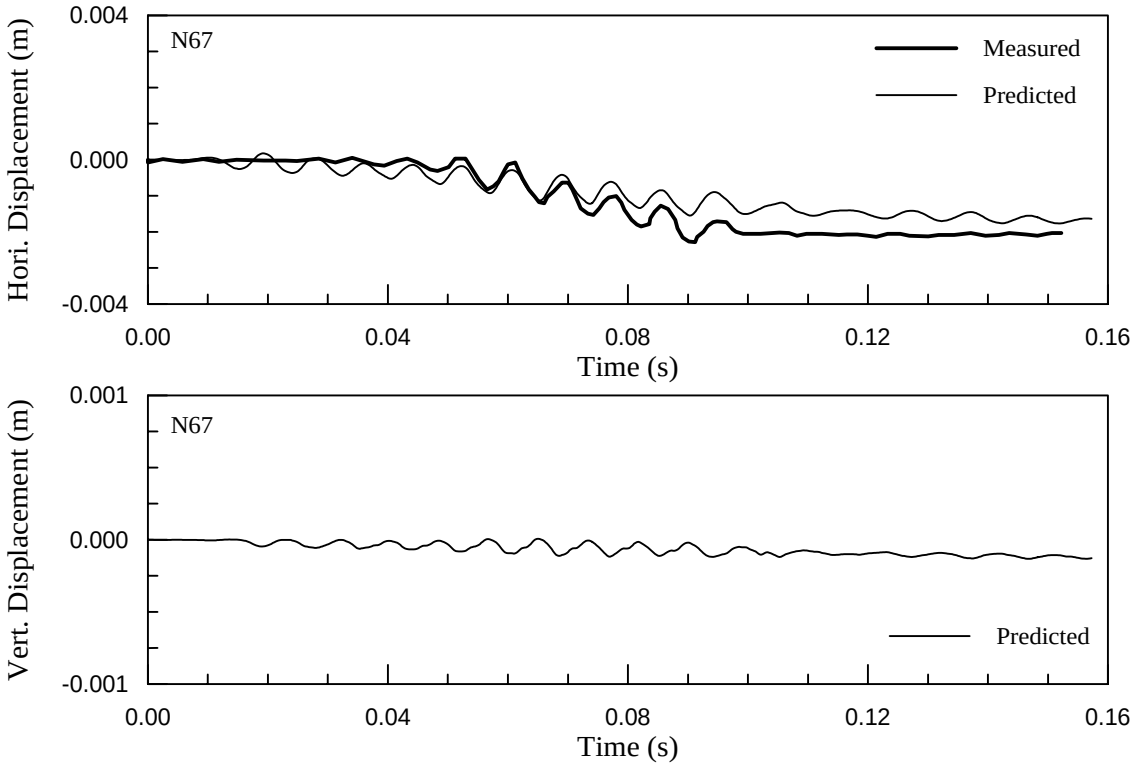

Figure 5.8: Comparison between the measured and predicted horizontal and vertical displacement-time histories at node N67

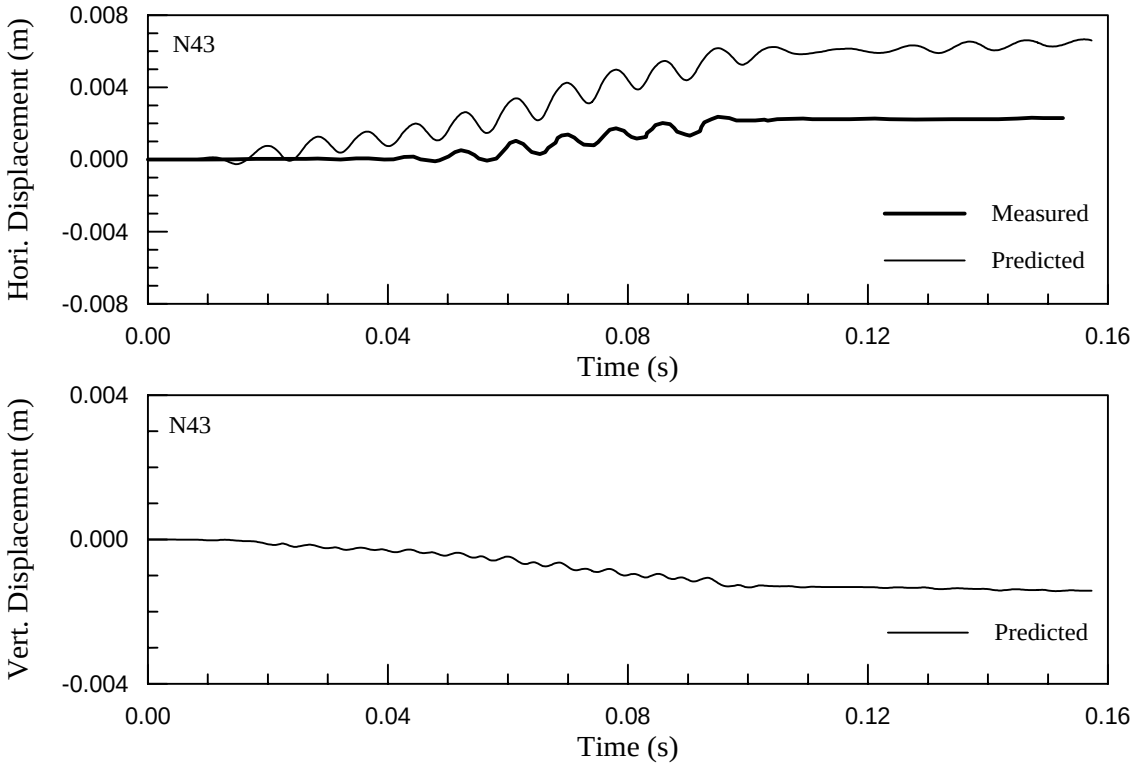

Figure 5.9: Comparison between the measured and predicted horizontal and vertical displacement-time histories at node N43

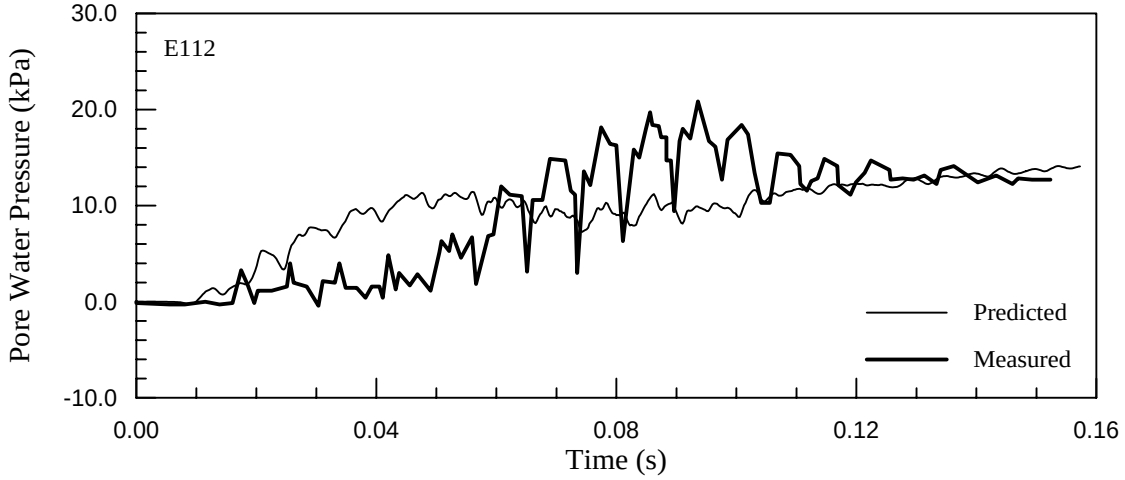

Figure 5.10:Comparison between the measured and predicted pore water pressure-time histories in elements E112

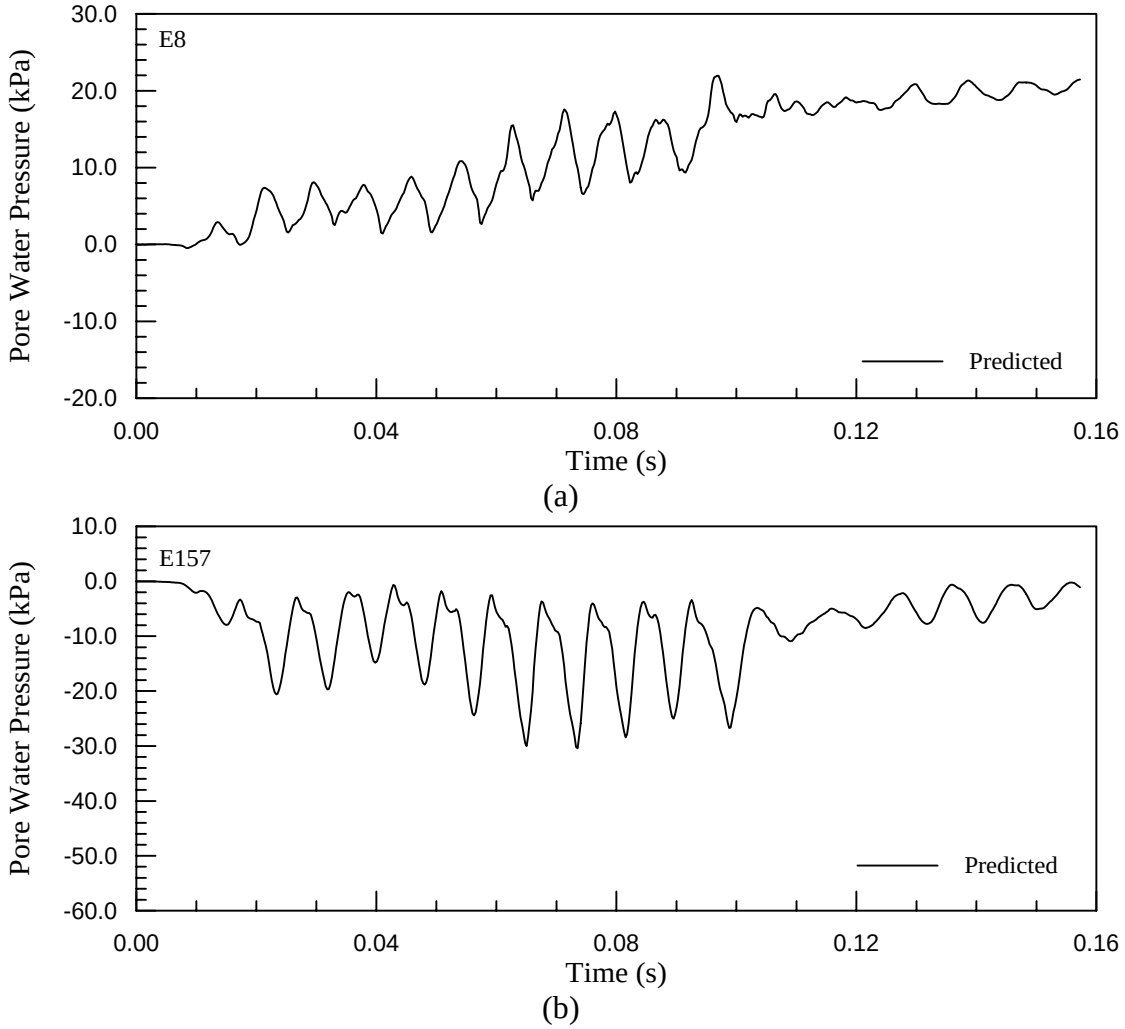

Figure 5.11: Predicted pore water pressure-time histories in elements E8 and E157

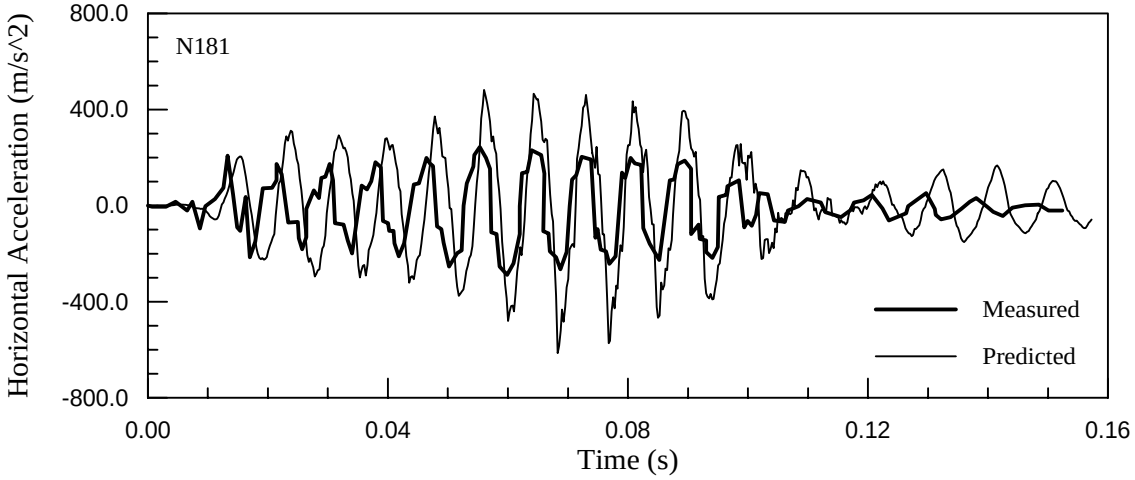

Figure 5.12: Comparison between the measured and predicted horizontal acceleration-time histories at node N181

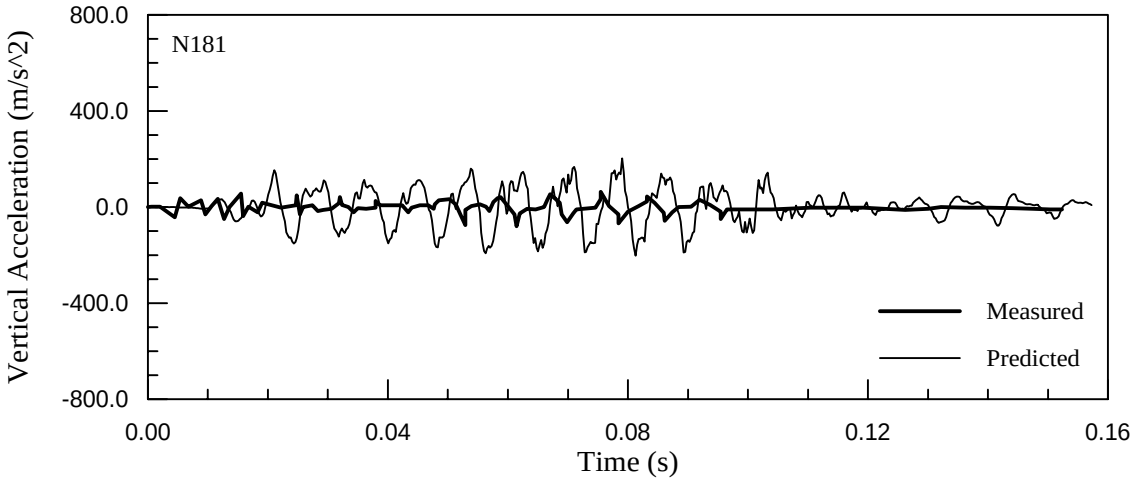

Figure 5.13: Comparison between the measured and predicted vertical acceleration-time histories at node N181

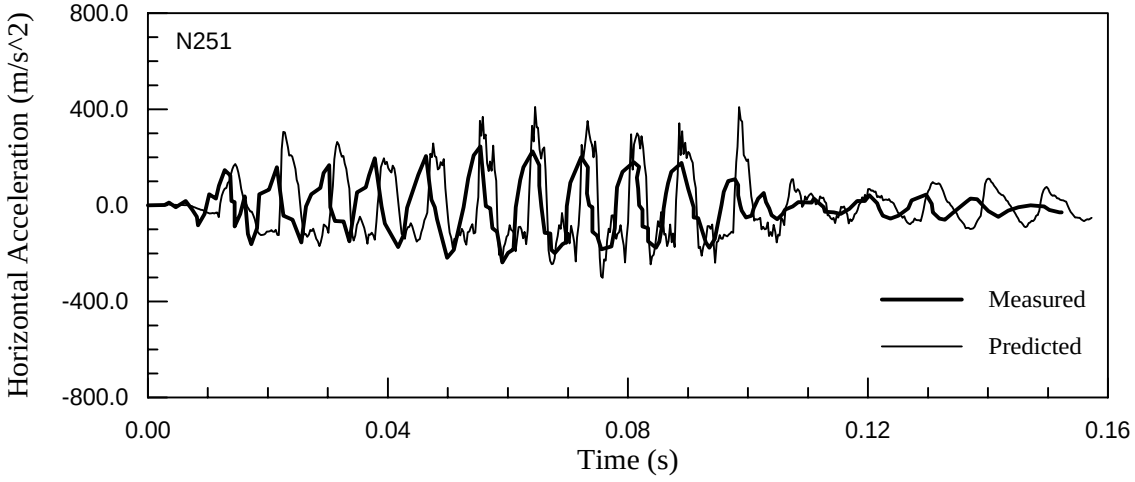

Figure 5.14: Comparison between the measured and predicted horizontal acceleration-time histories at node N251

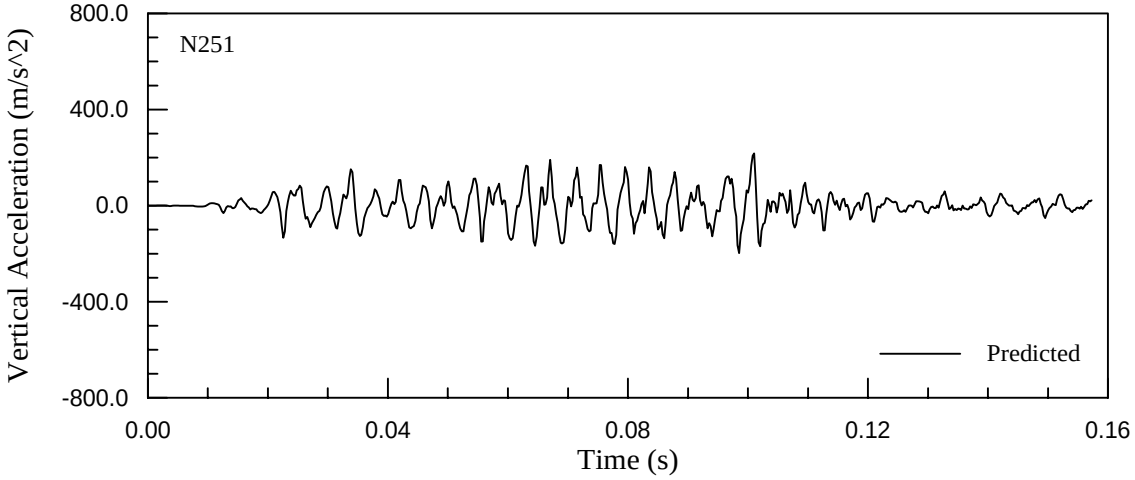

Figure 5.15: Predicted vertical acceleration-time history at node N251

5.5 Three-Dimensional Analysis

Three-dimensional finite element model for saturated porous media is also implemented into TeraDysac. A three-dimensional analysis was carried out and the predictions were compared with a 2-D plane strain analysis. Because of time limitation, a coarser mesh compared to the one used in Section 5.4 was prepared in 2-D and then extruded into a 3-D mesh (Fig. 5.16). The base motion shown in Fig. 5.6 was applied to the embankment. The horizontal and vertical displacement-time histories at nodes N1 (N281 for 3-D analysis) and N4 (N284 for 3-D analysis) are shown in Figs. 5.17 and 5.18, respectively. Pore water pressure-time histories in elements E23 (E191 in 3D) and E2 (E170 for 3D) are shown in Figs. 5.19 and 5.20, respectively. Elements E191 and E170 are located in the middle layer of the 3-D mesh. The results show that the predictions made by 2-D and 3-D analysis are very close. The slight differences in displacements and pore pressures can be attributed to the boundary effects in the third direction (z-direction). In terms of computational requirements, the 2-D analysis (56 elements) took 11 minutes and 3-D analysis (392 elements) took 26 hours on a 64-bit

Dual-Core Intel Xeon processor with 3.0 GHz clock speed. This clearly shows the need for parallel computing for 3-D problems.

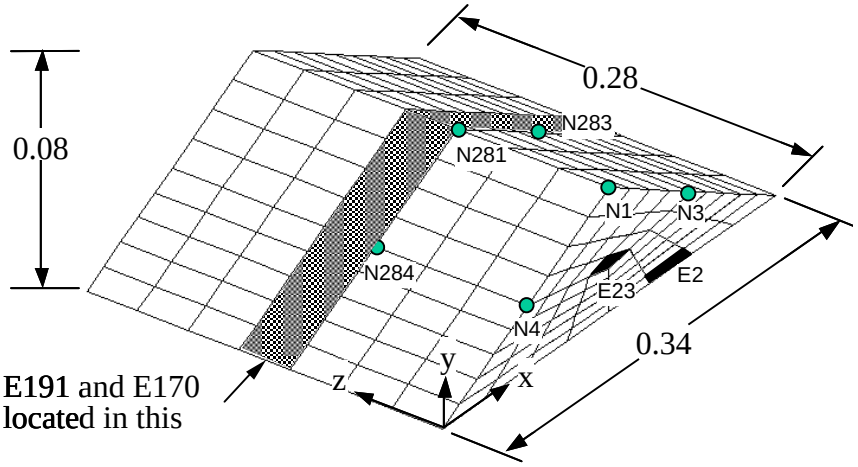

Figure 5.16: Finite element mesh for 3-D analysis (all dimensions are in meters)

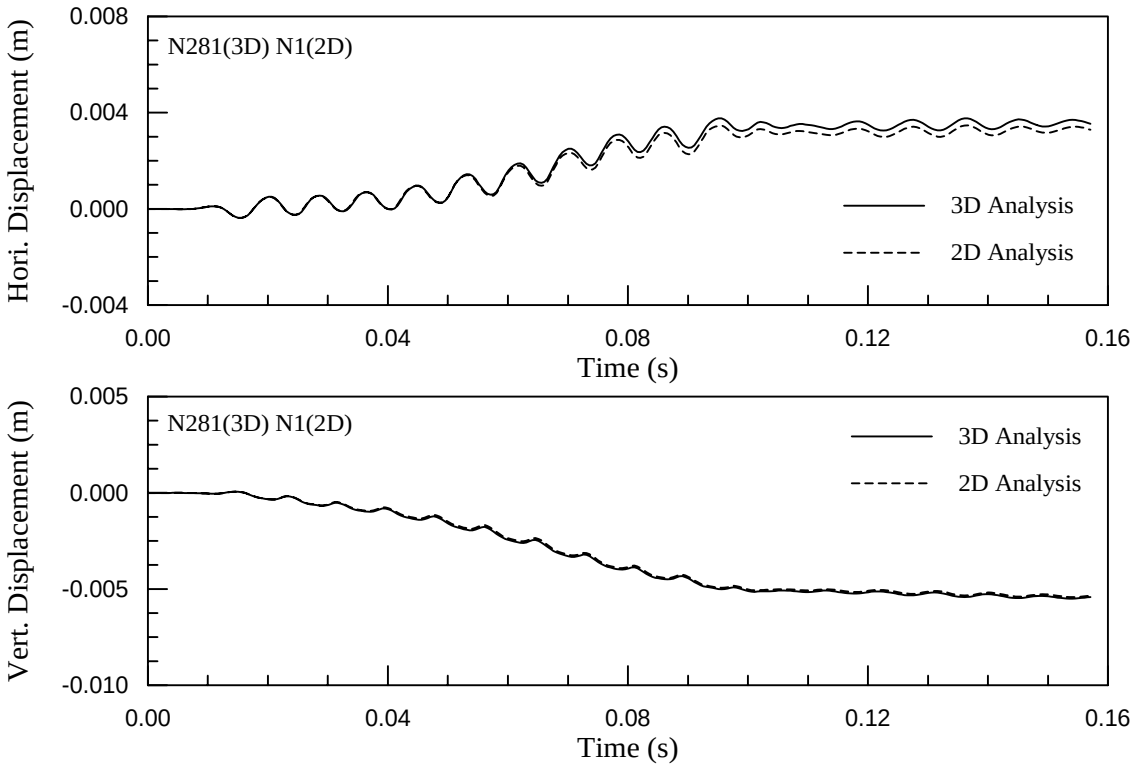

Figure 5.17: Comparison between 3-D and 2-D analysis – Displacement-time histories at node N281 (3D) and N1 (2D)

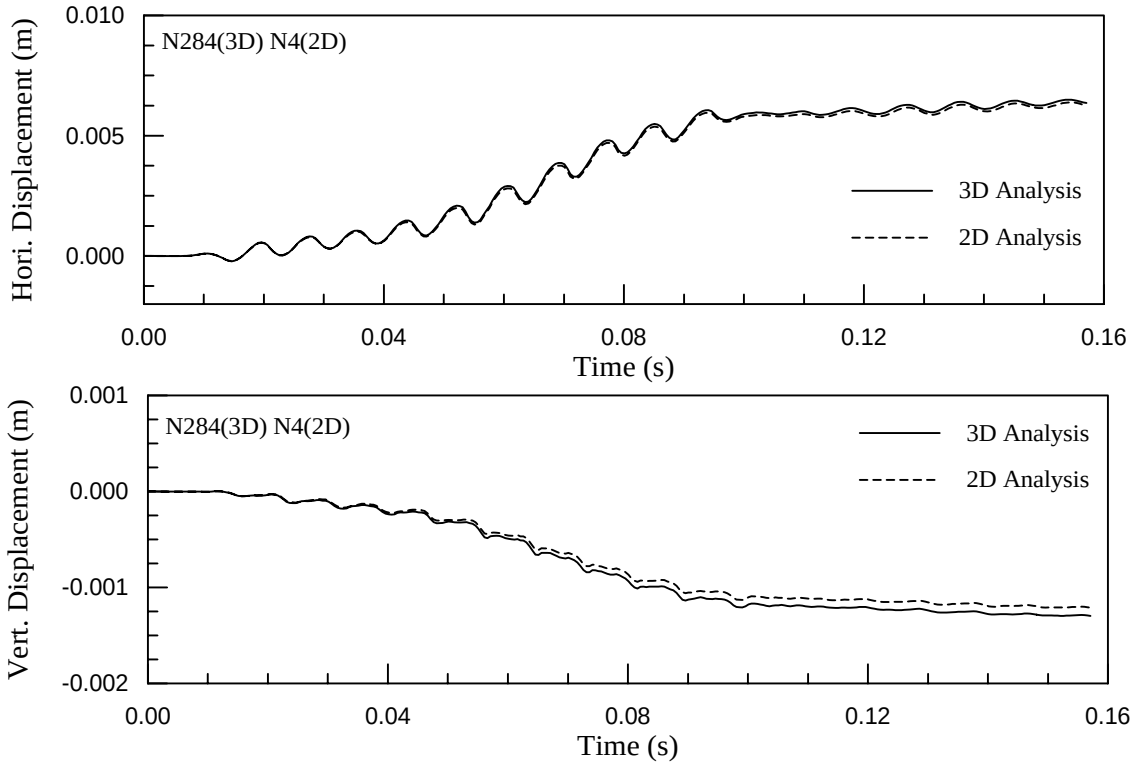

Figure 5.18: Comparison between 3-D and 2-D analysis – Displacement-time histories at node N284 (3D) and N4 (2D)

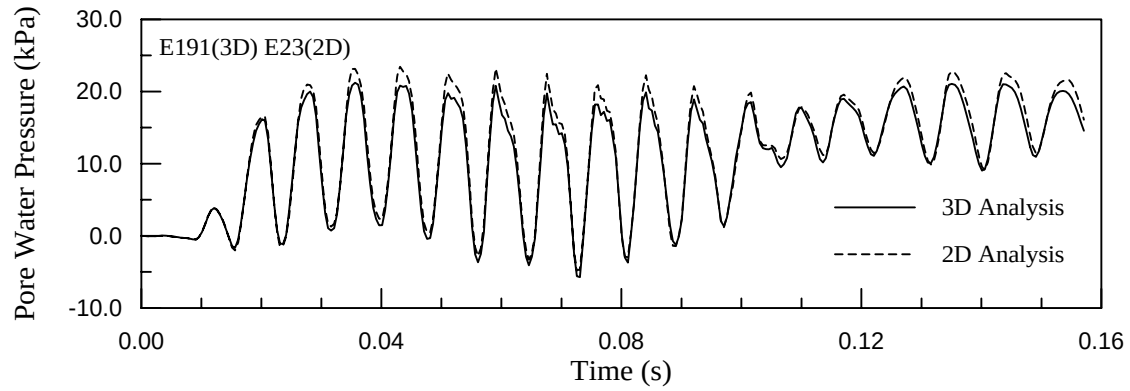

Figure 5.19: Comparison between 3-D and 2-D analysis - Pore pressure-time histories in E191 (3D) and E23 (2D)

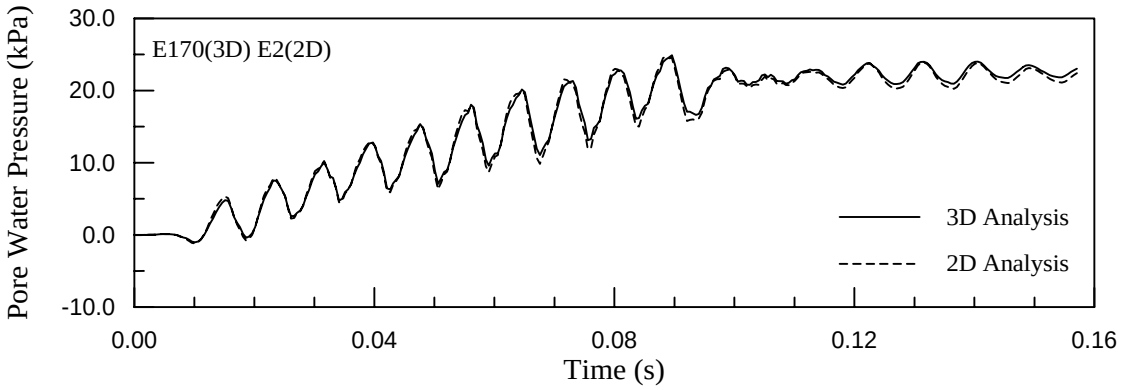

Figure 5.20: Comparison between 3-D and 2-D analysis - Pore pressure-time histories in E170 (3D) and E2 (2D)

5.6 Comparison of Computational Efficiency Between Traditional and Framework-Based Finite Element Codes

The 2-D problem discussed in Section 5.4.1.2 was run using DYSAC2 (Muraleetharan et al., 1988, 1997) and the new framework-based computer code TeraDysac to study the efficiency of the framework-based finite element approach. Both codes were run on a single Intel-Xeon processor with 3.0 GHz clock speed. The DYSAC2 took 1 hour 39 minutes and 32 seconds and the framework-based code TeraDysac took only 23 minutes and 30 seconds. By using the new computer code a 424% increase in computational efficiency was achieved over the traditional computer code. This increase in efficiency is attributed to the efficient, modern computational techniques, such as the robust global matrix equation solver and element matrix calculation algorithm, used in the framework-based method. The framework-based method incorporates modern computer science aspects at each and every calculation to increase the computational efficiency. On the other hand, in the traditional computer codes such as DYSAC2, more attention is paid to getting a working code rather than finding efficient ways to do the calculations.

In addition, the same problem was run on two processors with similar specifications using TeraDysac and a speedup of 1.43 was achieved (one processor took 23 minutes and 30 seconds and two processors took 16 minutes and 30 seconds). The DYSAC2 could not be run on two processors because it does not have the capability to run on multiple processors. The speedup of TeraDysac on multiple processors will increase even further for large 3-D problems because more time will be spent on calculations compared to message passing between processors.

6 PERFORMANCE OF THE UNIFORM GRADIENT ELEMENT

6.1 Introduction

As discussed in Chapter 2, the Gauss quadrature (GQ) method is typically used to evaluate the element matrices and vectors in finite element analyses. Four-node quadrilateral elements are commonly used in computational mechanics to achieve computational efficiency in large-scale simulations. However, these lower order elements lock volumetrically when fully integrated using the Gauss quadratue method for compressible or nearly incompressible materials. In order to avoid elements locking up and to achieve computational efficiency the Uniform Gradient (UG) method to calculate elements matrices and vectors can be used. The UG method uses a single point integration scheme, but requires a special hourglass control technique.

In this chapter, the applicability of uniform gradient method for evaluating the element matrices and vectors is investigated. Implementation of the uniform gradient element formulation in TeraDysac is verified using a 2-D fully coupled dynamic analysis code, DYSAC2 (Muraleetharan et al., 1988, 1997). The performance of the uniform gradient element is investigated by simulating the settlement of a footing and the dynamic behavior of a saturated clay embankment and a level ground. The performance

is also compared against the Gauss Quadrature (GQ) method. The effect of the hourglass control algorithm and the hourglass control parameters are also investigated.

6.2 Gauss Quadrature Element Formulation

The general form of the governing equations for the dynamics of multiphase porous media can be written using the usual notations as follows.

$$\mathbf{Ma} + \mathbf{Cv} + \mathbf{K}^f \mathbf{u} + \mathbf{f}^{\text{int}} = \mathbf{f}^{ext}$$

The mass matrix, damping matrix and internal loads ($\mathbf{f}^{\text{int}}$) are evaluated using full Gauss quadrature formulation, i.e. integrated over all four integration stations (Fig. 6.1) for a four-node quadrilateral element. The constitutive calculation is also performed at each integration station using the strains calculated at that integration station. The only exception is the evaluation of the fluid stiffness matrix. The fluid stiffness matrix is calculated using a uniform gradient element formulation because of the incompressible or nearly incompressible behavior of water in saturated porous media. The Gauss quadrature method has been implemented into the TeraDysac and this procedure is validated in Chapter 5.

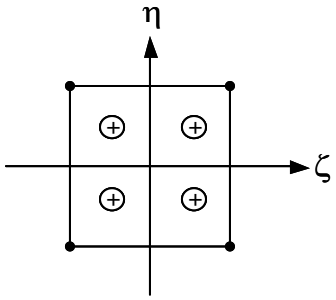

Figure 6.1: Gauss qudrature integration points for a 2-D quadrilateral element

6.3 Uniform Gradient Element Formulation

For the uniform gradient element formulation, the element fields are assumed to be uniform within the element and the integration is performed at one point as shown in Fig. 6.2. Since the values are evaluated at one point, looping over the integration stations is not required and thus a significant amount of computational effort can be saved for large scale and nonlinear elastoplastic calculations. Furthermore, the necessary footprint of the analysis is significantly reduced.

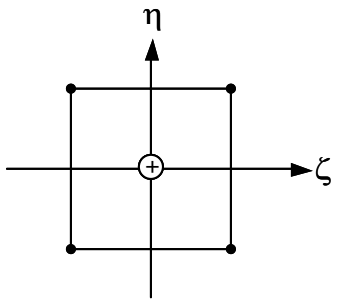

Figure 6.2: Single point integration for a 2-D quadrilateral element

It is dangerous to use single point integration without proper consideration for the zero energy or hourglass modes that exist. The mesh distortion due to hourglass modes is shown in Fig. 6.3. The evolution of hourglass modes can be eliminated by systematically calculating a resistance force.

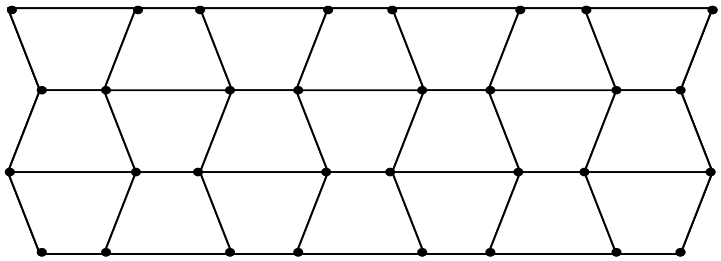

Figure 6.3: Hourglass patterns for 2D quadrilateral elements

Clearly, if the strains at the centroid of the elements shown in Fig 6.3 are evaluated, they will be zero and then the strain energy will also be zero.

6.4 Evidence of Excitation of Hourglass Modes in Fully Coupled Analysis of Porous Media

A rigid footing problem was selected to show the excitation of hourglass modes in the fully coupled analysis of porous media. The schematic of the problem is shown in Fig.6.4 (a). The footing was pushed down as shown in Fig. 6.4 (b) and the deformed mesh at 100 seconds is shown in Fig. 6.5. The analysis was done using the uniform gradient element formulation without any hourglass control with the foundation soil modeled as a saturated linear elastic material ($E = 3.0 \times 10^4\ kPa$, $\nu = 0.3$, $\rho^s = 2.62$, $\rho^f = 1.0$ and $porosity = 1.48$). The formation of hourglass modes can be seen around the surface and left and right boundaries but not close to the bottom boundary. The hourglass modes are not seen at the bottom boundary because the solid and liquid displacements are fixed at this boundary. The left and right boundaries are free to move in the vertical direction, but not in the horizontal direction. The top surface is a free surface. This caused the hourglass modes triggered by the stress gradients underneath the footing corners to propagate to the left, right, and top boundaries. It is also found through many numerical experiments that the level of excitation of hourglass modes is problem dependent. For example, the hourglassing shown in Fig. 6.5 will vary depending on the depth and the width of the soil layer and the maximum displacement of the footing. Kinematics behind the hourglass modes is discussed in the next section and a method to control hourglassing is proposed. In Section 6.7 this footing problem is analyzed again with proper hourglass control.

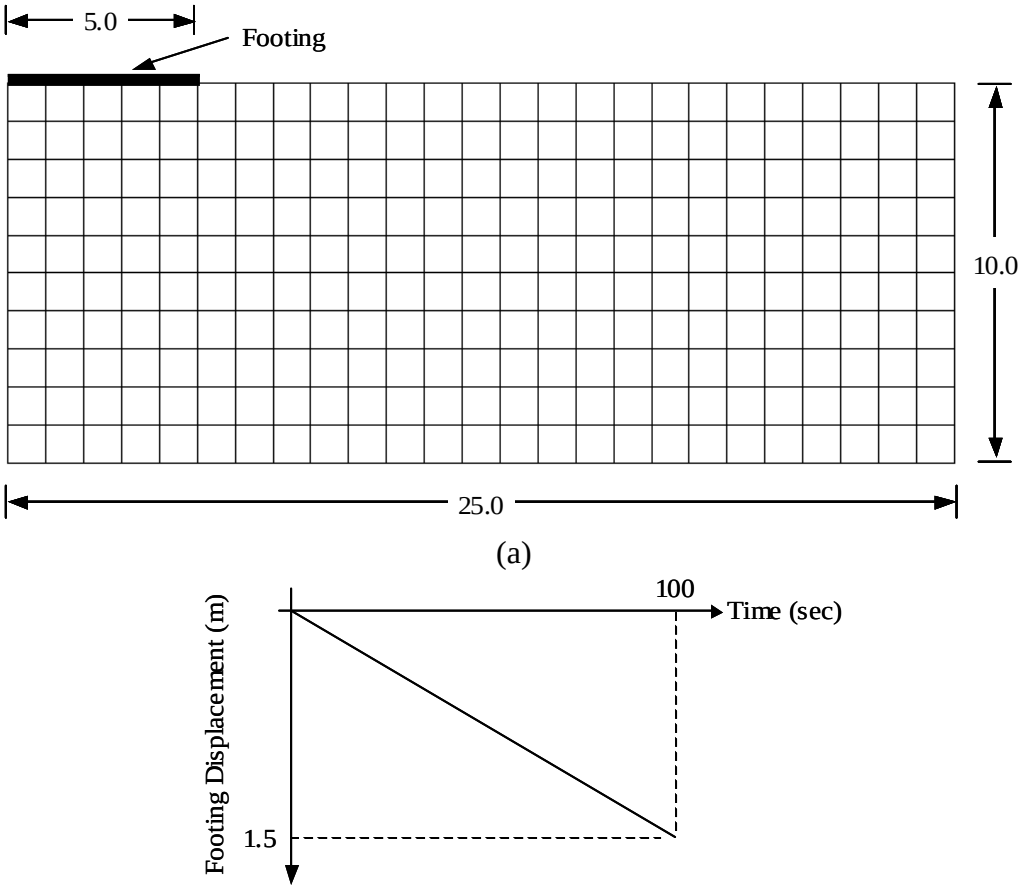

Figure 6.4: Schematic of the consolidation problem (all dimensions are in meters)

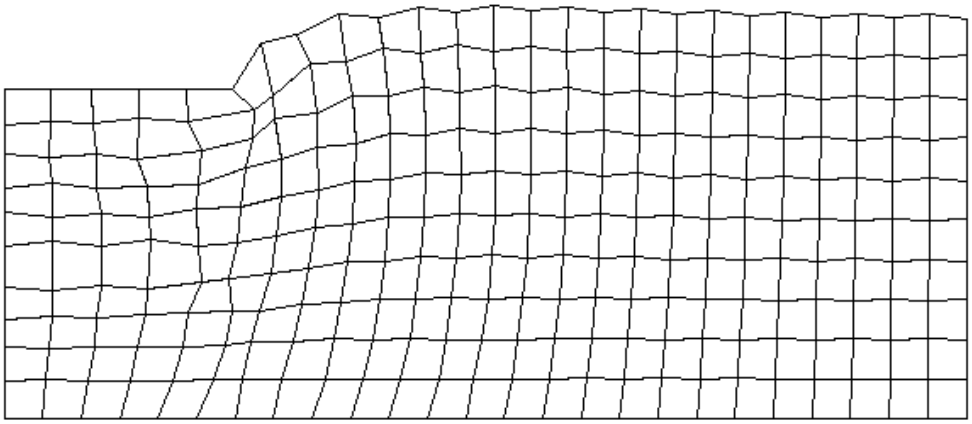

Figure 6.5: Deformed mesh at 100 seconds

6.5 Kinematics Behind the Single Point Integration and Hourglass Control Scheme

The hourglass control scheme presented by Flanagan and Belytschko (1981) are used in this study to control the hourglass mode and are summarized in this section.

6.5.1 Isoparametric Shape Function and Deformation Modes

Mapping of a unit square in ξ_i- space (ξ,η) to a general quadrilateral in x_i-space in two dimensions is shown in Fig 6.6 (a) and the displacement modes are shown in Fig 6.6(b). Choosing the center of the square at the origin in ξ_i-space, the shape functions can be expanded in terms of an orthogonal set of base vectors, Σ_I, Λ_{iI} and Π_I as shown in Eq. 6.1. The values of base vectors are listed in Table 6.1 for each node.

$$N_I = \frac{1}{4}\Sigma_I + \frac{1}{4}\xi\,\Lambda_{1I} + \frac{1}{4}\eta\,\Lambda_{2I} + \frac{1}{4}\eta\varsigma\,\Pi_I \tag{6.1}$$

In Eq. 6.1, Σ_I is the summation vector that accounts for rigid body translation. The Σ_I vectors are summation vectors since it may be employed in indicial notation to represent the algebraic sum of vectors. The linear base vectors Λ_{iI} may be readily combined to define two normal strain modes, two uniform shear strain modes and two rigid body rotation modes for the unit square. Thus the Λ_{iI} vectors are referred as the volumetric base vectors since they are the only base vectors, which appear in the element volume expression. The last vector Π_I gives rise to linear strain modes, which are neglected by one-point integration. These vectors define the hourglass patterns for a unit square.

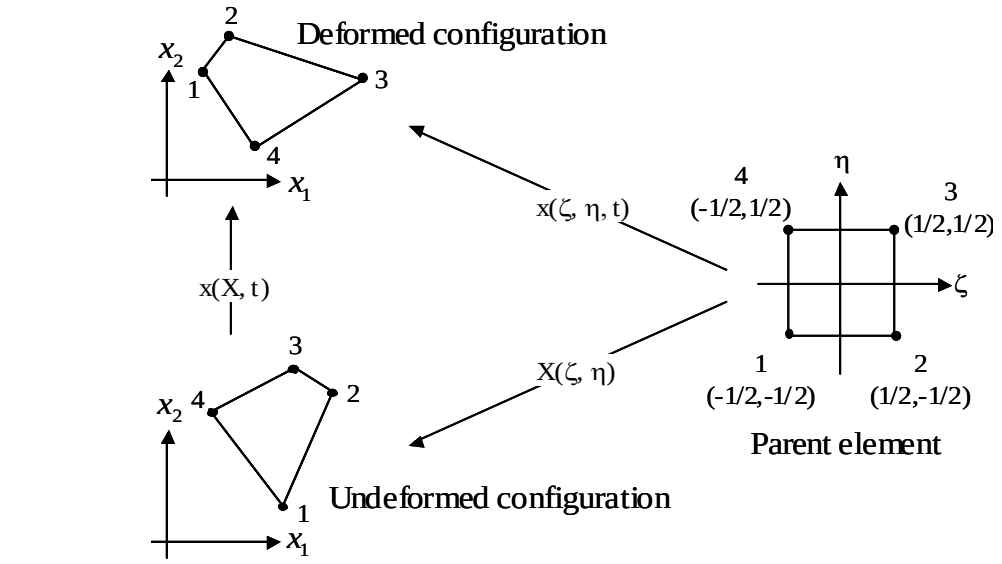

(a)

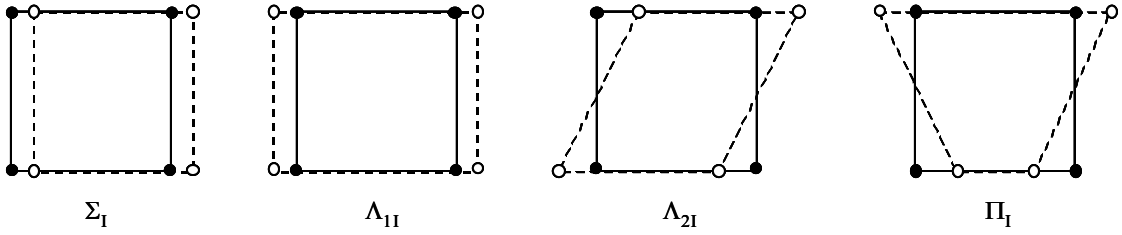

(b)

Figure 6.6: Quadrilaterals and its displacement modes; hourglass modes are Π_I

Table 6.1: Base vectors and their values at each node

Node	ξ	η	Σ_I	Λ_{1I}	Λ_{2I}	Π_I
1	-1/2	-1/2	1	-1	-1	1
2	1/2	-1/2	1	1	-1	-1
3	1/2	1/2	1	1	1	1
4	-1/2	1/2	1	-1	1	-1

6.5.2 One-Point Integration and the Calculation of Consistent Nodal Point Forces

The principle of virtual work gives us the following relationship for the element nodal forces f_{iI} :

$$\dot{u}_{iI} f_{iI} = \int_V \sigma_{ij} D_{ij} dV$$

where σ_{ij} is stress tensor, D_{ij} is deformation rate tensor and V is the volume of the element. The deformation rate tensor can be replaced by the velocity gradient since the Cauchy's stress tensor is symmetric. When the one-point integration is used, the nonlinear portion of the element displacement fields is neglected, and results in a uniform state of strain and stress. The preceding expression is approximated by

$$\dot{u}_{iI} f_{iI} = V \bar{\sigma}_{ij} \dot{\bar{u}}_{i,j}$$

where $\bar{\sigma}_{ij}$ represents the assumed uniform stress field and will be referred to as the mean stress tensor.

By neglecting nonlinear displacements, we assume that the mean stresses depend only on the mean strains. Mean kinematic quantities are defined by integrating over the element as follows:

$$\dot{\bar{u}}_{i,j} = \frac{1}{V} \int_V \dot{u}_{i,j} dV \tag{6.2}$$

The velocity gradient is expressed in terms of nodal displacement and shape functions as follows:

$$\dot{\bar{u}}_{i,j} = \frac{1}{V} \int_V \dot{u}_{iI} N_{I,j} dV \tag{6.3}$$

Define

$$B_{jI} = \int_V N_{I,j} dV$$

Then, the mean velocity gradient is given by:

$$\dot{\bar{u}}_{i,j} = \frac{1}{V}\dot{u}_{iI}B_{jI}$$

Therefore, the nodal forces are expressed by the following equation:

$$f_{iI} = \bar{\sigma}_{ij}B_{jI} \tag{6.4}$$

The B-matrix has to be evaluated to calculate the nodal forces. The B-matrix contains only components of the volumetric base vectors Λ_{iI}. Therefore, only the volumetric base vectors lead to stresses or nodal forces within the one-point integration framework.

The nodal point forces calculated using above equation can not resist the formation of hourglass modes. Therefore, the force contribution from the nonlinear displacement fields has to be calculated and added to resist the formation of hourglass modes as described in Section 6.5.4.

6.5.3 Stress-Strain Relationship

The integration scheme described above does not assume any constitutive law, i.e. it is material independent. The only stipulation is that the stress state does not depend on the nonlinear portion of the element displacement field. Hence the mean stress must be related only to the mean strain rates (as opposed to the full strain field) through the governing material law.

6.5.4 Anti-Hourglassing Force

The idea behind the use of hourglass control scheme is the application of additional force to resist the formation of hourglass modes. The resistant can be applied

as stiffness and or damping. In the case of fully saturated porous media, stiffness can be applied to the solid and pore fluid and damping can be applied to the solid and pore fluid. In this study, however, only solid stiffness, solid damping, and fluid stiffness are used to control the hourglass mode shapes. The equations for solid and fluid stiffnesses for a two dimensional quadrilateral element are derived in the later part of the this section.

The mean stress-strain formulation considers only a fully linear velocity field. The remaining portion of the nodal velocity field is the so-called hourglass field. Excitation of these modes may lead to severe, unresisted mesh distortion. The following method is used to isolate the hourglass modes so that they may be treated independently of the rigid body and uniform strain modes.

The hourglass field $\dot{u}_{iI}^{hg}$ may now be defined by removing the linear portion of the nodal velocity field:

$$\dot{u}_{iI}^{hg} = \dot{u}_{iI} - \dot{u}_{iI}^{lin}$$

It can be proved that the summation vectors and B-matrix are orthogonal to the hourglass field:

$$\dot{u}_{iI}^{hg} \Sigma_I = 0$$

$$\dot{u}_{iI}^{hg} B_{jI} = 0$$

Since the B-matrix is a linear combination of volumetric base vectors Λ_{iI}, the last contribution may be stated equivalently as:

$$\dot{u}_{iI}^{hg} \Lambda_{jI} = 0$$

From the above equation it can be said that the hourglass fields are orthogonal to all the base vectors as given in Table 6.1 except the hourglass base vectors. Therefore, the hourglass velocity fields can be expanded as a linear combination of the hourglass base vectors.

The contribution of the hourglass resistance to the nodal force is given by:

$$f_{iI}^{hg} = \frac{1}{2} Q_i \gamma_I \tag{6.5}$$

where Q_i are anti-hourglass stiffness (K_{hg}) or damping (C_{hg}) defined in the next sections and γ_I are the hourglass shape vectors. There are two types of hourglass resistances: artificial damping and artificial stiffness. The anti-hourglass stiffness and damping resistances are defined in terms of the maximum frequency and stiffness of the element. The stiffness and damping are given in the next section.

6.5.5 Anti-Hourglass Stiffness

The artificial solid hourglass stiffness resistance for a 2-D isoparametric element is given by:

$$K_{hg}^{s} = k^{s} \left(\frac{D_{4,4}}{8A_r} \right) K_{hgstiff} \tag{6.6}$$

where $D_{4,4}$ is the deviatoric component of the material stiffness matrix, k^s is solid hourglass stiffness coefficient, A_r is the aspect ratio and $K_{hgstiff}$ is the hourglass stiffness matrix. For an elastic analysis, $D_{4,4}$ will be $\lambda + 2\mu$.

The corrected solid stiffness matrix is the summation of solid stiffness matrix calculated using single point integration and the solid hourglass stiffness, i.e.

$$K^s = K^s_{sp} + K^s_{hg}$$

The artificial fluid hourglass stiffness resistance is given by:

$$K^f_{hg} = k^f \left(\frac{\Gamma}{8A_r} \right) K_{hgstiff} \tag{6.7}$$

where Γ is the bulk modulus of liquid, k^f is fluid hourglass stiffness coefficient, A_r is the aspect ratio and $K_{hgstiff}$ is the hourglass stiffness matrix

The equivalent fluid stiffness is,

$$K^f = K^f_{sp} + K^f_{hg}$$

6.5.6 Anti-Hourglass Damping

The artificial solid hourglass damping resistance is given by:

$C^s_{hg} = c^s \sqrt{\left(\frac{\rho^s D_{4,4}}{8} \right) K_{hgstiff}}$ and the equivalent solid damping is:

$$C^s = C^s_{sp} + C^s_{hg} \tag{6.8}$$

The artificial fluid hourglass damping resistance is given by:

$C^s_{hg} = c^s \sqrt{\left(\frac{\rho^f \Gamma}{8} \right) K_{hgstiff}}$ and the equivalent fluid damping is:

$$C^f = C^f_{sp} + C^f_{hg} \tag{6.9}$$

Flanagan and Belytschko (1981) emphasized that a more successful approach to combat hourglassing is to use an artificial stiffness, which allows only mild hourglassing. Unlike damping, hourglass stiffness does not attenuate global modes. Even though artificial stiffness and damping could be combined, it is found no evidence that additional

damping provides any improvement. However, the effect of artificial damping is also studied in this research. The solid stiffness, solid damping and fluid stiffness, hourglass control algorithms are implemented within TeraDysac.

6.6 Verification of the Numerical Model Using DYSAC2

The finite element model for saturated soil used in TeraDysac was verified using a fully coupled analysis code DYSAC2 (Muraleetharan, 1988, 1997). In DYSAC2, the constitutive calculation is done only at the center of the element. This value is used to calculate the consistent nodal point forces at all integration station. This procedure is same as to the uniform gradient calculation in TeraDysac without any hourglass control. The same problem was run using both codes and the results were compared. The mesh used in a two-element problem is shown in Fig. 6.7. The loading was a simple sinusoidal base shaking.

The vertical and horizontal displacements at nodes N4 and N5 (Fig. 6.7) are plotted in Fig. 6.8 and 6.9, respectively. The displacements predicted by DYSAC2 and TeraDysac matched very well. Therefore, it can be concluded that the implementation of the governing equation for saturated porous media using uniform gradient elements is correctly done in TeraDysac.

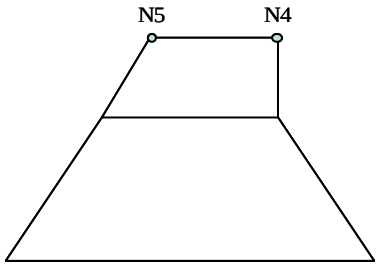

Figure 6.7: Two-element mesh for verification using DYSAC2

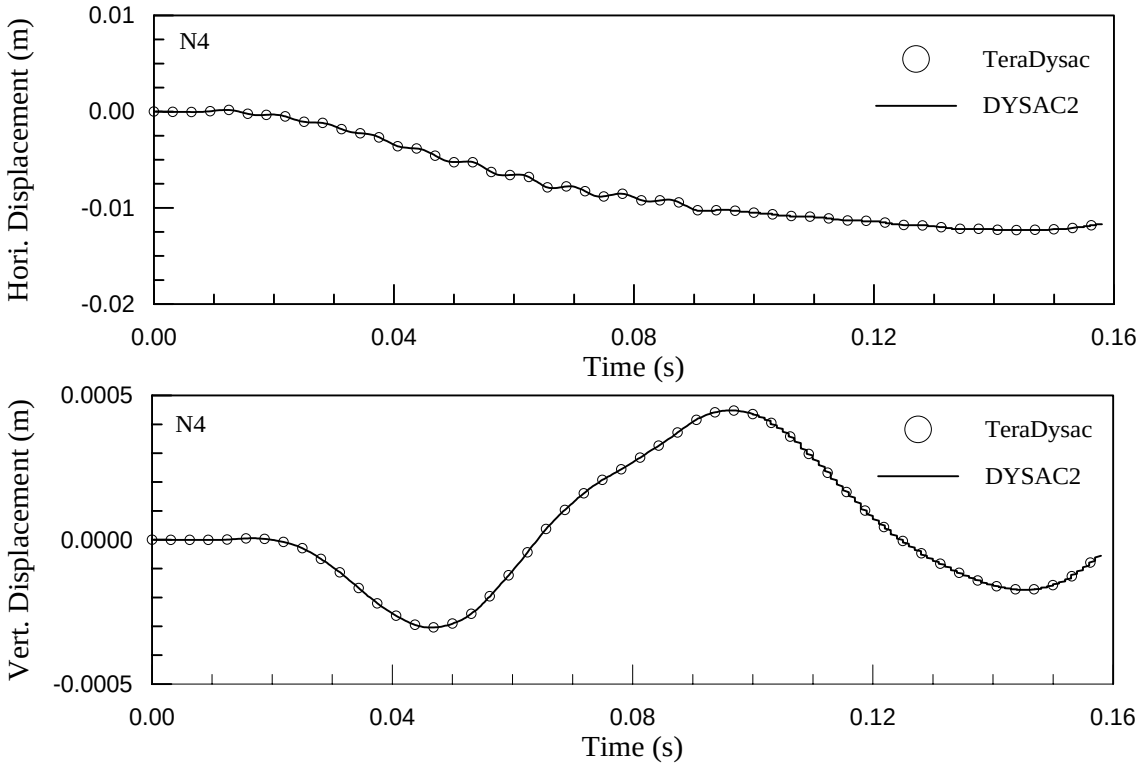

Figure 6.8: Comparison of horizontal and vertical displacement between TeraDysac and DYSAC2 at N4

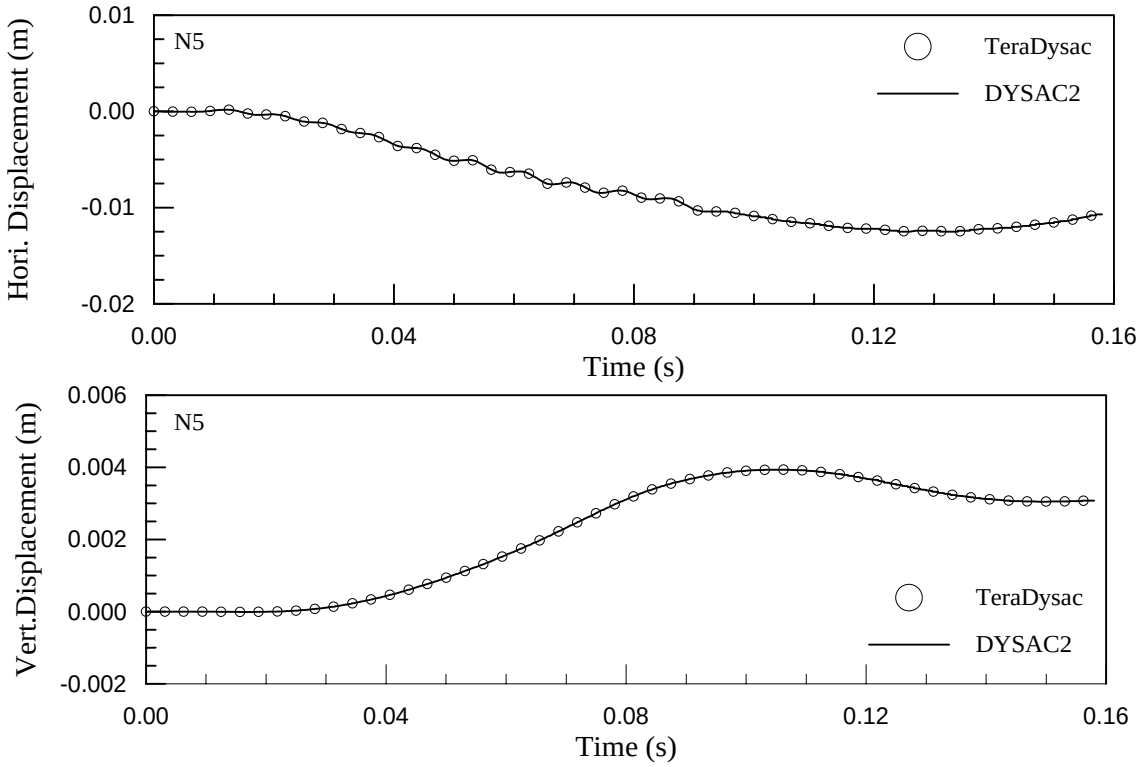

Figure 6.9: Comparison of horizontal and vertical displacement between TeraDysac and DYSAC2 at N5

6.7 Effectiveness of the Proposed Hourglass Control Method

The same problem used to show the excitation of the hourglass modes in Section 6.4 is simulated with proper hourglass control (solid stiffness parameter = 5%, solid damping parameter = 5%). The deformed mesh at 100 seconds is shown in Fig. 6.10. The deformed mesh shows that the proposed hourglass control methods effectively eliminated the excitation of hourglass modes. The critical places of formation of hourglass modes: surface and left and right boundaries were further examined by magnifying the deformed shape by different factors.

The performance of the uniform gradient element formulation and the effectiveness of the anti-hourglass method on the dynamic behavior of some of the common geotechnical engineering problems are discussed in the following sub sections.

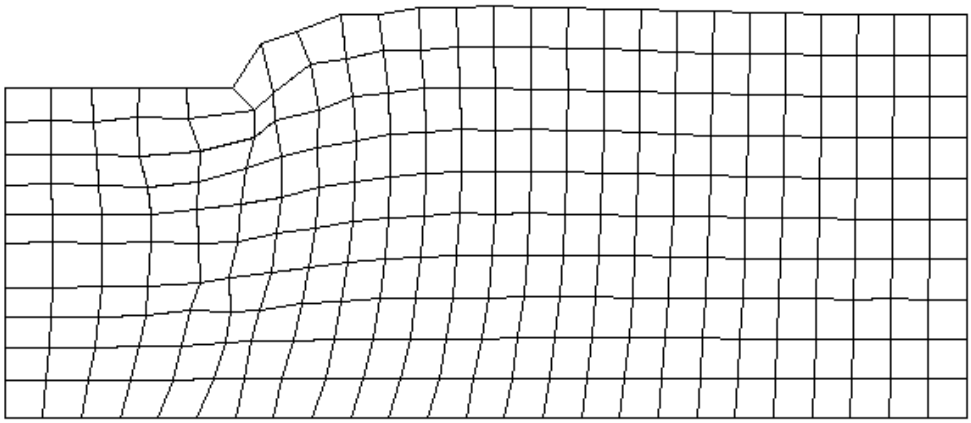

Figure 6.10: Deformed mesh with hourglass control

6.8 Performance of the Uniform Gradient Element Formulation for the Dynamic Behavior of Saturated Clay Embankment

The centrifuge model embankment described in Chapter 5 is used here. The experiment is simulated using both GQ method and the UG method. The finite element mesh for the embankment is shown in Fig. 6.11 and the base motion time history is

shown in Fig. 6.12. Simulation with UG method has been performed without any hourglass control and 5% of solid stiffness and 5% of solid damping as suggested by Flanagan and Belytschko (1981).

The deformed shapes and displacement vectors at mid (0.07875 sec) and end (0.1575 sec) of the analysis without hourglass control are shown in Fig. 6.13. Excitation of hourglass modes in this analysis is visible neither on the deformed shapes nor displacement vectors. The displacement-time histories predicted by the GQ and UG formulations at nodes N188 and N67 are shown in Fig. 6.14. Vertical displacement at node N188 is slightly under predicted by the UG formulation with and without hourglass control. The differences between the GQ and UG formulations with and without hourglass control are not very obvious. In some cases, for example for the vertical displacement time history at node N67, the GQ formulation and UG formulation without hourglass control fall on top of each other. The pore pressure time histories in element E112 and E157 are shown in Fig. 6.15. Pore pressures in E157 predicted by UG methods are slightly different than that predicted by the GQ method. The horizontal and vertical accelerations at nodes N181 and N251 are shown in Figs. 6.16 and 6.17, respectively. The amplitude and frequency of the acceleration predicted by GQ and UG formulations look similar.

At this point, the effect of single point integration (UG formulation) could not be seen in the overall dynamic behavior of the clay embankment. The consolidation problem discussed in Section 6.4 and 6.7 shows formation of hourglass. However, the dynamic problem discussed in this section does not show any hourglass modes. The reason for this difference is that the inertial load caused by the base shaking is a body force and does not

have sharp stress gradients as in the footing problem. Sharp stress gradients are needed to trigger hourglass modes. The effect of the UG element formulation on the acceleration time histories are further investigated using Fast Fourier Transformation in the next section.

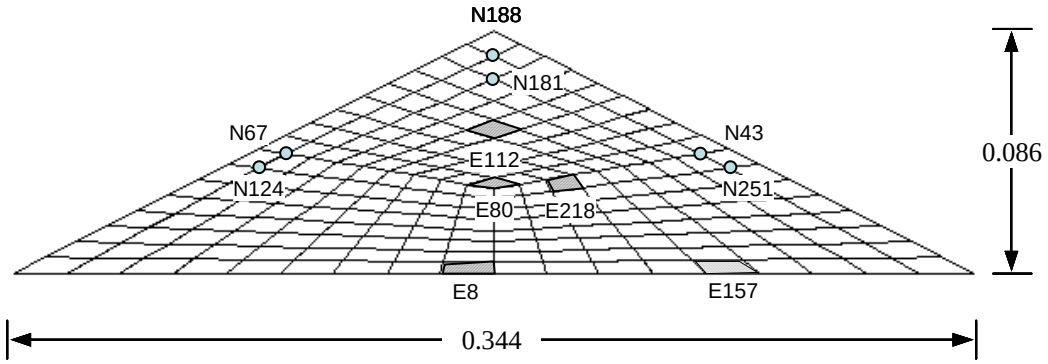

Figure 6.11: Finite element mesh of the model embankment (All dimensions are in meters and model scale)

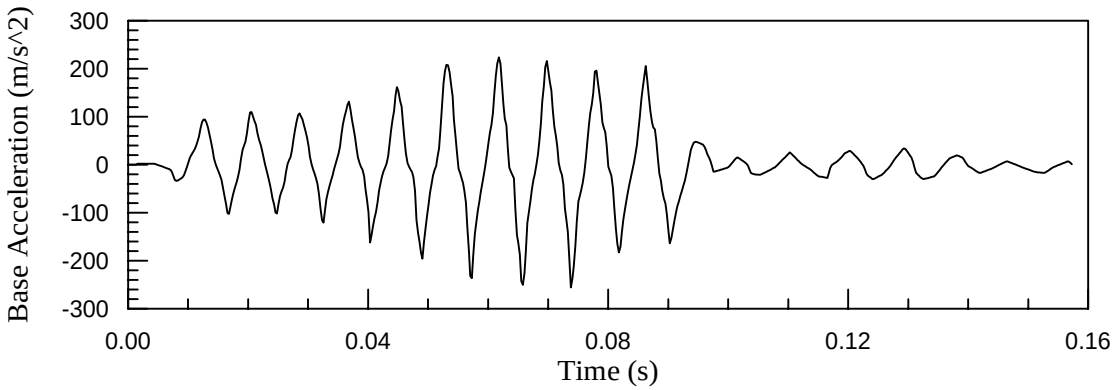

Figure 6.12: Horizontal base motion acceleration (model dimensions)

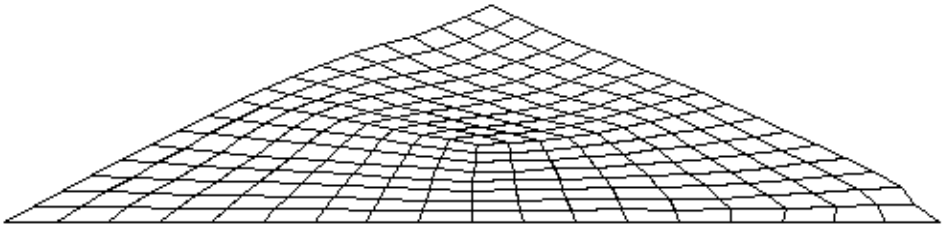

(a) Deformed mesh at 0.07875 sec (displacement magnified by 2)

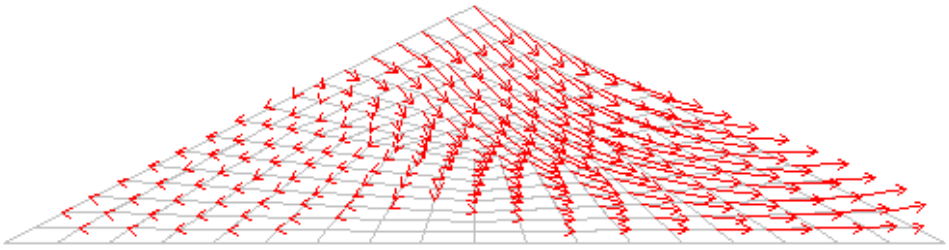

(b) Displacement vectors at 0.07875 sec

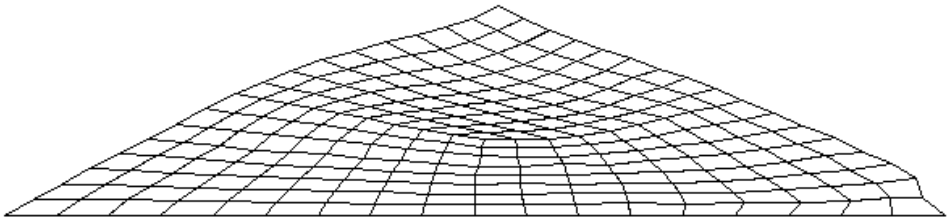

(c) Deformed mesh at 0.1575 sec (displacement magnified by 2)

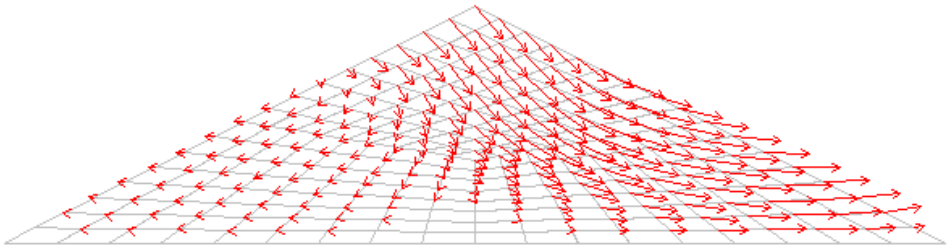

(d) Displacement vectors at 0.1575 sec

Figure 6.13: Deformed shapes and displacement vectors using UG formulation without hourglass control

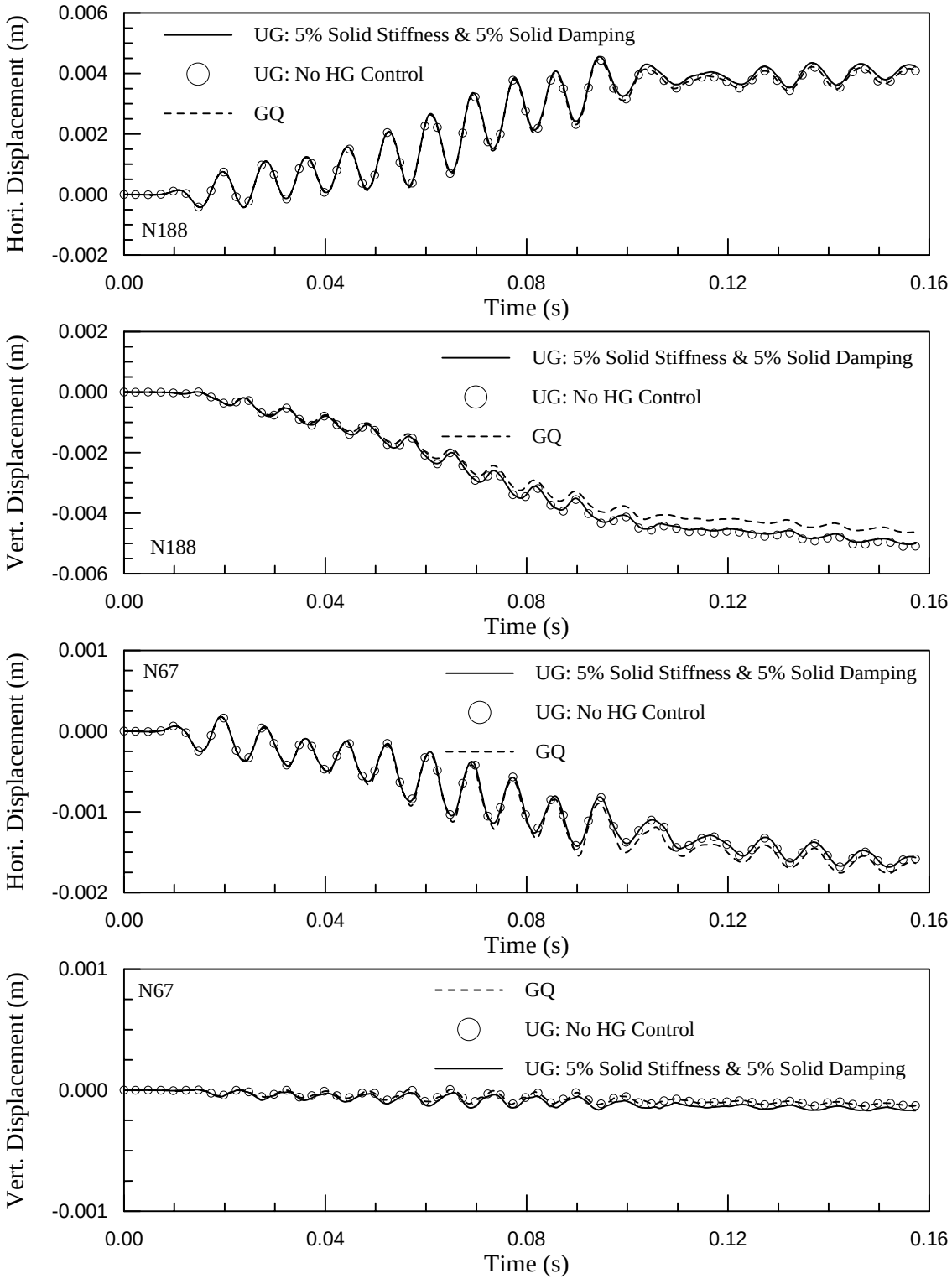

Figure 6.14: Comparison between the predicted horizontal and vertical displacement at nodes N188 and N67 using GQ and UG formulations

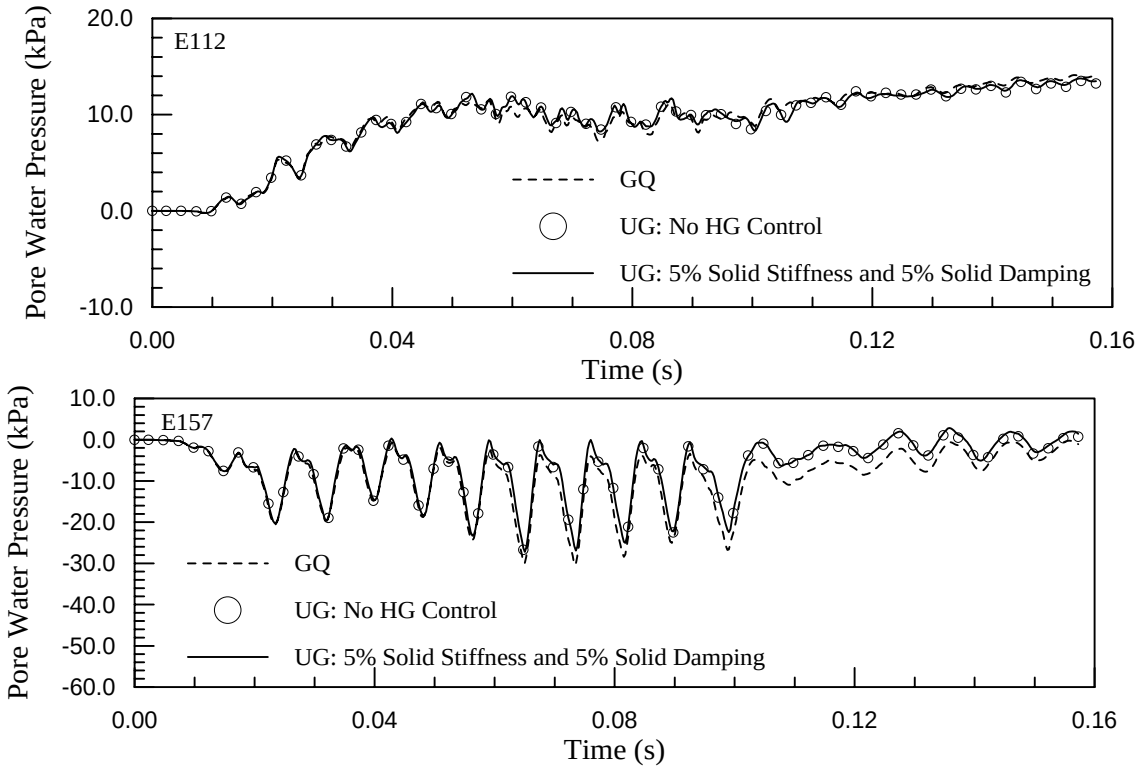

Figure 6.15: Comparison between predicted pore water pressures using GQ and UG formulations in elements E112 and E157

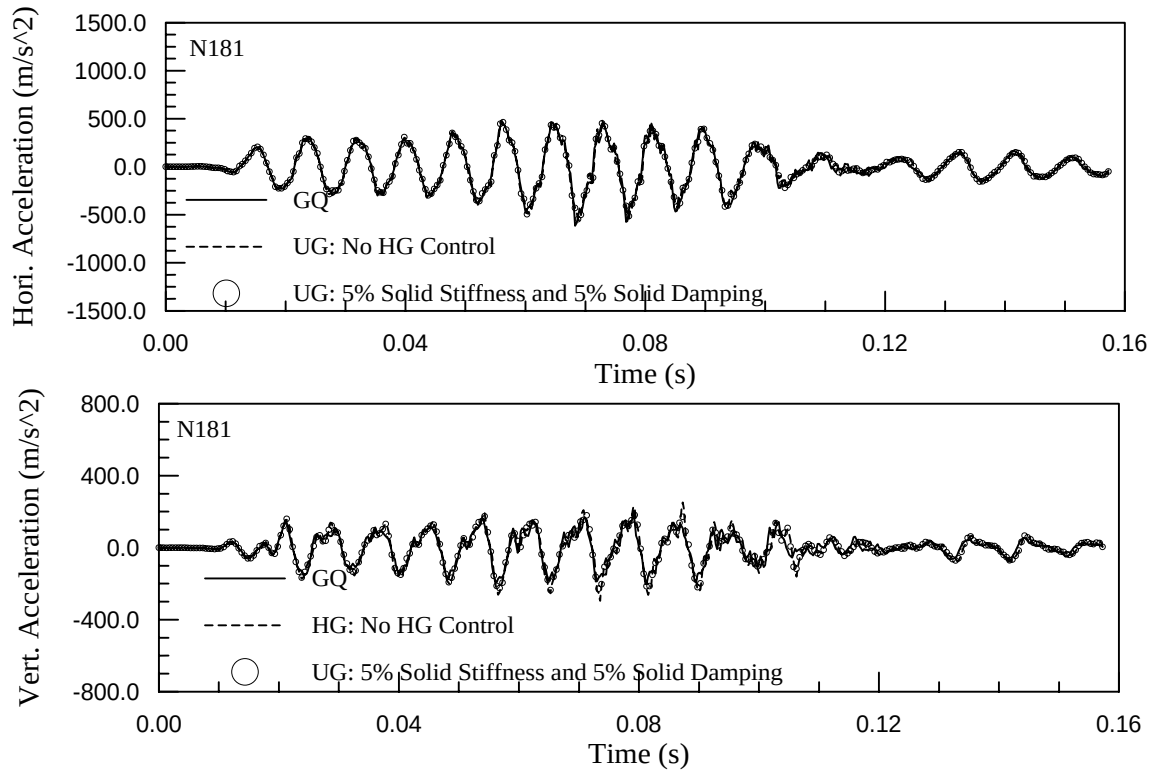

Figure 6.16: Comparison between predicted horizontal accelerations at node N181 using GQ and UG formulations

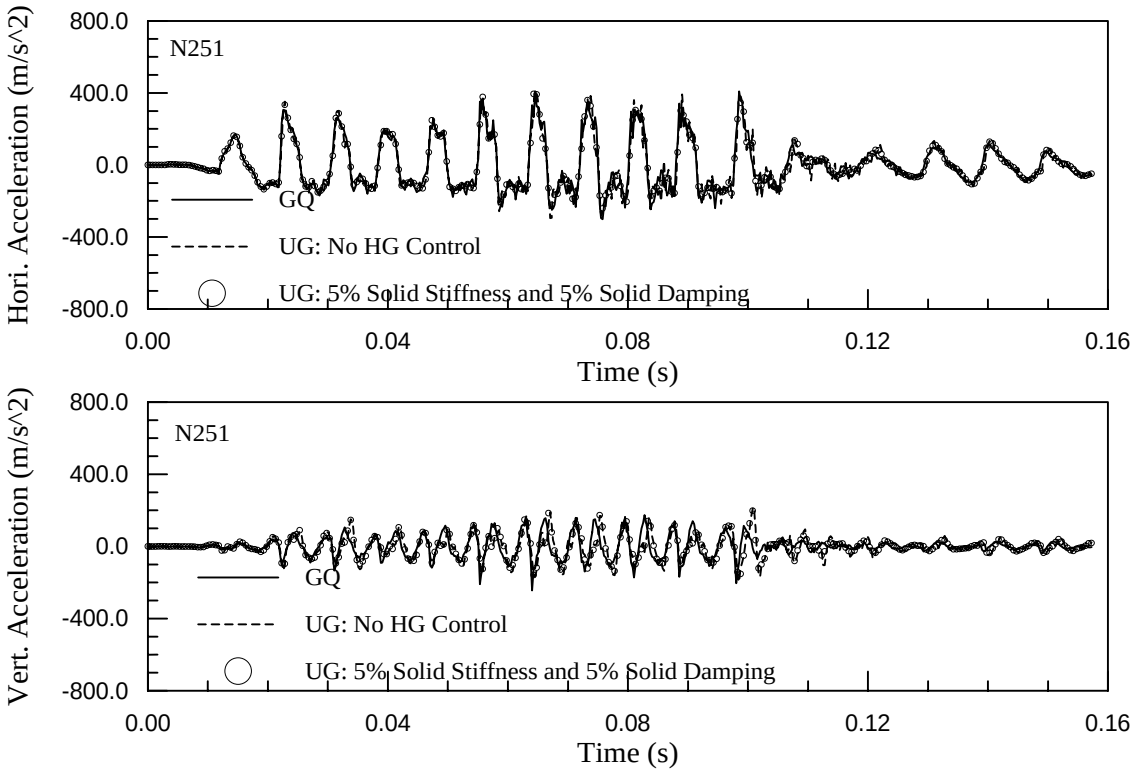

Figure 6.17: Comparison between predicted vertical acceleration at node N251 using GQ and UG formulations

6.8.1 Further Investigation of Acceleration Time Histories Using Fast Fourier Transformation

Hourglass effects were not apparent in the displacement, pore pressure and acceleration time histories. Fourier analysis was performed on the nodal accelerations to further investigate the performance of uniform gradient element formulation. Fourier analysis is based on the concept that real world signals can be approximated by a sum of series of sinusoidal functions. The normalized (with maximum amplitude of each acceleration) Fast Fourier Transform (FFT) of the horizontal and vertical accelerations with and without hourglass control at nodes N188 and N251 are shown in Figs. 6.18 and 6.19, respectively. The predominant frequency for the input motion is located around 120 Hz. There is only one predominant frequency for the horizontal accelerations at nodes N181 and it is located around 600 Hz. The predominant frequency for the vertical

acceleration is also located around 600 Hz, but there is a second predominant frequency around 1200 Hz. This is observed for both GQ and UG formulations. The predominant frequency for the horizontal acceleration at N251 is located around 600 Hz and the second predominant frequency is located around 1200 Hz. For the vertical acceleration, the predominant frequency is shifted to 1200 Hz. There is a difference in the third predominant frequencies produced by GQ and UG formulation without hourglass control. The third predominant frequency occurs around 1800 Hz for the GQ formulations and around 2400 Hz for the UG formulation without hourglass control. The amplitudes of the higher frequency modes for the UG formulation without hourglass control are in general higher than that of GQ formulation. The hourglass control scheme effectively reduces these high frequency amplitudes.

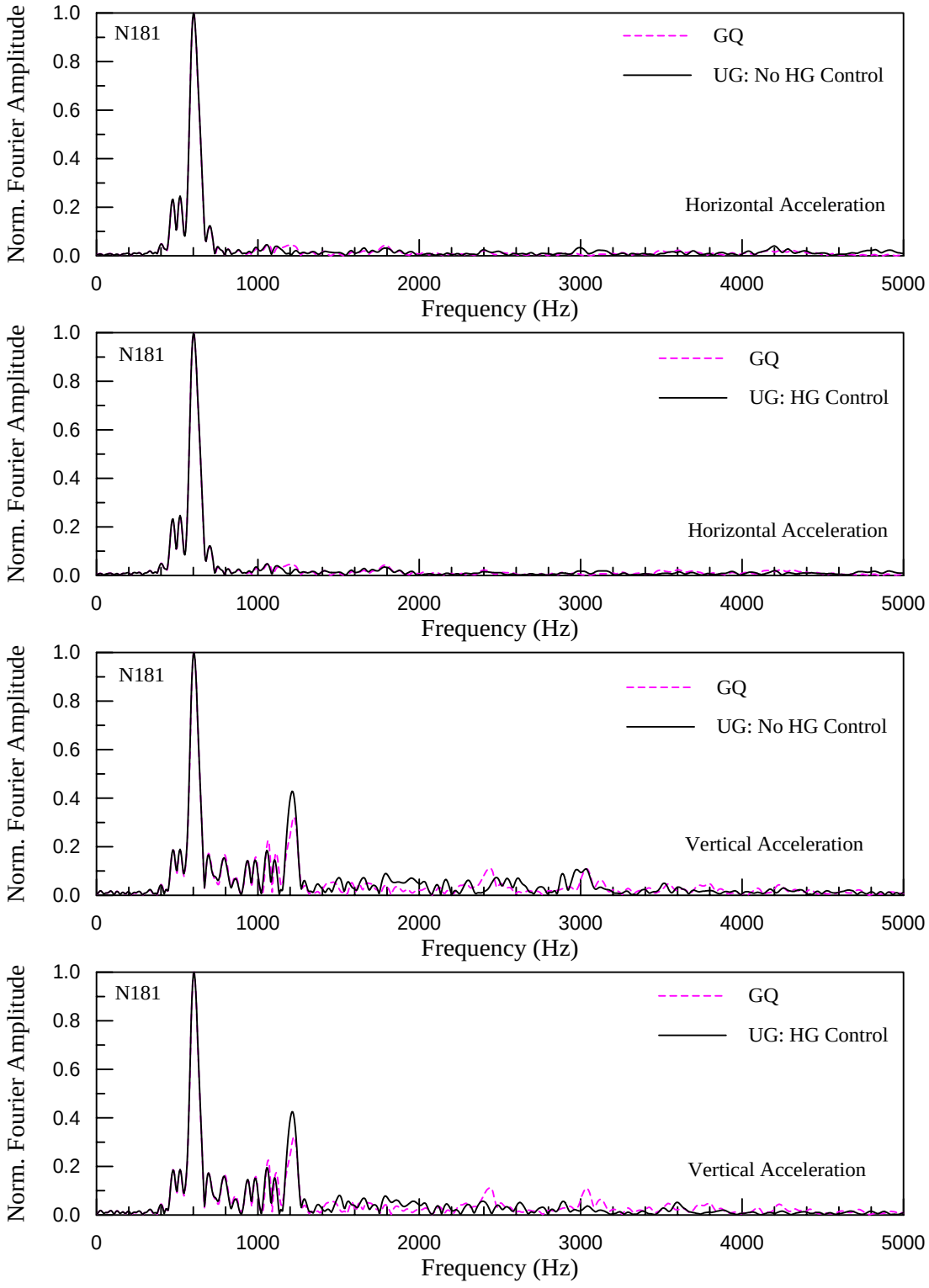

Figure 6.18: FFT of horizontal and vertical acceleration at N181

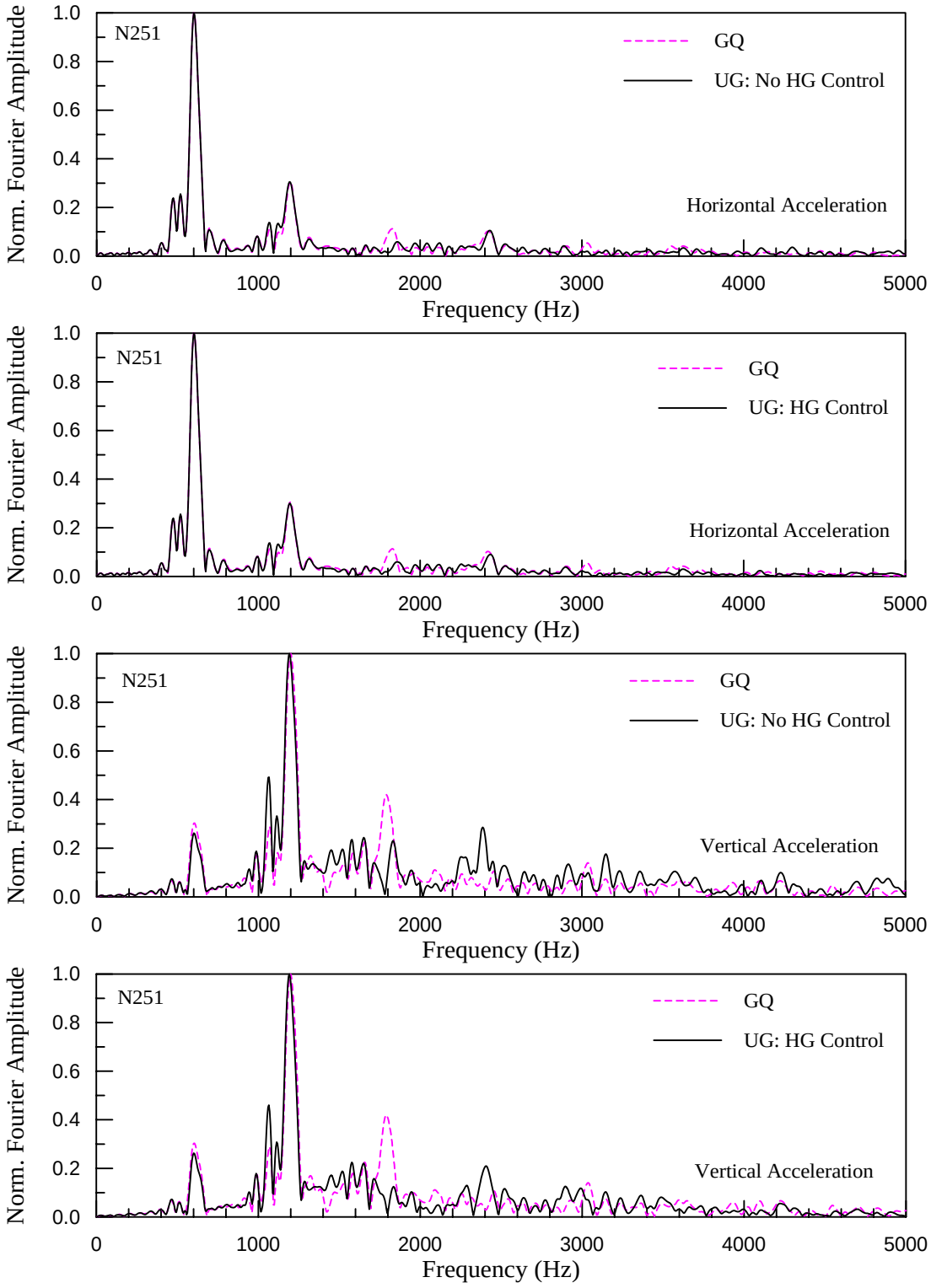

Figure 6.19: FFT of horizontal and vertical acceleration at N251

6.8.2 Parametric Study on Hourglass Control Parameters

The effect of solid stiffness, solid damping and fluid stiffness hourglass control parameters on the overall behavior of the saturated clay embankment is investigated in this section.

6.8.2.1 Effect of solid stiffness coefficient

The solid stiffness coefficient is the highly recommended parameter to be used in controlling the hourglass modes. To investigate the effect of the solid stiffness parameter on the overall behavior, the parameter was varied from 0 to 15%. The horizontal and vertical displacements at nodes N188 is shown in Fig. 6.20. The pore pressure-time history in element E112 is shown in Fig. 6.21. A slight decrease in displacements and slight increase in pore water pressures are observed with increasing solid stiffness coefficient. Similar trends were observed at nodes N67 and N43 and in elements E218, E80 and E8.

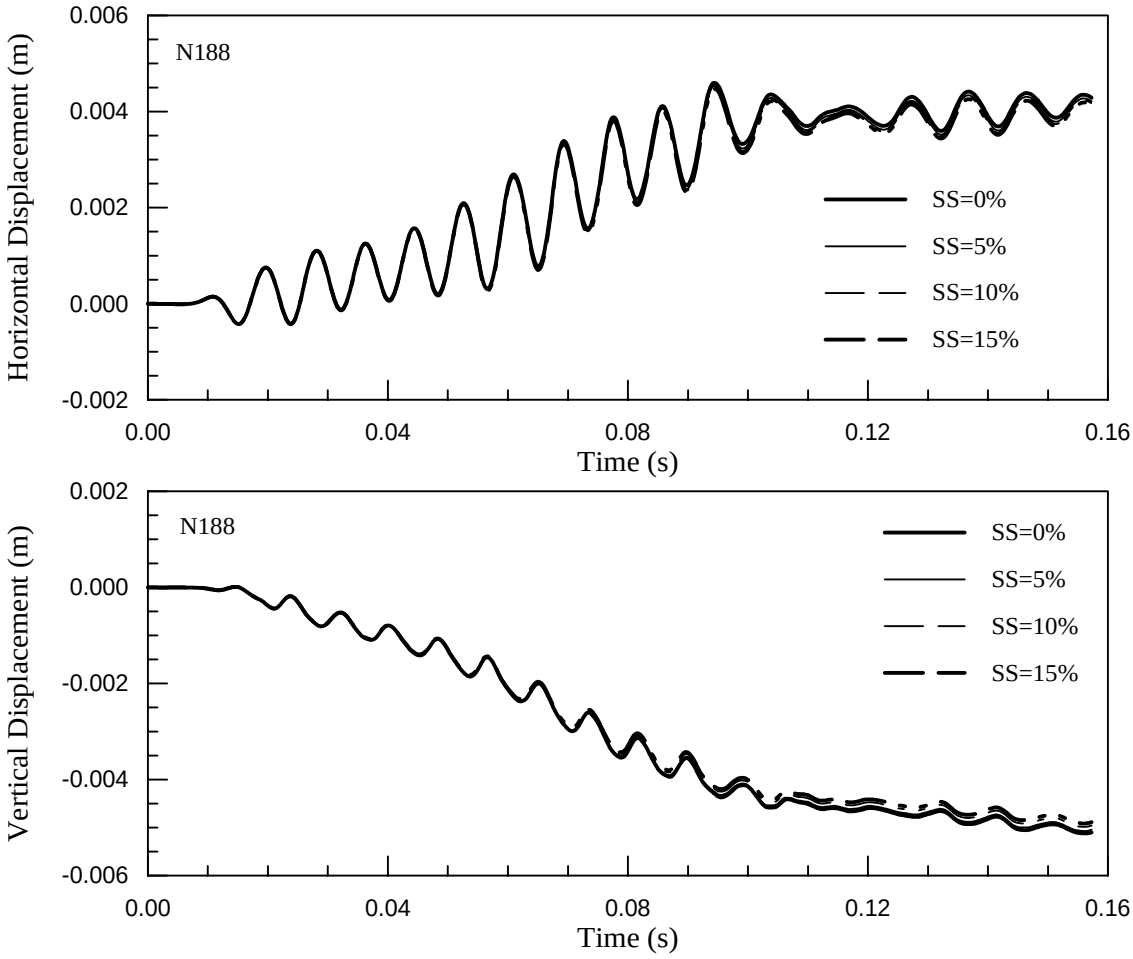

Figure 6.20: Effect of solid stiffness parameter on horizontal displacement

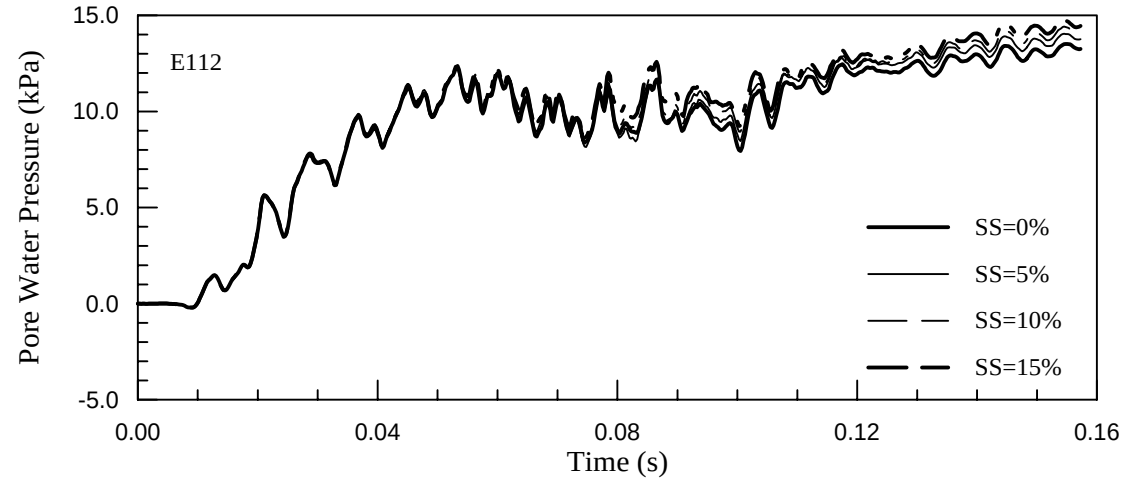

Figure 6.21: Effect of solid stiffness parameter on pore water pressure

6.8.2.2 Effect of solid damping coefficient

The solid damping coefficient was also varied from 0 to 15%. The horizontal and vertical displacements at nodes N188 is shown in Fig. 6.22. The pore pressure-time histories in element E112 is shown Fig. 6.23. It is observed that the solid damping coefficient does not affect the solution. Similar behavior was observed at other nodes and elements.

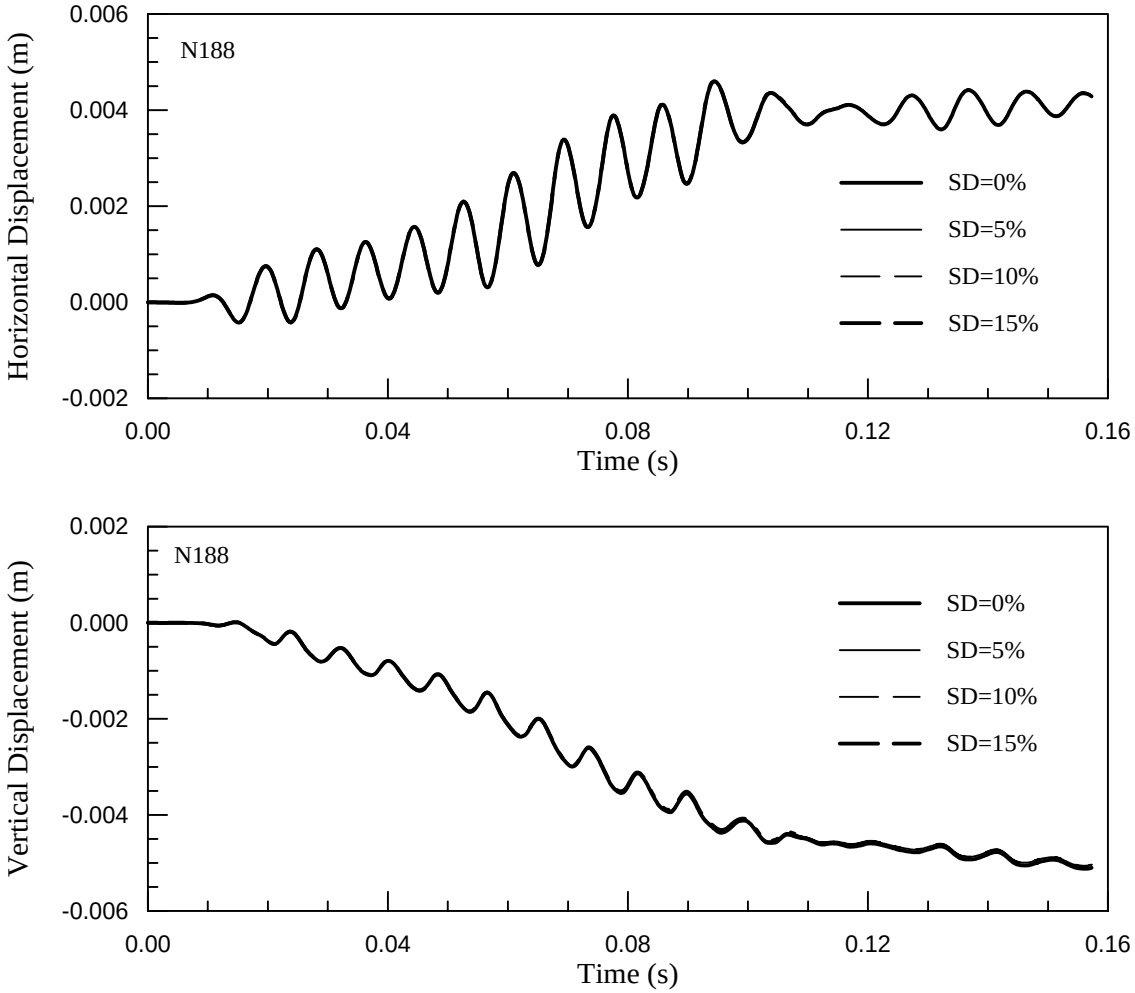

Figure 6.22: Effect of solid damping parameter on vertical displacement

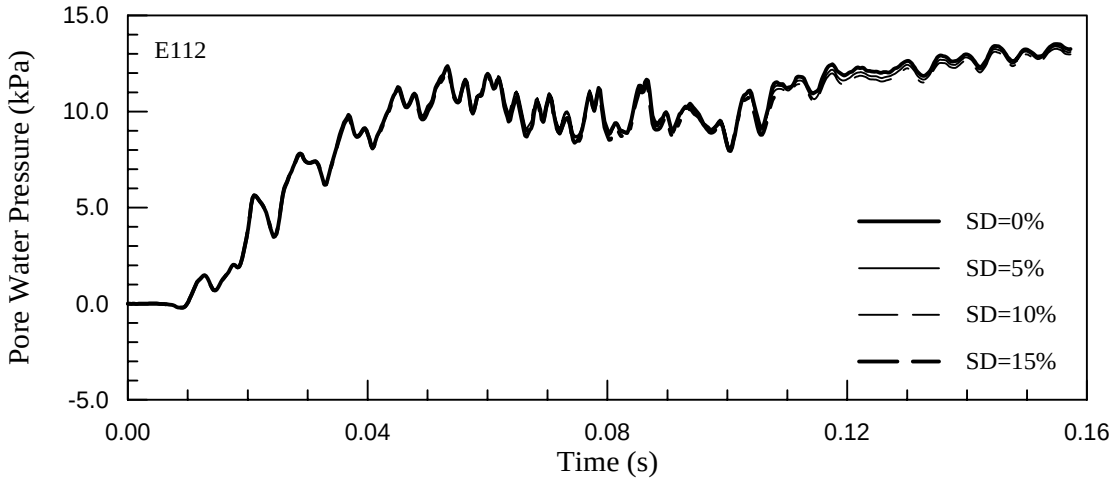

Figure 6.23: Effect of solid stiffness parameter on pore water pressure

6.8.2.3 Effect of fluid stiffness coefficient

Since the saturated porous media consist of a solid and a liquid phase, similar to the solid stiffness, the fluid stiffness was also applied to control the hourglass modes. The fluid stiffness parameter can not be varied form from 0 to 15% because the bulk modulus of liquid (Γ) used in the calculation of anti-hourglass fluid stiffness is very high (2.2 Gpa). Therefore, the appropriate percentages to use for the parametric study were calculated by dividing the corresponding solid stiffness parameters by $\frac{\Gamma}{\lambda + 2\mu}$.

where λ and μ are Lame's elastic constants and Γ is the bulk modulus of liquid phase. The following values were used for these constants:

$\lambda = 1.7 \times 10^4\ kPa$

$\mu = 1.15 \times 10^4\ kPa$

($E = 3.0 \times 10^4\ kPa$ and $\nu = 0.3$)

$\Gamma = 2.2 \times 10^6\ kPa$

The displacements and pore pressures time histories are shown in Figs. 6.24, 6.25 and 6.26. Unlike solid stiffness hourglass control, the fluid stiffness hourglass control parameters affect the response of the embankment. Horizontal displacement at node N188 and N43 are under predicted and at N67 is over predicted by the application of fluid stiffness hourglass control. Similar trend is observed in the vertical displacement time histories at these nodes also. The difference increases with increasing value of fluid stiffness hourglass control parameter. As shown in Fig. 6.26 pore water pressures in element E112, E80 and E8 are over predicted by the use of anti-hourglass fluid stiffness parameter. The differences in pore water pressures increase with increasing value of fluid stiffness parameter. The pore pressure in element E8 is severely altered by the hourglass control method.

From the above discussion, it is obvious that a small percentage (0.1) of fluid stiffness anti-hourglass parameter has greater influence on some vertical displacement and pore pressures and alter the overall solution considerably. Therefore, it is recommended that fluid stiffness coefficient smaller than 0.1 % has to be used to control the hourglass modes.

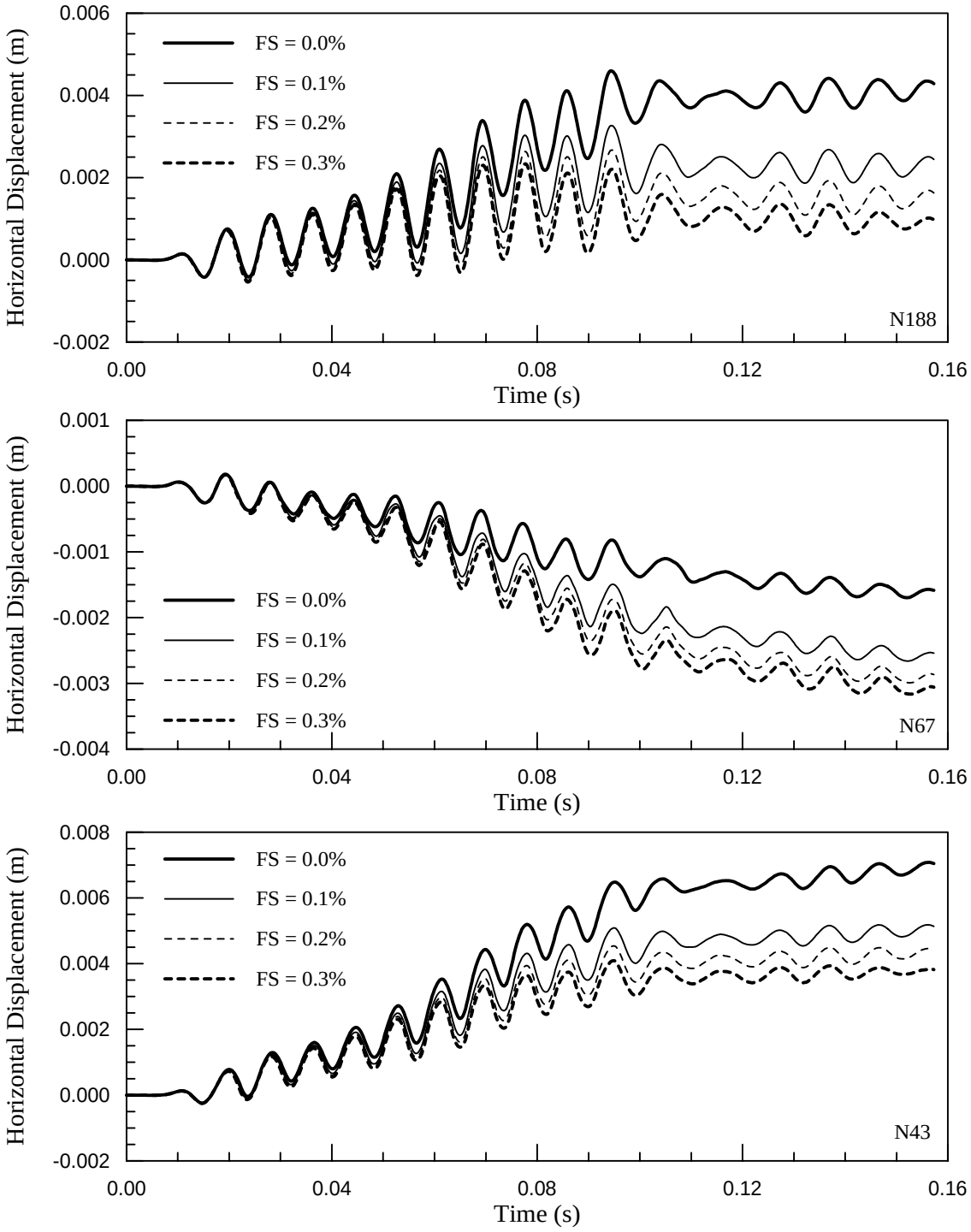

Figure 6.24: Effect of fluid stiffness parameter on horizontal displacement

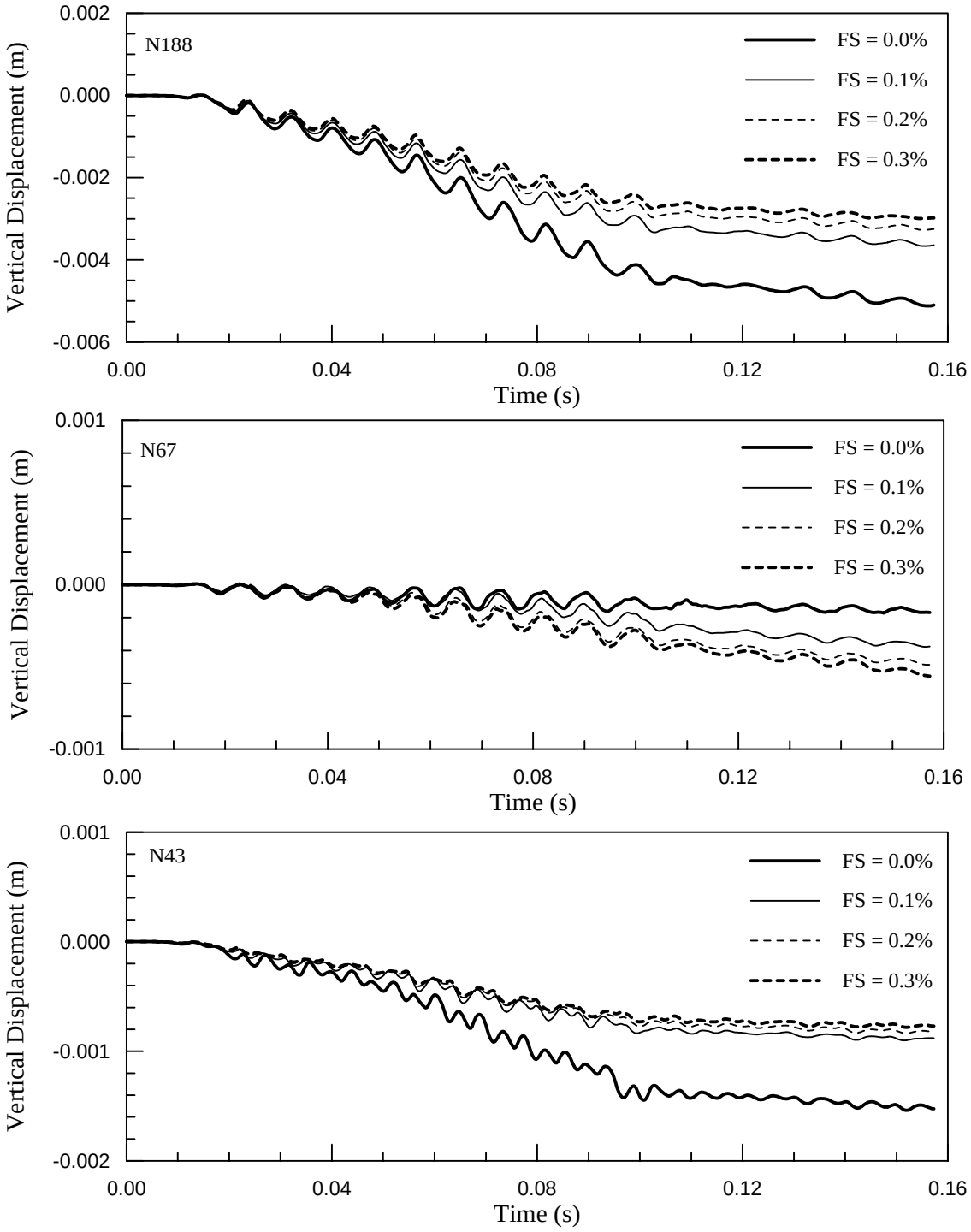

Figure 6.25: Effect of fluid stiffness parameter on vertical displacement

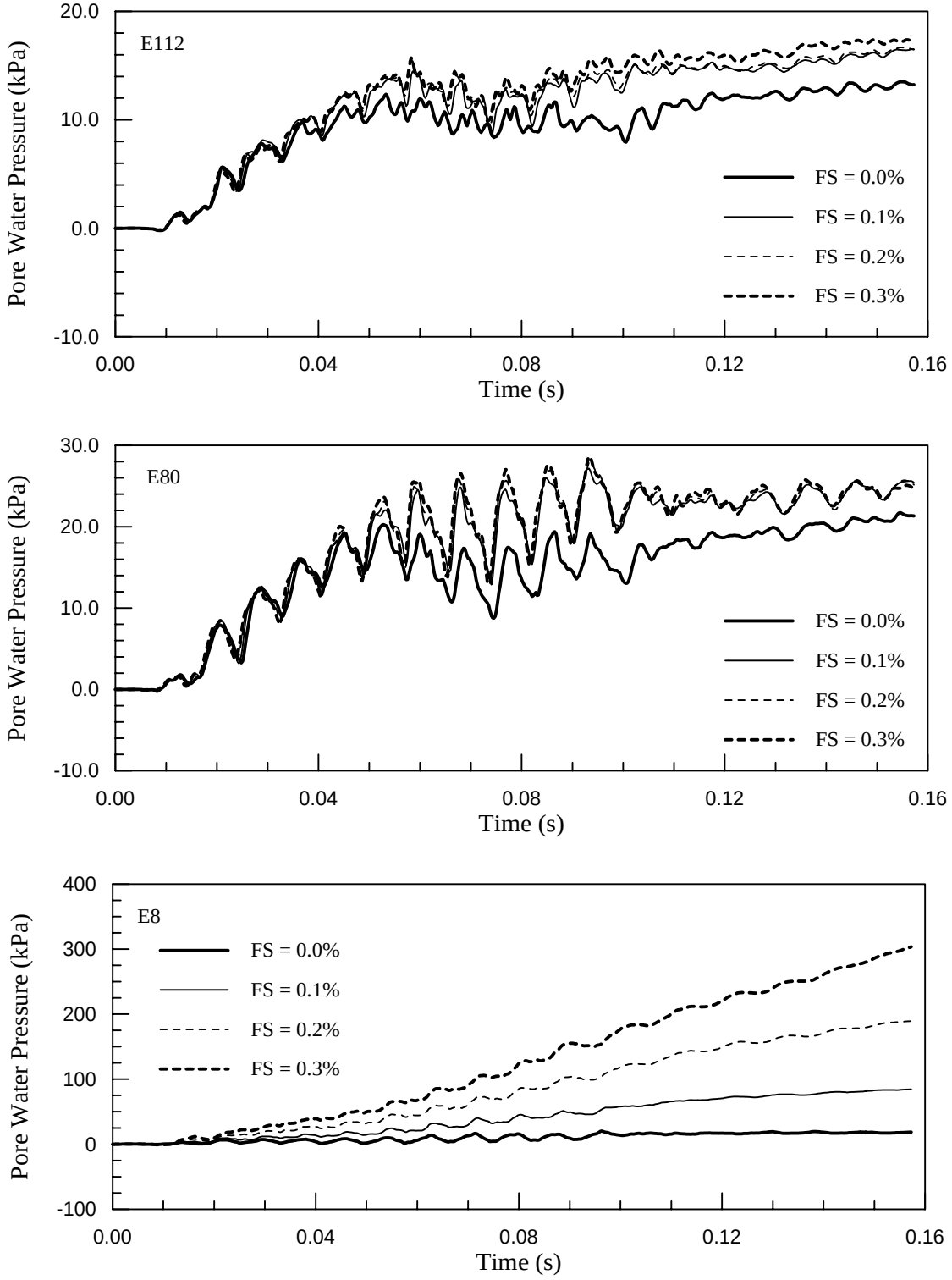

Figure 6.26: Effect of fluid stiffness parameter on pore pressure development

6.9 Performance of the Uniform Element Formulation on the Dynamic Behavior of Saturated Level Ground

The hourglass modes were not observed in the analysis of saturated clay embankment. Therefore, a different problem was picked to investigate the occurrence of hourglass modes. In this case, a level ground with 22.8 m width and 10.00 m height was picked (Fig. 6.27). This model is similar to the Model #1 of the VELACS project (Arulanandan and Scott, 1993), but the soil profile in this analysis consists of Speswhite Kaolin instead of sand. The bottom boundary was fixed in all direction for solid and liquid and the left and right boundaries were fixed in horizontal direction and allowed to move in the vertical direction for both solid and liquid.

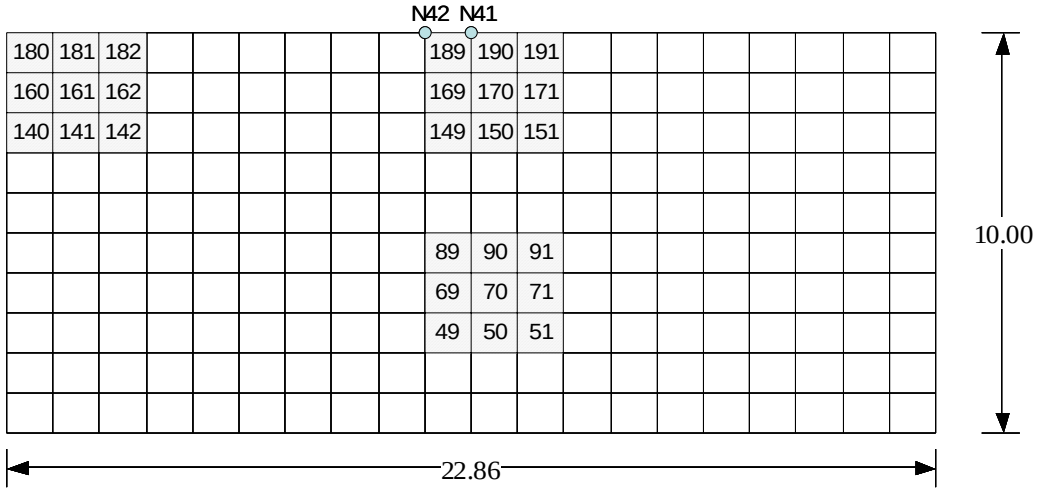

Figure 6.27: Finite element mesh of the level ground (all dimensions are in meters and prototype scale)

The initial stresses were calculated at the center of each layer. A K_0 value of 0.5 was used to calculate the lateral pressures. Bounding surface model parameters used in the previous case (Table 5.1) were used again. The model was shaken with an El Centro earthquake base motion (Fig. 6.28(a)) in the horizontal direction and 10% of the horizontal motion was used in the vertical direction (Fig. 6.28(b)). The predictions by the

UG method with (5% solid stiffness and 5% solid damping) and without hourglass control are compared with the GQ method to investigate the apparent formation of hourglass modes in this particular problem.

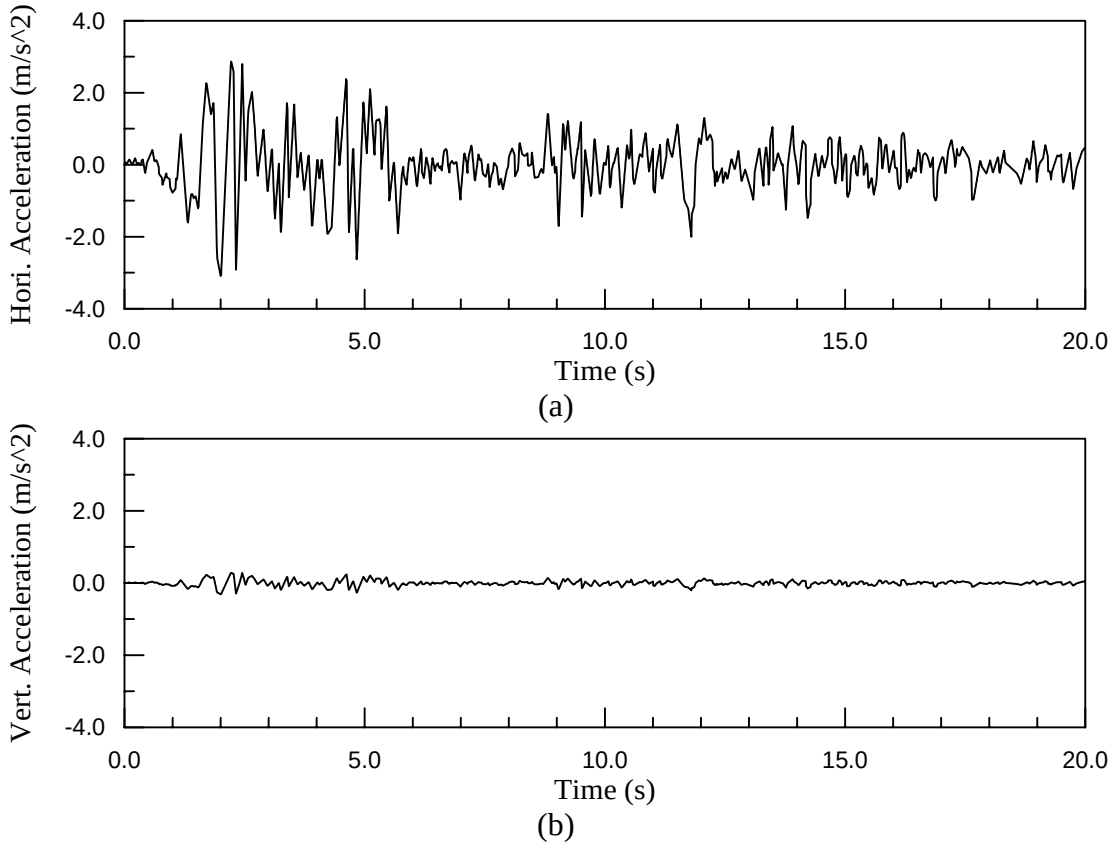

Figure 6.28: Horizontal and vertical base acceleration-time histories

The deformed shape and nodal solid displacement vectors at 2 seconds and 10 seconds for UG methods without hourglass control are shown in Figs. 6.29 and 6.30, respectively. Excitation of hourglass modes is visible neither on deformed shape nor on the displacement vectors. Horizontal and vertical displacements at adjacent nodes N41 and N42 are shown in Figs. 6.31 and 6.32, respectively. FFT of the horizontal and vertical accelerations at nodes N41 and N42 are shown in Figs. 6.33 and 6.34, respectively. Unlike in the embankment, considerable difference between GQ and UG formulations in the displacement-time histories is observed. The difference is small in the

horizontal displacement and large in the vertical displacements. The effect of hourglass control can be readily seen in the displacement-time histories. The displacements predicted with hourglass control fall in between those predicted with GQ formulation and UG formulation without hourglass control.

Similar difference is also seen in the normalized FFT amplitude of the horizontal and vertical accelerations. At nodes N41 and N42, the predominant frequencies of horizontal accelerations appear at 2.1 Hz for all three formulations. The UG formulation without hourglass control has shifted the vertical acceleration predominant frequency at node N41 to 18.41 Hz. When the hourglass control is applied, the predominant frequency is brought back to 2.1 Hz.

Three problems were discussed to study the performance of the hourglass modes: one quasi-static problem and two dynamic problems. The footing problem was used to show the evidence of hourglass modes in the fully coupled analysis of porous media. The level of excitation of hourglass modes seems problem dependent. Severe hourglassing was observed in the footing problem discussed in Section 6.4 and 6.7 that had higher stress gradients. The effectiveness of the hourglass control scheme was also shown through this problem. Hourglassing was not seen in the dynamic analysis of saturated clay embankment that involves only body forces and did not have higher stress gradients. At the same time, the dynamic analysis of level ground showed some effect of the UG element formulation in the displacement time histories. The effect of hourglass control scheme could also be seen in the dynamic analysis of level ground. With the experience gained from this study, it is safe to use the hourglass control scheme to avoid any distortion of solution.

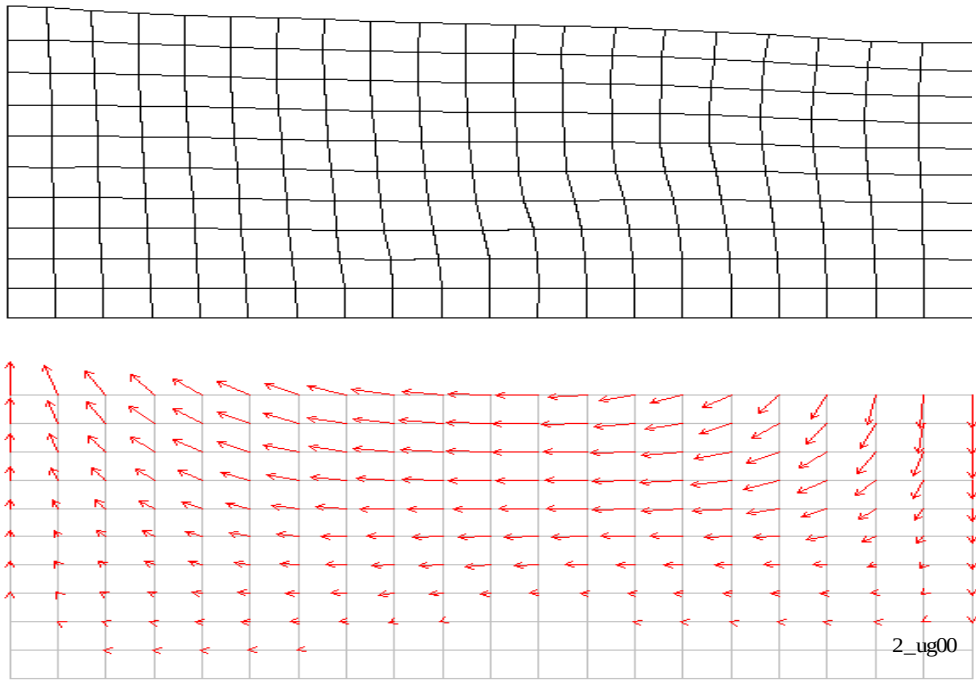

Figure 6.29: Deformed shape and displacement vectors at 2 sec using UG element formulation without hourglass control (displacement magnified by 10)

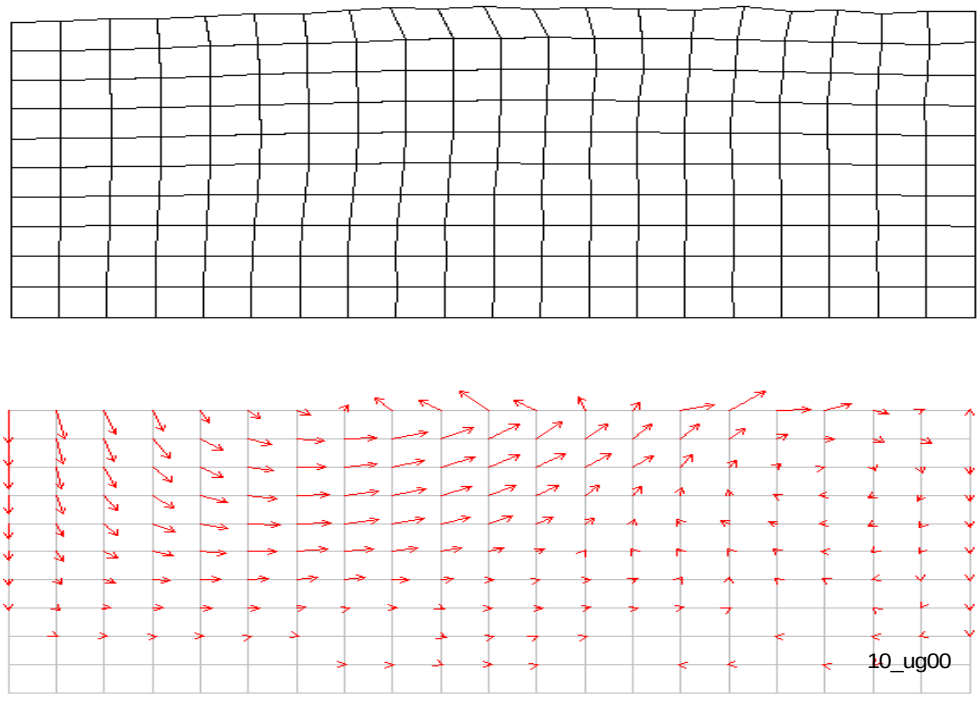

Figure 6.30: Deformed shape and displacement vectors at 10 sec using UG element formulation without hourglass control (displacement magnified by 10)

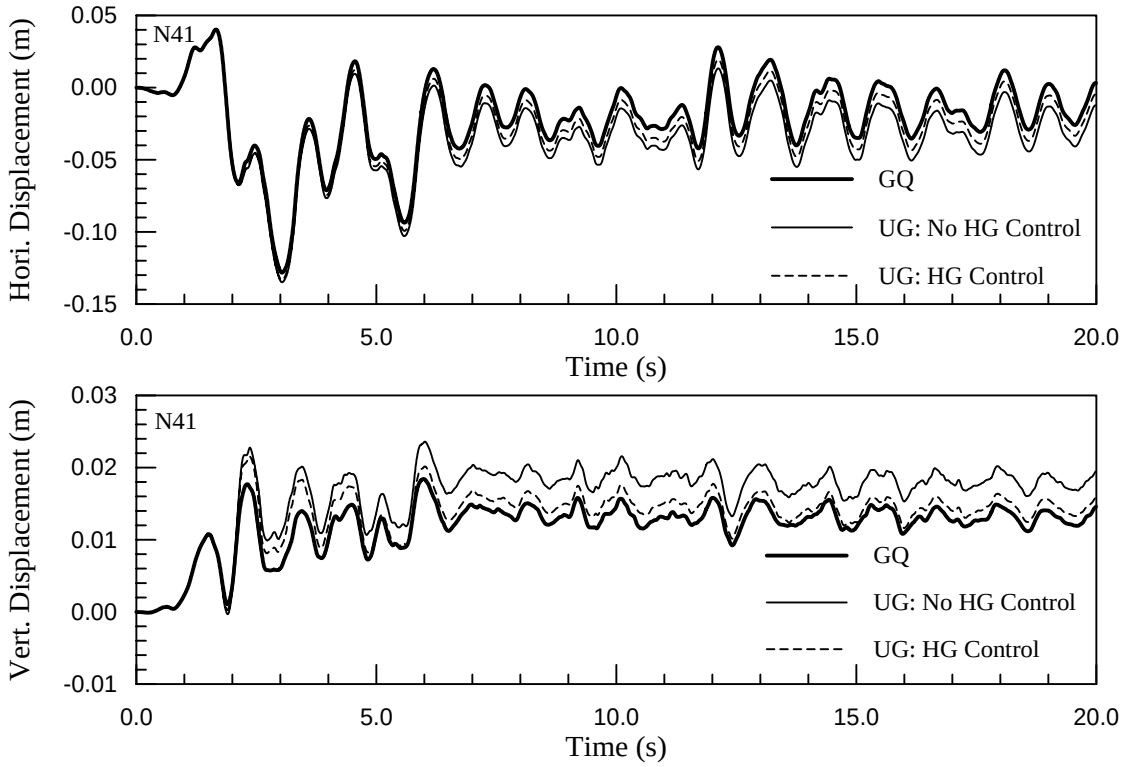

Figure 6.31: Horizontal and vertical displacements at node N41- comparison between GQ and UG formulation

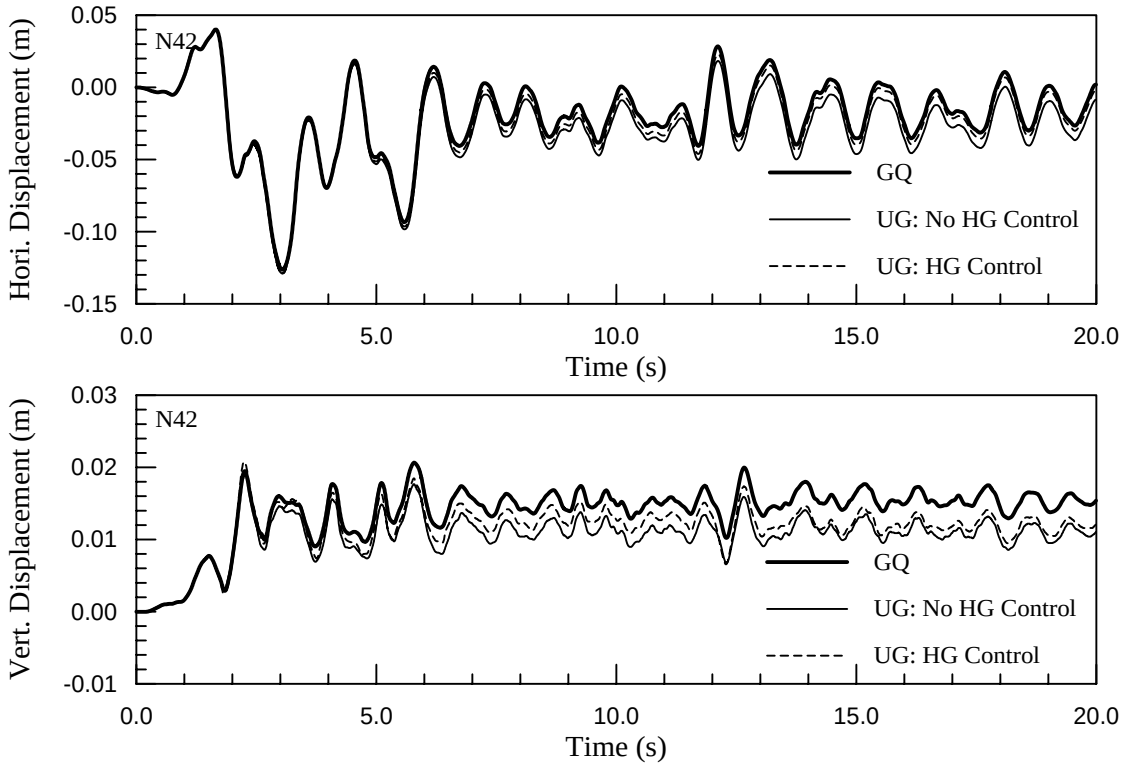

Figure 6.32: Horizontal and vertical displacements at node N42- comparison between GQ and UG formulation

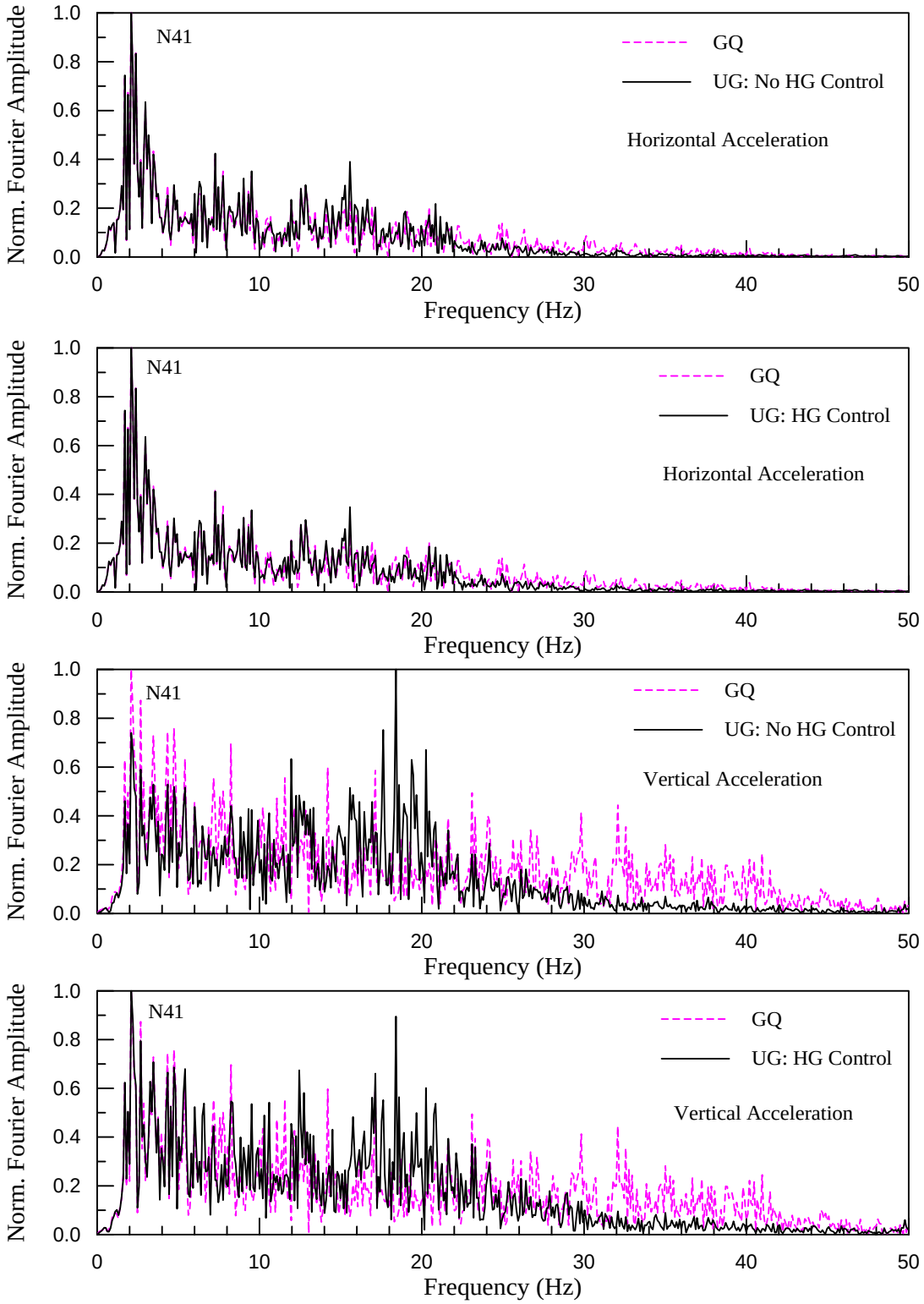

Figure 6.33: FFT of horizontal and vertical accelerations at node N41- comparison between GQ and UG formulation

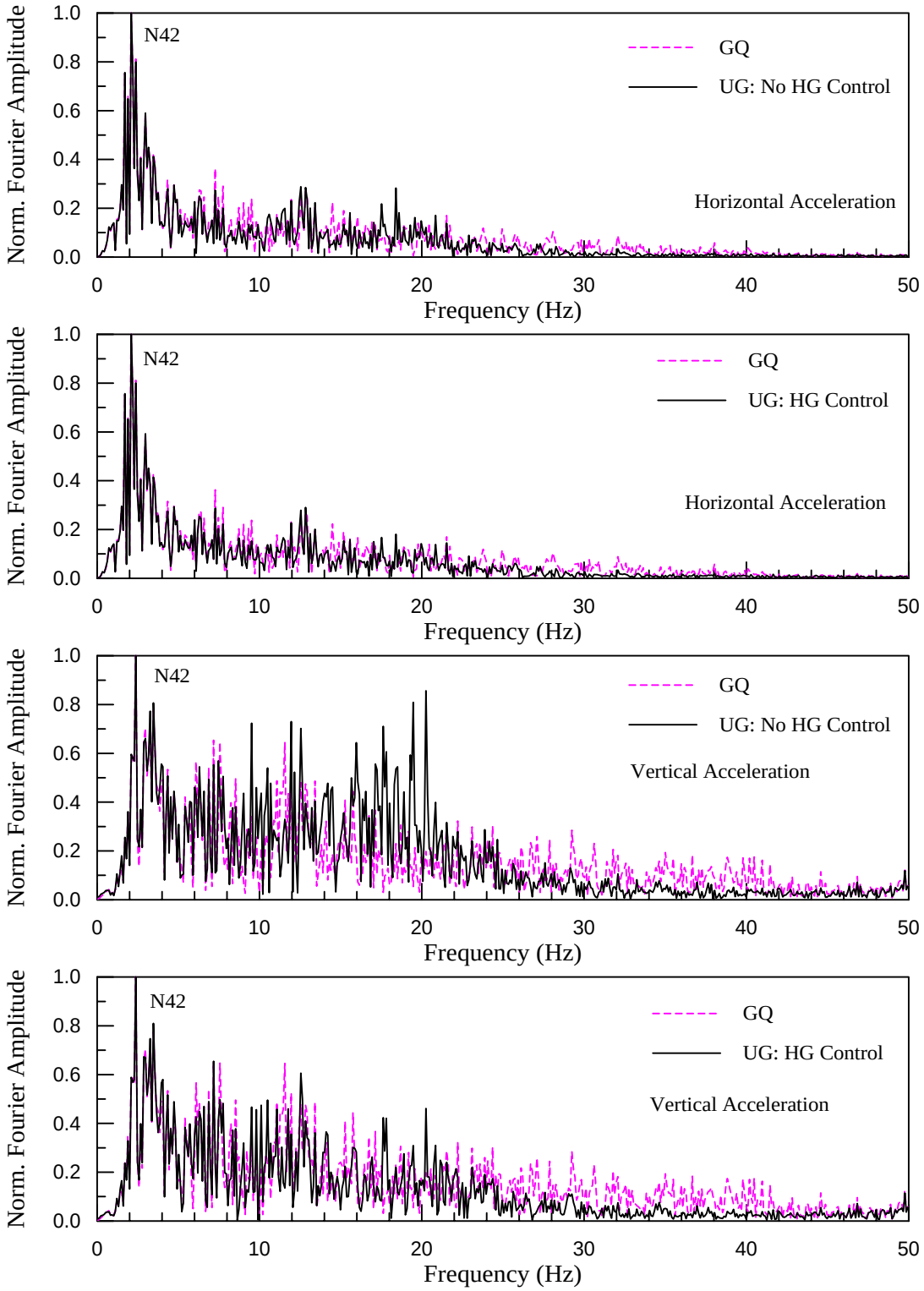

Figure 6.34: FFT of horizontal and vertical accelerations at node N42- comparison between GQ and UG formulation

6.9.1.1 Checker-boarding effect of uniform gradient element

The single point integration procedure has produced checker-boarding effect on the pressure field. The checker-boarding causes pressure fields in two adjacent elements to be mirror image of each other, but with opposite signs (see Section 2.6.5). Therefore, this effect is also investigated in this study for completeness. For this purpose, three locations were selected: E161, E170 and E70 (see Fig. 6.27). The element E170 is located at the surface and away from all the boundaries. Element E161 is also at the surface, but closer to the left boundary. Element E70 is located middle-center of the level ground. The pore pressures around elements E170, E70 and E161 are shown in Figs. 6.35, 6.36 and 6.37, respectively. The pore pressures show gradual increase in all elements. Elements located at higher depths show higher pore water pressures compared to those located at shallow depths. There is no checker-boarding effect observed without hourglass control.

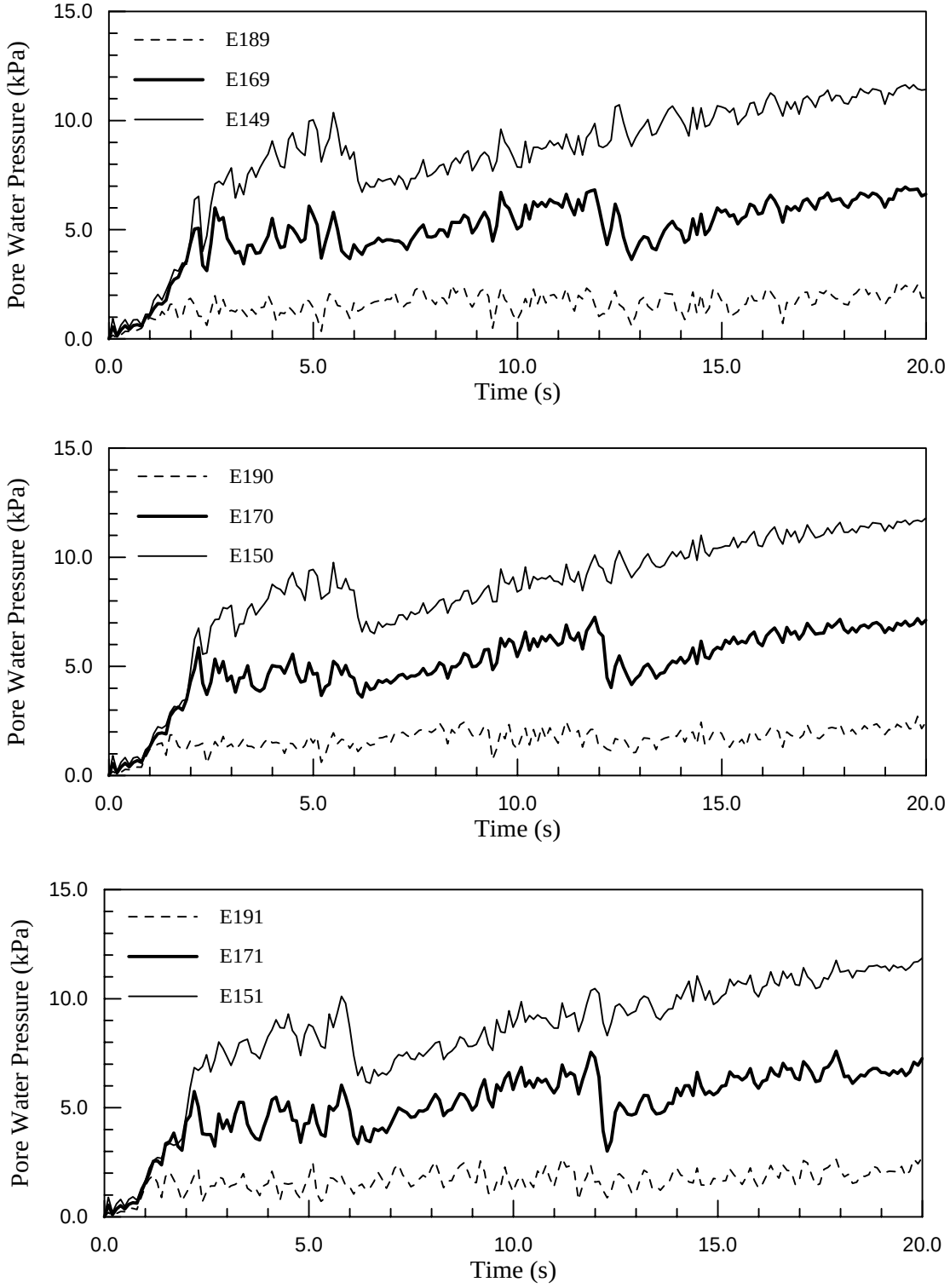

Figure 6.35: Pore pressure-time histories around element E170-UG formulation without hourglass control

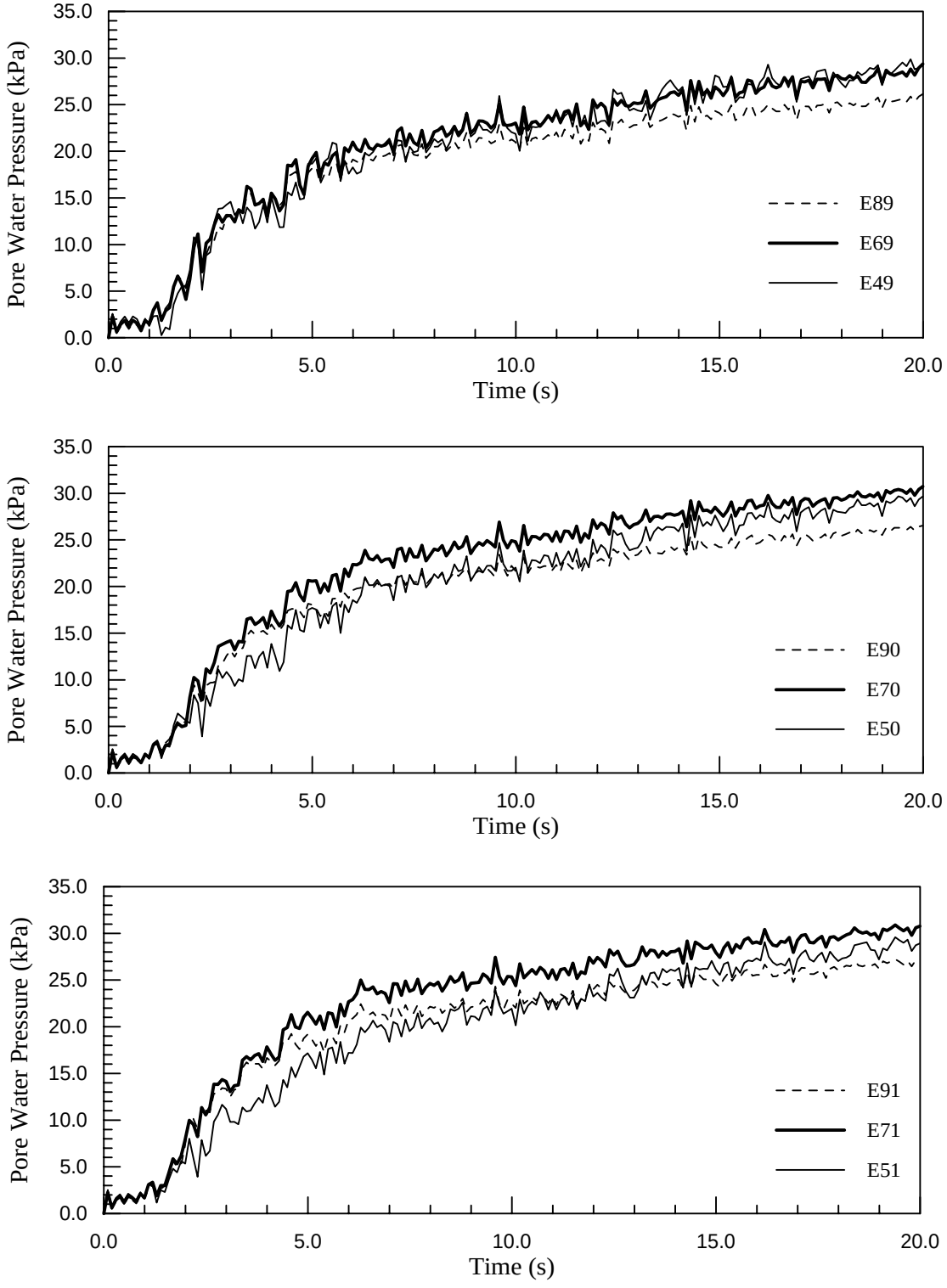

Figure 6.36: Pore pressure-time histories around element E70-UG formulation without hourglass control

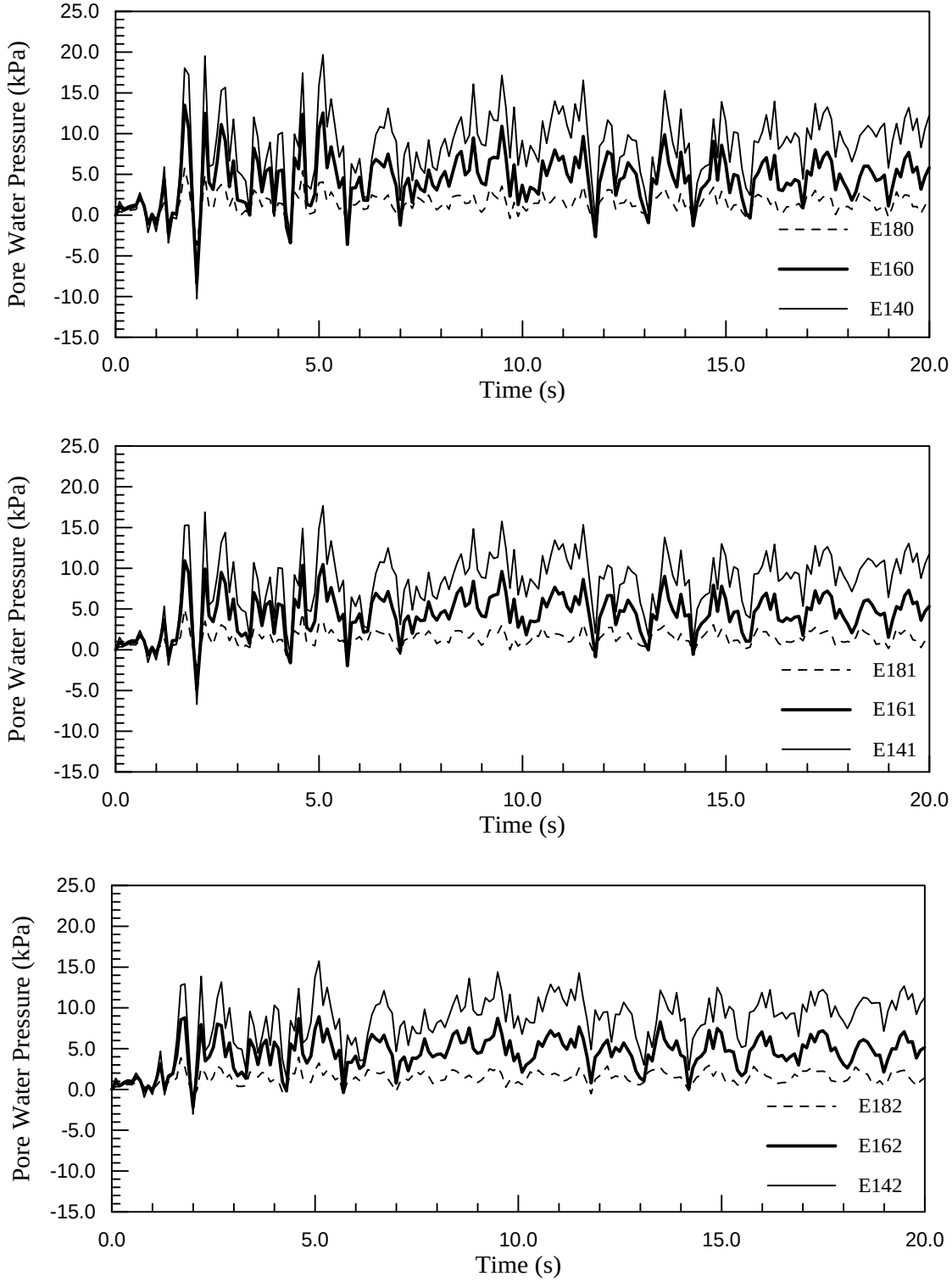

Figure 6.37: Pore pressure-time histories around element 161-UG formulation without hourglass control

7 LARGE DEFORMATION ANALYSIS FOR SATURATED POROUS MEDIA

7.1 Importance of Large Deformation Analysis in Porous Media

Fully coupled nonlinear dynamic analysis of porous media and its computer implementation using the finite element method has been treated in great detail. However, significantly less effort has been spent on introducing the equally important concepts of finite strain/large deformation in soil mechanics, despite the fact that many geotechnical engineering problems involve large deformations. Liquefaction induced flow failure is one of the most dramatic consequences of liquefaction that may cause significant lateral spreading, in the case of mild slopes, and may lead to flow slide and slope instability in embankments containing liquefiable soils. Wetting induced slope failures in unsaturated soils also involves large deformation. Most of the current liquefaction analysis procedures, however, use a small deformation and small strain assumption even for fully coupled nonlinear analyses.

In this chapter, the governing equations for the dynamics of saturated porous media undergoing large deformation are derived. The governing equations are implemented within the TeraScale framework. The importance of large deformation analysis is discussed by simulating a centrifuge model tests.

7.2 Fully Coupled Field Equations for Large Deformation Analysis

7.2.1 Choice of Formulation

For a saturated earthen structure, which occupies an initial volume of ${}^0\Omega$ with the boundary surface ${}^0S$ at time 0, we seek to establish the governing field equations necessary to evaluate its equilibrium positions and entire history of response during a quasi-static or transient process of deformation.

It is assumed that the specified displacements, and surface tractions for solid and liquid phases are defined on different portions of the boundary surface ${}^{t+\Delta t}S$ at a generic time $t+\Delta t$. The governing equations are established without imposing any restrictions on the magnitude of the displacements and strains. Adopting an incremental analysis because of the nonlinear behavior of the soils, an equilibrium position at time $t+\Delta t$ is searched assuming that the solutions for all time steps from 0 to t are known.

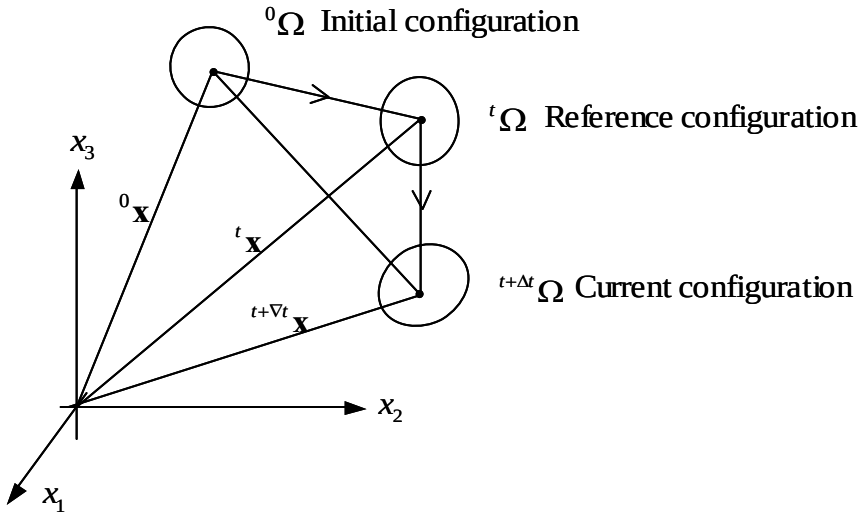

Figure 7.1: Configurations of a body at different times

Lagrangian and Eulerian formulations are commonly used to derive the field equations for large deformation analysis. In solid mechanics, the Lagrangian formulations

and meshes are most popular. Their attractiveness stem from the ease with which they handle complicated boundaries and their ability to follow the material points. Therefore, the history-dependent material, such as soils, can be treated accurately. In the developments of Lagrangian finite elements, two approaches are commonly taken: Total Lagrangian formulation and Updated Lagrangian formulation. In this study, the updated Lagrangian formulation is used to derive the field equations.

7.2.2 Summary of Governing Equations

The dynamic behavior of the saturated soil system is expressed by the following three governing equations.

Linear momentum balance for the mixture:

$$\sigma_{ji,j} + \rho b_i - \rho \ddot{u}_i - \rho^l \ddot{w}_i = 0 \text{ in } {}^{t+\Delta t}\Omega$$

Linear momentum balance for the liquid phase:

$$-p_{,i} + \rho^l b_i = \rho^l \ddot{u}_i + \frac{\rho^l}{n^l} \ddot{w}_i + k_{ij}^{-1} \dot{w}_j \text{ in } {}^{t+\Delta t}\Omega$$

Mass balance for the mixture:

$$\dot{p} = -\Gamma\left(\dot{w}_{i,i} + \dot{u}_{i,i}\right) \text{ in } {}^{t+\Delta t}\Omega$$

The pressure terms can be removed from the above equations by using the mass balance equation. The irreducible form of the governing equations, where solid displacement and fluid displacements are considered as nodal unknowns, will be considered in the subsequent derivation of the governing equations.

7.2.3 Principle of Virtual Work

The principle of virtual work requires that the virtual work performed, when the soil body undergoes a virtual displacement $\delta\mathbf{u}$, is equal to the external work done by the body force and traction, i.e.

$$ {}^{t+\Delta t}W^{\text{int}} = \int_{{}^{t+\Delta t}\Omega} {}^{t+\Delta t}\sigma_{ij}\,\delta\,{}^{t+\Delta t}e_{ij}\,{}^{t+\Delta t}d\Omega \tag{7.1} $$

$$ \begin{aligned} {}^{t+\Delta t}W^{ext} &= \int_{{}^{t+\Delta t}\Omega} {}^{t+\Delta t}\rho\,{}^{t+\Delta t}b_i\,\delta u_i\,{}^{t+\Delta t}d\Omega - \int_{{}^{t+\Delta t}\Omega} {}^{t+\Delta t}\rho\,{}^{t+\Delta t}\ddot{u}_i\,\delta u_i\,{}^{t+\Delta t}d\Omega \\ &- \int_{{}^{t+\Delta t}\Omega} {}^{t+\Delta t}\rho\,{}^{t+\Delta t}\ddot{w}_i\,\delta u_i\,{}^{t+\Delta t}d\Omega + \int_{{}^{t+\Delta t}S^T} {}^{t+\Delta t}f_i^{\,t}\,\delta u_i\,{}^{t+\Delta t}dS \end{aligned} \tag{7.2} $$

where the ${}^{t+\Delta t}\sigma_{ij}$ are the Cartesian components of the Cauchy total stress tensor, and ${}^{t+\Delta t}e_{ij}$ are the Cartesian components of the strain tensor. There are four contribution to the external work of the system: contribution from the body force, contribution from the inertial force of the solid skeleton, contribution from the inertial force of the pore fluid and the contribution from the surface traction. Similar equation can be derived for the motion of the pore fluid. There are two major difficulties in applying the above equations for large deformation problems, which involve rotation and change in configuration, for saturated porous media. First, the configuration at time $t+\Delta t$ is unknown and the integrals over the volume ${}^{t+\Delta t}\Omega$ and surface ${}^{t+\Delta t}S$ can not be evaluated before calculating the equilibrium position at time $t+\Delta t$. Therefore, the virtual work equations have to be transformed to the reference configuration at time $t+\Delta t$. The second difficulty is the presence of total stress in the internal work equation. The total stress does not have any direct influence on the mechanical behavior of the soil. Therefore, the principle of

effective stress, which is expressed in terms of Cauchy stress, has to be applied with proper consideration for the large deformation.

7.2.4 Principle of Effective Stress for Saturated Soils

The single stress state variable, which governs the mechanical behavior of the saturated soil, is the effective stress. Terzaghi's principle of effective stress can be written as:

$$\boldsymbol{\sigma} = \boldsymbol{\sigma}' - p\mathbf{I} \tag{7.3}$$

where $\boldsymbol{\sigma}$ is the total stress tensor, $\boldsymbol{\sigma}'$ is the effective stress tensor, and p is the pore water pressure. The conventional solid mechanics sign convention is used in the above equation, i.e. tensile stresses are considered positive. Since the effective stress principle is defined in terms of Cauchy stress tensor, which is not an objective measure of stress, it is important to establish a suitable rate form for the effective stress equation. Taking the time derivative of Eq. 7.3

$$\frac{D}{Dt}\boldsymbol{\sigma} = \frac{D}{Dt}\boldsymbol{\sigma}' - \frac{D}{Dt}p\mathbf{I} \tag{7.4}$$

The Terzaghi's effective stress equations can be rewritten in the co-rotational form as follows

$$\boldsymbol{\sigma}^{\nabla} = \boldsymbol{\sigma}'^{\nabla} - \dot{p}\mathbf{I} \tag{7.5}$$

where $\boldsymbol{\sigma}^{\nabla}$ is the objective total stress tensor, $\boldsymbol{\sigma}'^{\nabla}$ is the objective effective stress tensor and $\dot{p}$ is the pore water pressure. The objective form of the effective stress principle can be incorporated into the virtual work equation with an objective measure of stress.

7.2.5 Constitutive Equation for the Solid Skeleton

When dealing with large deformation effects, involving large rotations, care must be taken in the material frame invariance of the constitutive law. Before discussing frame indifference of stress measures, lets discuss the strain measures. During the elastoplastic deformation of the body from a reference configuration to the current configuration, the material undergoes elastic, reversible, deformation and plastic, irreversible, deformation. Define three configurations: a reference configuration ${}^{t}\Omega$, a virtual intermediate configuration ${}^{i}\Omega$ and a current configuration ${}^{t+\Delta t}\Omega$.

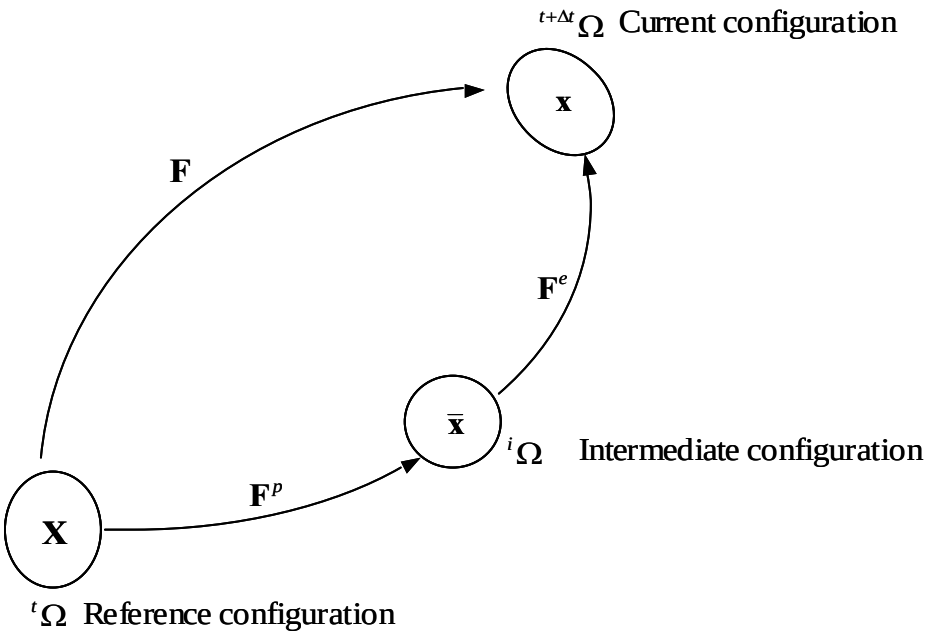

Figure 7.2: Elastic-plastic deformation

The motion of the body from ${}^{t}\Omega$ to ${}^{t+\Delta t}\Omega$ is considered in two steps: motion of the body from ${}^{t}\Omega$ to ${}^{i}\Omega$ and then from ${}^{i}\Omega$ to ${}^{t+\Delta t}\Omega$. The motion form ${}^{t}\Omega$ to ${}^{i}\Omega$ is purely plastic and irreversible. Therefore, the configuration Ω^{i} can be considered as an unstressed configuration. The motion from ${}^{i}\Omega$ to ${}^{t+\Delta t}\Omega$ is purely elastic and reversible.

The deformation gradient for the motion from ${}^{t}\Omega$ to Ω^{i} is denoted by $\mathbf{F}^{p}$ and the deformation gradient from ${}^{i}\Omega$ to ${}^{t+\Delta t}\Omega$ is denoted by $\mathbf{F}^{e}$. When the motion from ${}^{t}\Omega$ to ${}^{t+\Delta t}\Omega$ is continuous, the deformation gradient has the following non-cumulative representation in its plastic and elastic part (Bannmann and Johnson, 1987; Lee, 1981).

$$\mathbf{F} = \frac{\partial \mathbf{x}}{\partial \bar{\mathbf{x}}} \frac{\partial \bar{\mathbf{x}}}{\partial \mathbf{X}} = \mathbf{F}^{e}\mathbf{F}^{p} \tag{7.6}$$

where $\mathbf{x}$ is the spatial coordinates, $\mathbf{X}$ is the material coordinates and $\bar{\mathbf{x}}$ is the intermediate coordinates. Since the deformation measures are not linearly expressed in terms of displacements, generally the elastic and plastic components are not summable. In fact, choosing a representation of the elastic part of deformation independent from rigid body motion, the deformation rate tensor is given by the symmetric part of the velocity gradient (Lee, 1981; Lubarda and Lee, 1981)

$$\mathbf{L} = \dot{\mathbf{F}}^{\mathbf{e}} \cdot \left(\mathbf{F}^{\mathbf{e}}\right)^{-1} + \mathbf{F}^{\mathbf{e}}\dot{\mathbf{F}}^{\mathbf{p}}\left(\mathbf{F}^{\mathbf{p}}\right)^{-1}\left(\mathbf{F}^{\mathbf{e}}\right)^{-1}$$

$$\mathbf{D} = \mathbf{D}^{e} + \left(\mathbf{F}^{e}\mathbf{D}^{p}\mathbf{F}^{e^{-1}}\right)_{s} + \left(\mathbf{F}^{e}\mathbf{W}^{p}\mathbf{F}^{e^{-1}}\right)_{s} \tag{7.7}$$

where $\mathbf{L} = \mathbf{D} + \mathbf{W}$

If the elastic components of the total strain are assumed to be small, which is true for most soils, $\mathbf{F}^{e} \approx 1$ and the last term in Eq. 7.7 is also small. Then the rate of deformation reduces to

$$\mathbf{D} = \mathbf{D}^{e} + \mathbf{D}^{p}$$

$$d\boldsymbol{\varepsilon} = d\boldsymbol{\varepsilon}^{e} + d\boldsymbol{\varepsilon}^{p}$$

where $\mathbf{D}^{e}$ and $\mathbf{D}^{p}$ are the elastic and plastic parts of the total strain rate. This formulation is also called the additive decomposition of the rate of deformation in large

deformation finite element plasticity. It should also be noted here that the additive decomposition is the simplification of the exact kinematics.

Now, lets discuss the frame indifference of the stress measures. The corotational form of the stress-strain relationship for the elastoplatic material is expressed in the following form:

$$\dot{\boldsymbol{\sigma}}'^{\nabla} = \mathbf{C}^{ep} : \mathbf{D}$$

where $\mathbf{C}^{ep}$ is the tangential elastoplastic stiffness tensor which may be a function of the current state of effective stress, strains and some internal variables.

There are different forms of objective stress rates developed and used in the large deformation analysis. The Jaumann stress rate, which is most commonly used in solid mechanics, shows oscillation at very large strain values (Szabo and Balla, 1988). Therefore, the Green-Naghdi stress rate is used in this study. The Green-Naghdi rate differs from the Jaumann rate only in using a different measure of rotation of the material: the Green-Naghdi rate employs the angular velocity $\boldsymbol{\Omega}$. It has been observed that the use of different rotation measure changes the behavior of the material model markedly. The Green-Naghdi stress rate is expressed as follows:

$$\boldsymbol{\sigma}^{\nabla} = \frac{D}{Dt}\boldsymbol{\sigma} - \boldsymbol{\Omega}\cdot\boldsymbol{\sigma} - \boldsymbol{\sigma}\cdot\boldsymbol{\Omega}^{T} \tag{7.8}$$

The angular velocity is given by

$$\boldsymbol{\Omega} = \dot{\mathbf{R}}\cdot\mathbf{R}^{T}$$

The rotation tensor $\mathbf{R}$ can be calculated by the polar decomposition theorem. The Polar decomposition theorem states that any deformation gradient tensor $\mathbf{F}$ can be multiplicatively decomposed into product of an orthogonal matrix $\mathbf{R}$ and a symmetric tensor $\mathbf{U}$, called the right stretch tensor.

$$F_{ij} = \frac{\partial x_i}{\partial X_j} = R_{ik} U_{kj}$$

Rearranging the objective rates, and applying the effective stress principle for total objective rate, the effective stress is expressed as

$$\frac{D\sigma_{ij}}{Dt} = \overset{\nabla}{\sigma}_{ij} - \delta_{ij}\dot{p} + \Omega_{ik}\sigma_{kj} + \sigma_{ik}\Omega_{kj}^{T}$$

$$\frac{D\sigma_{ij}}{Dt} = C_{ijkl}^{ep} D_{kl} - \delta_{ij}\dot{p} + \Omega_{ik}\sigma_{kj} + \sigma_{ik}\Omega_{kj}^{T} \tag{7.9}$$

7.2.6 Boundary Conditions

Solid and liquid displacement, solid traction and pore pressure boundary conditions are assumed to exist in this derivation. These boundary conditions are specified on different portion of the boundary surface ${}^{t+\Delta t}S$ of the saturated soil body at a generic time $t + \Delta t$ and defined as follows:

- Solid displacement boundary condition

${}^{t+\Delta t}u_i = {}^{t+\Delta t}\overline{u}_i$ on ${}^{t+\Delta t}S_u$

where ${}^{t+\nabla t}\overline{u}_i$ is the specified value of displacement on the boundary surface ${}^{t+\Delta t}S_u$ at time $t + \Delta t$.

- Liquid displacement boundary condition

${}^{t+\Delta t}U_i = {}^{t+\Delta t}\overline{U}_i$ on ${}^{t+\Delta t}S_U$

where ${}^{t+\nabla t}\overline{U}_i$ is the specified value of liquid displacement on the boundary surface ${}^{t+\Delta t}S_U$ at time $t + \Delta t$.

- Traction boundary condition

$${}^{t+\Delta t}\sigma_{ij} n_j = {}^{t+\Delta t} f_i^{\,t} \text{ on } {}^{t+\Delta t} S_T$$

where ${}^{t+\nabla t} f_i^{\,t}$ is the specified value of traction on the boundary surface ${}^{t+\Delta t} S_T$ at time $t + \Delta t$. n_j is the unit normal and ${}^{t+\Delta t}\sigma_{ij}$ is the total Cauchy stress tensor acting on the neighborhood of ${}^{t+\Delta t} S_T$.

- Pore Pressure Boundary Condition

$${}^{t+\nabla t} p = {}^{t+\nabla t}\overline{p} \text{ on } {}^{t+\nabla t} S_p$$

where ${}^{t+\nabla t}\overline{p}$ is the specified value of the pore water pressure at time $t + \Delta t$.

7.3 Virtual Work Equations in Reference Configuration

The stress measure in the linear momentum balance equation in the current configuration is the Cauchy stress tensor and the strain measure is the rate of deformation. These stress and strain measures have to be pulled back to the reference configuration through appropriate methods. It is well known that the second Piola-Kirchhoff stress tensor and Green–Lagrange strain tensors are work conjugate pairs of stress and strain measures which relates the ${}^{t+\Delta t}\boldsymbol{\sigma}$ and ${}^{t+\Delta t}\mathbf{E}$ to the configuration at time t. The pull back transformations for the stress and strain measures are given by the following equations.

$$S_{ij} = J F_{ik}^{-1} \sigma_{kl} F_{lj}^{-T}$$

$$E_{ij} = F_{ik}^{T} e_{kl} F_{lj}$$

The following transformation can be obtained though the axiom of mass balance equation:

$${}^{0}\rho \, {}^{0}d\Omega = {}^{t}\rho \, {}^{t}d\Omega = {}^{t+\Delta t}\rho \, {}^{t+\Delta t}d\Omega$$

In general the, the external loading, such as the surface traction, external water pressure, gravitational and centrifugal loading is deformation dependent, i.e., the magnitude and direction of a load changes when the shape of the body changes. However, in most geotechnical structures, the change in aforementioned loadings due to change in configuration can be neglected. Therefore, it is reasonable to assume that the magnitude and directions of surface and body forces are independent of the configuration of the soil body, i.e.

$${}^{t+\Delta t}b_i = {}^{t+\Delta t}_{t}b_i$$

$${}^{t+\Delta t}f_i^{\,t}\;{}^{t+\Delta t}dS = {}^{t+\Delta t}_{t}f_i^{\,t}\;{}^{t}dS$$

In other words, the load stiffness contribution to the total stiffness is neglected. Then, the internal virtual work equation can be rewritten as follows on the reference configuration:

$${}^{t+\Delta t}W^{\text{int}} = \int_{{}^{t}\Omega} {}^{t+\Delta t}S_{ij}\,\delta\,{}^{t+\Delta t}\varepsilon_{ij}\;{}^{t}d\Omega$$

Substituting the total stress tensor in terms of effective stress and pore water pressure the following equation can be derived for internal work.

$${}^{t+\Delta t}W^{\text{int}} = \int_{{}^{t}\Omega} {}^{t+\Delta t}_{t}S_{ij}\,\delta\,{}^{t+\Delta t}_{t}\varepsilon_{ij}\;{}^{t}d\Omega - \int_{{}^{t}\Omega} {}^{t+\Delta t}_{t}h_{ij}\,\delta\,{}^{t+\Delta t}_{t}\varepsilon_{ij}\;{}^{t}d\Omega \tag{7.10}$$

where ${}^{t+\Delta t}_{t}h_{ij} = JF_{ik}^{-1}\left(p\delta_{kl}\right)F_{lj}^{-T}$

The external work equation can be written as

$$\begin{aligned}{}^{t+\Delta t}W^{ext} &= \int_{{}^{t}\Omega} {}^{t}\rho\;{}^{t+\Delta t}_{t}b_i\,\delta u_i\;{}^{t}d\Omega - \int_{{}^{0}\Omega} {}^{0}\rho\;{}^{t+\Delta t}\ddot{u}_i\delta u_i\;{}^{0}d\Omega - \int_{{}^{0}\Omega} {}^{0}\rho\;{}^{t+\Delta t}\ddot{w}_i\delta u_i\;{}^{0}d\Omega \\ &+ \int_{{}^{t}S^T} {}^{t+\Delta t}f_i^{\,t}\delta u_i\;{}^{t}dS\end{aligned} \tag{7.11}$$

7.4 Incremental Equations and Newton's Method

The equilibrium state of the soil body is known at some time t and the state $\mathbf{\Pi}$ can be defined by the known stresses, tractions, deformations and history of the soil body. Let the right hand side and the left hand side of the virtual work equation in the reference configuration be $I(\mathbf{\Pi})$ and $E(\mathbf{\Pi})$, respectively. At time $t+\Delta t$ a new equilibrium state must be established for the body. Let $\Delta\mathbf{\Pi}$ be the change in the state which is the solution of

$$\left[I(\mathbf{\Pi}+\Delta\mathbf{\Pi})-E(\mathbf{\Pi}+\Delta\mathbf{\Pi})\right]\cdot\delta\mathbf{v}=0$$

Denoting, $\overline{\mathbf{\Pi}}$ as a guess for the new equilibrium state, the above equation can be expanded about the new guessed state

$$\left[I(\mathbf{\Pi}+\Delta\mathbf{\Pi})-E(\mathbf{\Pi}+\Delta\mathbf{\Pi})\right]\cdot\delta\mathbf{v}=\left[I(\overline{\mathbf{\Pi}})-E(\overline{\mathbf{\Pi}})\right]\cdot\delta\mathbf{v}+\left[\frac{\partial I(\overline{\mathbf{\Pi}})}{\partial\overline{\mathbf{\Pi}}}\partial\overline{\mathbf{\Pi}}-\frac{\partial E(\overline{\mathbf{\Pi}})}{\partial\overline{\mathbf{\Pi}}}\partial\overline{\mathbf{\Pi}}\right]\cdot\delta\mathbf{v}+\cdots$$

where the $\partial\overline{\mathbf{\Pi}}$ is the increment between the correct equilibrium state $\mathbf{\Pi}+\Delta\mathbf{\Pi}$ and the guessed equilibrium state $\overline{\mathbf{\Pi}}$. Taking first order approximation, the above equation reduces to

$$\left[\frac{\partial I(\overline{\mathbf{\Pi}})}{\partial\overline{\mathbf{\Pi}}}\partial\overline{\mathbf{\Pi}}-\frac{\partial E(\overline{\mathbf{\Pi}})}{\partial\overline{\mathbf{\Pi}}}\partial\overline{\mathbf{\Pi}}\right]\cdot\delta\mathbf{v}=-\left[I(\overline{\mathbf{\Pi}})-E(\overline{\mathbf{\Pi}})\right]\cdot\delta\mathbf{v}$$

Successive solution of the above equation for various trial states $\overline{\mathbf{\Pi}}$ can be found until the right hand side of the equation becomes zero, i.e. $\overline{\mathbf{\Pi}}$ equal $\mathbf{\Pi}+\Delta\mathbf{\Pi}$ and equilibrium is satisfied.

These stress measures can be substituted in Eq. 7.9 and replacing the rate form with increments we get the following equations.

$$\dot{S}_{ij}=JF_{ik}^{-1}\left(C_{klmn}^{ep}D_{mn}+\Omega_{km}\sigma_{ml}+\sigma_{km}\Omega_{ml}^{T}\right)F_{lj}^{-T}$$

$$\partial S_{ij} = JF_{ik}^{-1}\left(C_{klmn}^{ep}\partial D_{mn} + \partial\Omega_{km}\sigma_{ml} + \sigma_{km}\partial\Omega_{ml}^{T}\right)F_{lj}^{-T} \tag{7.12}$$

Eq. 7.12 can be substituted into Eq. 7.10 and the incremental internal virtual work equation can be expressed as follows:

$$\begin{aligned}\partial^{t+\Delta t}W^{\text{int}} &= \int_{{}^{t}\Omega}\left(JF_{ik}^{-1}\left(C_{klmn}^{ep}\partial D_{mn} + \partial\Omega_{km}\sigma_{ml} + \sigma_{km}\partial\Omega_{ml}^{T}\right)F_{lj}^{-T}\right)\delta^{t+\Delta t}\varepsilon_{ij}\,{}^{t}d\Omega \\ &- \int_{{}^{t}\Omega}{}_{t}^{t+\Delta t}h_{ij}\delta^{t+\Delta t}{}_{t}\varepsilon_{ij}\,{}^{t}d\Omega\end{aligned} \tag{7.13}$$

Eq. 7.13 together with other components can be simplified by instantaneously choosing the current configuration to coincide with the reference configuration. Then, the deformation gradient simply becomes the identity tensor and all the stress measures remain the same. This choice of reference configuration is called the Updated Lagrangian method. This method is very easy to use in the computer programming because it requires only the coordinates of the body to be updated after each iteration so that the current configuration is also the reference configuration.

7.5 Initial Stress Stiffness

The gradients in the above equation can be symbolically represented with respect to the independent variables as follows.

$$\frac{\partial I\left(\overline{\mathbf{\Pi}}\right)}{\partial\overline{\mathbf{\Pi}}}\partial\overline{\mathbf{\Pi}} = \frac{\partial I}{\partial\boldsymbol{\sigma}}\frac{\partial\boldsymbol{\sigma}}{\partial\boldsymbol{\varepsilon}}\partial\boldsymbol{\varepsilon} + \frac{\partial I}{\partial\boldsymbol{\sigma}}\frac{\partial\boldsymbol{\sigma}}{\partial\mathbf{v}}\partial\mathbf{v}$$

$$\frac{\partial E\left(\overline{\mathbf{\Pi}}\right)}{\partial\mathbf{\Pi}}\partial\mathbf{\Pi} = \frac{\partial E}{\partial\boldsymbol{\sigma}}\partial\boldsymbol{\sigma} + \frac{\partial E}{\partial\mathbf{v}}\partial\mathbf{v}$$

These gradients give rise to different stiffness matrices such as initial stress stiffness matrix, small strain stiffness matrix and initial load stiffness matrix, which is neglected in Section 7.3. In addition to the usual small strain stiffness, the initial stress stiffness has to

be added to obtain the final stiffness matrix. This initial effective stress stiffness is given by the following equations in terms of Viot's stress notations for plane strain case:

$$\mathbf{K}_{\sigma} = \begin{bmatrix} \begin{pmatrix} -\sigma_{11}\dfrac{\partial N}{\partial x}\dfrac{\partial N^T}{\partial x} \\ -\dfrac{1}{2}(\sigma_{11}-\sigma_{22})\dfrac{\partial N}{\partial y}\dfrac{\partial N^T}{\partial y} \end{pmatrix} & \begin{pmatrix} -\dfrac{1}{2}(\sigma_{11}-\sigma_{22})\dfrac{\partial N}{\partial y}\dfrac{\partial N^T}{\partial x} \\ -\sigma_{21}\left(\dfrac{\partial N}{\partial x}\dfrac{\partial N^T}{\partial x}+\dfrac{\partial N}{\partial y}\dfrac{\partial N^T}{\partial y}\right) \end{pmatrix} \\ \begin{pmatrix} -\dfrac{1}{2}(\sigma_{11}-\sigma_{22})\dfrac{\partial N}{\partial x}\dfrac{\partial N^T}{\partial y} \\ -(\sigma_{12})\left(\dfrac{\partial N}{\partial x}\dfrac{\partial N^T}{\partial x}+\dfrac{\partial N}{\partial y}\dfrac{\partial N^T}{\partial y}\right) \end{pmatrix} & \begin{pmatrix} -\sigma_{22}\dfrac{\partial N}{\partial y}\dfrac{\partial N^T}{\partial y} \\ -\dfrac{1}{2}(\sigma_{22}-\sigma_{11})\dfrac{\partial N}{\partial x}\dfrac{\partial N^T}{\partial x} \end{pmatrix} \end{bmatrix}$$

where N is the shape function.

7.6 Numerical Simulation

The field equations for the saturated porous media undergoing large deformation have been implemented using the TeraScale framework. It was initially planned to validate the large deformation finite element code developed in this study by simulating the centrifuge experiment on sand embankment undergoing large deformations. However, due to some unexpected problems encountered in the constitutive model for sand, as a first step, the centrifuge experiment on the clay embankment (Chapter 5) was used to verify the large deformation capabilities. The finite element mesh for the centrifuge model is shown in Fig.7.3. The uniform gradient element formulation together with 5% solid stiffness and 5% solid damping was used for both small and large deformation analyses.

7.7 Comparison of Small and Large Deformation Analyses for a Small Earthquake

In this case, the centrifuge model test described in Chapter 5 was simulated using both small and large deformation analysis computer codes. The base motion applied to the model is shown in Fig. 7.4. The displacement-time histories at nodes N188 and N251 are shown in Figs.7.5 and 7.6. The predicted responses by both analysis methods are similar to each other. This is because the embankment did not under go large deformation. The surface settlement is only about 5% of the embankment. When the deformations are small, both analysis methods predicted similar responses. The pore water pressure-time history in element E80 is shown in Fig. 7.7. Pore pressures predicted by both the analyses show a slight difference. This difference in pore pressure can be attributed to incompressible nature of the pore fluid, i.e., the very large value of the bulk modulus of the liquid used in the calculation of the pore pressure amplified the small difference in the predicted displacements. These analyses show that the predictions made by both analyses are similar when the material undergoes small deformation, i.e., the small deformation theory is a subset of the large deformation theory. *There is no error associated with using a large deformation theory to solve a small deformation problem.*

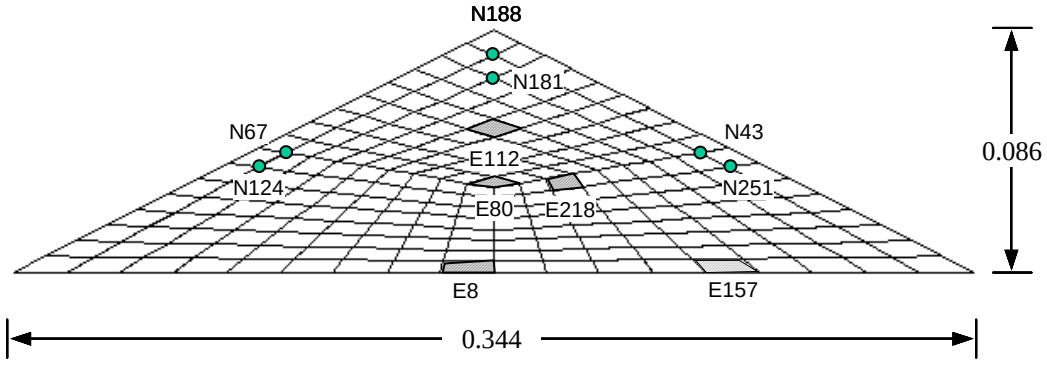

Figure 7.3: Finite element mesh for large deformation analysis (all dimensions are in meters and model scale)

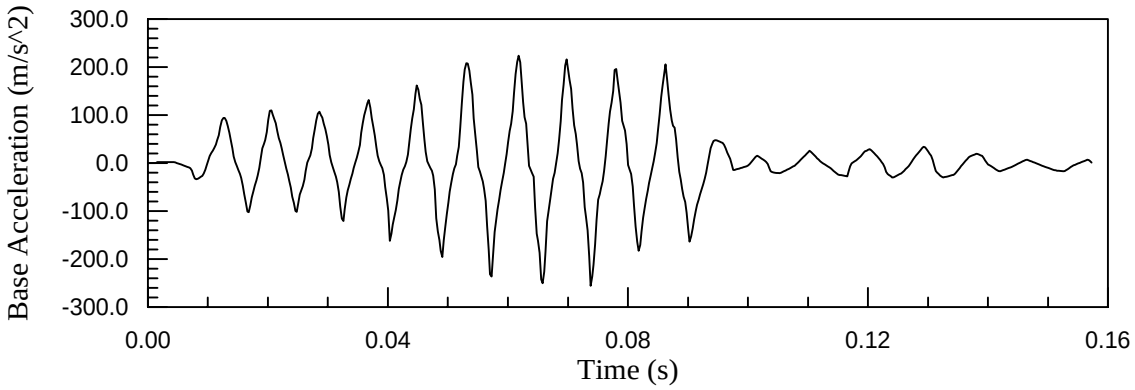

Figure 7.4: Horizontal base motion (model dimension)

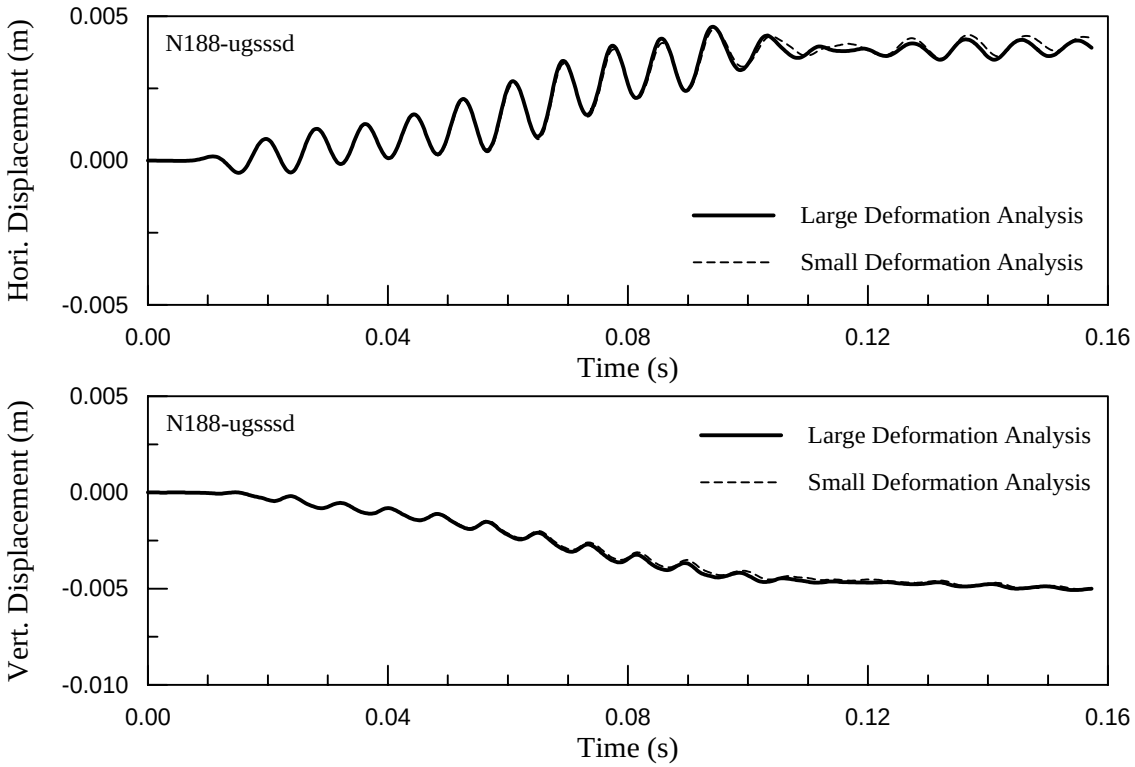

Figure 7.5: Horizontal and vertical displacement-time histories at node N188-Comparison between small and large deformation analysis

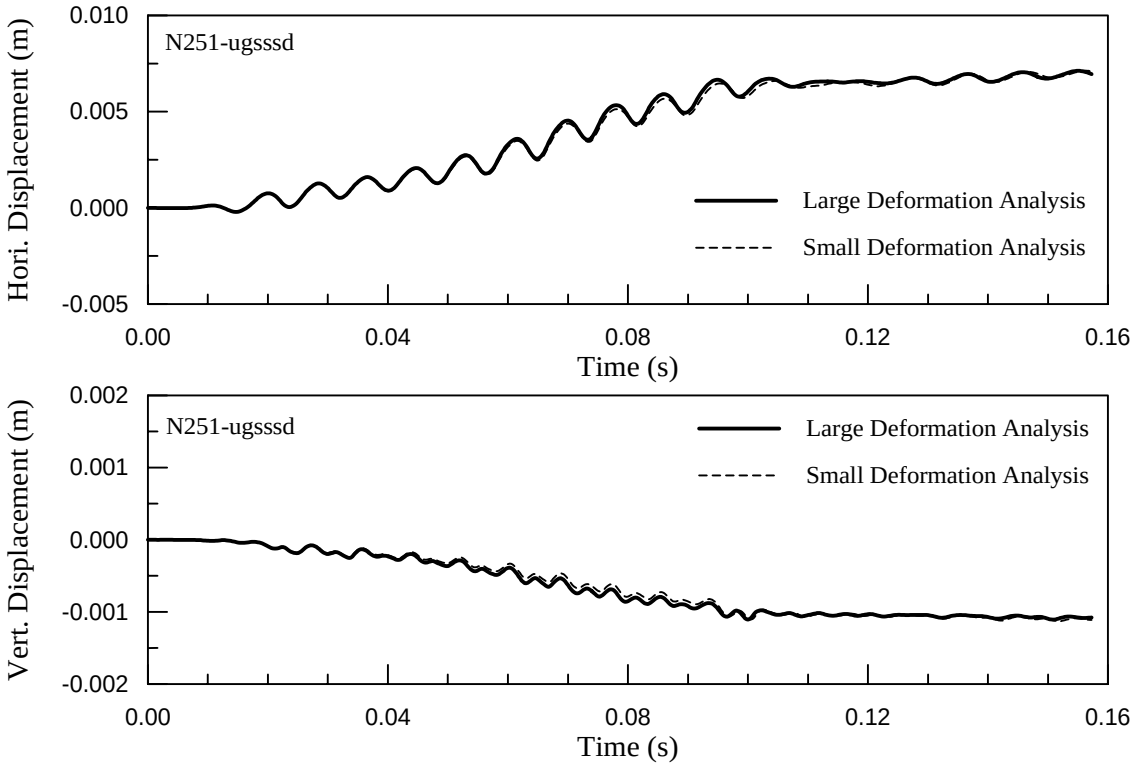

Figure 7.6: Horizontal and vertical displacement-time histories at node N251-Comparison between small and large deformation analysis

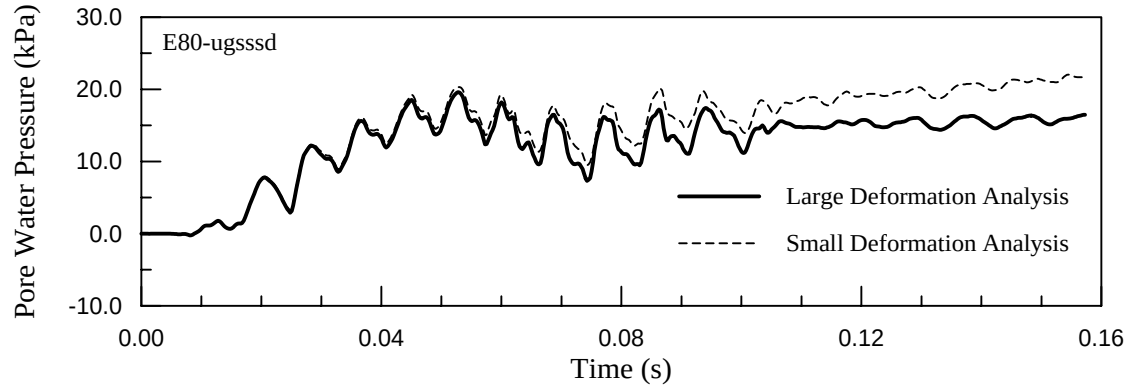

Figure 7.7: Pore water pressure-time histories in element E80-Comparison between small and large deformation analysis

7.8 Comparison of Small and Large Deformation Analyses for a Large Earthquake

In this case, a large deformation problem was created by applying five times larger earthquake motion than that was used Section 7.7. The vertical and horizontal displacements at nodes N188, N251 and N67 are shown in Figs. 7.8, 7.9 and 7.10, respectively. The small deformation analysis shows considerably larger displacements at all nodes compared to the large deformation analysis, i.e., the large deformation formulation is stiffer than the small deformation formulation. This is because of the initial stress stiffness added to the total stiffness in the large deformation formulation (see Section 7.5). The final vertical and horizontal displacements predicted by small deformation analysis are almost two times that of large deformation analysis. When the material undergoes large deformations such as in this problem, the small deformation analysis will not predict the true response of the structure. This clearly shows the importance of large deformation analysis for correctly predicting the response of structures. Comparisons to experimental results will validate this further.

The pore pressure in elements E8, E80 and E112 are shown in Fig. 7.11. The pore pressure in E8 is predicted by both methods very closely. It should be noted here that the element E8 is located at the center and bottom of the embankment. The strain experienced by the element is small and the difference in small deformation and large deformation analysis could not be seen. However, large deformation analysis shows more cyclic behavior compared to the small deformation analysis in element E80 and even more cyclic component in element E112 that is located above element E80. These regions undergo large cyclic loading. Therefore, the cyclic behavior predicted is justifiable.

The horizontal and vertical acceleration time histories at nodes N188, N251, and N67 are shown in Figs. 7.12 - 7.17. The accelerations predicted by both the analyses are comparable.

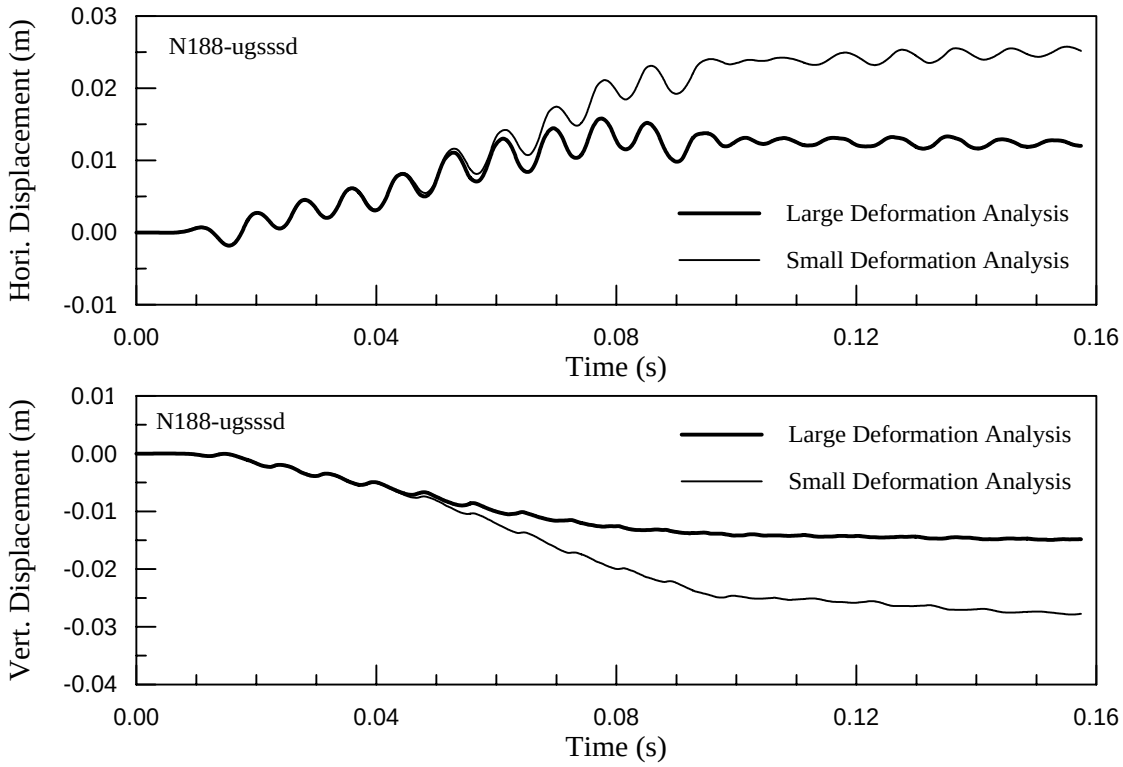

Figure 7.8: Horizontal and vertical displacement-time histories at node N188- Comparison between small and large deformation analysis

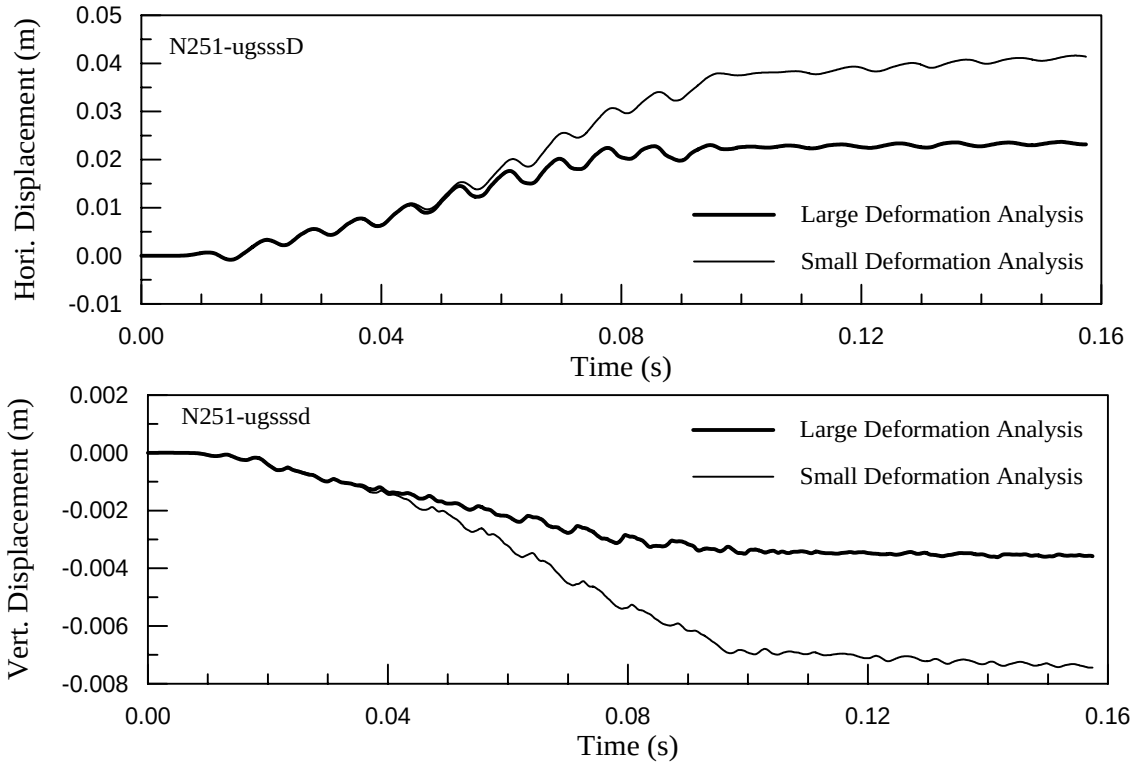

Figure 7.9: Horizontal and vertical displacement-time histories at N251-Comparison between small and large deformation analysis

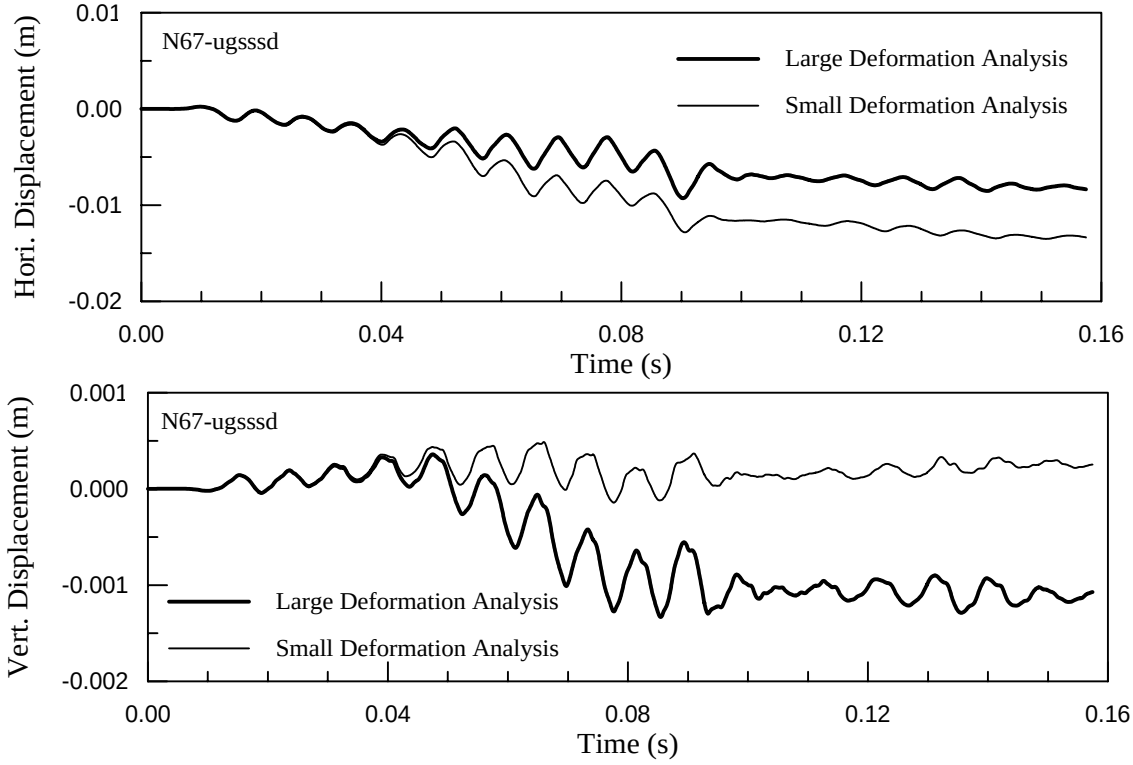

Figure 7.10: Horizontal and vertical displacement-time histories at N67-Comparison between small and large deformation analysis

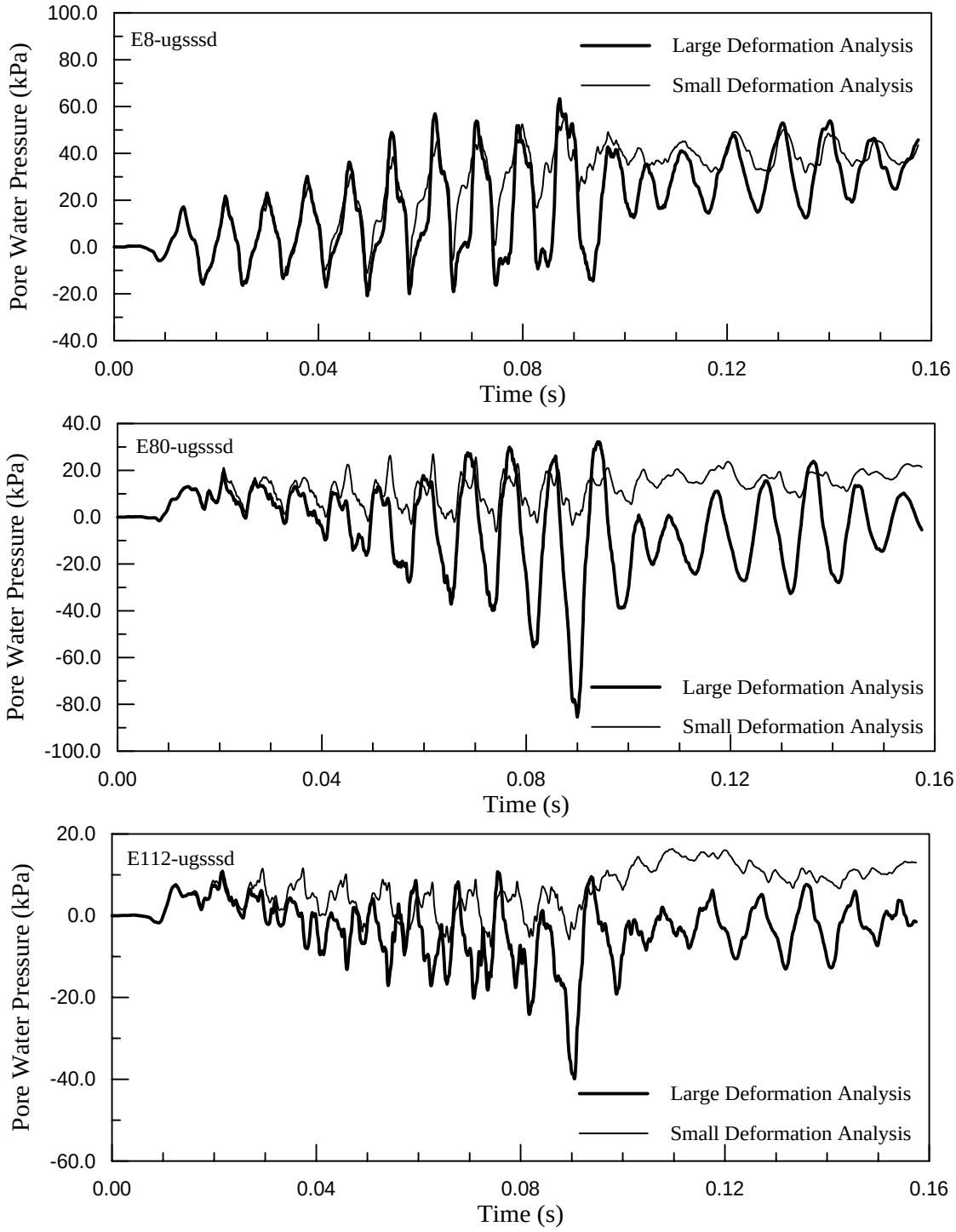

Figure 7.11: Pore water pressure-time histories in selected elements-Comparison between small and large deformation analysis

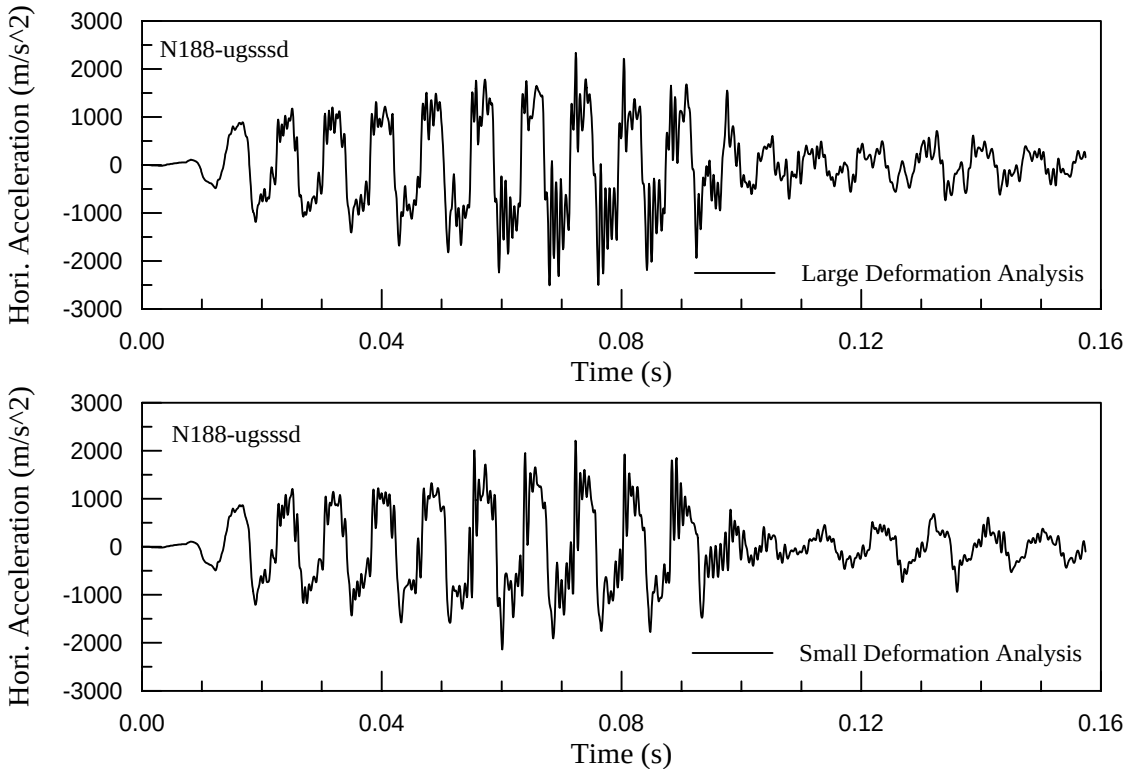

Figure 7.12: Horizontal acceleration-time histories at N188-Comparison between small and large deformation analysis

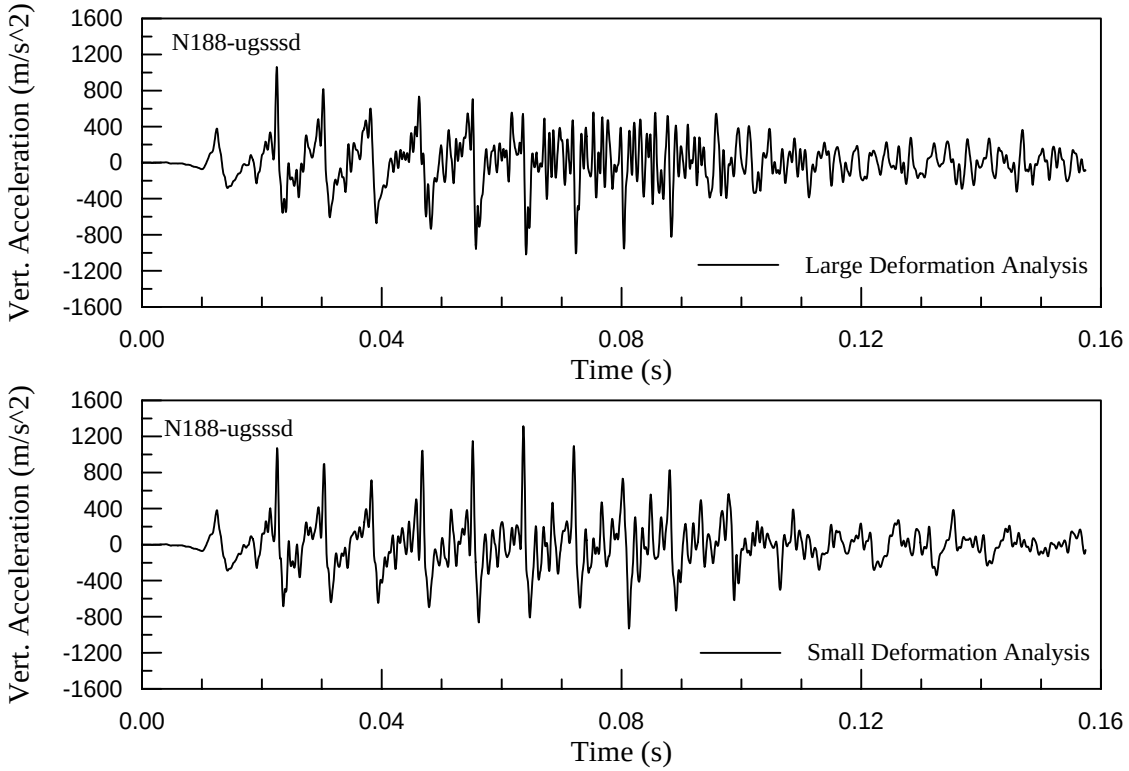

Figure 7.13: Vertical acceleration-time histories at N188-Comparison between small and large deformation analysis

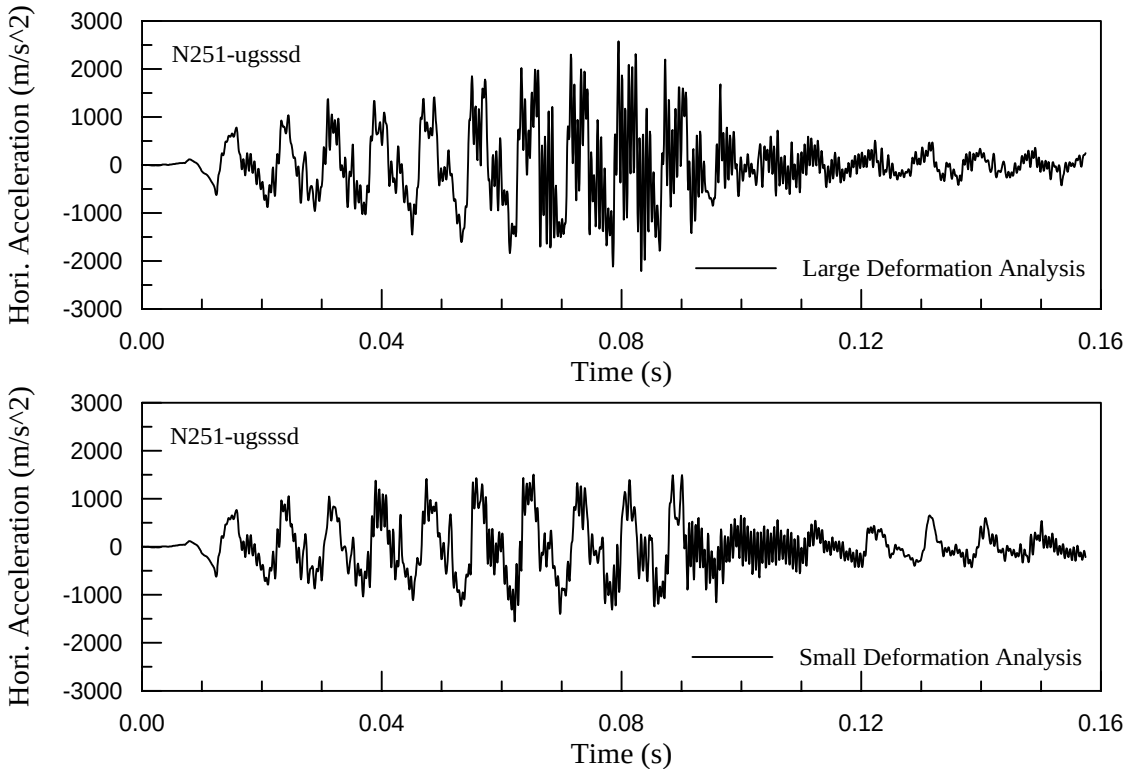

Figure 7.14: Horizontal acceleration-time histories at N251-Comparison between small and large deformation analysis

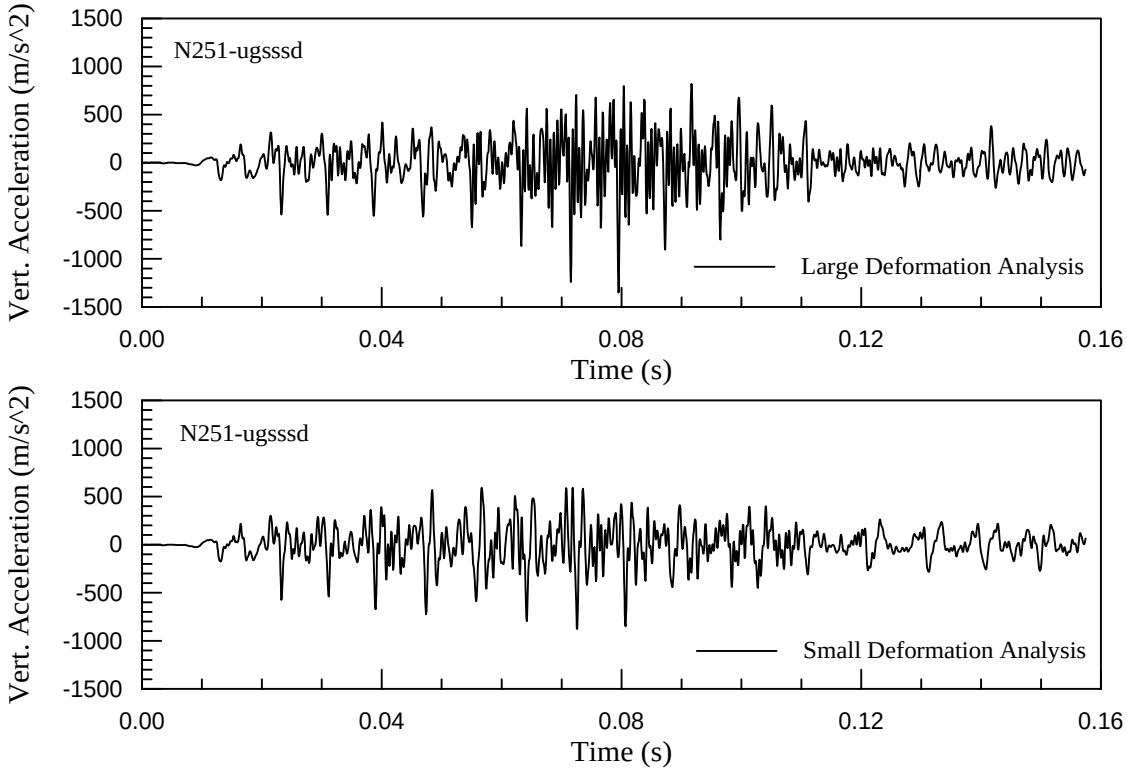

Figure 7.15: Vertical acceleration-time histories at N251-Comparison between small and large deformation analysis

8 DYNAMICS OF UNSATURATED POROUS MEDIA

8.1 Introduction

The equations governing the dynamic behavior of unsaturated soils derived in Chapter 3 are implemented within the TeraScale framework, which is described in Chapter 4. The importance of the large deformation analysis over the small deformation analysis is also discussed. The effect of relative accelerations and velocities on the overall behavior of the unsaturated soil embankment is studied by simulating a centrifuge test on unsaturated soil embankment (Deshpande, 1997). The implementation of the governing equations for the unsaturated porous media is similar to that of saturated porous media and the differences are summarized in the next section.

8.2 Updated Lagrangian Formulation of Governing Equations

The updated Lagrangian formulation of the governing equations and the constitutive relations for the unsaturated soils can be derived in a manner similar to that of saturated soils. The net stress for the unsaturated soils is given by:

$$\boldsymbol{\sigma} = \boldsymbol{\sigma}'' - p^g \mathbf{I}$$

The objectivity of the effective stress principle for the saturated porous media can be extended to the net stress for the unsaturated soils. The objectivity for the net stress can be written as:

$$\boldsymbol{\sigma}^{\nabla} = \boldsymbol{\sigma}''^{\nabla} - \dot{p}^{g}\mathbf{I}$$

The equilibrium equation on the current configuration for the reduced formulation is written as follows:

$$\int_{t+\Delta t\Omega} \phi_j^s \left(\rho \ddot{u}_j\right) d\Omega - \int_{t+\Delta t\Omega} \left(\phi_j^s\right)_{,i} \delta_{ij}\, \mu^g u_{k,k}\, d\Omega + \int_{t+\Delta t\Omega} \left(\phi_j^s\right)_{,i} \left(\sigma_{ij}''\right) d\Omega = \int_{t+\Delta t\Omega} \phi_j^s \left(\rho\, g_j\right) d\Omega + \int_{t+\Delta t\Gamma_t} \phi_j^s \hat{t}_j\, d\Gamma$$

The coefficients are defined in Chapter 3. The general framework for the large deformation analysis described in Chapter 7 can be extended to the unsaturated soils. The equations can be transformed to the reference configuration and then the incremental equations can be derived.

8.3 Validation of the Numerical Model

8.3.1 Centrifuge Experiment

The numerical model developed for an unsaturated soil is validated using a centrifuge model test results (Deshpande, 1997). The schematic of the centrifuge model embankment used in the centrifuge test is shown in Fig. 8.1. The locations of the Linear Variable Displacement Transducers (LVDT), pore pressure transducers and accelerometers are shown in Table 8.1. All dimensions are given in model scale. The Minco silt was used to prepare the model. The properties of Minco Silt are listed in Table 8.2.

The centrifuge test was done in two steps: static test and dynamic test. In the static test, the centrifuge was brought to 50 g gradually, in about 30 minutes. This procedure

simulated the construction procedure of the embankment at prototype scale. The centrifuge was then spun for another 10 minutes at 50 g to allow the soil to consolidate. At the end of the static test, while the centrifuge was spinning at constant speed, vertical and horizontal base motions were applied to the model.

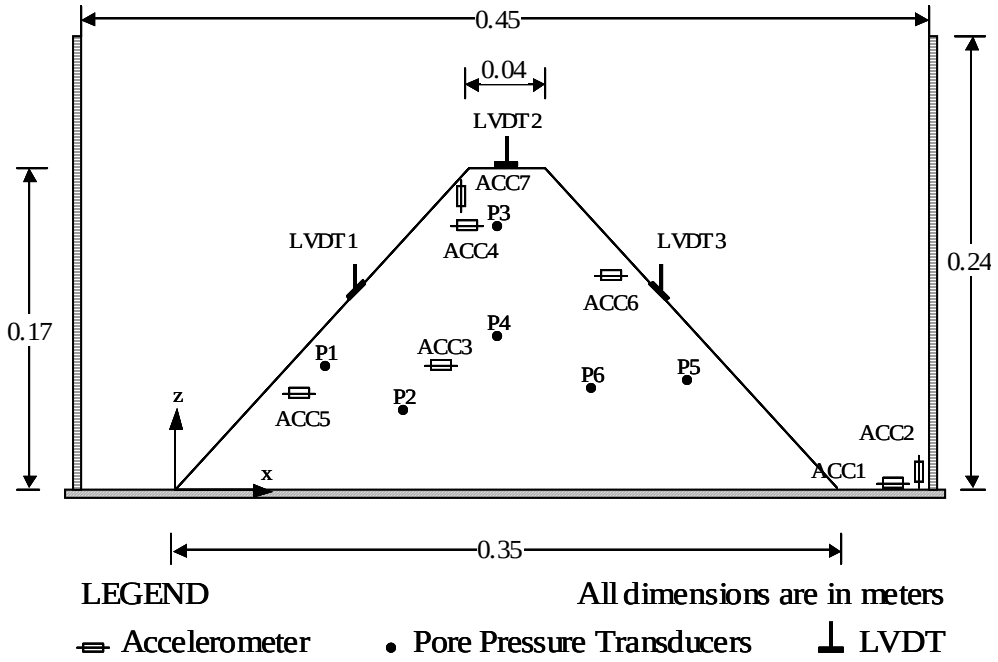

Figure 8.1: Schematic illustration of centrifuge model and instrument locations (after Desphande, 1997)

Table 8.1: Initial locations of the instruments

	x (m)	z(m)
ACC 1	Base H	0.00
ACC 2	Base V	0.00
ACC 3	0.140	0.064
ACC 4	0.155	0.140
ACC 5	0.065	0.051
ACC 6	0.230	0.112
ACC 7	0.150	0.155
LVDT 1	0.095	0.105
LVDT 2	0.160	0.170
LVDT 3	0.250	0.110

	x(m)	z(m)
PPT 1	0.080	0.067
PPT 2	0.120	0.042
PPT 3	0.170	0.140
PPT 4	0.170	0.080
PPT 5	0.270	0.058
PPT 6	0.220	0.053
PPT 7	-0.050	0.00

Table 8.2: Physical and engineering properties of the Minco silt

Property	Value
Specific gravity of solids	2.67
Liquid limit, %	28.0
Plastic limit, %	20.0
Gravel, %	0.0
Sand, %	27.0
Fines, %	73.0
Clay size fraction, %	18.0
USCS Classification	CL
Maximum dry unit weight, kN/m^3	17.9
Optimum moisture content, %	12.8
Model dry unit weight, kN/m^3	14.2
Model moisture content, %	14.0

8.3.2 Numerical Modeling

The centrifuge experiment is simulated using the numerical model developed for the unsaturated soils using both small and large deformation formulations. The finite element mesh for the unsaturated soil embankment used in this study is shown in Fig. 8.2. The simulation is carried out on the model scale and the results are also reported on the model scale. The prototype values can be calculated by using centrifuge-scaling laws. The calibration of the soil water characteristic curve and the constitutive model are described in the following sections.

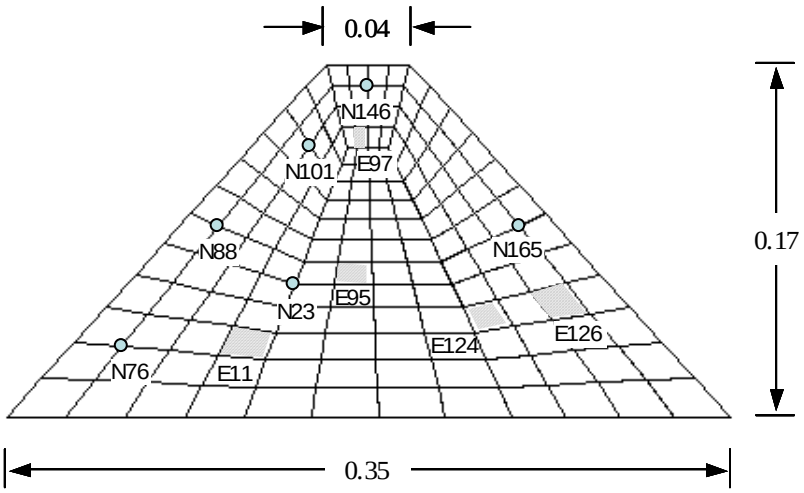

Figure 8.2: Finite element mesh of unsaturated model embankment (All dimensions are in meters)

8.3.3 Calibration of Soil Water Characteristic Curve

The soil water characteristic curve proposed by van Genuchten (1980) is used in this simulation to represent the relationship between matric suction and degree of saturation in an unsaturated soil. The SWCC model parameters were determined by adjusting the model parameters until the model matches the experimental curve (Ananthanathan, 2002). The calibrated van Genuchten's model and the experimental results are shown in Fig. 8.3.

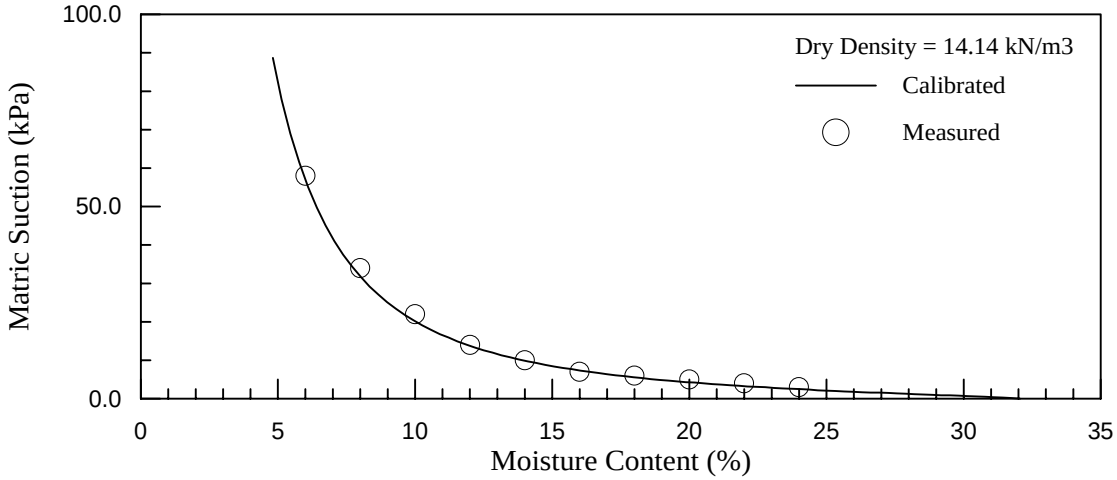

Figure 8.3: Calibration of soil water characteristic curve model parameters

It was found that there was a discrepancy in the measured suction (30 kPa) at a moisture content of 13.82 % and a density of 14.23 kN/m^3 (Vinayagam, 2004) and that obtained from SWCC shown in Fig. 8.3 (10 kPa). This difference may be attributed to the different initial compaction moisture contents used in both cases. A 6% of initial compaction moisture content was used for generating the SWCC shown in Fig. 8.3. The centrifuge model soil had a compaction moisture content of 14.0%. This is closer to the moisture content used by Vinayagam (2004) and therefore, the SWCC was shifted to obtain 30 kPa for moisture content of 13.82 % (no reliable initial suction measurements are available for the centrifuge model soil). The shifted model parameters are listed in Table 8.3.

Table 8.3: Calibrated van Genuchten model parameters

Parameter	**van Genuchten model values**
Dry Density (kN/m^3)	14.14
Parameter a	0.172
Parameter n	1.500
Parameter m	0.333
Irreducible saturation	0.005

8.3.4 Constitutive Equation

The stress strain behavior of unsaturated Minco Silt is modeled using an elastoplastic constitutive model based on the bounding surface concept. The schematic illustration of the bounding surface on stress invariant space is shown in Fig. 8.4. The original three-surface model developed for cohesive soils (Dafalias and Herrmann, 1986) was modified for unsaturated soils by Muraleetharan and Nedunuri (1998). Additional parameters related to matric suction have been incorporated into the original model. This

model uses two stress state variables: net stress ($\sigma_{ij} - p^g \delta_{ij}$) and matric suction ($S$). The original bounding surface model is considered as the base model at zero suction. The bounding surface expands when the matric suction increases. The modifications to the base model to incorporate the suction effects are based on the concepts proposed by Alonso et al., (1990), Wheeler and Sivakumar (1995) and Wheeler (1996) for unsaturated soils.

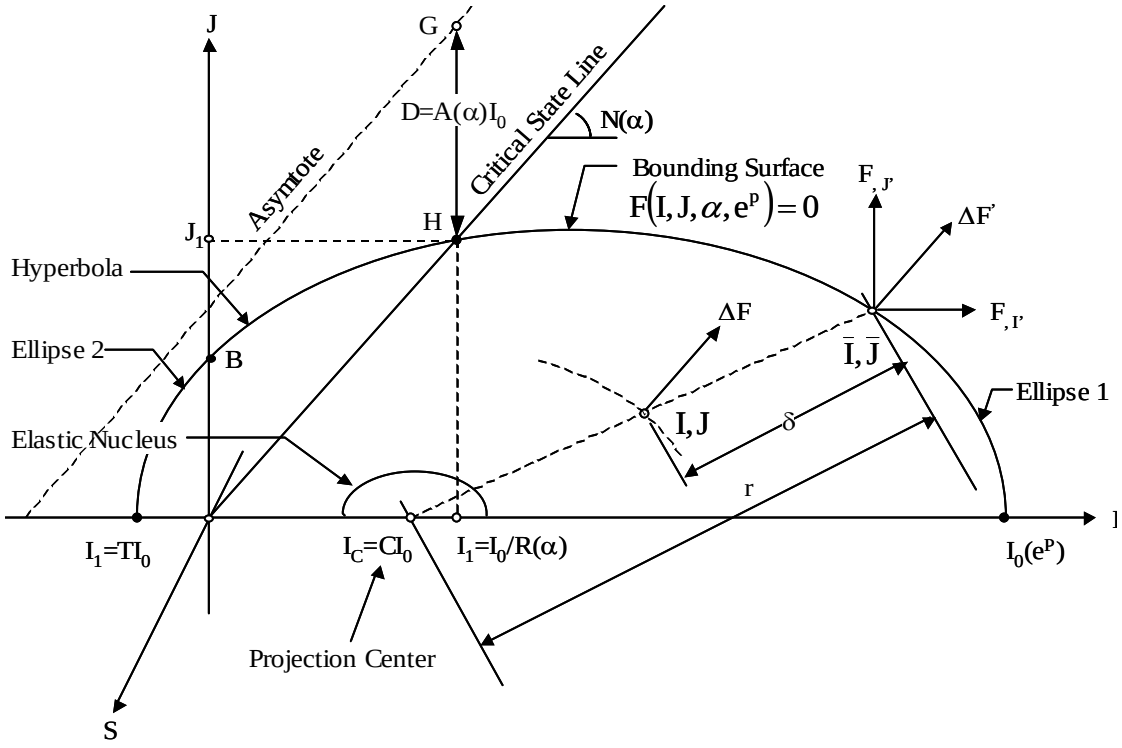

Figure 8.4: Schematic illustration of bounding surface constitutive model in stress invariant space

8.3.5 Calibration of the Constitutive Model Parameters

The bounding surface material model requires 25 input parameters. The parameters defining the initial state of the material, elasoplastic model parameters, traditional material constants, surface configuration parameters. Some of the parameters were calculated directly from experimental results (Vinayagam, 2004) and others were determined by calibrating the model against the experimental results.

The parameters determined by calibrating the constitutive model against the monotonic loading did not predict the cyclic behavior well (Vinayagam, 2004). For the dynamic analysis, the model parameters have to be calibrated against a cyclic test so that the model behavior can replicate the actual material behavior. The cyclic test was performed in two steps: loading the specimen monotonically for a certain stress level (200 kPa) and then unloading and reloading cycles were applied. Keeping the directly calculated model parameters constant, other parameters were adjust to predict the cyclic test results. Capabilities of the current constitutive model for predicting the cyclic behavior were found to be very limited. This is expected since the base model used (Dafalias and Herrmann, 1986) is a model for clay. A base sand model is expected to yield better predictions for Minco Silt and one such model is currently under development. It is impossible to predict the cyclic loading portion after matching the monotonic loading portion with the current model. Therefore, a reasonable judgment had to be made to use the existing constitutive model with reasonable values for model parameters. Since the dynamic behavior is related to the cyclic behavior, the model was calibrated to reach the same amount of total plastic strain with the same number of cycles used in the experiment. The calibrated model parameters are shown in Table 8.4.

The calibrated and measured deviatoric stress, change is suction and change in volumetric strain are plotted against axial strain as shown in Figs. 8.5(a), (b) and (c), respectively. The experimental results show complexity in the cyclic loading region not only for the deviatoric stresses but also for the change in suction and change in volumetric strain. However, the final values are predicted well by the model.

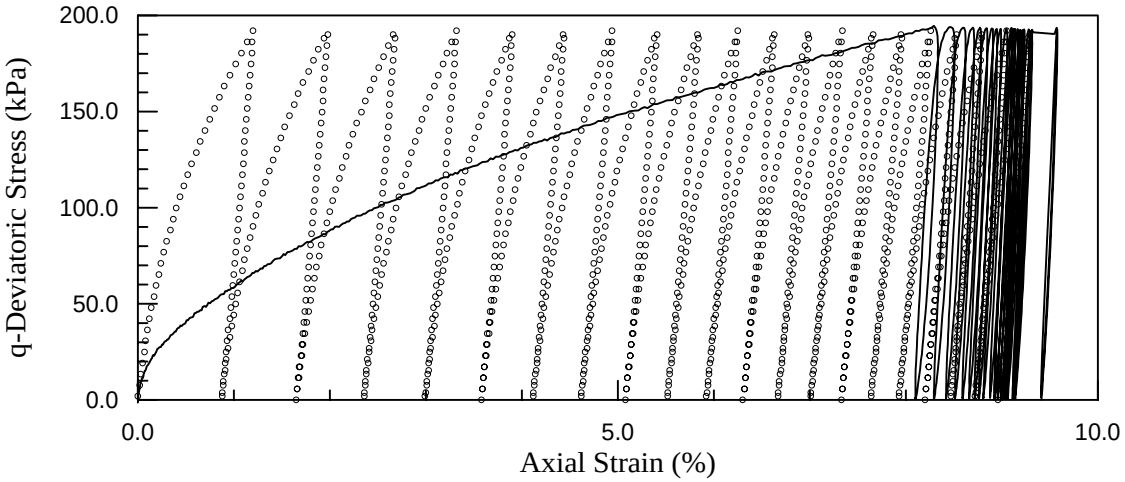

(a)

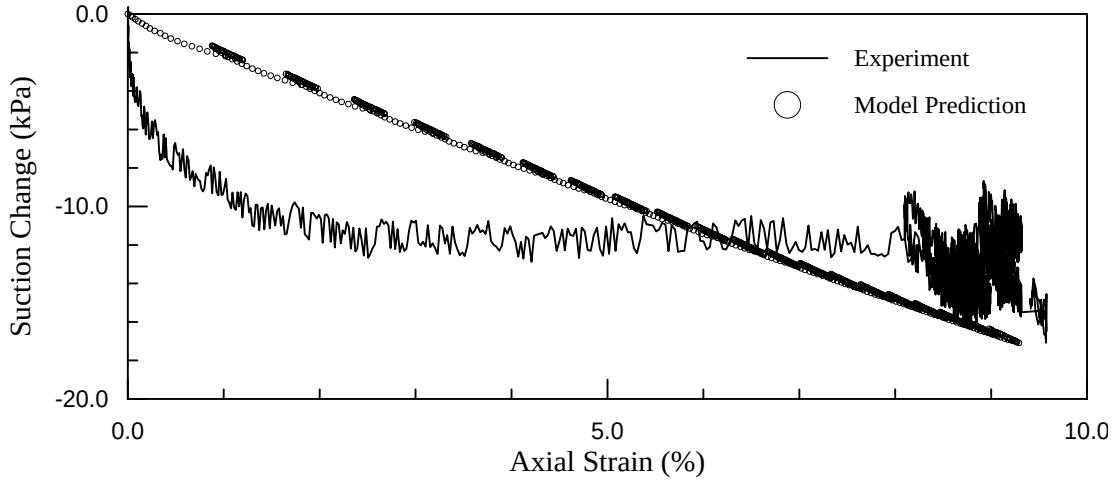

(b)

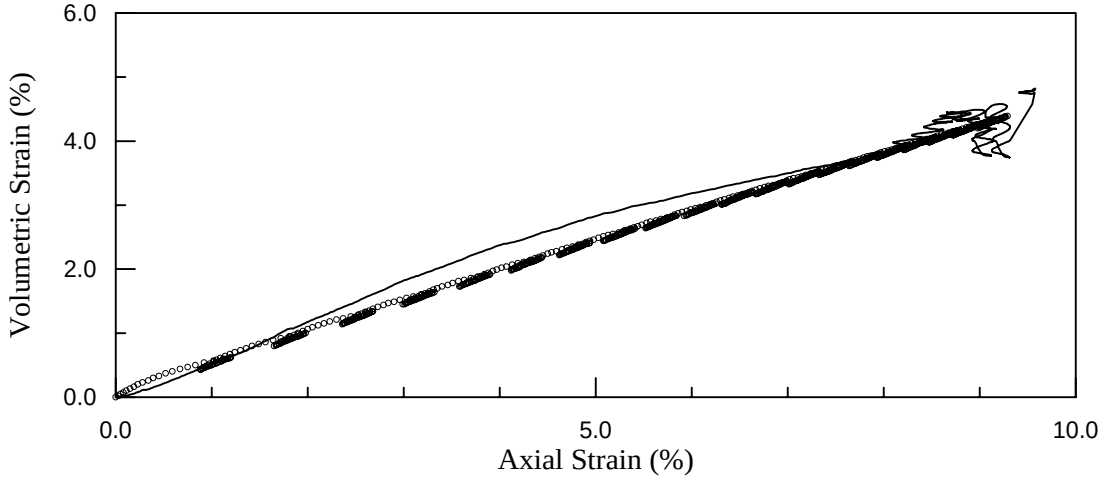

Figure 8.5: Measured and calibrated model curves (a) deviatoric stress versus axial strain, (b) suction change versus axial strain and (c) volumetric strain versus axial strain

Table 8.4: Calibrated model parameters for Minco Silt

No	Parameters	Values
(a)	**Traditional Model Parameters**	
1	Slope of isotropic consolidation line, λ	0.0954
2	Slope of elastic rebound line, κ	0.0103
3	Slope of bounding surface line OA in compression, M_c	1.2678
4	Ratio of extension to compression value of M, M_e/M_c	1.0
5	Poisson ratio or elastic shear modulus, υ	0.2
6	Limit pressure, P_l (kPa)	33.8
7	Atmospheric pressure, P_a (kPa)	101.3
(b)	**Surface Configuration Parameter**	
8	Parameter defining the ellipse 2, T	0.01
9	Bounding surface shape parameter in compression, R_c	2.41
10	Ratio of triaxial extension to triaxial compression value of R, R_e/R_c	1.0
11	Value of parameter defining the hyperbola in compression, A_c	0.05
12	Ratio of triaxial extension to triaxial compression value of A, A_e/A_c	1.0
13	Elastic nucleus parameter, S	1.03
14	Projection center parameter, C	0.0
(c)	**Hardening Parameters**	
15	Hardening parameter, m	0.02
16	Shape hardening parameter in compression, h_c	0.8
17	Ratio of extension to compression value of H, h_e/h_c	1.0
18	Shape hardening parameter on the I-Axis, H_0	0.8
(d)	**Suction Related Parameters**	
19	Suction dependent parameter, $\mu(s)$	4.7028
20	Suction dependent parameter, $\alpha(s)$	0.0889
21	Suction dependent parameter, $N(s)$	1.752
22	Suction dependent parameter, $A(s)$	0.3587
23	Suction dependent parameter, $r(s)$	3.0
24	Suction dependent parameter, $\beta(s)$	0.5

8.3.6 Static Analysis

The initial stresses for the dynamic analysis are determined by performing static analysis. To save computational time, static analysis is performed using the reduced formulation. The static analysis is calculated dynamically, by setting the algorithmic Newmark parameters in the integration scheme to $\alpha = 0$, $\beta = 1.0$ and $\gamma = 1.5$. The stresses at the end of the static analysis are used as the initial stresses for the dynamic analysis. At the end of consolidation, the nodal displacements, velocities and accelerations are set to zero, i.e. the stresses are applied to an undeformed mesh for the dynamic analysis. The elastoplastic constitutive model requires initial stresses even for static analysis. Therefore, 20% of the vertical stress (10 g values) at the middle height of the embankment is used as the initial stresses for the static analysis. During the static analysis the maric suction was kept constant. Then, the gravity load is increased from 10 g to 50 g in 300 seconds as shown in Fig 8.6.

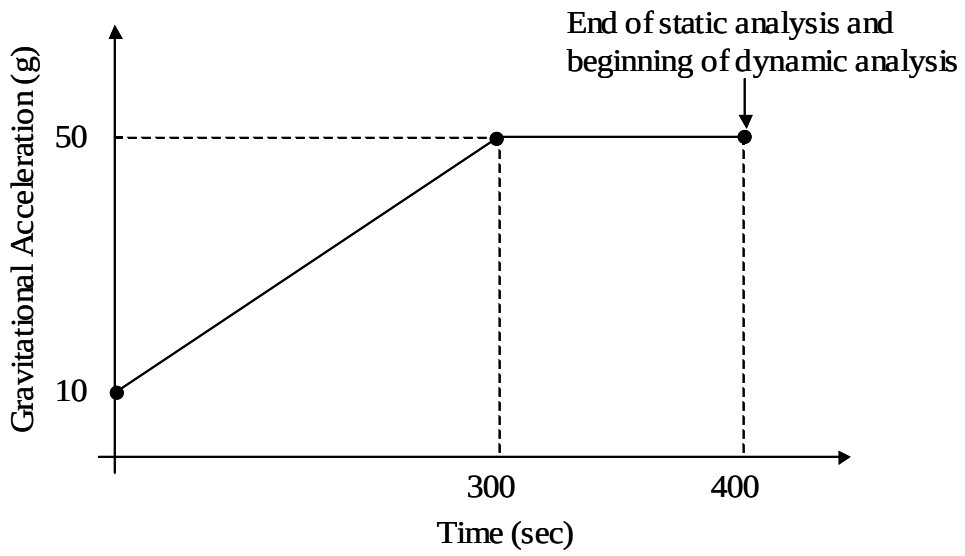

Figure 8.6: Centrifuge spin-up time history for static analysis

8.3.7 Dynamic Analysis

The stresses at the end of static analysis were used as the initial stresses for the dynamic analysis. The time integration parameters were changed to $\alpha = -0.3$, $\beta = 0.4225$ and $\gamma = 0.8$. The model embankment was shaken with the horizontal and vertical accelerations shown in Fig. 8.7. The validation of the numerical model against the experimental results is shown for the large deformation analysis with reduced formulation (Section 3.5). The vertical settlements at nodes N88 and N146 are compared with the experimental results in Fig. 8.8. The change in pore liquid pressures in elements E126, E124, E16, and E11 are compared with the experimental results in Fig. 8.9.

The predicted settlements at nodes N88 and N146 are higher than the measured values, but some general trends are predicted. For example, more settlement is observed and predicted at node N146 than N88. The major factor contributing to this softer behavior is the constitutive model parameters. As discussed before, the constitutive model used is not ideally suited for simulating Minco Silt behavior.

The pore liquid prediction in element E126 is very close to the measured value. Pore liquid pressure predictions at other locations are off from the measured values. It was reported that some of the pore pressure transducers did not function well (Deshpande, 1997). The pore liquid pressures in elements E126, E124 and E11 show a gradual increase. The pore liquid pressure in element E16 decreases at the beginning and then increases.

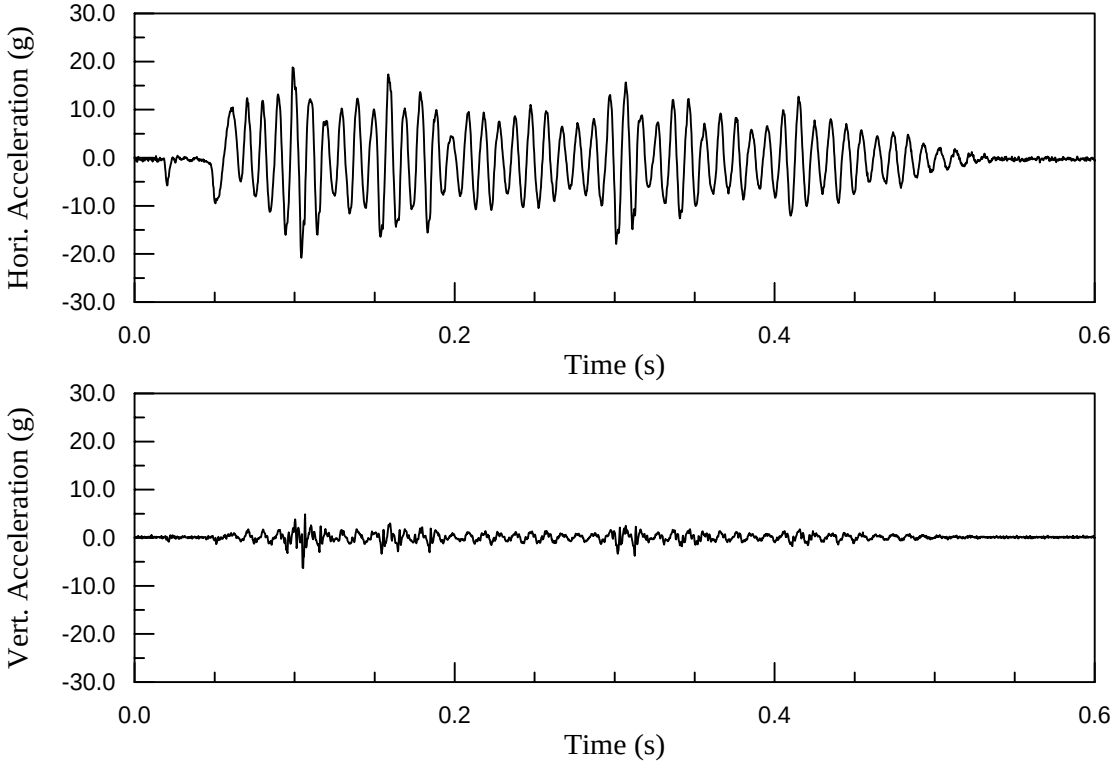

Figure 8.7: Horizontal and vertical input base acceleration-time history (model dimensions)

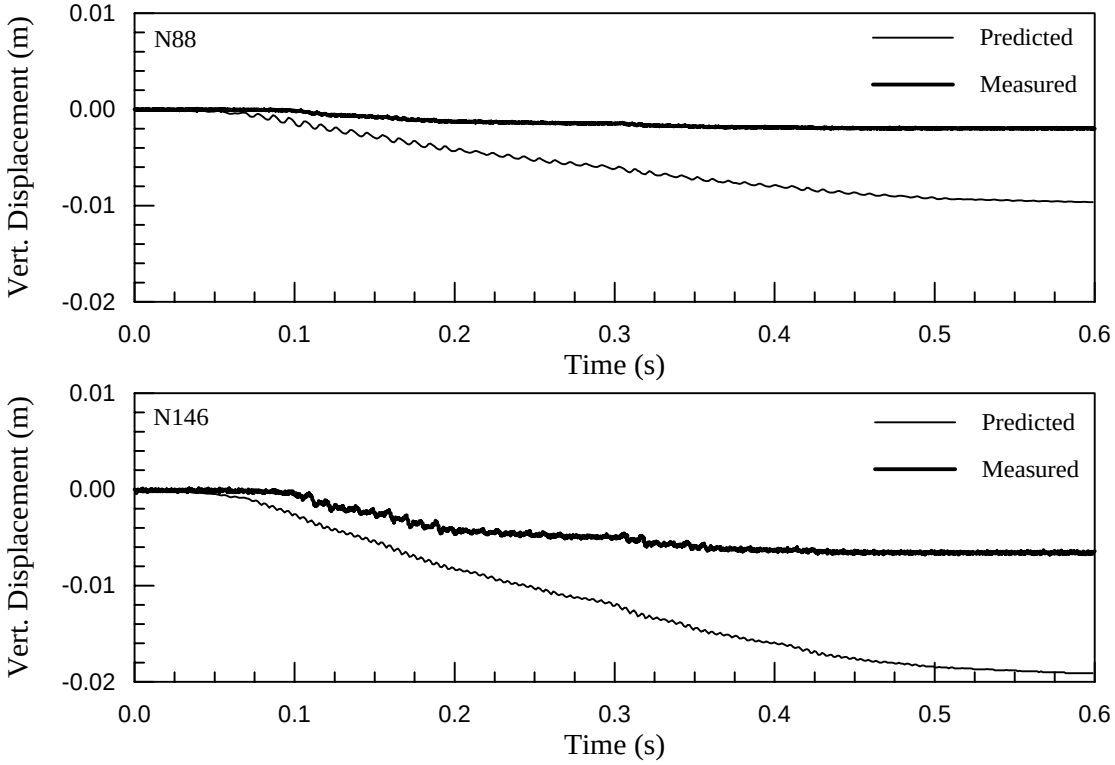

Figure 8.8: Comparison between the measured and predicted displacements at node N88 and N146

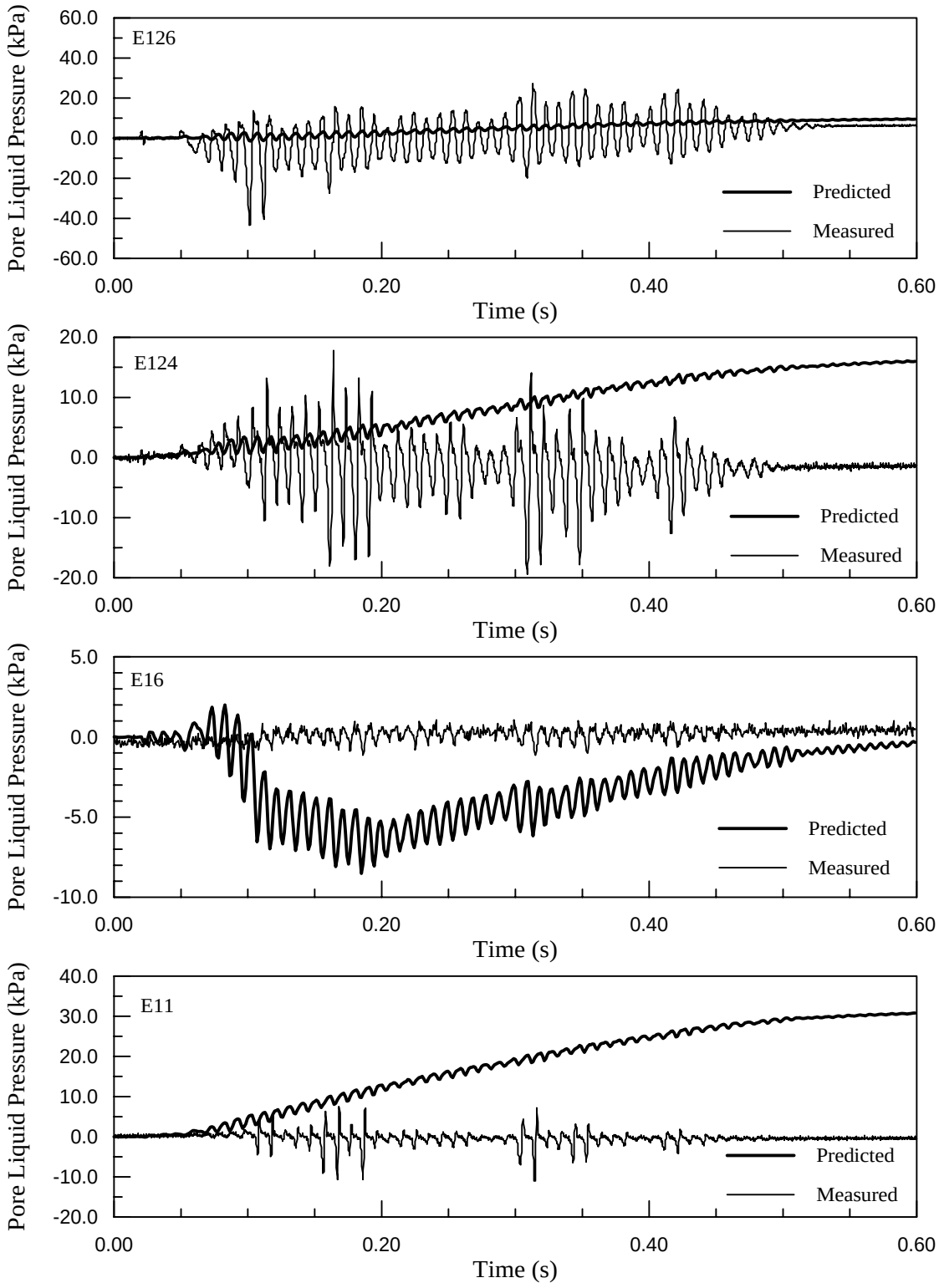

Figure 8.9: Comparison between the measured and predicted pore liquid pressures

8.4 Comparison Between Complete and Reduced Formulation

The centrifuge experiment was simulated using the complete formulation and the reduced formulation to study the effect of fluid accelerations and velocities on the overall behavior of the unsaturated soils under earthquake loading. The matrices of the complete formulation are highly nonlinear and the simulation could not be completed with initially calibrated model parameters. Two of the bounding surface model parameters, λ and κ, were decreased ($\lambda = 0.02$, $\kappa = 0.002$) to make the model embankment more stiff, as observed in the centrifuge experiment, and then the complete formulation was run. The reduced formulation was also run with the new model parameters. Large deformation analyses were carried out with these two formulations.

The displacement time histories from these two formulations are compared in Figs. 8.10 through 8.12. The reduced formulation shows more displacements compared to the complete formulation. The reduced formulation assumes an undrained condition and the complete formulation allows the liquid and gas to flow. Therefore, the predictions are consistent with the drained and undrained behavior of the soil. Similar responses are observed at other nodes also.

The time histories of the pore liquid pressure, pore gas pressure, matric suction and degree of saturation are shown in Fig. 8.13. An interesting phenomenon is observed in the liquid pressure time history. The pore liquid pressure increases at the beginning and shows some dissipation after shaking subsides. This behavior is obviously not observed in the reduced formulation. The matric suction time history shows this phenomenon clearly.

Looking at the results from both these formulations, it can be concluded that both formulations predict the overall behavior reasonably well. However, the accelerations and velocities of the pore fluids do have some influence on the overall behavior. The major disadvantage of using the full formulation is that it requires tremendous computational resources. It is also found that the complete formulation requires very small time steps. It is approximately calculated that the complete formulation requires 36 times more computational effort than reduced formulation. Finally, it can be concluded that the reduced formulation can be used to simulate the earthquake behavior of the unsaturated soils such as the Minco Silt and reasonable preliminary results can be obtained. For soils with larger permeabilities (e.g. sands) caution should be exercised when using the reduced formulation.

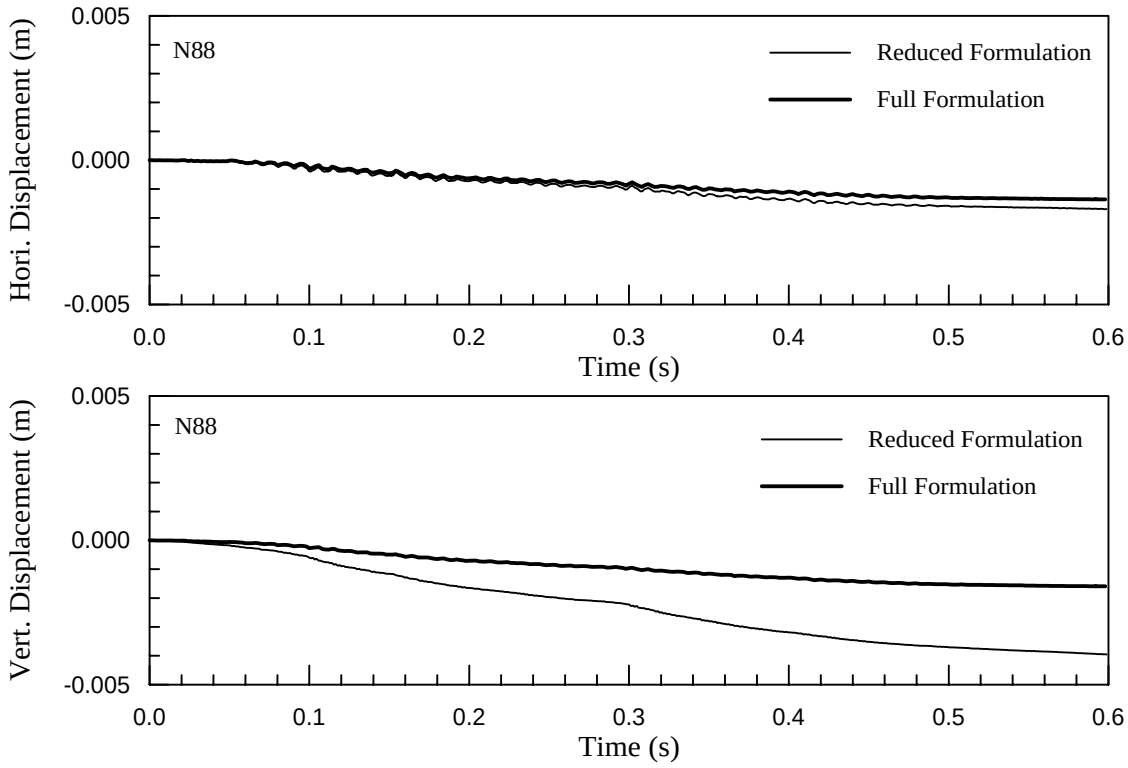

Figure 8.10: Horizontal and vertical displacements at node N88

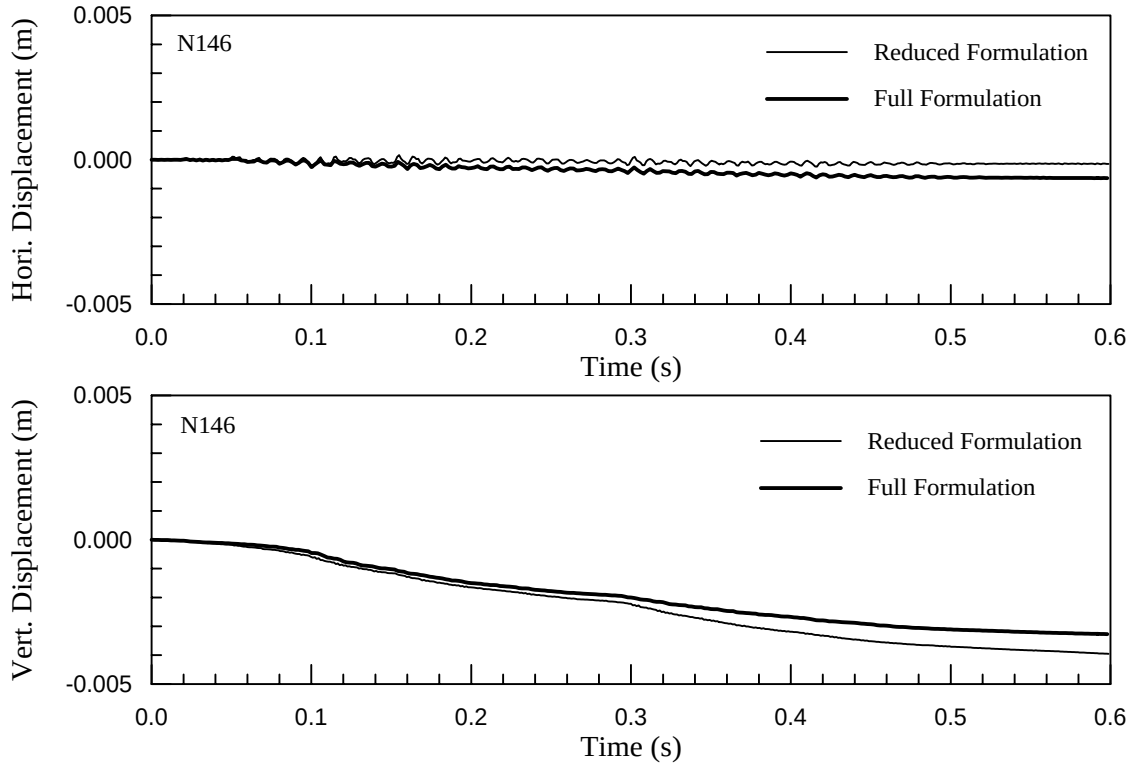

Figure 8.11: Horizontal and vertical displacements at node N146

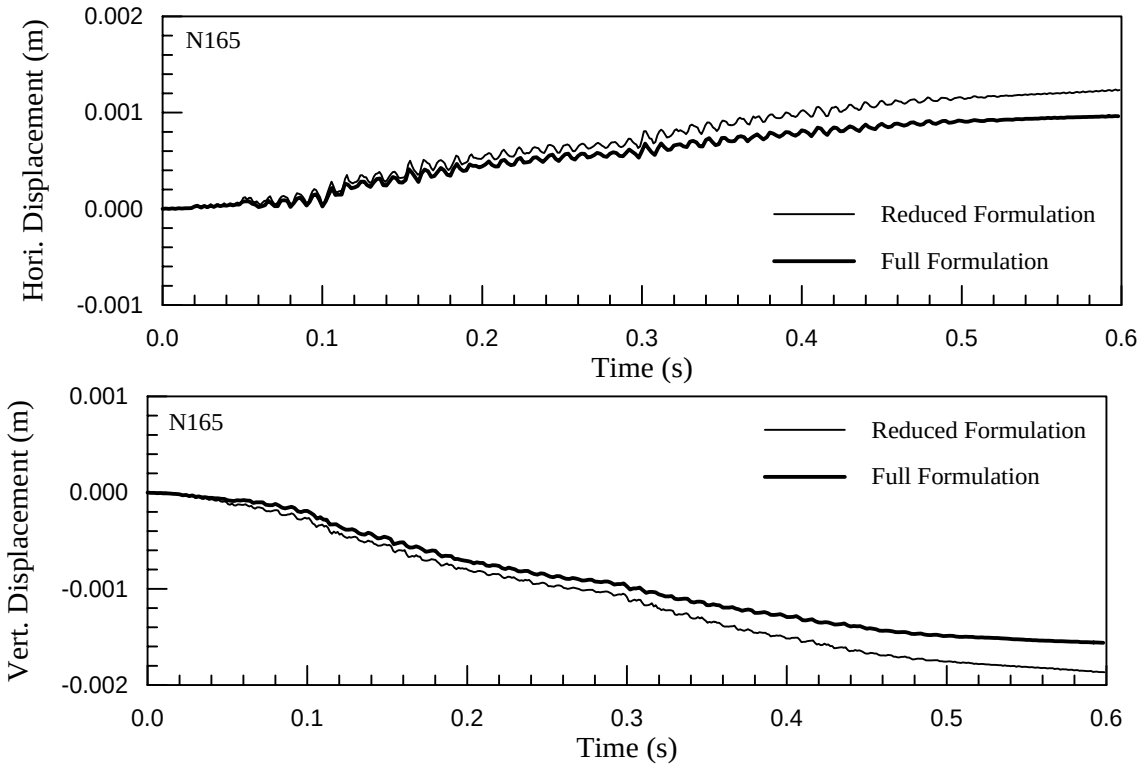

Figure 8.12: Horizontal and vertical displacements at node N165

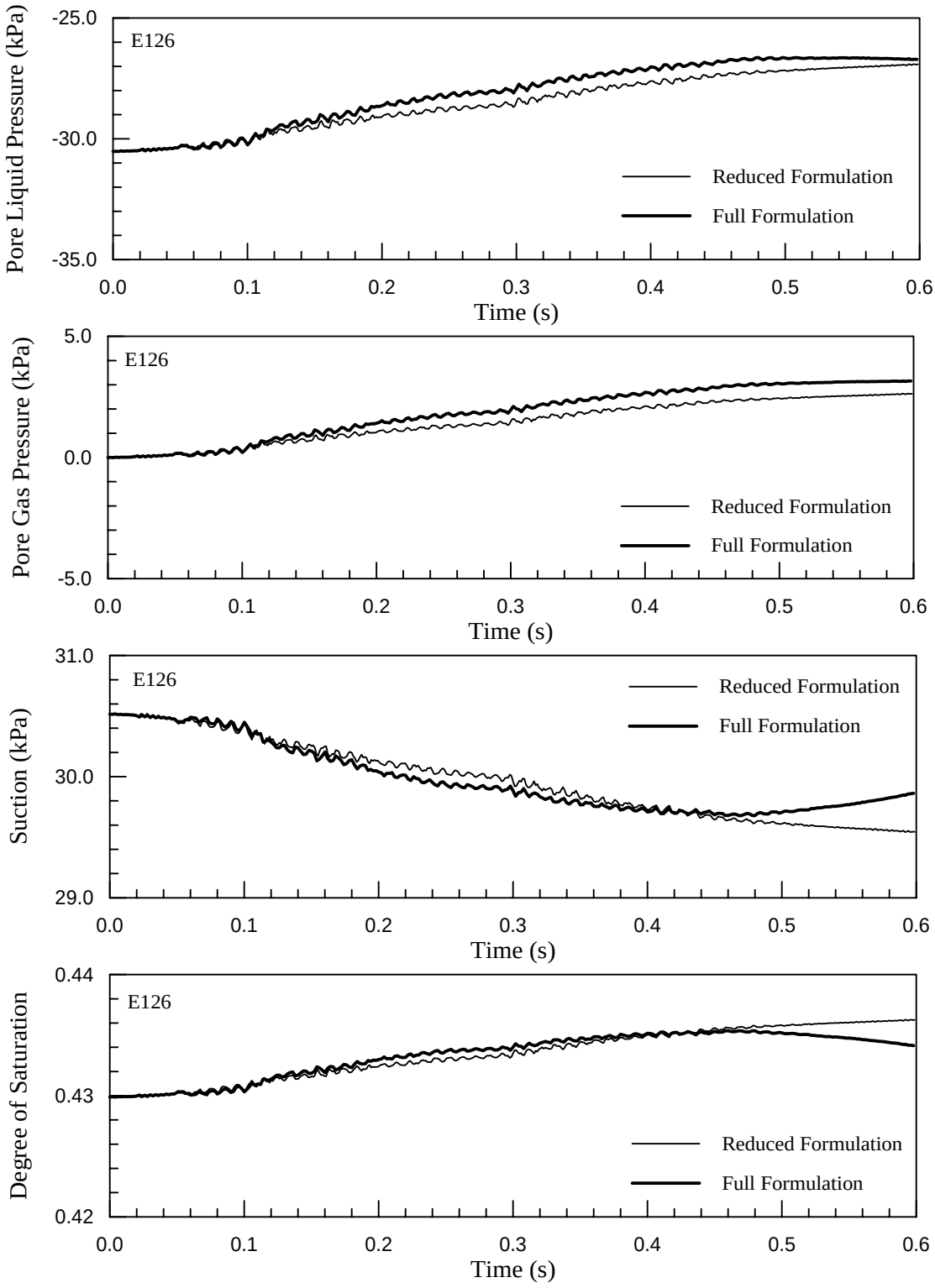

Figure 8.13: Fluid pressures, suction, and degree of saturation at element E126

8.5 Comparison Between Small and Large Deformation Analysis

Small and large deformation theories for the dynamics of unsaturated porous media have been implemented within the Terascale framework. The response of the unsaturated soil embankment discussed in Section 8.3 is analyzed using both methods utilizing the reduced formulation. Horizontal and vertical displacements at nodes N88, N146 and N165 are shown in Figs. 8.14, 8.15 and 8.16, respectively. It is found that the large deformation analysis gives smaller vertical and horizontal displacements compared to the small deformation analysis. Time histories of pore liquid pressure, pore gas pressure, matric suction and degree of saturation in element E126 are shown in Fig. 8.17. The pore liquid and gas pressures show slightly higher values for the large deformation analysis.

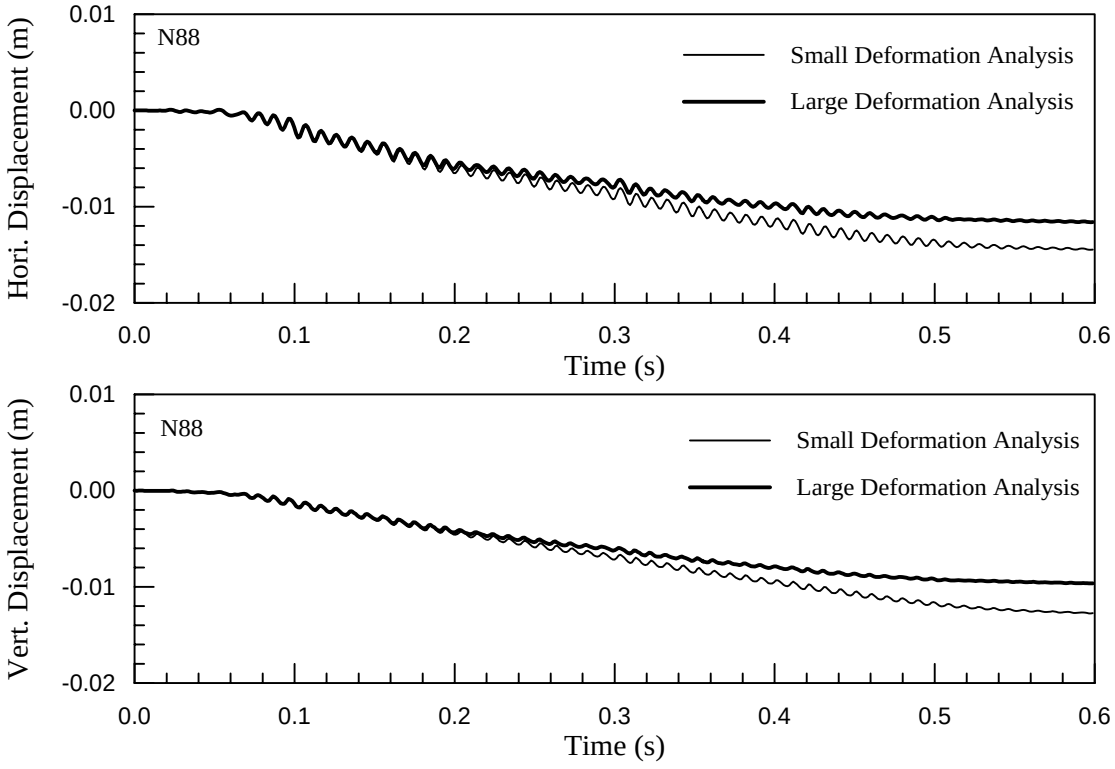

Figure 8.14: Horizontal and vertical displacements at node N88

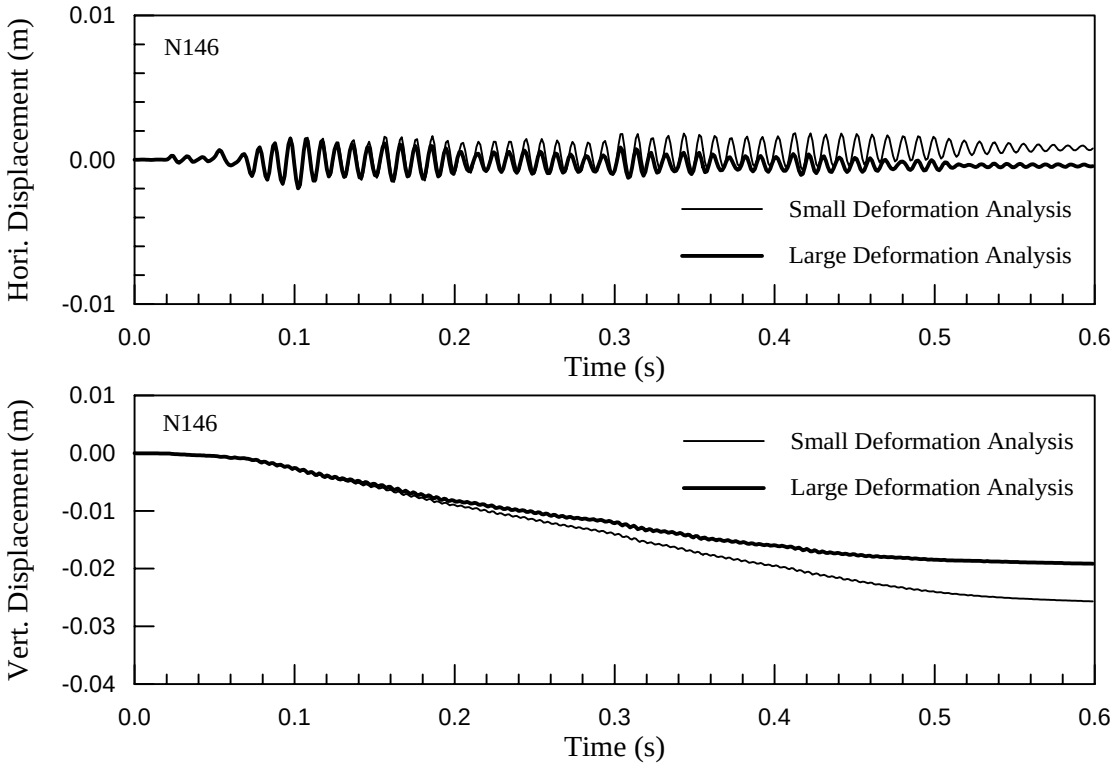

Figure 8.15: Horizontal and vertical displacements at node N146

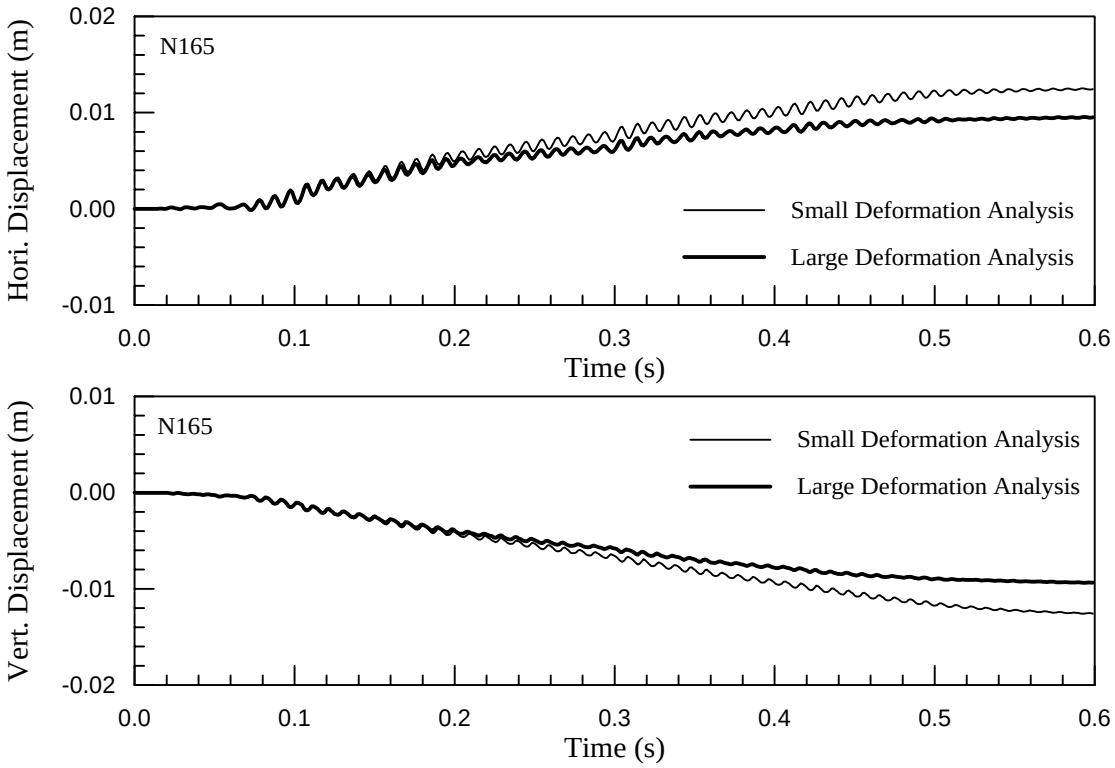

Figure 8.16: Horizontal and vertical displacements at node N165

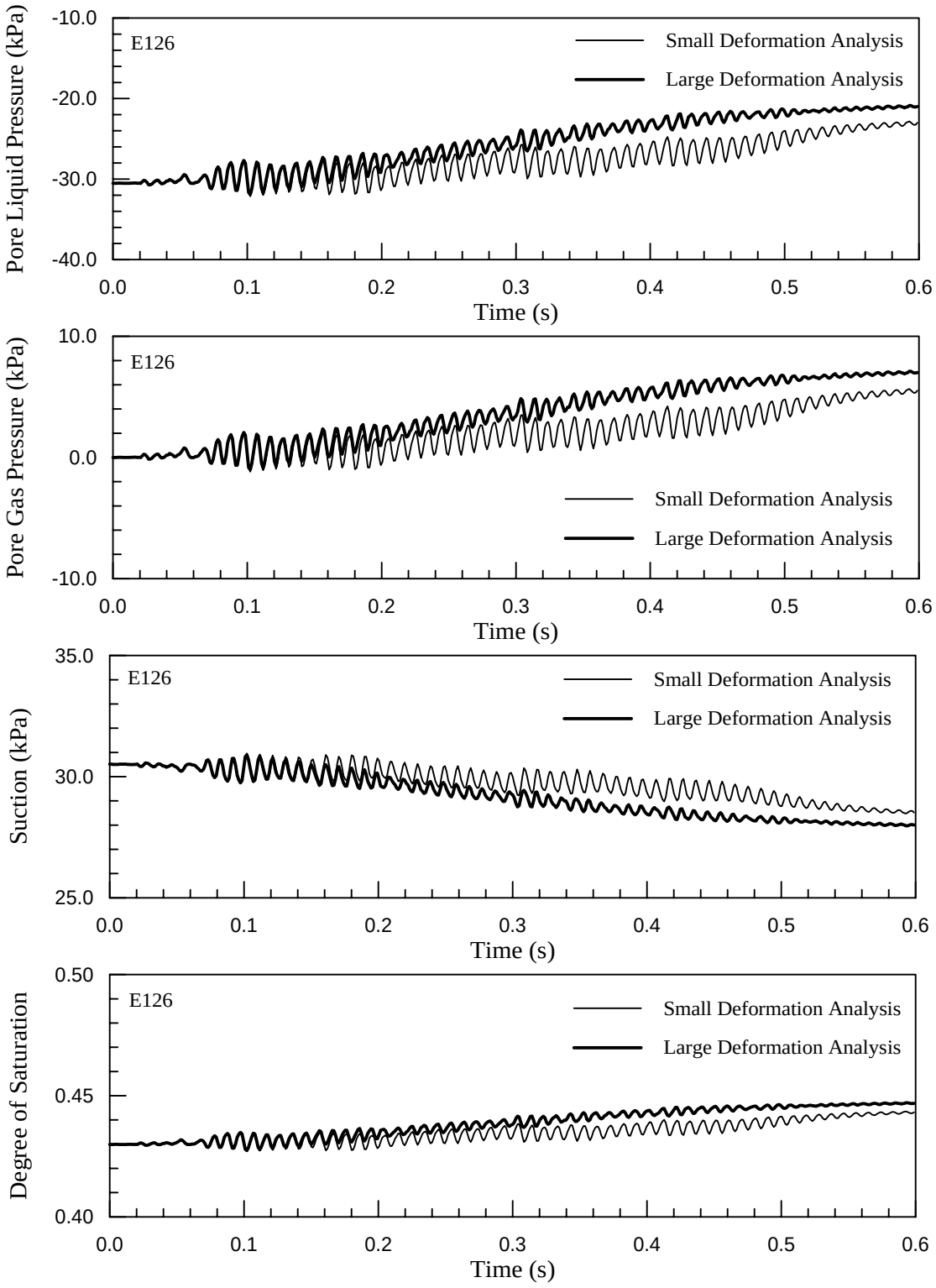

Figure 8.17: Time histories of fluid pressures, suction and degree of saturation in element E126

8.6 Parametric Study on Bounding Surface Model Parameters

To further investigate the softer simulation response of the embankment, a parametric study on the constitutive model parameters was performed. Out of many model parameters used, the influence of λ and κ on the behavior of the embankment is investigated here. The selection of these two parameters is also supported by discrepancies found in these parameters calculated using different experimental results (Vinayagam, 2004; Ananthanathan, 2002).

The values of λ and κ were reduced by approximately 4.8 times and 1.6 times and the response is compared. The values reduced by 4.8 times are equal to the values calibrated from a different set of experimental results (Ananthanathan, 2002). The horizontal and vertical displacements at nodes N88, N146 and N165 are shown in Figs. 8.18, 8.19 and 8.20, respectively. The element variables, pore liquid pressure, pore gas pressure, matric suction and degree of saturation, in element E126 are shown in Fig. 8.21. Reduction in λ and κ greatly alters the simulation results. The response gets stiffer as λ and κ reduce. The vertical settlement at the top of the embankment is reduced almost by a factor of 10. Similar response is also observed on the horizontal displacement at the left (N88) and right (N165) sides of the embankment. Reduced λ and κ also shows slight decrease in pore liquid and pore gas pressures development.

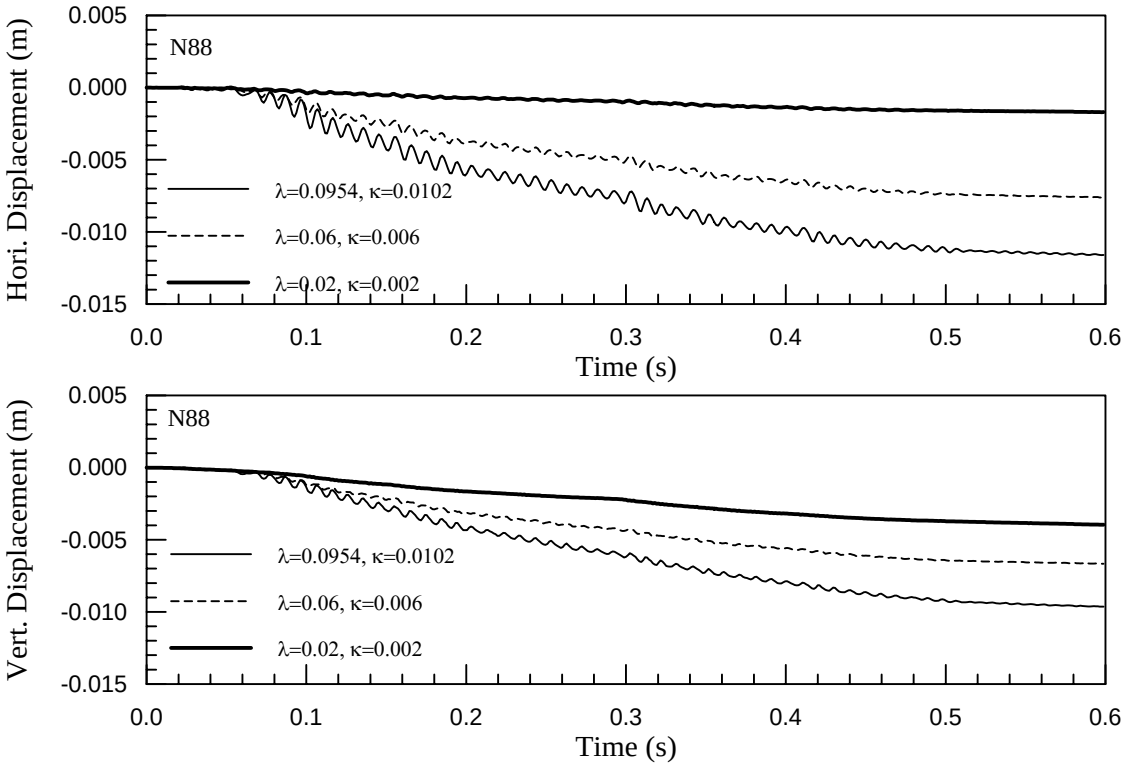

Figure 8.18: Horizontal and vertical displacement at node N88

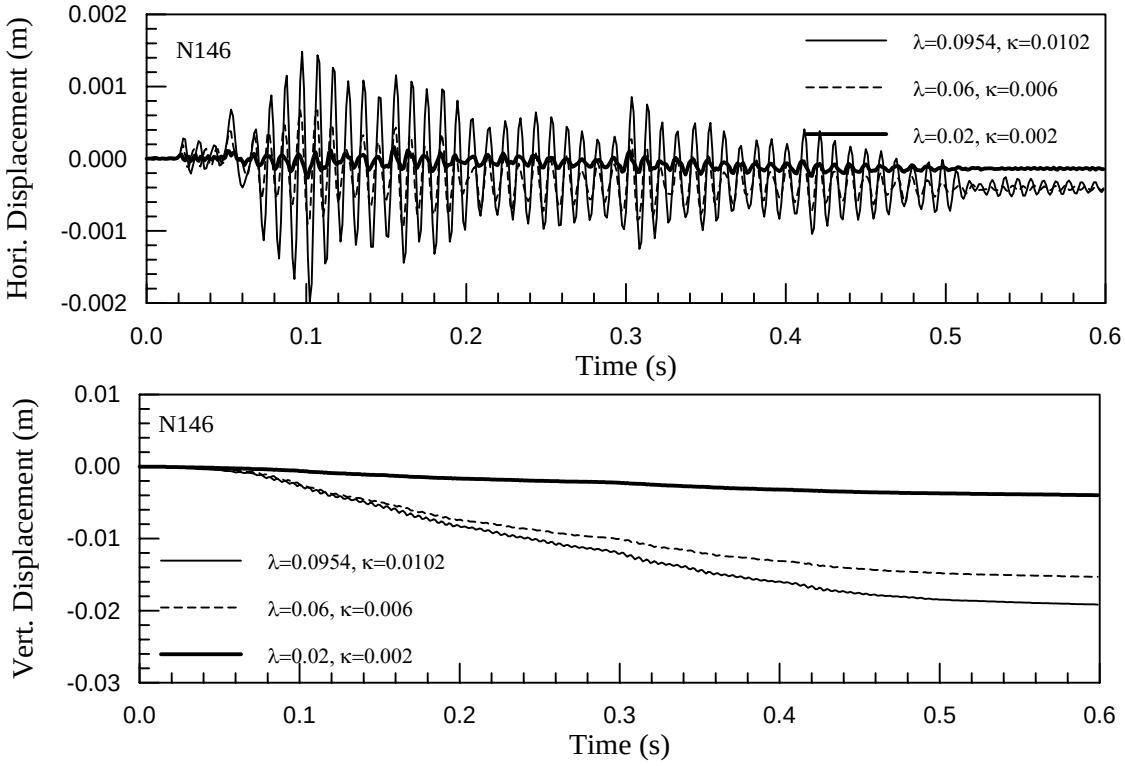

Figure 8.19: Horizontal and vertical displacement at node N146

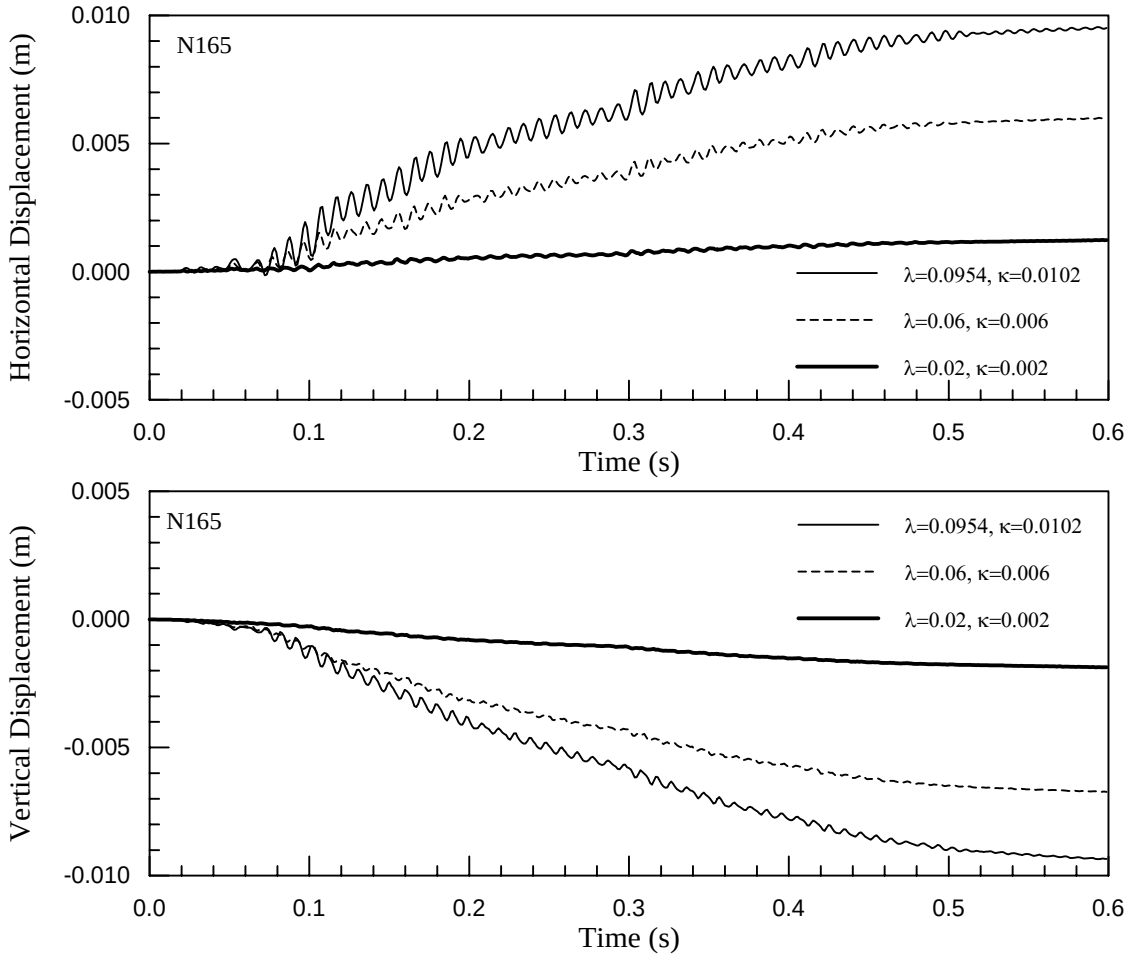

Figure 8.20: Horizontal and vertical displacement at node N165

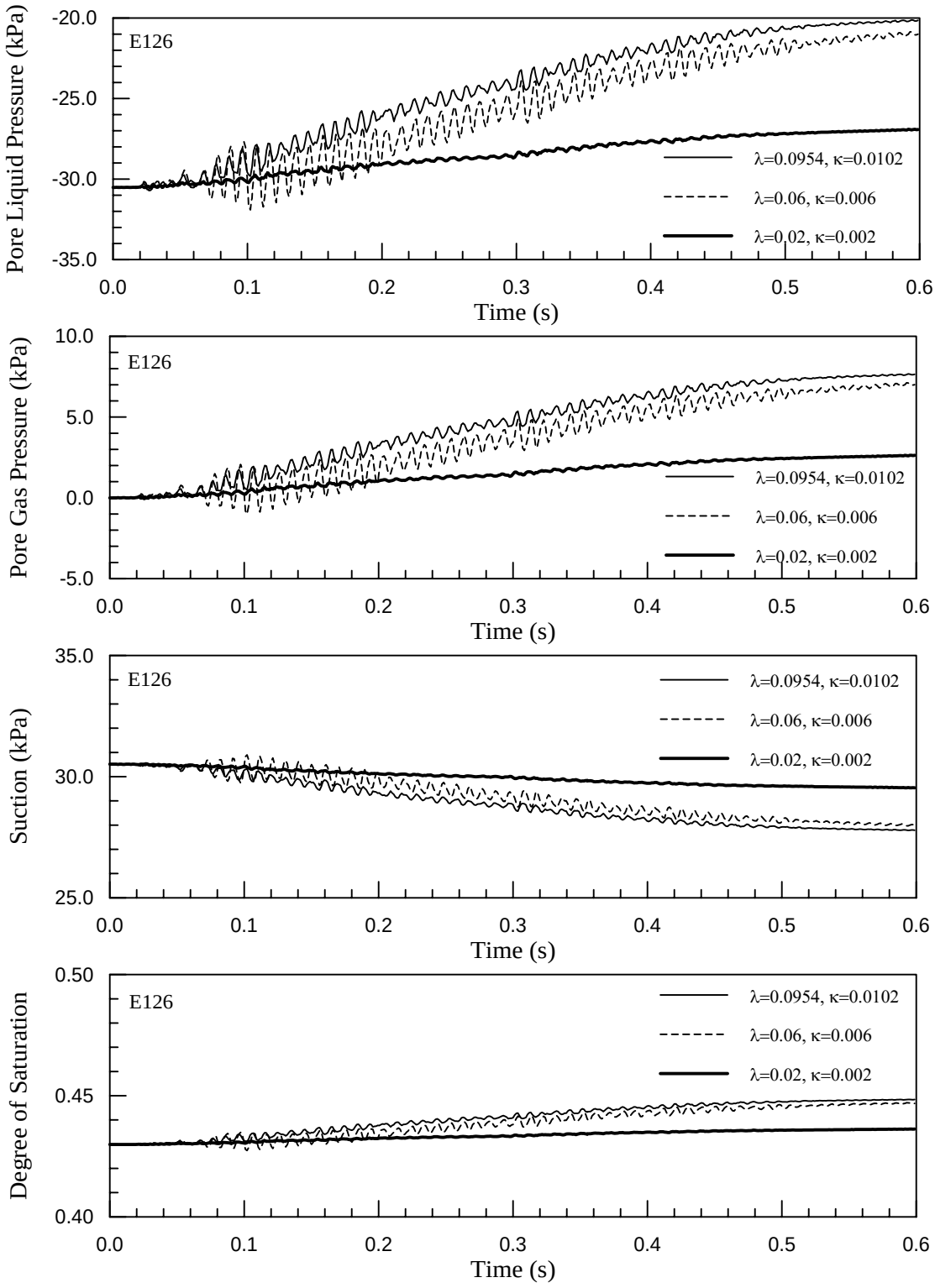

Figure 8.21: Fluid pressures, suction, and degree of saturation at element E126

8.7 Parametric Study on Overconsolidation Ratio

The value of the overconsolidation ratio is a difficult parameter to determine for compacted soils. For this study, the overconsolidation ratio could not be calculated from experimental results. A value of 12.6 was used in the calibration of model parameters (see Fig. 8.5). Therefore, a parametric study was performed to investigate the influence of the overconsolidation ratio.

Different values for overconsolidation ratios (20.0 and 27.4) were used and the predicted responses were compared. The horizontal and vertical displacement at nodes N88, N146 and N165 are shown in Figs. 8.22 to 8.24. Various element variables are shown in Fig. 8.25. The comparison shows that the increase in overconsolidation ratio shows stiffer response. Reductions in settlements, pore liquid pressure and pore gas pressure developments are observed.

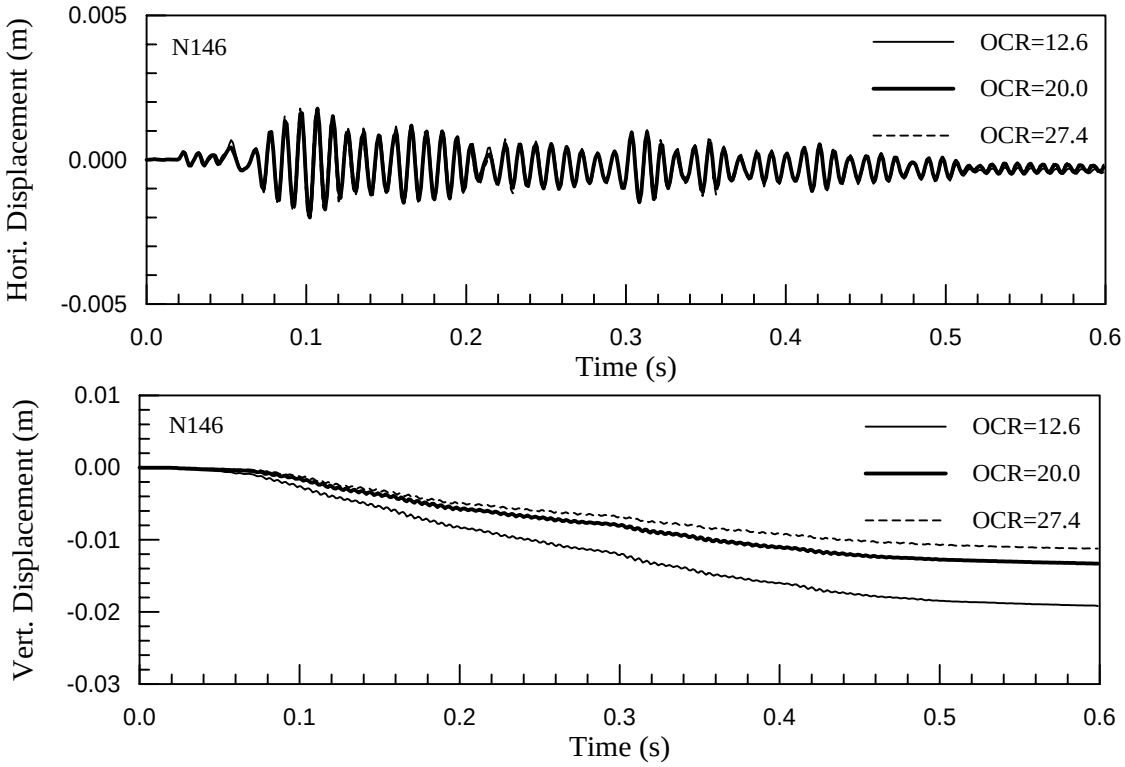

Figure 8.22: Horizontal and vertical displacements at node N146

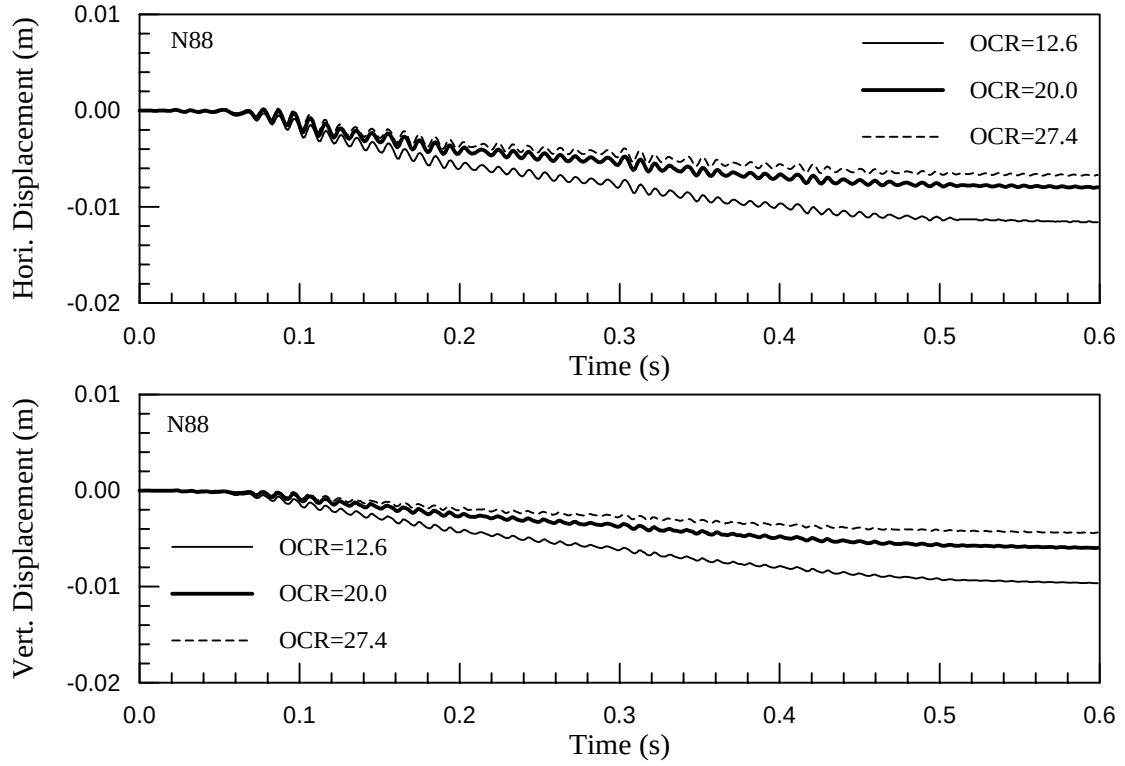

Figure 8.23: Horizontal and vertical displacements at node N88

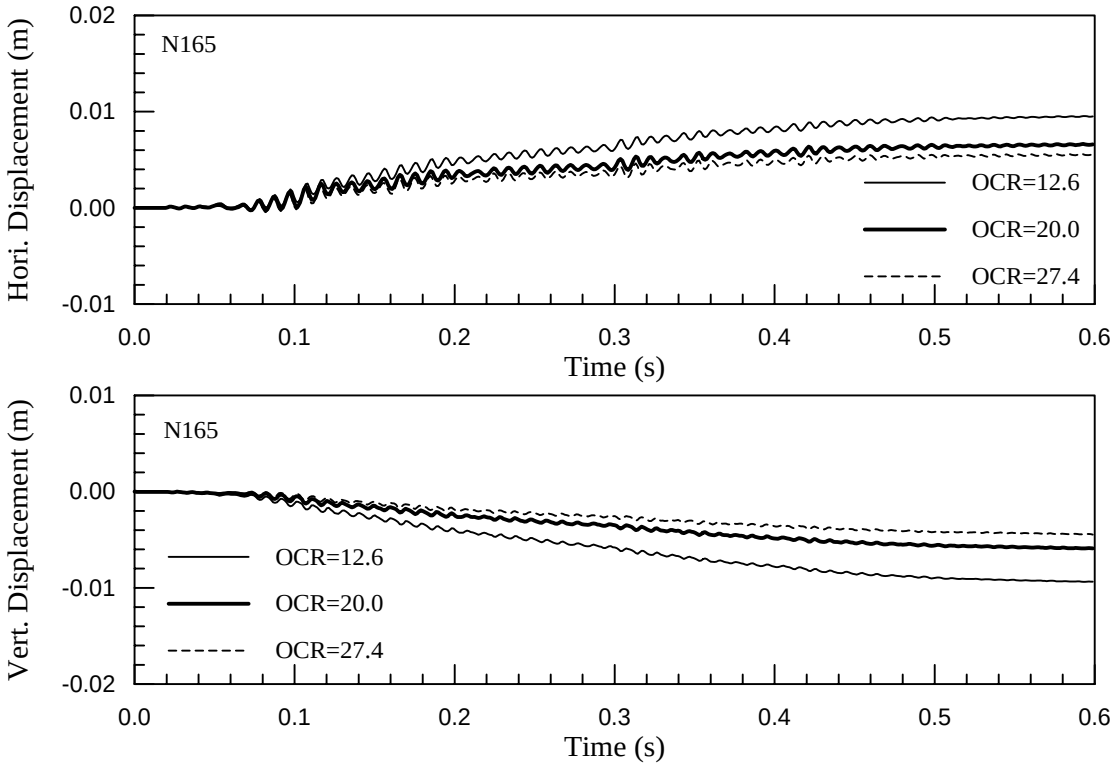

Figure 8.24: Horizontal and vertical displacements at node N165

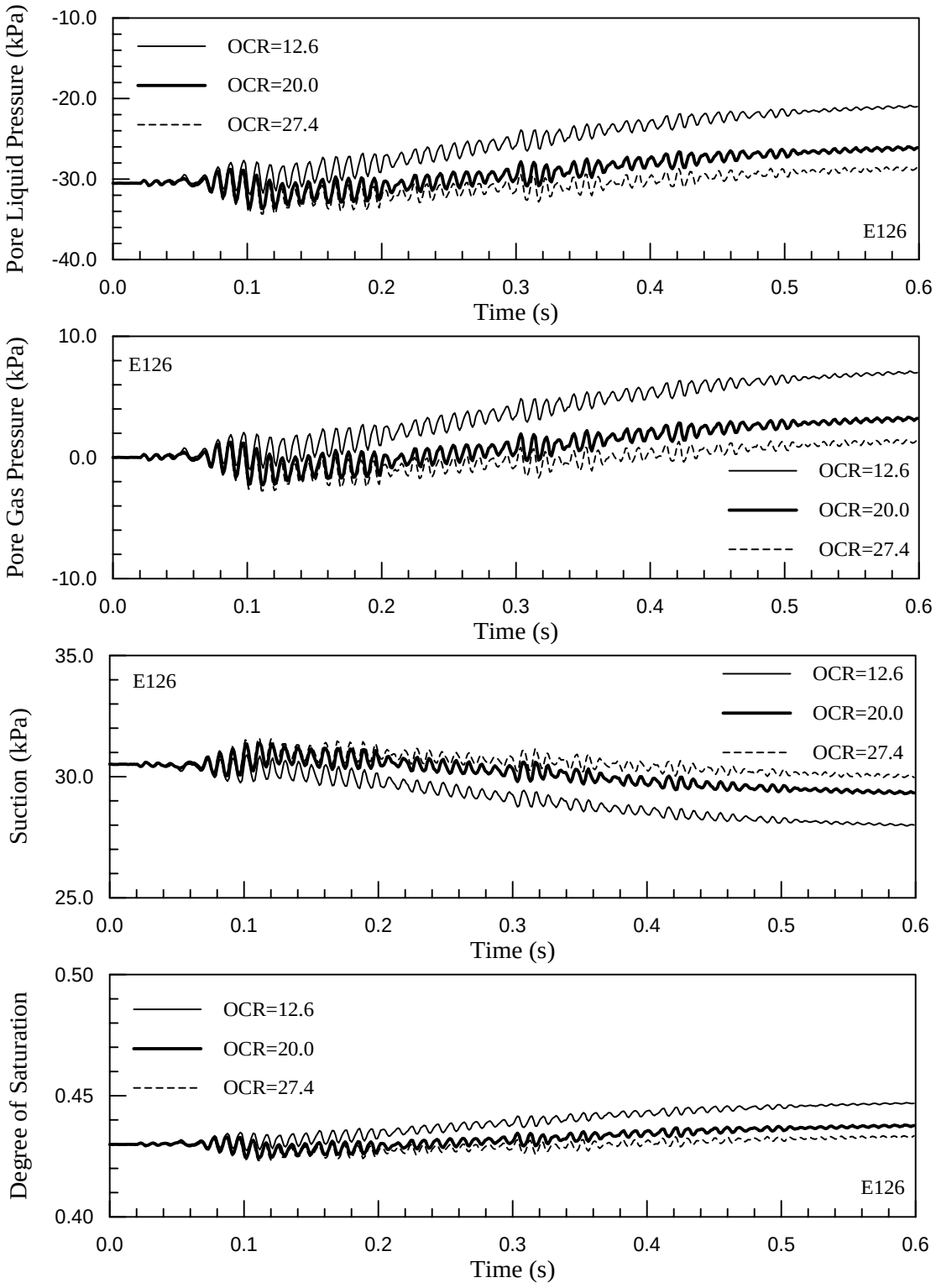

Figure 8.25: Fluid pressures, suction, and degree of saturation at element E126

9 CONCLUDING REMARKS AND FUTURE WORK

9.1 Conclusions

The following conclusions are made from this study.

- The governing equations for the dynamics of saturated and unsaturated soils have been successfully implemented within the TeraScale framework. It is found that the framework-based approach to develop a high performance computing tool is a promising approach for future research.
- The uniform gradient element formulation together with hourglass control scheme is found to be applicable for the simulation of dynamic behavior of porous media. Significant hourglassing is seen for a footing problem with large stress gradients when the uniform gradient elements were used without any hourglass control. The proposed hourglass control scheme is shown to be effective in controlling the hourglassing. For base shaking problems involving only body forces very little hourglassing was seen even when no hourglass controls were used. It is found that the solid stiffness and solid damping hourglass control parameters have minor impact on the displacement and pore pressure time histories. It is also found that the fluid stiffness hourglass control parameter has significant influence on the displacement

and pore pressure time histories. From the parametric study on the fluid stiffness anti-hourglass parameter, it is recommended that this parameter should be less than 0.1%.

- The large and small deformation theories for saturated and unsaturated soils have been implemented within the TeraScale framework. The small deformation analysis is observed to predict larger displacements than the large deformation analysis. These analyses should be compared to experimental results with larger deformations to determine the significance of this observation.
- The complete formulation for unsaturated soil has been successfully solved. Some effects of fluid accelerations and velocities on the overall behavior of unsaturated soils are observed. However, the reduced formulation is found to be computationally very efficient and captures the overall behavior well for the soil studied (Minco Silt) and can be used for preliminary evaluation of earthquake effects on similar unsaturated soils.

9.2 Recommendations

Following recommendations are made for the future research.

- Numerical predictions of the dynamic behavior of unsaturated soils highly depend on the constitutive model used to represent the stress-strain behavior of the soil. A better constitutive model should be developed to predict the behavior of silts such as Minco Silt.
- The complete formulation is highly nonlinear and seems computationally inefficient. Its use and computational efficiency should be further evaluated.

- Centrifuge experiments involving large deformations of saturated and unsaturated soils are needed to validate the numerical models.
- Even though, the transition from saturated to unsaturated soil can be achieved at the governing equation level, it is very difficult to implement the transition into a finite element code. This is mainly due to the different nodal variables used for saturated and unsaturated soils for the finite element implementation. It is important to find an efficient way to implement the changes in primary unknowns and model the transition so that saturated, unsaturated and dry soils can be analyzed using a single finite element implementation.

10 REFERENCES

Aitchison, G. D. (1965). "Moisture Equilibria and Moisture Changes in Soils Beneath Covered Areas." Australia: Butterworths , 278.

Aitchison, G. D., Peter, P., and Martin, R. (1973). "The Instability Indices I_{pm} and I_{ps} in Expansive Soils." *Proceedings of 3rd International Conference in Expansive Soils*, Haifa, Istrail, 2, 101-104.

Alonso, E. E., Gens, A., and Josa, A. (1990). "A Constitutive Model for Partially Saturated Soils." *Geotechnique*, 40(3), 405-430.

Anandarajah, A., and Dafalias, Y. F. (1986). "Bounding Surface Plasticity III: Application to Anisotropic Cohesive Soils." *Journal of Engineering Mechanics*, ASCE, 112(12), 1260-1291.

Ananthanathan, P. (2002). "Laboratory Testing of Unsaturated Minco Silt." M.Sc. Thesis, University of Oklahoma, Norman.

Arulanandan, K., and Scott, R.F. (*editors*) (1993). "Verification of Numerical Procedures for the Analysis of Soil Liquefaction Problems." *Proceeding of the International Conference*, Davis, CA.

Bannmann, D. J., and Johnson, G. C. (1987). "On the kinematics of finite deformation plasticity." *Acta Mechanica*, 70, 1-13.

Barden, L., Madedor, A. O., and Sides, G. R. (1969). “Volume Change Characteristics of Unsaturated Soils.” *Journal of Soil Mechanics and Foundation Division*, 95, 33-52.

Belytschko, T. B. (1974). “Finite Element Approach to Hydrodynamics and Mesh Stabilization.” Computation methods in Nonlinear Mechanics, The Texas Institute for Computational Mechanics.

Belytschko, T. B., Liu, W.K., and Kennedy, J. M., (1983). “Hourglass control in linear and nonlinear problems”, Recent Development in Computer methods for linear and nonlinear analysis, A.S.M.E. Symposium, Houston.

Biot, M. A. (1941). “General Theory of Three-Dimensional Consolidation.” *Journal of Applied Physics*, 12, 155-164.

Bishop, A. W. (1959). “The Principle of Effective Stress.” Teknisk Ukeblad, 106(39), 859-863.

Bishop, A. W., and Eldin, A. K. G. (1950). “Undrained Triaxial Tests on Saturated Sands and Their Significants in the General Theory of Shear Strength.” *Geotechnique*, 2, 13-22.

Brezzi, F. and Fortin, M. (1991), “Mixed and Hybrid Finite Element Methods.” Berlin, Heidelberg, New York: Springer.

Brooks, R. and Corey, A. (1964). “Hydraulic Properties of Porous Media.” Hydrology Paper, 3, Colorado State University, Forts Collins, Colorado.

Butterworth, D., and Hewitt, G. F. (1979). “Two-Phase Flow and Heat Transfer.” Oxford University Press, London, ISBN 0198517181.

Dafalias, Y.F., and Herrmann, L.R. (1982). “Bounding Surface formulation of soil plasticity.” *Journal of Engineering Mechanics*, ASCE, 112(2), 1260-1291.

Dafalias, Y.F. (1986). " Mathematical Foundation and Hypoelasticity." *Journal of Engineering Mechanics*, ASCE, 112(12), 1292-1319.

Dafalias, Y.F., and Herrmann, L.R. (1986). "Bounding Surface Plasticity II: Application to Isotropic Cohesive Soils." *Journal of Engineering Mechanics*, ASCE, 112(2), 1260-1291.

Deshpande, S. D. (1997). "Static and Dynamic Centrifuge Modeling of Unsaturated Soil Embankments." MS Thesis, University of Oklahoma, Norman.

Doherty, W. P., Wilson, E. L., and Taylor, R. L. (1969). "Stress Analysis of Axisymmetric Solids Utilizing Higher Order Quadrilateral Finite Elements." SESM Report No. 69-3, Department of Civil Engineering, University of California, Berkeley.

Flanagan, D.P., and Belytschko, T. (1984). "Eigenvalues and Stable Time Steps for the Uniform Strain Hexahedron and Quadrilateral." *Journal of Applied Mechanics*, 51, 35-40.

Flanagan, D.P., and Belytschko, T. (1981). "A Uniform Strain Hexahedron and Quadrilateral with Orthogonal Hourglass Control." *International Journal for Numerical in Engineering*, 17, 679-706.

Fraeijs de Veubeke, B. (1965). "Displacement and Equilibrium Models in the Finite Element Method." in stress analysis, eds. O.C.Zienkiewicz and G.S.Holister. London:John Wiley.

Fredlund, D. G., and Morgenstern, N. R. (1977). "Stress State Variables for Unsaturated Soil." *ASCE Journal of Geotechnical Engineering Division*, 103, 447-466.

Fredlund, D. G. (1978). “Two-Dimensional Finite Element Program using Constant Strain Triangles (FINIEL).” University of Saskatchewan Transportation and Geotech. Group, Internal Report CD-2.

Fredlund, D. G., and Rahardjo, H. (1993). “Soil Mechanics for Unsaturated Soils.” A Wiley-Interscience Publication, John Wiley and Sons, INC, New York, ISBN 0-471-85008-X, 517 pages.

Fredlund, D. G., and Xing, A. (1994). “Equation for the Soil Water Characteristic Curve.” *Canadian Geotechnical Journal*, 31, 521-532.

Gardner, W. R. (1958). “Laboratory Studies of Evaporation from Soil Column in the Presence of a Water-Table.” Soil Science of America, 85, 244.

Gouse, S. W. (1966). “An Index to the Two-Phase Gas-Liquid Flow Literature.” M.I.T. Press, Cambridge, Massachusetts.

Hassanizadeh, S. M., and Gray, W. G. (1979). “General Conservation Equation for Multi-Phase System: 1. Averaging Procedure.” *Advances in Water Resources*, 2, 131-144.

Herrmann, L. R. (1965). “Elasticity Equations for Incompressible and Nearly Incompressible Materials by Variational Theorem.” *American Institute of Aeronautics and Astronautics Journal*, 3(10), 1896-1900.

Herrmann, L. R., and Mish, K.D. (1983). “User’s Manual for SAC2: A Two-Dimensional, Nonlinear, Time Dependent, Soil Analysis Code using the Bounding Surface Plasticity Model.” Technical Report, University of California, Davis.

Hilber, H. M., Hughes, J. R., and Taylor, R. L. (1977). “Improved Numerical Dissipation for Time Integration Algorithms in Structural Dynamics.” *Earthquake Engineering and Structural Dynamics*, 5, 283-292.

Hughes, T. J. R. (1983). "Analysis of Transient Algorithms with Particular Reference to Stabiliy." in Computational Methods for Transient Analysis, T.J.R. Hughes and T. Belyschko(eds.), North-Holland, Amsterdam.

Hughes, T. J. R. (1984). "Numerical Implementation of Constitutive Models: Rate Independent Deviatoric Plasticity." in: S. Nemat- Nasser, R. Asaro and G. Hegemier, eds., Theoretical Foundations for Large-Scale Computations of Nonlinear Material Behaviour, Martinus Nijhoff, Dordrecht.

Hughes, T. J. R., and Allik, H. (1969). "Finite Elements for Compressible and Incompressible Continua." *Proceedings of the Symposium on Civil Engineering*, Vanderbit University, Nashville, Tennessee, 27-62.

Hughes, T. J. R., Liu, W. K., and Brooks, A. (1979). "Review of Finite Element Analysis of Incompressible Viscous Flows by the Penalty Function Formulation." *Journal of Computational Physics*, 30(1), 1-60.

Hughes, T. J. R., and Pister, K. S. (1978). "Consistent Linearization in mechanics of Solids." *Computers and Structures*, 8, 391-397.

Jennings, E., and Burland, J. B. (1962). "Limitations to the Use of Effective Stresses in Partly Saturated Soils." *Geotechnique*, 12(2), 125-144.

Kiousis, P. D., Voyiadjis, G. Z., and Tumay, M, T. (1988). "A Large Strain Theory and its Application in the Analysis of the Cone Penetration Mechanism." *International Journal for Numerical and Analytical Methods in Geomechanics*, 12, 45-60.

Kutter, B. L. (1982). "Centrifugal Modeling of the Response of the Clay Embankments to Earthquakes." PhD Dissertation, Cambridge University, England.

Lee, E. H. (1981). “Some comments on elastic-plastic analysis.” *International Journal of Solids and Structures*, 17, 859-872.

Li, X., and Zienkiewicz, O. C. (1992). “Multiphase Flow in Deforming Porous Media and Finite Element Solutions.” *Computers and Structures*, 45(2), 221-227.

Li, X., Thomas, H. R., and Fan, Y. (1999). “ Finite Element method and Constitutive Modeling and Computation for Unsaturated Soils.” *Computer Methods in Applied Mechanics and Engineering*, 169, 135-159.

Lubarda, V. A., and Lee, E. H. (1981). “A correct definition of elastic and plastic deformation and its computational significance.” *Journal of Applied Mechanics*, 48, 35-40.

Malkus, D. S., and Hughes, T. J. R. (1978). “Mixed Finite Element Methods-Reduced and Selective Integration Techniques: A Unification of Concepts.” *Computer Methods in Applied Mechanics and Engineering*, 15, 63-81.

Maechen, G., and Sack, S. (1964). “The Tensor Code.” *Methods in Computational Physics*, 3, Academic Press, 181-210.

Manzari, T. M. (1996). “On Finite Deformation Dynamic Analysis of Saturated Soils.” Achieves of Mechanics, 48(2), 281-310.

Manzari, T. M. (2004). “Large Deformation Analysis in Dynamics of Saturated Soils.” 17th ASCE Engineering Mechanics Conference, University of Delaware, Newark, DE.

Matyas, E. L., and Radhakrishna, H. S. (1968). “Volume Change Characteristics of Partly Saturated Soils.” *Geotechnique*, 18(4), 432-448.

Muraleetharan, K.K., Mish, K.D., and Arulanandan, K., (1994). "A Fully Coupled Nonlinear Dynamic Analysis Procedure and its Verification Using Centrifuge Test Results." *International Journal for Numerical and Analytical Methods in Geomechanics*, 18, 305-325.

Muraleetharan, K.K., Mish, K.D., Yogachandran, C., and Arulanandan, K. (1988). "DYSAC2 (Version 1.0): Dynamic soil analysis code for 2-dimensional problems." Computer Code, University of California, Davis.

Muraleetharan, K.K., Mish, K.D., Yogachandran, C., and Arulanandan, K. (1997). "User's manual for DYSAC2 (Version 7.0): Dynamic soil analysis code for 2-dimensional problems." Technical Report, University of Oklahoma, Norman.

Muraleetharan, K. K., and Nedunuri, P.R. (1998). "A Bounding Surface Elastoplastic Constitutive Model for Monotonic and Cyclic Behavior of Unsaturated Soils." *Proceedings (in CD ROM), 12th Engineering Mechanics Conference*, ASCE, La Jolla, CA, 1331-1334.

Muraleetharan, K. K., and Wei, C. –F. (1999a). "Dynamics Behavior of Unsaturated Porous Media: Governing Equations using the Theory of Mixtures with Interfaces (TMI)." *International Journal of Numerical Methods in Geomechanics*, 23, 1579-1608.

Muraleetharan, K. K., and Wei, C. –F. (1999b). "U_DYSAC2: Unsaturated Dynamic Soil Analysis Code for 2-dimensional Problems." Computer Code, University of Oklahoma, Norman.

Muraleetharan, K. K., Wei, C. –F., and Liu, C. (2005). "A Comprehensive approach to modeling the behavior of unsaturated soils using an elastoplastic framework."

Proceeding of the Second Japan-U.S. workshop on Geomechanics, Kyoto, Japan, September, ASCE, GeoInstitute (in print).

Nagtegaal, J. C., and de Jong, J. E. (1981). "Some Aspects of Non-isotropic Work-hardening in Finite Strain Plasticity." *in: E.H. Lee and i R.L. Mallet, eds.*, Plasticity of Metals at Finite Strains, Proc. Research Workshop, Stanford University, 65-102.

Newmark, N. M. (1959). "A Method for Computation of Structural Dynamics." *Proceedings ASCE*, 85 EM3, 67-94.

Petschek, A. G., and Hanson, M. E. (1968). " Difference Equations for two-dimensional elastic flow." *Journal of Computational Physics*, 3, 307-321.

Prevost, J. H. (1980). "Mechanics of Continuous Porous Media." *International Journal of Engineering Science*, 18(6), 787-800.

Prevost, J.H. (1983). "Implicit-explicit Schemes for Nonlinear Consolidation." *Computer Methods in Applied Mechanics and Engineering*, 39(2), 225-239.

Ravichandran, N., Muraleetharan, K.K., and Taylor, L.M., (2004). "Dynamics of Multiphase Porous Media using a Finite Element Framework." 17th ASCE Engineering Mechanics Conference, University of Delaware, Newark.

Schrefler, B. A., Simoni, L., Li Xikui and Zienkiwicz, O. C. (1990). "Mechanics of Partially Saturated Porous Media." in Desai, C. S. and Gioda, G. (eds), Numerical Methods and Constitutive Modelling In Geomechanics, CISM Lecture Notes, Springer-Verlag, Wein, 169-209.

Simo, J. C. (1992). "Algorithms for Static and Dynamic Multiplicative Plasticity that Preserve the Classical Return Mapping Schemes of the Infinitesimal Theory." *Computer Methods in Applied Mechanics Engineering*, 99, 61-112.

Simo, J. C., and Hughes, T. J. R. (1986). “Elastoplasticity and Viscoplasticity-Computational Aspects.” Springer Ser. Applied Mathematics, Springer, Berlin.

Simo, J. C., and Rifai, M. S. (1990). “A Class of Assumed Strain Methods and the Method of Incompatible Modes.” *International Journal for Numerical Methods in Engineering*, 29, 1595-1638.

Simo, J. C., and Taylor, R. L. (1991). “Quasi-incompressible Finite Elasticity in Principal Stretches: Continuum Basis and Numerical Algorithms.” *Computer Methods in Applied Mechanics and Engineering*, 85, 273-310.

Skempton, W. (1961). “Effective Stress in Soils, Concrete and Rocks” Conference on Pore Pressure, London: Butterworths, 4-16.

Szabo, L., and Balla, M. (1988). “Comparison of Some Stress Rates.” *International Journal of Solids and Structures*, 25(3), 279-297.

Taylor, L. M., and Becker, E. B. (1983). “Some Computational Aspects of large Deformation, Rate-Dependent Plasticity Problems.” Computer Methods in Applied Mechanics and Engineering, 41, 251-277.

TeraScale Framewrok. (2001). “The TeraScale Framework”, Version 1.0 TeraScale, LLC, Cedar Crest, NM.

Terzaghi, K. (1936). “The Shear Resistance of Saturated Soils”, 1st International Conference on Soil Mechanics and Foundation Engineering, 1, 54-56.

Truesdell, C., and Toupin, R. (1960). “The Classical Field Theories.” Handbook der Physik, 3(1), Springer, Berlin.

van Genuchten, M. Th. (1980). “A closed form equation predicting the hydraulic conductivity of unsaturated soils.” *Soil Science Society of America Journal*, 44, 892-898.

Vaunat, J., Cante, J. C., Ledesma, A., and Gens, A. (2000). “A Stress Point Algorithm for an Elastoplastic Model in unsaturated Soils.” *International Journal of Plasticity*, 16, 121-141.

Vinayagam, T. (2004). “Understanding the Stress-Strain Behavior of Unsaturated Minco Silt using Laboratory Testing and Constitutive Modeling.” M.S. Thesis, University of Oklahoma, Norman.

Wei, C. –F. (2001). “Static and Dynamic Behavior of Multi-Phase Porous Media: Governing Equations and Finite Element Implementation.” PhD Dissertation, University of Oklahoma, Norman.

Wei, C. -F., and Muraleetharan, K.K. (2002a). “ A continuum theory of porous media saturated by multiphase fluids: I. Linear poroelasticity.” *International Journal of Engineering Science*, 40, 1807-1833.

Wei, C. -F., and Muraleetharan, K.K. (2002b). “A continuum theory of porous media saturated by multiphase fluids: II. Lagrangian discription and variational structure.” *International Journal of Engineering Science*, 40, 1835-1854.

Wheeler, S. J., and Sivakumar, V. (1995). “An Elasto-plastic Critical State Framework for Unsaturated Soil.” *Geotechnique*, 45(1), 35-53.

Wheeler, S. J. (1996). “Inclusion of Specific Water Volume Within an Elasto-Plastic Model for Unsaturated Soil.” *Canadian Geotechnical Journal*, 33(1), 42-57.

Xikui, L., and Zienkiwicz, O. C. (1992). “Multiphase Flow in Deforming Porous Media and Finite Element Solution.” *Computers and Structures*, 45(2), 211-227.

Zienkiewicz, O. C., Taylor, R.L., and Too. J. M. (1971). “Reduced Integration Technique in General Analysis of Plates and Shells.” *International Journal for Numerical Methods in Engineering*, 3, 275-290.

Zienkiewicz, O. C., and Godbole, P. N. (1975). “Viscous Incompressible Flow with Special Reference to Non-Newtonian(Plastic) Fluids.” in Finite Elements Methods in Fluids, 1, London: John Wiley.

Zienkiewicz, O. C., Humpheson, C., and Lewis, R. W. (1977). “A Unified Approach to Soil Mechanics Problems (Including Plasticity and Viscoplasticity).” G. Gudehus, (Ed.) in Finite Elements in Geomechanics, Wiley, 151-178.

Zienkiewicz, O. C., and Shiomi, T. (1984). “ Dynamic Behavior of Saturated Porous Media; The Generalized Biot Formulation and its Numerical Solution.” *International Journal for Numerical Methods in Geomechanics*, 8, 71-96.

Zienkiewicz, O.C., Taylor, R.L. (2000). “The Finite Element Method.” The Basis, Butterworth-Heinemann Publication, Linacre House, Jordan Hill, Oxford, ISBN 0 7506 5049 4, 1, Fifth Edition, 663 pages.

Zienkiewicz, O. C., and Taylor, R.L. (2000). “The Finite Element Method.” Solid Mechanics, Butterworth-Heinemann Publication, Linacre House, Jordan Hill, Oxford, ISBN 0 7506 5055 9, 2, Fifth Edition, 459 pages.